國 立 交 通 大 學

土木工程學系

博 士 論 文

時域反射量測技術改良及於水土混和物之應用

Improved Time Domain Reflectometry Measurements and Its

Application to Characterization of Soil-Water Mixtures

研 究 生：鐘志忠

指導教授：林志平　教授

中華民國九十七年七月

Improved Time Domain Reflectometry Measurements and Its Application to Characterization of Soil-Water Mixtures

研 究 生：鐘志忠   Student：Chih-Chung Chung

指導教授：林志平   Advisor：Chih-Ping Lin

國 立 交 通 大 學

土 木 工 程 學 系

博 士 論 文

A Thesis

Submitted to Department of Civil Engineering

College of Engineering

National Chiao Tung University

in partial Fulfillment of the Requirements

for the Degree of

Doctor of Philosophy

in

Civil Engineering

July 2008

HsinChu, Taiwan, Republic of China

中華民國九十七年七月

時域反射量測技術改良及於水土混和物之應用

學生：鐘志忠　　　　　　　　　　　　　指導教授：林志平 博士

國立交通大學土木工程學系

中文摘要

時域反射法(Time domain reflectometry, TDR)為可量測物體的視介電度(Apparent dielectric constant)、導電度(Electrical conductivity)以及介電頻譜(Dielectric spectroscopy)特性之新穎技術，且具現地量測及多工(Multi-function)優勢，因此近來被廣泛應用至土壤或混擬土等材料性質量測。然而目前 TDR 視介電度及導電度量測方法有待釐清之處，且 TDR 的介電頻譜量測方法過於複雜，高頻量測結果可靠性不足，所以本研究的目的在於發展改良 TDR 量測方法，並提出 TDR 感測器製作原則，提供正確穩定的量測資料，以應用於土水混和物之電學性質探討。

TDR 視介電度可由不同走時分析方法求得，但此一量測值缺乏實際物理意義，因此本研究採用數值模擬方法，探討視介電度及其等效對應頻率受材料導電度、介電頻散特性及纜線阻抗等因子影響，瞭解視介電度量測實務限制，進而提倡介電頻譜量測之重要性。本文並以實際量測與數值模擬，分析介電頻譜量測靈敏度與可靠度，探討介電頻譜量測誤差來源與可能改善方法。鑑於 TDR 介電頻譜高頻量測限制，本研究發展 TDR 頻率域相位速度分析方法，模擬分析結果顯示此一方法能有效提供材料高頻的相位速度，且於土壤含水量量測應用，不受導電度、土壤種類與纜線電阻影響，具有極大發展潛力。

本研究另外針對 TDR 導電度量測，建立考慮纜線電阻之 TDR 導電度量測理論與系統誤差率定方法，配合模擬分析與實驗結果，並考量穩定反應所需之資料擷取時間長度，證實所提理論與率定方法可克服系統電阻以及系統誤差影響，提供材料正確導電度量測。

本研究另採用 3D 電磁波模擬分析工具，以及量測靈敏度理論推導，提供 TDR 感測器製作原則。為達到深層土壤（岩石）性質探討目的，研發之 TDR 圓錐貫入器 (TDR penetrometer)可同時提供材料之視介電度及導電度量測。配合此一 TDR 圓錐貫入器，於石門水庫進行水庫底層淤泥性質探討，基於底泥導電度量測結果，可推估底層淤泥含量與工程物理性質。由於近來台灣水庫因洪颱事件而產生大量入庫泥沙之危機，本研究進一步利用視介電度與感測器製作研究成果，發展新式走時分析方法以及 TDR 相位速度分析方法，研發高精度懸浮泥沙濃度量測技術，期以 TDR 多工多點的優勢，建置 TDR 自動化懸浮泥沙濃度量測。唯未來研究將建議持續現場量測驗證，以提供穩定量測資料。

Improved Time Domain Reflectometry Measurements and Its Application to Characterization of Soil-Water Mixtures

Student: Chih-Chung Chung   Advisor: Dr. Chih-Ping Lin

Department of Civil Engineering

National Chiao Tung University

ABSTRACT

Time domain reflectometry (TDR) can be used to measure apparent dielectric constant, electrical conductivity, and dielectric permittivity as a function of frequency. This relatively new technique is gaining popularity in characterization of engineering materials, such as suspended suspension, soil, concrete, etc, due to its versatility and applicability in field measurements. However, some disputes about the measurement methods for apparent dielectric constant and electrical conductivity (EC) have not been resolved. And dielectric spectroscopy remains relatively difficult in practice. The objectives of this study were to investigate and improve the TDR measurement techniques, provide guidelines for TDR probe design, and, as an application example, apply TDR to characterization of soil-water mixture.

Since the apparent dielectric constant derived from various travel time analyses dose not have clear physical meanings, this study first investigated the influence factors, such as electrical conductivity, dielectric dispersion, and cable resistance, and associated effective frequencies. The applicability and limitations of travel time analyses are revealed with emphasis on the importance of dielectric spectroscopy. The dielectric spectrum, although more informative, is difficult to be reliably obtained. This study further examined the

sensitivity and reliability of dielectric spectroscopy to identify the source of uncertainty and provide preferred guidelines. A novel approach to obtain dielectric permittivity at high frequencies was proposed based on the frequency domain phase velocity.

The TDR EC measurement is more straightforward, but methods accounting for the cable resistance remain controversial; and the effect of TDR recording time has been underrated when long cables are used. A comprehensive full waveform model and the DC analysis were used to show the correct method for taking account of cable resistance and guideline for selecting proper recording time. In addition, a system error in typical TDR EC measurements was identified and a countermeasure was proposed, leading to a complete and accurate procedure for TDR EC measurements.

Following the studies on TDR dielectric permittivity and EC measurements, this study further investigated the factors associated with probe designs for both types of measurements. The sensitivity of TDR measurements as affected by the probe parameters was discussed to provide guidelines for probe design. In addition, a penetrometer type of TDR probes was developed to allow simultaneous measurements of dielectric permittivity and electrical conductivity during cone penetration for measurements at depths.

Although the aforementioned TDR measurement methodology was originally developed with soil applications in mind, the sediment problems in Shihmen Reservoir manifested by the Typhoon Aere in 2004 provides imperative opportunities for TDR applications. The TDR measurement techniques were adapted for characterization of soil-water mixtures. TDR penetrometer was integrated with the Marchetti dilatometer (DMT) and the TDR/DMT probe was pushed into the bottom mud to determine simultaneously, the solid concentration, stiffness and stress state of the bottom mud. A novel TDR probe and measurement procedure were further developed for accurate monitoring of suspended sediment concentration in fluvial and reservoir environment.

誌謝

TABLE OF CONTENTS

LIST OF TABLES

LIST OF FIGURES

LIST OF SYMBOLS

A: Resistance correction factor

A_s: Specific surface area of soil particle (m^2 g^{-1})

B: Magnetic flux density (Wb m^{-2})

c: Light velocity in vacuum ($2.998 * 10^8$ m sec^{-1})

E: Electrical field (N C^{-1} or volt m^{-1})

F_m: Magnetic force (N)

F_r: Volumetric percentage of inclusion

H: Magnetic field (A m^{-1})

$H(f)$:   TDR system function

f: Frequency (Hz)

f_{bw}:   Frequency bandwidth (Hz)

f_{rel}:   Relaxation frequency (Hz)

J: Current density (A m^{-2})

j: $\sqrt{-1}$

K_a: Apparent dielectric constant

K_p: Geometric factor of TDR probe (m^{-1})

K_{ss}:   Apparent dielectric constant of soil solid

K_w: Apparent dielectric constant of water

L: Probe length (m)

M: Magnetization (A m^{-1})

N_x: Depolarization factor in the x-direction of Cartesian coordinate system

P: Polarization vector (C m^{-2})

q: Electric charge ($-1.602 * 10^{-19}$ C)

R_{cable}:   Cable resistance (Ω)

R_L: Load resistance (Ω)

R_{sample}:   Sample resistance (Ω)

S_{11}:   System scatter function

SS: Volumetric percentage of suspended sediment

$S_{\bar{m}}$:   Normalized sensitivity by physical parameter m

t_0:   Time difference between selected point and start reflection point (sec)

t_r: 10% ~ 90% rise time (sec)

t_s:	True travel time in the measuring probe (sec)
u:	velocity vector (m sec^{-1})
v_r:	Reflection voltage (volt)
v_s:	Source pulse level of TDR pulser (volt)
v_0:	Input step pulse level (volt)
v_∞:	Steady state of TDR waveform (volt)
V_a:	Apparent velocity (m sec^{-1})
V_{ph}:	Phase velocity (m sec^{-1})
Z_c:	Characteristic impedance (Ω)
Z_{in}:	Input impedance (Ω)
Z_L:	Terminal impedance (Ω)
Z_p:	Characteristic impedance in air (Ω)
Z_S:	Source impedance (Ω)
α:	Constant shape factor for dielectric mixing model
$\alpha(f)$:	Attenuation constant (m^{-1})
α_R:	Resistance loss factor (sec$^{-1/2}$)
β:	Probe constant (S m^{-1})
$\beta(f)$:	Imaginary part of propagation constant (m^{-1})
γ:	Propagation constant (m^{-1})
γ_d:	Dry density of soil (g cm^{-3})
γ_s:	Gravity density of soil solid (g cm^{-3})
γ_w:	Gravity density of water (g cm^{-3})
Δt:	Apparent TDR travel time in the measuring probe (sec)
$\Delta\tau$:	Measured TDR travel time = $t_0 + t_s$ (sec)
$\Delta\phi$:	Phase angle of cross-spectral density
ε:	Absolute permittivity (F m^{-1})
ε_0:	Permittivity of free space (8.854*10^{-12} F m^{-1})
ε_r:	Relative permittivity or dielectric constant
ε_r':	Real part of relative permittivity
ε_r'':	Imaginary part of relative permittivity
ε'_{dc}:	Real part of relative permittivity lower than resonant frequency
ε'_∞:	Real part of relative permittivity higher than resonant frequency
ε_{eff}'':	Effective imaginary permittivity

ε_r^*:	Equivalent complex permittivity
ε_r^{ii}:	Imaginary part of equivalent complex permittivity
ξ:	Factor accounting possible spread in relaxation frequency
η_0:	Intrinsic impedance ($\fallingdotseq 120\pi$ Ω)
μ:	Magnetic permeability (H m^{-1})
μ_0:	Magnetic permeability in free space ($4\pi*10^{-7}$ H m^{-1})
μ_r:	Relative magnetic permeability
μ_e:	Electron mobility
ρ:	Reflection coefficient
ρ':	Reflection coefficient without system error
ρ_e:	Charge density of drift electrons (c m^{-1})
ρ_{open}:	Reflection coefficient in open-end case
ρ_{scale}:	Scaled reflection coefficient
ρ_w:	Density of water (g cm^{-3})
ρ_∞:	Steady state of reflection coefficient
$\rho_{\infty, air}$:	Steady state of reflection coefficient in air
$\rho_{\infty, SC}$:	Steady state of reflection coefficient in shorted-end case
$\rho_{\infty, scale}$:	Scaled reflection coefficient by series resistors model
σ:	Electrical conductivity (S m^{-1})
σ_{dc}:	DC conductivity (S m^{-1})
σ_{eff}:	Effective conductivity (S m^{-1})
σ_{GT}:	Electrical conductivity estimated by Giese and Tiemann method (S m^{-1})
σ_w:	Electrical conductivity of water(S m^{-1})
χ_e:	Electric susceptibility
χ_m:	Magnetic susceptibility
ω:	Soil water content
ω_{res}:	Resonant frequency

1 Introduction

1.1 Motivation

Electrical properties are highly correlated with the physical and mechanical properties of a composite material and are more conveniently measured or monitored. Hence, electrical methods hold great potential to characterize composite materials, such as soil, concrete, and suspensions. For instance, direct current (DC) resistivity method is commonly applied to measure resistivity (reciprocal of electrical conductivity, EC) of soils and concrete. However, resistivity alone is not uniquely related to complex composition of a composite material. Electrical properties include dielectric constant and electrical conductivity, and dielectric constants of composite materials are often functions of frequency due to interactions between phases.

The technique of Time Domain Reflectometry (TDR) was firstly applied for fault detection in transmission lines in the 50's. TDR is composed of a pulser and a transmission line. The pulser sends a step pulse into the transmission line and the reflection signal (or the waveform) caused by impedance mismatch along the transmission line is recorded by the sampler in the time domain. By analyzing the reflected signal, the fault in the transmission line can be easily located. Topp et al. (1980) adopted the TDR technique for the estimation of the soil moisture content, in which apparent dielectric constant (K_a) was defined by the apparent travel time in the TDR waveform and experimentally related to soil water content. TDR was found also capable of determining the EC through the steady state of signal (Giese and Tiemann, 1975; Topp et al., 1988; Zegelin et al., 1989). Furthermore, combining transmission line theory and spectral analysis of reflected signals leads to estimation of dielectric permittivity at various frequency (i.e. dielectric spectroscopy) (Heimovaara, 1992; Lin, 1999). These developments open new TDR applications on material characterization in

geotechnical engineering, agriculture engineering, and environmental engineering.

TDR is gaining popularity in characterizing materials based on electrical properties due to its versatility (simultaneous measurements of apparent dielectric constant, electrical conductivity, and dielectric spectrum) and applicability in field measurements. However, improvement of TDR measurements remains an active research topic. First of all, various travel time analyses have been proposed to determine the apparent dielectric constant. But the physical meaning of the apparent dielectric constant is not clear. How actual electrical properties and system parameters affect the apparent dielectric constant have not been extensively investigated. The dielectric spectrum, although more informative, is difficult to be reliably obtained. Works remain to be done to increase the stability and frequency range of dielectric spectroscopy. The TDR EC measurement is straighter forward, but methods accounting for the cable resistance remain controversial, and the effect of TDR recoding time has been underrated when long cables are used. The probe design also plays an important role for each type of TDR measurement. The sensitivity of TDR measurement as affected by the probe parameters and design of probe type for geotechnical and hydrological applications require further study.

Since methodologies and probe design of TDR technology remain disputes so far, measurements of dielectric properties using TDR may lead improprieties in engineering implementation; therefore, this study will present improved TDR measurements and its applications to the characterization of materials.

1.2 Objectives

The objectives of this study were to investigate and improve the TDR measurement techniques, provide guidelines for TDR probe design, and, as an application example, apply TDR to characterization of soil-water mixture.

Chapter 2 of this thesis firstly reviews electromagnetic properties of materials and TDR methods, including K_a, EC, and dielectric spectroscopy.   Chapter 3 deals with measurement of dielectric permittivity. It first investigates the effects of EC, dielectric dispersion, and cable resistance on the apparent dielectric constant and associated effective frequency. The applicability and limitations of travel time analysis are revealed with emphasis on the importance of dielectric spectroscopy. The second part of the chapter 3 examines the sensitivity and reliability of dielectric spectroscopy to identify the source of uncertainty and provides guidelines. A novel approach to obtain the dielectric permittivity at high frequency, where dielectric spectroscopy is most uncertain, based on the frequency domain phase velocity.

In chapter 4, a comprehensive full waveform model and the DC analysis were used to show the correct method for taking account of cable resistance and guideline for selecting proper recording time. In addition, a system error in typical TDR EC measurements was identified and a countermeasure was proposed, leading to a complete and accurate procedure for TDR EC measurements.   Meanwhile, chapter 5 investigated the factors associated with probe designs for both types of measurements. The sensitivity of TDR measurements as affected by the probe parameters was discussed to provide guidelines for probe design. In addition, a penetrometer type of TDR probes was developed to allow simultaneous measurements of dielectric permittivity and electrical conductivity during cone penetration for measurements at depths.

Although the aforementioned TDR measurement methodology was originally developed with soil applications in mind, the sediment problems in Shihmen Reservoir manifested by the Typhoon Aere in 2004 provides imperative opportunities for TDR applications. The TDR measurement techniques were adopted for characterization of soil-water mixtures. Therefore, in the first part of chapter 6, TDR penetrometer was integrated with the Marchetti dilatometer

(DMT) and the TDR/DMT probe was used to determine the solid concentration, stiffness and stress state of the bottom mud. A novel TDR probe and measurement procedure were further developed for accurate monitoring of suspended sediment concentration (SSC) in fluvial and reservoir environment.

2 Literature Review

2.1 Introduction

TDR is a sensing technology based on electromagnetic wave. A TDR device sent out an electromagnetic pulse into a transmission line connected to a sensing waveguide (or probe), and records the reflected signal from the sensing waveguide. The reflected signal contains information related to the electromagnetic properties of the medium surrounding the sensing waveguide. The electromagnetic properties and principle of TDR technology are reviewed in the following.

2.2 Electromagnetic Properties of Materials

2.2.1 Basic Electromagnetic Properties

Electromagnetic properties of a material include: magnetic permeability, electrical conductivity, and dielectric permittivity. These properties will be briefly introduced in this section.

Magnetic permeability

When a charge q (which is negative for electrons) is in motion in a magnetic field H (ampere m^{-1}). The charge q would experience a force called the magnetic force, F_m. The characteristics of F_m can be described by defining a vector field quantity, the magnetic flux density B, thus the magnetic force can be expressed as (Cheng, 1989):

$$F_m = q\mathbf{u} \times B \qquad\qquad [2\text{-}1]$$

where u (m s^{-1}) is the velocity vector, and B is measured in webers per square meter (Wb m^{-2}).

On the other hand, as predicted by the *Biot-Savart* law, moving charges q generates magnetic field, H.   The magnetization M (ampere per meter, A m^{-1}) of a material depends on the field H and the magnetic properties of the medium. Therefore, magnetic field or magnetic field intensity H can define as (Cheng, 1989):

$$H = \frac{B}{\mu_0} - M \qquad\qquad [2\text{-}2]$$

where the μ_0 (= $4\pi*10^{-7}$H m^{-1}) is the permeability of free space. The use of the vector H can write a curl equation relating the magnetic field and the distribution of free current in any medium.

As the magnetic properties of the medium are linear and isotropic, the magnetization is directly proportional to the magnetic field intensity (Cheng, 1989):
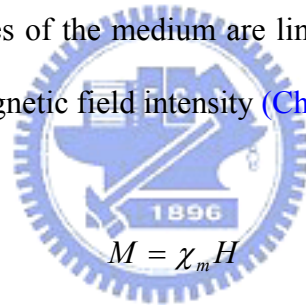
$$M = \chi_m H \qquad\qquad [2\text{-}3]$$

where χ_m is a dimensionless quantity called magnetic susceptibility.   Therefore, by substituting Eq. [2-3] into Eq. [2-2] yields (Cheng, 1989):

$$B = \mu_0(1 + \chi_m)H = \mu_0\mu_r H = \mu H \qquad\qquad [2\text{-}4]$$

where μ_r is another dimensionless quantity called relative permeability of the medium. The parameter μ is the absolute permeability (or sometimes just permeability) of the medium. For simple media (linear, isotropic, and homogeneous), χ_m and μ_r are constants.

The permeability of most materials is very close to μ_0. For ferromagnetic materials such

as iron, nickel, and cobalt, μ_r could be very large.   The relative permeability of some selected

materials is listed in Table 2-1.

Table 2-1   Relative permeability data for selected materials (modified from Cheng, 1989)

Material	Relative Permeability (μ_r)
Nickel	250
Cobalt	600
Iron (pure)	4,000
Aluminum	1.000021
Magnesium	1.000012
Palladium	1.00082
Titanium	1.00018
Bismuth	0.99983
Gold	0.99998
Copper	0.99999
Water	1

Electrical conductivity

Consider N number of charges q across a surface with velocity u, it is convenient to

define a vector point function, volume current density, or simply current density, J, in amperes

per square meter (Cheng, 1989)

$$J = Nqu \qquad\qquad [2\text{-}5]$$
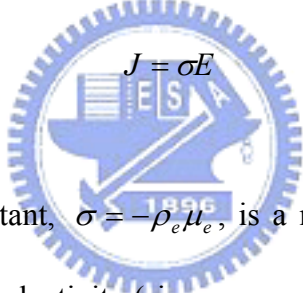
Since the conduction currents are the results of the drift motion of charges carried under

the influence of an applied electric field E (newtons per coulomb, N C^{-1} or, equivalently, volts

per meter, V m^{-1}), it can be justified that for most conducting materials the average drift

velocity is directly proportional to the electric field intensity.   For metallic conductors

(Cheng, 1989):

$$u = -\mu_e E \qquad\qquad [2\text{-}6]$$

where μ_e is the electron mobility measured in ($m^2V^{-1}s^{-1}$). Therefore, substituting Eq. [2-6] into [2-5], the current density, J, can be written as:

$$J = -\rho_e \mu_e E \qquad\qquad [2\text{-}7]$$

where $\rho_e = Nq$ is the charge density of the drifting electrons and is a negative quantity. Eq. [2-7] then can be rewritten as:

$$J = \sigma E \qquad\qquad [2\text{-}8]$$

where the proportionality constant, $\sigma = -\rho_e \mu_e$, is a macroscopic constitutive parameter of the medium called electrical conductivity (siemens per meter, S m^{-1}) (Cheng, 1989). Table 2-2 shows the electrical conductivities of some frequently used materials.

Table 2-2   Electrical conductivities of materials (modified from Cheng, 1989)

Material	Conductivity, S m^{-1}
Silver	6.17×10^7
Copper	5.80×10^7
Aluminum	3.54×10^7
Iron	10^7
Seawater	4
Fresh water	10^{-3}
Distilled water	2×10^{-4}
Dry soil	10^{-5}
Glass	10^{-12}
Fused quartz	10^{-17}

Dielectric permittivity

Before the discussion of the dielectric permittivity, phenomenon of polarization should be introduced. Polarization arises when a force displaces a charge from some equilibrium position. However, polarization cannot occur instantaneously given that charges possess inertia; therefore, polarization is a dynamic phenomenon with a characteristic time-scale (Santamarina et al., 2001).

In the static case (or zero frequency), when the dielectric properties of the medium are linear and isotropic, the polarization is directly proportional to the electric field intensity, *E*, and the proportionality constant is independent of the direction of field, thus the polarization vector *P* can be written as:

$$P = \varepsilon_0 \chi_e E \qquad \text{[2-9]}$$

where ε_0 ($\doteqdot$ $1/36\pi * 10^{-9}$ farad per meter, F m^{-1}) is the permittivity of free space, χ_e is a dimensionless quantity called electric susceptibility. A dielectric medium is linear if χ_e is independent of *E* and homogenous if χ_e is independent of space coordinates.

Therefore, a new fundamental field quantity, called the electric flux density or electric displacement, *D*, can be defined with polarization vector *P* as:

$$\begin{aligned} D = \varepsilon_0 E + P &= \varepsilon_0 (1 + \chi_e)E \\ &= \varepsilon_0 \varepsilon_r E = \varepsilon E \end{aligned} \qquad \text{[2-10]}$$

where ε_r is a dimensionless quantity known as relative permittivity or dielectric constant of the medium. The coefficient $\varepsilon = \varepsilon_0 \varepsilon_r$ is the absolute permittivity of the medium and is measured in farads per meter (F m^{-1}). Table 2-3 lists the relative permittivity of some often

used materials (Cheng, 1989).

For single component and homogenous materials (like fluid) may experience three types of polarization mechanisms: electronic, ionic, and dipolar. Electronic polarization occurs when the externally applied electric field causes a shift in the atom's positive and negative charges, as shown in Fig. 2-1a. Equilibrium is attained when the internal Coulomb attractive force produced by the charge separation balances the applied force. When a charge separation occurs, it essentially has a microscopic electric dipole. Ionic polarization occurs in molecules composed of positively and negatively charged ions (cations and anions). An externally applied electric field again results in a microscopic separation of charge centers thus resembling a dipole of charge, as shown in Fig. 2-1b. Dipolar polarization, on the other hand, occurs in materials that possess permanent, microscopic separations of charge center. In the absence of an applied electric field, these permanent dipoles are randomly oriented. In the presence of an applied electric field, these permanent dipoles tend to rotate to align with the applied field as shown in Fig. 2-1c (Lin, 1999).

In the dynamic case, polarization mechanisms display one of two characteristic spectra: resonance or relaxation. Polarization mechanisms that trigger restoring forces, in general, display a resonance spectrum (This is the case of electronic and ionic polarization). The complex permittivity for resonance is described as (Santamarina et al., 2001)

$$\varepsilon_r = \varepsilon_r' - j\varepsilon_r'' = \varepsilon_\infty' + \frac{1}{2}\frac{\varepsilon_{dc}' - \varepsilon_\infty'}{\left(1 - \dfrac{\omega}{\omega_{res}}\right) + j\dfrac{\beta}{\omega_{res}}} \qquad [2\text{-}11]$$

where ε_{dc}' and ε_∞' are the real permittivity at frequencies much lower and higher than the resonant frequency ω_{res}, ω is radian frequency, which equals $2\pi f$ (f is frequency), $j = \sqrt{-1}$, and β represents the viscous drag coefficient in the equation of motion of a single degree of

freedom system.

If the polarization does not restore forces or if damping prevails over inertial forces, the material exhibits a relaxation spectrum.   This is the case for molecular, spatial, and double layer polarizations.   A typical relaxation equation as well-known Debye's equation is

$$\varepsilon_r = \varepsilon_r' - j\varepsilon_r'' = \varepsilon_\infty' + \frac{\varepsilon_{dc}' - \varepsilon_\infty'}{1 + j\dfrac{\omega}{\omega_{rel}}} \qquad \text{[2-12a]}$$

where ω_{rel} is the characteristic relaxation frequency, and

$$\varepsilon'_r = \varepsilon_\infty + \frac{\varepsilon_{de} - \varepsilon_\infty}{1 + (\omega/\omega_{rel})^2} \qquad \text{[2-12b]}$$

$$\varepsilon''_r = \frac{(\varepsilon_{dc} - \varepsilon_\infty)\omega/\omega_{rel}}{1 + (\omega/\omega_{rel})^2} \qquad \text{[2-12b]}$$
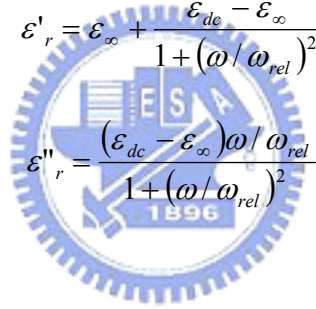
As discussed above, Fig. 2-2 shows frequency response of permittivity and loss factor for a hypothetical dielectric by various contributing phenomena.   Polarizations form different mechanisms accumulate towards lower frequency.   As a result, the real permittivity ε'_r increases with decreasing frequency, and resonant mechanisms shows a peak near resonance.

After introducing the polarization mechanism and the dielectric permittivity, the effective imaginary permittivity combining polarization losses and conduction losses can be defined as:

$$\varepsilon_{eff}'' = \varepsilon_r'' + \frac{\sigma_{dc}}{\omega\varepsilon_0} \qquad \text{[2-13]}$$

where σ_{dc} means the electric conductivity at DC condition.   These losses can also be

expressed in terms of the "effective alternating current (AC) conductivity":

$$\sigma_{eff} = \sigma_{dc} + \varepsilon_r^{"}\omega\varepsilon_0 \qquad \text{[2-14]}$$

Therefore, it is convenient in electric field analysis to combine the dielectric loss and conductive loss terms. The resulting equivalent complex permittivity becomes

$$\varepsilon_r^* = \varepsilon_r' - j\varepsilon_r^{ii} = \varepsilon_r' - j\left(\varepsilon_r'' + \frac{\sigma_{dc}}{\omega\varepsilon_0}\right) \qquad \text{[2-15]}$$

in which $\varepsilon_r^{ii} = \varepsilon_r'' + \sigma_{dc}/(\omega\varepsilon_0)$ is the equivalent imaginary part of the permittivity.

Table 2-3   Relative permittivity of some often used materials [modified from Cheng, 1989]

Material	Relative Permittivity
Air	1.0
Glass	4 - 10
Mica	6.0
Oil	2.3
Polyethylene	2.3
Rubber	2.3 – 4.0
Distilled water	80
Dry soil	3 - 4
Teflon	2.1
Sea water	72
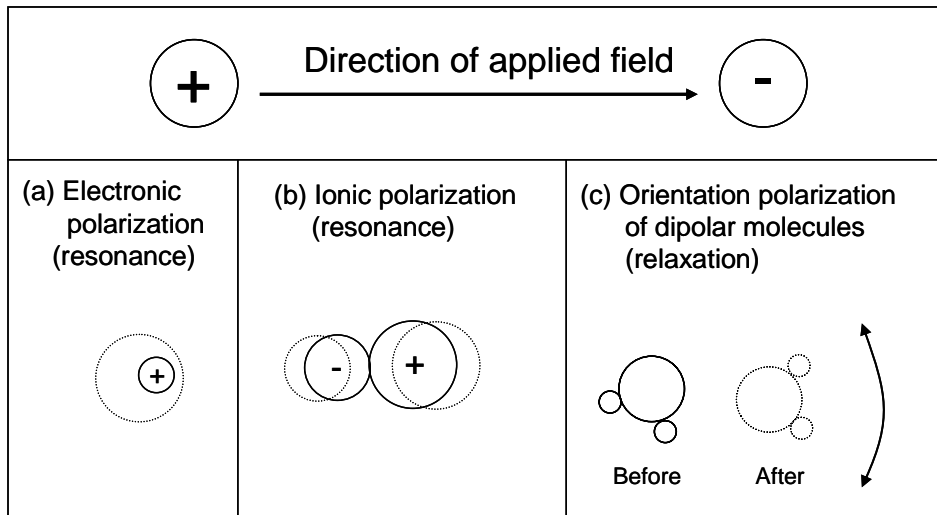
Fig. 2-1   Polarization mechanisms in single component materials (modified from Santamarina et al., 2001)
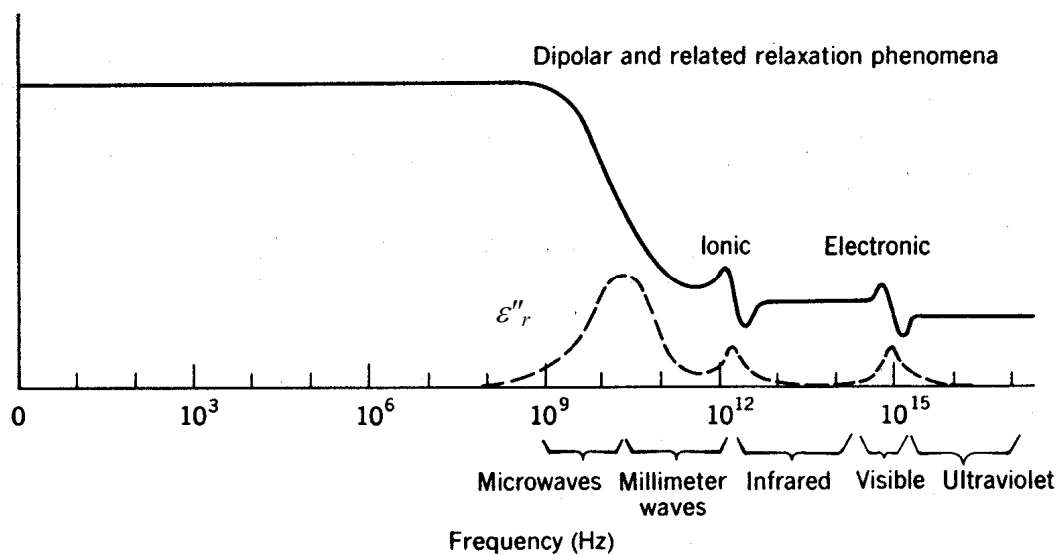
Fig. 2-2   Frequency response of permittivity and loss factor for a hypothetical dielectric showing various contributing phenomena (Ramo et al., 1994)

2.2.2   Dielectric Behavior of Water and Soil Solid

Dielectric behavior of water

The frequency dependence of the dielectric permittivity of pure water, ε_w, is given by

Debye's equation in Eq. [2-12a] with parameters ε_{wdc}, $\varepsilon_{w\infty}$, and ω_{wrel} as the static dielectric

13

constant, high-frequency limit, and relaxation frequency of ε_w, respectively.   In addition to the dependence on frequency, the dielectric permittivity of water is also temperature dependent because the dielectric loss of the orientational polarization results from thermal effects.

Stogryn (1971) determined the high-frequency dielectric constant for pure water to be $\varepsilon_{w\infty}$ = 4.9.   At high frequency, the contribution of the dielectric constant is from the electronic and ionic polarizations, which are a mechanical effect rather than a thermal effect.   The dependence of $\varepsilon_{w\infty}$ on temperature is so weak that for computational purpose $\varepsilon_{w\infty}$ may be considered a constant, thus

$$\varepsilon_{w\infty} = 4.9 \qquad [2\text{-}16]$$

Stogryn (1971) obtained an expression for ω_{wrel} by fitting a polynomial to the data reported by Grant et al. (1957) as:

$$2\pi\tau_{wr}(T) = 1.1109\times10^{-10} - 3.824\times10^{-12}T + 6.938\times10^{-14}T^2 - 5.096\times10^{-16}T^3 \quad [2\text{-}17]$$

where $\tau_{wr} = 1/\omega_{wrel}$, T is in °C.   The relaxation frequency of pure water, $f_{wr} = 1/(2\pi\tau_{wr})$, lies in the microwave region where $f_{wr}(0°C) \approx 9$ GHz and $f_{wr}(20°C) \approx 17$ GHz.   Klein and Swift (1977) generated a regression fit for $\varepsilon_{wdc}(T)$ from dielectric measurements conducted at 1.43 GHz and 2.65 GHz this resulted in

$$\varepsilon_{wdc}(T) = 88.045 - 0.4147T + 6.295\times10^{-4}T^2 + 1.075\times10^{-5}T^3 \qquad [2\text{-}18]$$

In addition, Peping et al. (1995) also indicated the ε_{wdc} of water is temperature dependent as:

$$\varepsilon_{wdc}(T) = 78.54 \cdot \left(1 - 4.58 \cdot 10^{-3}(T - 25) + 1.19 \cdot 10^{-5}(T - 25)^2 - 2.8 \cdot 10^{-8}(T - 25)^3\right)$$

[2-19]

in which the ε_{wdc} of water would be equals 78.54 when temperature is 25 °C.

Dielectric behavior of soil solid

Soil is a three-phase system consisting of air, solid particles, and water. The dielectric permittivity of air is approximately equal to 1.0 (i.e. no polarization in a free space). The conductivity of air is equal to 0. Solid particles in a soil are non-polar materials. Their dielectric polarization is only due to electronic and ionic polarization mechanisms, which have relaxation frequencies above 1 THz (10^{12} Hz). Therefore, they have a low value of dielectric permittivity ($\varepsilon_r \approx 5$), and are nearly lossless, independent of frequency and temperature at frequencies less than 1 THz (Weast, 1986).
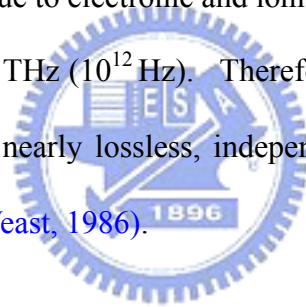
2.2.3   Interfacial Polarization of Soil-water Mixture

The dielectric property of each soil phase can be described by the dielectric mechanisms mentioned above. The heterogeneity of soil-water mixture, however, adds to the complexity of its dielectric properties. There are three major effects due to this heterogeneity: bound water polarization, double layer polarization, and the Maxwell-Wagner effect.

The bound water polarization results from the fact that water can be bounded to the soil matrix as shown Fig. 2-3a. The degree of binding varies from unbound or free water at a great distance from the matrix surface, to heavily bound or absorbed water. If water becomes bounded to the soil matrix, it is not capable of doing as much work and hence looses energy. The relaxation frequency of bound water is less than that of free water (Hilhorst, 1998).

Considering the composition of each phase of soil-water mixture, double layer polarization of soil-water mixture could be different in three conditions: low particle concentration in deionized water, low particle concentration in an electrolyte, and high particle concentration (Santamarina et al., 2001). For the condition of low particle concentration in deionized water, double layer polarization is due to the relative displacement of the double layer counterion cloud with respect to the charged particle in response to an electric field, as shown in Fig. 2-3b. If the polarization occurs, the movement of charges leaves one end of the particle with an excess of surface charges and the other end with and excess of counterions.

For the case of low particle concentration in an electrolyte, the double layer polarization is hindered in an electrolyte because displaced ions are replaced by the diffusion of ions and out of the bulk solution, as shown in Fig. 2-3c. Double layer polarization is also hindered in high particle concentration since ions in the double layer can move from one particle to a neighboring particle in response to the applied electric field, as shown in Fig. 2-3d. This situation develops even if the bulk fluid is deionized water.

The Maxwell-Wagner effect is the most important phenomenon that affects the low-frequency end of the dielectric spectrum of soils or soil-water mixtures. The Maxwell-Wagner effect is a macroscopic phenomenon that depends on the differences in dielectric properties of the soil constituents, as shown in Fig. 2-3e. It is a result of the distribution of conducting and non-conducting areas in the soil matrix. This interfacial effect is dominant at frequencies less than 150 MHz, below the frequencies where bound water relaxation plays a dominant role (Hilhorst, 1998).

A qualitative representation of the dielectric properties of wet soils is presented in Fig. 2-4 (Hilhorst and Dirkson, 1994). The dielectric spectrum can be roughly divided into two parts with the dividing frequency at about 150 MHz. The higher frequencies are dominated by the

bound water relaxation and the lower frequencies are dominated by the Maxwell-Wagner effect. The TDR frequencies lie from the higher end of the Maxwell-Wagner effect to the lower end of free water relaxation.
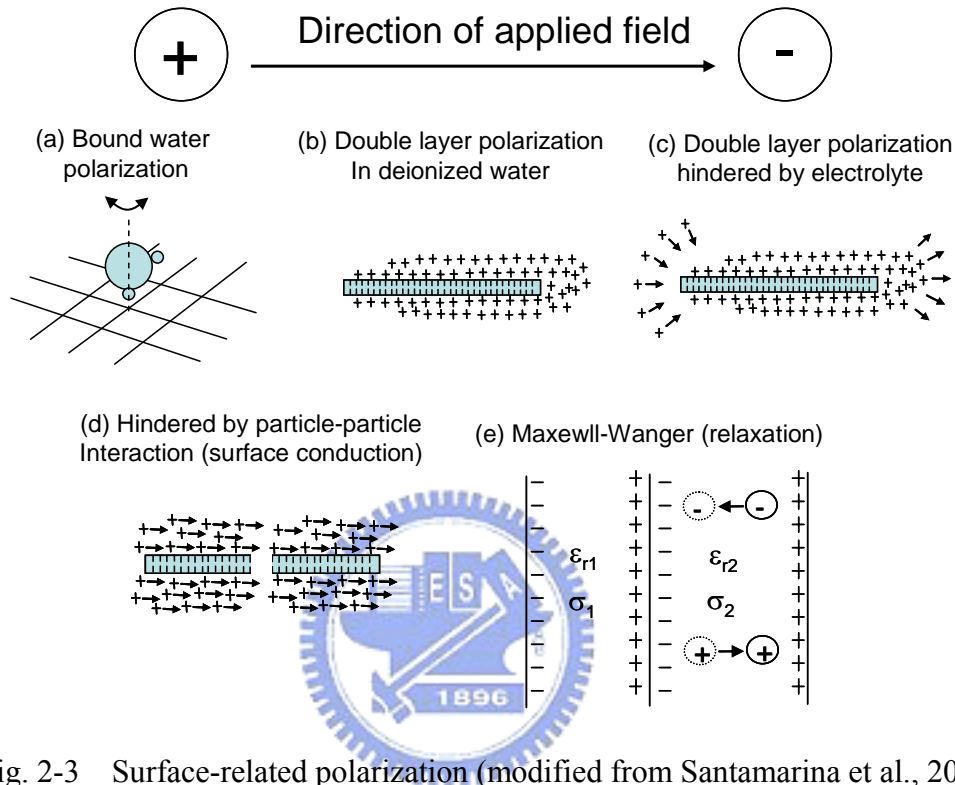
Fig. 2-3   Surface-related polarization (modified from Santamarina et al., 2001)
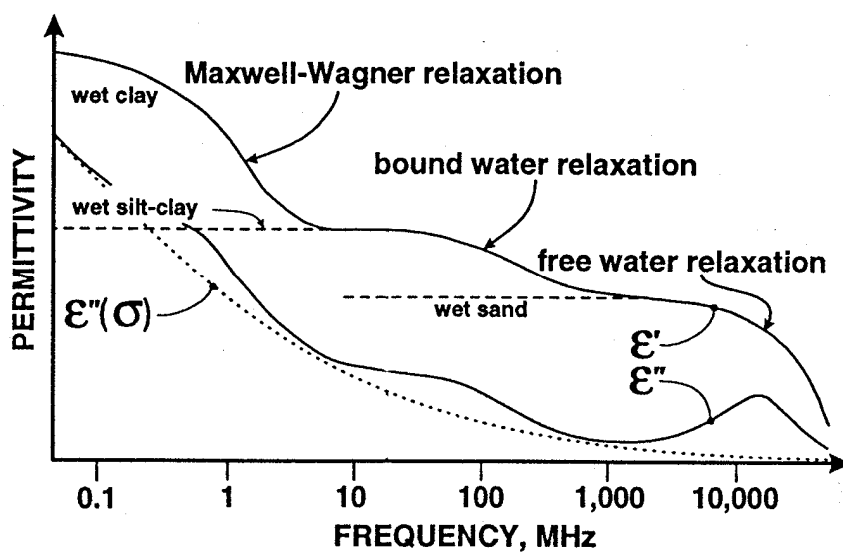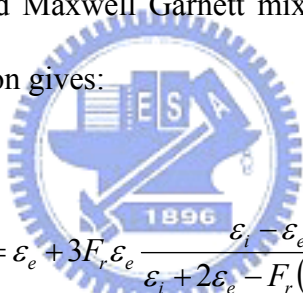
Fig. 2-4   Qualitative representation of dielectric properties of wet soils as a function of frequency (modified from Hilhorst and Dirkson, 1994)

2.2.4   Dielectric Mixing Model

The dielectric behavior of composite materials depends on the compositions. Great attempts on describing bulk dielectric properties of mixtures in terms of their compositions have been proposed through dielectric mixing modeling. In this section, several mixing models will be discussed from different aspects.

Classical mixing model

Figure 2-5 shows spherical inclusions with permittivity ε_i occupy random positions in the environment of permittivity ε_e. Let the fraction F_r of the total volume be occupied by the inclusion phase, and the volume fraction 1-F_r left for the host. Thus, a classical mixture rule with spherical inclusions called Maxwell Garnett mixing formula (Maxwell Garnett, 1904) with the polarizability expression gives:

$$\varepsilon_{eff} = \varepsilon_e + 3F_r\varepsilon_e \frac{\varepsilon_i - \varepsilon_e}{\varepsilon_i + 2\varepsilon_e - F_r(\varepsilon_i - \varepsilon_e)} \qquad [2\text{-}20]$$

where ε_{eff} is the effective permittivity of a mixture, and this formula is in wide use in the very diverse fields of application. However, this analysis treated the media as a plain and pure dielectric, and no charge flow took place when fields were incident on the materials. A bold and straightforward application of the Maxwell Garnett mixing formula gives for the complex effective permittivity of lossy materials:

$$
\begin{aligned}
\varepsilon_{eff} &= \varepsilon'_{eff} - j\varepsilon''_{eff} \\
&= \varepsilon'_e - j\varepsilon''_e + 3F_r(\varepsilon'_e - j\varepsilon''_e)\frac{\varepsilon'_i - \varepsilon'_e - j(\varepsilon''_i - \varepsilon''_e)}{(1-F_r)\varepsilon'_i + (2+F_r)\varepsilon'_e - j[(1-F_r)\varepsilon''_i + (2+F_r)\varepsilon''_e]} \qquad [2\text{-}21]
\end{aligned}
$$

in which the inclusions are assumed to be spherical, and complex permittivity, which includes

the electrical conductivity, of the environment is $\varepsilon_e = \varepsilon_e - j\sigma / \omega = \varepsilon'_e - j\varepsilon''_e$, and the same

with the complex permittivity of the inclusion as $\varepsilon_i = \varepsilon'_i - j\varepsilon''_i$. If the volume fraction of

the inclusion phase is small, the effective conductivity $\sigma_{eff} = \omega\varepsilon''_{eff}$, calculated from Eq. [2-21],

is:

$$\sigma_{eff} = \frac{9\varepsilon_e^2 F_r \sigma_i}{\left(\varepsilon'_i + 2\varepsilon_e\right)^2 + \sigma_i^2 / \omega^2} \qquad [2\text{-}22]$$

However, the derivation of the Maxwell Garnett mixing formula was based on the

algebraic dependence of the internal filed, and it is known that for time-dependent field,

losses entail exponential attenuation of the field amplitudes which can be considerable if the

extent of the lossy medium is large compared with the penetration depth. Hence the

requirements of allowed use of the Maxwell Garnett mixing formula for time-dependent fields

is that the inclusion size must not be larger than the skin depth of the wave in the lossy

medium $\sqrt{2/(\omega\mu_i\sigma_i)}$ with μ_i being the magnetic permeability of the inclusion material.
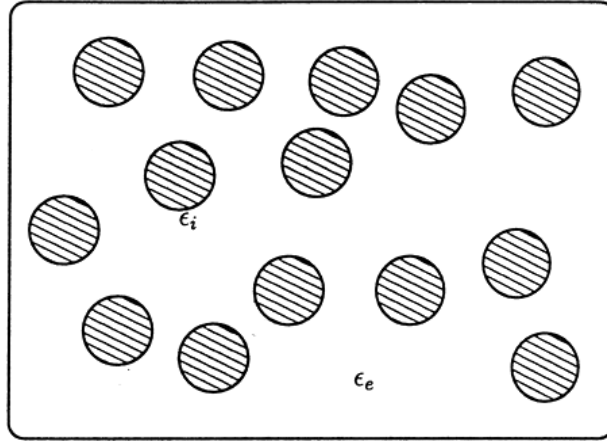
Fig. 2-5   Dielectric spheres are guests in the dielectric background host. (after Sihvola, 1999)

Mixing model for anisotropic mixtures

The original Maxwell Garnett mixing formula basically has an assumption that the inclusion and the background material are isotropic. However, mixtures such as soil and suspensions may have anisotropic inclusions and/or anisotropic background material.

Now we consider inclusions as ellipsoids, as shown in Fig. 2-6, the depolarization factor N_x (the factor in the a_x-direction of Cartesian co-ordinate system) is

$$N_x = \frac{a_x a_y a_z}{2} \int_0^\infty \frac{ds}{\left(s + a_x^2\right)\sqrt{\left(s + a_x^2\right)\left(s + a_y^2\right)\left(s + a_z^2\right)}} \qquad [2\text{-}23]$$

where s is the integration variable, whose value is between zero and infinity. For other depolarization factor N_y (N_z), interchange a_y and a_x (a_z and a_x) in the above integral. Collecting those in a single dyadic (the elementary dyadic analysis could refer to Appendix A), the depolarization dyadic for an ordinary ellipsoid reads:

$$\overline{\overline{L}} = \sum_{i=x,y,z} N_i v_i v_i = \frac{\det \overline{\overline{A}}}{2} \int_0^\infty ds \, \frac{\left(\overline{\overline{A}}^2 + s\overline{\overline{I}}\right)^{-1}}{\sqrt{\det\left(\overline{\overline{A}}^2 + s\overline{\overline{I}}\right)}} \qquad [2\text{-}24]$$

where v_i is unit vectors along the three orthogonal eigendirections, and the symmetric and positive-definite dyadic

$$\overline{\overline{A}} = \sum_{i=x,y,z} a_i v_i v_i \qquad [2\text{-}25]$$

with $\det \overline{\overline{A}} = a_x a_y a_z$

If the ellipsoid, which is anisotropic with permittivity $\overline{\overline{\varepsilon}}_i$, is located in an anisotropic material $\overline{\overline{\varepsilon}}_e = \overline{\overline{\varepsilon}}_r \varepsilon_0$, and exposed to a uniform external electric field E_e, as shown in Fig. 2-7. The internal electric field E_i can be shown to be

$$E_i = \left[\overline{\overline{\varepsilon}}_e + \overline{\overline{L'}} \cdot \left(\overline{\overline{\varepsilon}}_i - \overline{\overline{\varepsilon}}_e\right)\right]^{-1} \cdot \overline{\overline{\varepsilon}}_e \cdot E_e \qquad [2\text{-}26]$$

where the transformed depolarization dyadic $\overline{\overline{L'}}$, which is that of real geometry of the ellipsoid after it has been transformed affinely by the anisotropy of the environments, can be calculated from:

$$\overline{\overline{L'}} = \frac{\det \overline{\overline{A}}}{2} \int_0^\infty ds\, \overline{\overline{\varepsilon}}_r \cdot \frac{\left(\overline{\overline{A}}^2 + s\overline{\overline{\varepsilon}}_r\right)^{-1}}{\sqrt{\det\left(\overline{\overline{A}}^2 + s\overline{\overline{\varepsilon}}_r\right)}} \qquad [2\text{-}27]$$

Because the permittivity dyadic of a reciprocal material is symmetric, although it can be

anisotropic, it is natural to accept that a mixture composed of reciprocal materials must display reciprocal electromagnetic behavior. Therefore, the Maxwell Garnett equation can be adapted in the following from:

$$\overline{\overline{\varepsilon}}_{eff} = \overline{\overline{\varepsilon}}_e + F_r\left[\left(\overline{\overline{\varepsilon}}_i - \overline{\overline{\varepsilon}}_e\right)^{-1} + \left(1 - F_r\right)\overline{\overline{\varepsilon}}_e^{-1} \cdot \overline{\overline{L'}}\right]^{-1}$$
[2-28]
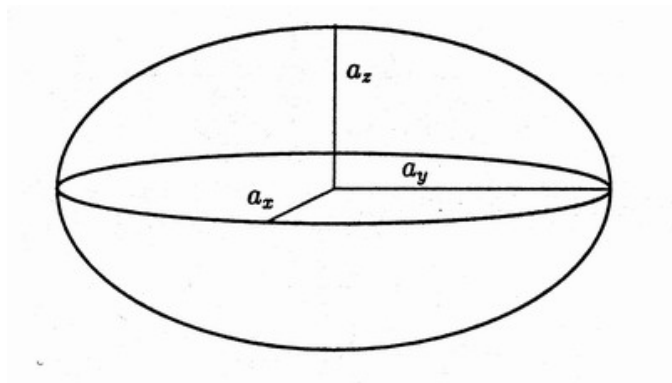
Fig. 2-6   The geometry of an ellipsoid. The semi-axis a_x, a_x, and a_x fix the Cartesian co-ordinate system. (after Sihvola, 1999)
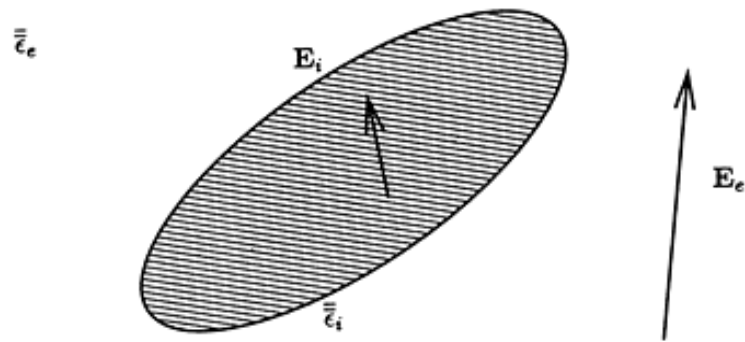
Fig. 2-7   Anisotropic ellipsoid (with permittivity $\overline{\overline{\varepsilon}}_i$) in anisotropic environment ($\overline{\overline{\varepsilon}}_e = \overline{\overline{\varepsilon}}_r\varepsilon_0$). E_i refers to the internal electric field. (after Sihvola, 1999)

Generalized mixing model

The *Bruggeman formula* is an important mixing rule which is widely used in

electromagnetic literatures, and it is also known by other names: *Polder-van Santen formula* and *de Loor formula*. The essence of the Bruggeman mixing rule is the absolute equality between phases in the mixture (Sihvola, 1999), and it for the case when the inclusions are randomly oriented ellipsoids is

$$\varepsilon_{eff} = \varepsilon_e + \frac{f}{3}\left(\varepsilon_i - \varepsilon_e\right) \sum_{j=x,y,z} \frac{\varepsilon_{eff}}{\varepsilon_{eff} + N_j\left(\varepsilon_i - \varepsilon_{eff}\right)} \qquad [2\text{-}29]$$

where N_j are the depolarization factors as shown in Eq. [2-24]. Dobson et al. (1985) used the de Loor formula for determining the dielectric constant ε_m of the four-component mixing for a soil mixture, which is composed of dry soil solids, bound water in the Stern layer, bulk water in the Gouy layer, and air. In additional, Dobson et al. (1985) assumed that the ellipsoid depolarization factors lead to $N_j = (0,0,1)$, ε_{eff} has a potential range of $\varepsilon_s \le \varepsilon_{eff} \le \varepsilon_m$, thus the ε_m can be written as:

$$\varepsilon_m = \frac{3\varepsilon_s + 2V_{fw}\left(\varepsilon_{fw} - \varepsilon_s\right) + 2V_{bw}\left(\varepsilon_{bw} - \varepsilon_s\right) + 2V_a\left(\varepsilon_a - \varepsilon_s\right)}{3 + V_{fw}\left(\dfrac{\varepsilon_s}{\varepsilon_{fw}} - 1\right) + V_{bw}\left(\dfrac{\varepsilon_s}{\varepsilon_{bw}} - 1\right) + V_a\left(\dfrac{\varepsilon_s}{\varepsilon_a} - 1\right)} \qquad [2\text{-}30]$$

in which V_i refers to the volume fractions of the inclusions, and subscripts s, a, f_w and b_w refer to dry soil solids, air, free Gouy layer water, and Stern layer water, respectively. Hallikainen et al. (1985) found a relationship between ε_s and soil gravity density γ_s from an empirical fitting of the experimental data as:

$$\varepsilon_s = \left(1.01 + 0.44\gamma_s\right)^2 - 0.062 \qquad [2\text{-}31]$$

Dobson et al. (1985) also adopted the *Birchak formula* which is also called *Power-law model* [Birchak et al. 1974] or *refractive index model*, to provide a four-phase semi-empirical dielectric mixing model for soil mixture,

$$\varepsilon_m^\alpha = \sum_i V_i \varepsilon_i^\alpha = V_s \varepsilon_s^\alpha + V_a \varepsilon_a^\alpha + V_{fw} \varepsilon_{fw}^\alpha + V_{bw} \varepsilon_{bw}^\alpha \qquad \text{[2-32]}$$

in which V_i is the volumetric fraction of the soil component i, the subscripts s, a, f_w and b_w refer to the solid soils, air, free water and bound water, respectively. The exponent α is a constant shape factor, and Mironov et al. (2004) presented a generalized refractive mixing dielectric model based on $\alpha = 0.5$.

Heimovaara et al. (1994b) and Lin (2003b) formulated the four-component dielectric mixing equation based on the Dobson's semi-empirical formula, in terms of physical parameters of soil as:

$$\varepsilon_m^\alpha = \left(\frac{\gamma_d}{\gamma_s}\right)\varepsilon_s^\alpha + \left(\theta - \delta\gamma_d A_s\right)\varepsilon_{fw}^\alpha + \left(\delta\gamma_d A_s\right)\varepsilon_{bw}^\alpha + \left(1 - \frac{\gamma_d}{\gamma_s} - \theta\right)\varepsilon_a^\alpha \qquad \text{[2-33]}$$

where γ_d is soil bulk dry density, γ_s is the gravity density of solid, the $\delta\gamma_d A_s$ product represents the volumetric bound water content, δ is the average thickness of the bound water, and A_s is the specific surface of the soil.

2.3 TDR Principle and Analysis

2.3.1   Basics of TDR

The basic principle of TDR is the same as radar.   But instead of transmitting a 3-D wave front, the electromagnetic wave in a TDR system is confined in a waveguide.   Fig. 2-8 shows a typical TDR measurement setup composed of a TDR device and a transmission line system.   A TDR device generally consists of a cable tester (or pulse generator), a sampler, and an oscilloscope. The transmission line system consists of a leading coaxial cable and a measurement waveguide.   The pulse generator sends an electromagnetic pulse along a transmission line and the oscilloscope is used to observe the returning reflections from the measurement waveguide due to impedance mismatches.

The propagation behavior of electromagnetic wave is determined by the Maxwell's Equation (Cheng, 1989).   The propagation behavior of electromagnetic wave can be controlled by two major parameters: *Propagation Constant γ*, and *Characteristic Impedance Z_c*.   For a coaxial transmission line, the equation of these two parameters can be written as (Ramo et al., 1994)

$$\gamma = \frac{j2\pi f}{c}\sqrt{\varepsilon_r^*} = \alpha + j\beta \qquad\qquad [2\text{-}34]$$

$$Z_c = \frac{\ln(b/a)}{2\pi}\sqrt{\frac{\mu_0}{\varepsilon_0}}\frac{1}{\sqrt{\varepsilon_r^*}} = \frac{Z_p}{\sqrt{\varepsilon_r^*}} \qquad\qquad [2\text{-}35]$$

where c is the velocity of the light (= 2.998*10^8 m/s), a and b are the radii of the outer and inner conductors, α and β are the attenuation coefficient and phase constant, respectively. Z_p is the impedance of an ideal air-filled coaxial transmission line or probe, and it is a function of the cross-sectional geometry of the transmission line, and ε_r^* is the equivalent complex

dielectric permittivity of measured material as shown in Eq. [2-15]. The propagation constant is a function of equivalent complex dielectric permittivity of measured material. The real part of the propagation constant represents the attenuation of the wave. The imaginary part of the propagation constant is the spatial frequency, which gives the velocity of wave propagation when divided by temporal frequency ($2\pi f$). The characteristic impedance is an intrinsic property of the transmission line, and it is controlled by cross-sectional geometry of the transmission line and the equivalent complex dielectric permittivity of measured material. For a line with sections having different impedances, reflection and transmission of waves can occur at the section interfaces.

Fig. 2-9 shows a traditional TDR measured response, which contains several reflections due to impedance mismatches, and a reflection coefficient ρ can be defined at a mismatch interface as:

$$\rho = \frac{v_r}{v_0} = \frac{Z_{c,i+1} - Z_{c,i}}{Z_{c,i+1} + Z_{c,i}} \qquad [2\text{-}36]$$

where the v_r represents the reflection voltage, v_0 is input voltage form step generator, and $Z_{c,i}$ and $Z_{c,i+1}$ are characteristic impedance for i^{th} section and $(i+1)^{th}$ section, respectively.
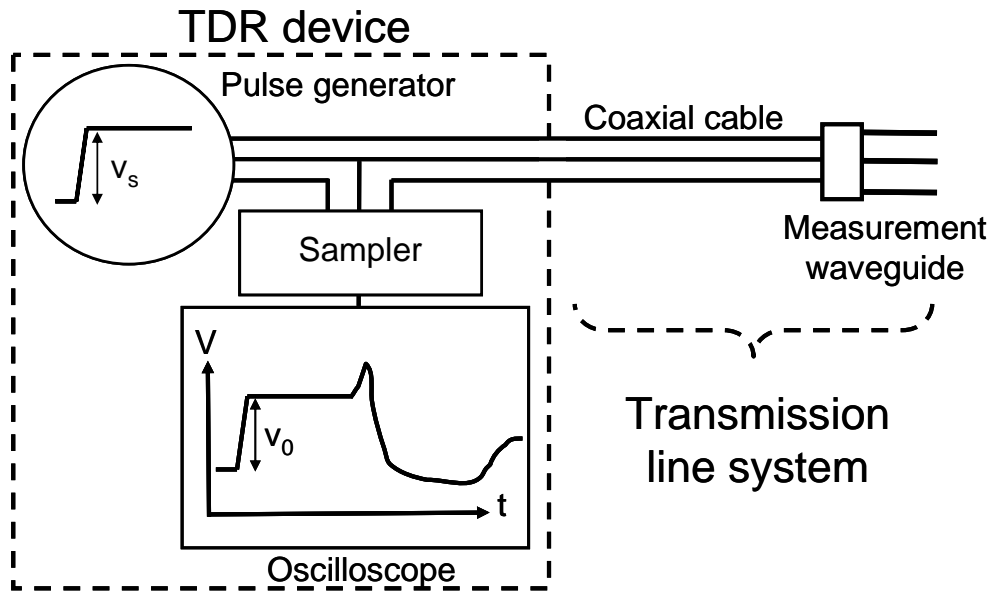
Fig. 2-8　TDR system configuration
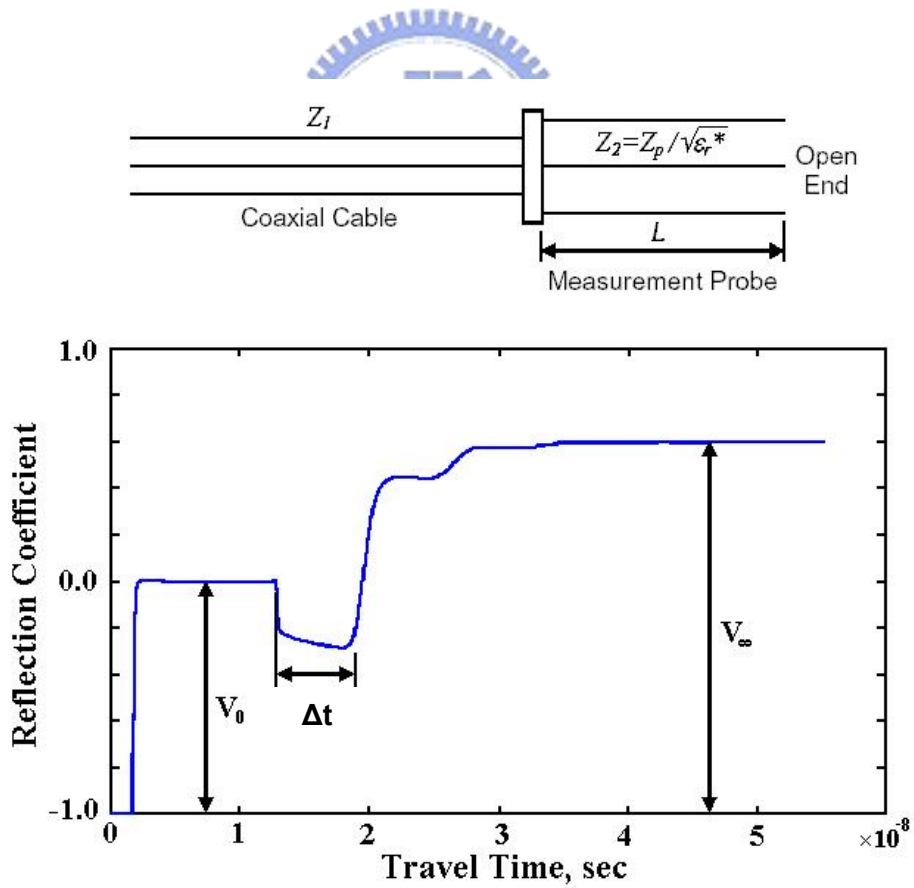
Fig. 2-9　A typical TDR response

2.3.2   TDR Travel Time Analysis

Definition and application of apparent dielectric constant

As Eq. [2-15] shows, the equivalent complex dielectric permittivity is a function of frequency, and the frequency dependence of dielectric property is called the dielectric dispersion. Therefore, the propagation velocity of electromagnetic wave in a transmission line is also a function of frequency, and it can be (Topp, et al., 1980):

$$V(\omega) = \frac{\omega}{\beta} = \frac{c}{\sqrt{\dfrac{\varepsilon'(\omega)}{2}\left[1 + \sqrt{1 + \left(\dfrac{\varepsilon^{ii}(\omega)}{\varepsilon'(\omega)}\right)^2}\right]}} \qquad [2\text{-}37]$$

The dielectric property of material between the waveguide conductors affects the propagation behavior of electromagnetic wave in a transmission line.   If the geometric factors of the sensing waveguide are fixed, according to the transmission line parameters from Eq. [2-34] and [2-35], the reflections occur with system characteristic impedance mismatches as the material dielectric property differs.   Methods for determining the dielectric dispersion are proposed in literatures (Fellner-Felldeg, 1969; Giese and Tiemann, 1975; Heimovaara, 1994a; Weerts et al., 2001). These methods involve spectral analysis and will be further introduce in section 2.3.5.

Dielectric spectroscopy is complex, thus a simplified analysis of TDR waveform to capture apparent dielectric constant has been proposed.   Topp et al. (1980) defined the apparent dielectric constant, K_a, as the quantity determined from the measured velocity of the electromagnetic wave travelling through a transmission line.   The apparent propagation velocity, V, of an electromagnetic wave in a transmission line is related to the apparent

dielectric constant K_a, as

$$V = \frac{c}{\sqrt{K_a}}$$ [2-38]

in which K_a represent a velocity factor as imaginary part of ε_r^* is much smaller than real part of ε_r^*. Topp et al. (1980) indicated that apparent velocity of the electromagnetic wave travelling through a transmission line is obtained by travel time analysis using a tangent line approximation to find the inflection points. The TDR device sends a step pulse down the cable that is reflected from both the beginning and end of the probe due to impedance mismatches. The two reflections cause two discontinuities in the resulting signal. The time difference between these two discontinuities is the time (Δt) required by the signal to travel twice the length (L) of the probe in soil. So the apparent dielectric constant K_a can be formulated:

$$K_a = \left(\frac{c\Delta t}{2L}\right)^2$$ [2-39]

Topp et al. (1980) also proposed an experimental relation for determining the volumetric water content (θ) of soil from K_a:

$$\theta = -5.3 \times 10^{-2} + 2.92 \times 10^{-2} K_a - 5.5 \times 10^{-4} K_a^2 + 4.3 \times 10^{-6} K_a^3$$ [2-40]

Equation [2-40] is a monumental development for the volumetric water content (θ) of soil. However the coefficients in the Eq. [2-40] may depend on soil type. For example, Eq. [2-40] may not suitable for organic soils and fine-texture soils (Herkelrath et al., 1991; Dasberg and Hopmans, 1992).

Considering the effect of the bulk density γ_d of soil, Topp's equation can be approximated by $\sqrt{K_a} = a + b\theta$ and using gravimetric water content ($\theta = w\cdot\gamma_d$). The relation between K_a and gravimetric water content w can be described as (Siddiqui and Drnevich, 1995; Lin et al., 2000)

$$\frac{\sqrt{K_a}}{\gamma_d}\gamma_w = a + bw \qquad [2\text{-}41]$$

in which γ_w is density of water, a and b are calibration coefficients. Nevertheless, the relation between K_a and soil water content w in Eq. [2-41] also depends on the soil type, particularly in high plastic index (PI) soils.

Methodology for determining the travel time Δt

In order to calculate the round-trip travel time Δt in the measured probe, the reflection arrival should be first determined. One way is to locate the reflection arrival is located at the intersection of the two tangents to the reflection curve, marked as point A in Fig. 2-10(a) and called the "dual tangent method". While the second tangent line can be drawn at the point of maximum gradient in the rising limb, the location to draw the first tangent line often lacks a clear definition. To facilitate automation, Baker and Allmaras (1990) used a horizontal line tangent to the waveform at the local minimum (or local maximum for the start reflection). The intersection of this line with the second tangent line is defined as the reflection arrival, marked

as point *B* in Fig. 2-10(a) and called the "single tangent method". The single tangent method appears to be less arbitrary than the dual tangent method because the points of the local minimum and the maximum gradient can be clearly defined mathematically.

Timlin and Pachepsky (1996) and Klemunes et al. (1997) compared both methods and concluded that the latter provided a more accurate calibration equation for water content determination. However, Or and Wraith (1999) concluded that the dual tangent method is more accurate for conditions of high electrical conductivity. A second methodology is based on the apex of the derivative, as marked by point *c* in Fig. 2-10(b) and called the "derivative method". This relatively new method was proposed in research studied discussing the probe calibration (Mattei et al. 2005) and effective frequency of apparent dielectric constant (Robinson et al., 2005).

Furthermore, the electrical length *L* of the probe needs to be calibrated to convert the travel time to apparent velocity (and thereby apparent dielectric constant as shown in Eq. [2-39]). Water is typically used for such a purpose since it has a well-known and high dielectric permittivity value as discussed in section 2.2.2. But the start reflection at the interface between probe head and soil typically may not be clearly defined as the start reflection due to the probe head mismatch. Heimovaara (1993) defined a consistent first reflection point and denoted the round-trip travel time as $\Delta\tau$ and the time difference between selected point and the actual start reflection point as t_0, as shown in Fig. 2-10(a), and it can be written as:

$$\Delta\tau = t_0 + t_s = t_0 + 2L\sqrt{\varepsilon_r^*}/c \qquad [2\text{-}42]$$

where the t_s is the true travel time in the measuring probe.

The probe length and t_0 were then calibrated using measurements in air and water. The air-water calibration method was demonstrated by Robinson et al. (2003) to be accurate across

the range of permittivity values in non-dispersive media. They also showed that calibration performed solely in water (i.e. only for probe length) using the apex of the first reflection as the first reference start point could introduce a small error at low permittivity values. Based on calibration of probe length only, Mattei et al. (2006) showed that the tangent line method (dual tangent) gives inconsistent probe length calibration in air and water while the derivative method can yield consistent probe length calibration. The anomalous result provided by the tangent line method was explained by dispersion effects. However, the dielectric dispersion of water is not significant in the TDR frequency range. The inconsistent probe length calibration may be attributed to error in defining the start reflection, as pointed out by Robinson et al. (2003) that the location of first time marker should be just to the right of the apex of the sensor head reflection.

The apparent dielectric constant traditionally determined by the travel time analysis using a tangent-line method does not have a clear physical meaning and is influenced by several system and material parameters. Lin (2003b) examined how TDR bandwidth, probe length, dielectric relaxation, and electrical conductivity affect travel time analysis by the automated single tangent method. The effects of TDR bandwidth and probe length could be quantified and calibrated, but the calibration equation for soil moisture measurements is still affected by dielectric relaxation and electrical conductivity, due to differences in soil texture and density. Using the spectral analysis, Lin (2003b) suggested that the optimal frequency range, in which the dielectric permittivity is most invariant to soil texture, lies between 500 MHz and 1 GHz, as illustrated in Fig. 2-11. Robinson et al. (2005) investigated the effective frequencies, defined by the 10-90% rise time of the reflected signal, of the dual tangent and derivative methods, considering only the special case of non-conductive TDR measurements. Their results indicated that the effective frequency corresponds with the permittivity determined from the derivative method and not from the conventional dual tangent method. Nevertheless, Evett et al.

(2005) tried to incorporate bulk electrical conductivity and effective frequency defined primarily by the slope of the rising limb of the end reflection, into the water content calibration equation in a hypothesized form, and showed reduced calibration root mean square error (RMSE). However, the hypothesized form does not have a strong theoretical basis. The effects of dielectric dispersion, EC, cable length and effective frequency need further investigations.
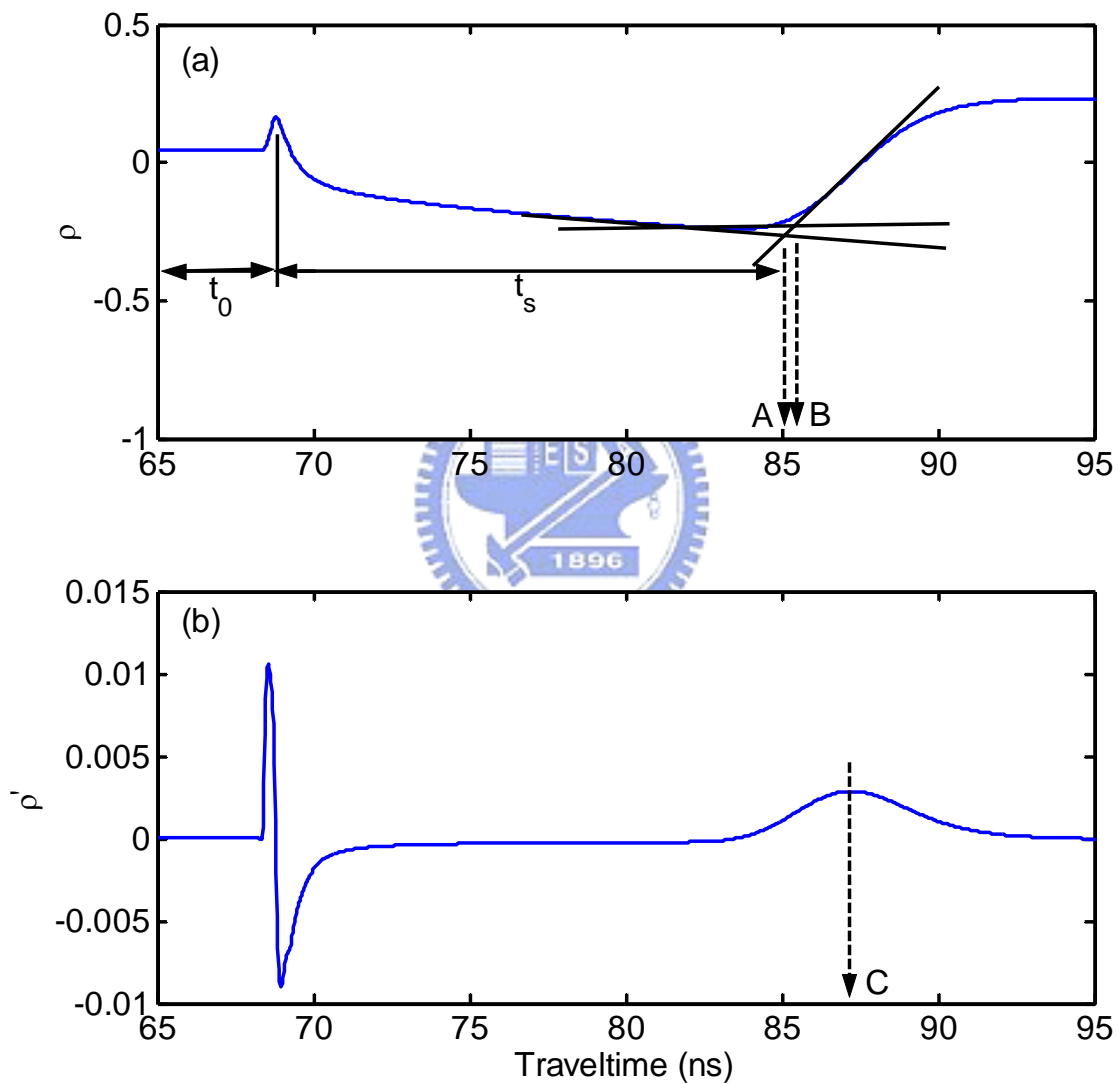
Fig. 2-10   Illustration of various methods of travel time analysis: (a) locating the end reflection by the dual tangent (A point) and single tangent (B point) methods; (b) the derivative methods locates the end reflection by the apex of the derivative (C point) (modified after Robinson et al., 2005)

Optimal frequency for soil moisture measurement
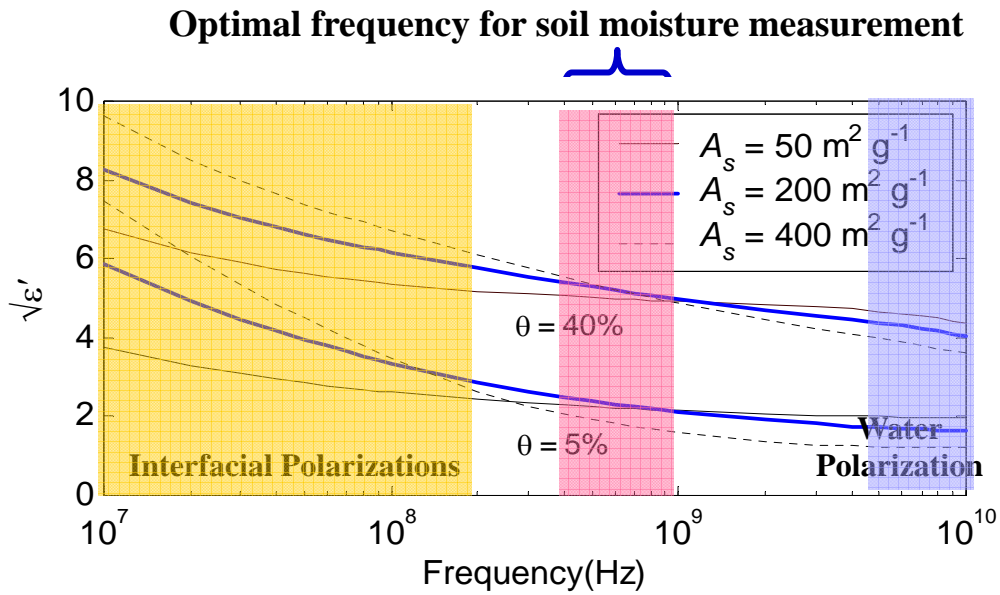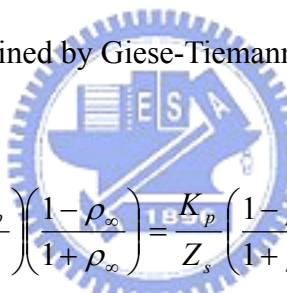
Fig. 2-11   The optimal frequency range in which the dielectric permittivity is dominated by water content and least affected by electrical conductivity and dielectric dispersion due to soil-water interaction. (modified after Lin, 2003b)

2.3.3   TDR Electrical Conductivity Analysis

The bulk electrical conductivity (EC) of a soil or soil-water mixture is an important physical parameter for salinity assessment (Rhoades et al., 1989), studying solute transport (Kachanoski et al., 1992; Ward et al., 1994; Vanclooster et al., 1995), and correlating with hydraulic conductivity (Mualem and Friedman, 1991; Friedman and Seaton, 1998; Purvance and Andricevic, 2000).   Contaminants also influence soil EC as they change the electrical properties of the pore fluid (Campanella and Weemees, 1990).   However, soil water content plays an important role in these problems as well.   Due to the ability to measure dielectric permittivity, which in turn can be used to estimate soil water content, and electrical conductivity in the same sampling volume, it is advantageous to measure soil EC based on TDR rather than the conventional DC resistivity method.

In soil science, early attempts to measure soil EC using TDR utilized the magnitudes of first reflections from the start and end of the probe (Dalton et al., 1984; Topp et al., 1988; Zegelin et al., 1989), whose locations were somewhat arbitrary due to frequency-dependent

attenuation. Later works replaced the magnitude of the first end reflection with the steady state reflection magnitude in the algorithm for calculating EC (Yanuka et al., 1988; Zegelin et al., 1989). These early algorithms suffered from several over-simplified assumptions, including the neglect of cable resistance, dielectric dispersion, and multiple reflections in a conductive medium. Topp et al. (1988) and Zegelin et al. (1989) presented the Giese-Tiemann method (G-T method) obtained from the thin sample theory (Giese and Tiemann, 1975) as an alternative method for EC measurement. The applicability of the thin sample theory was not ascertained but the experimental results indicated that it gives more reliable estimates than other methods. Nadler et al. (1991) rediscovered the Giese-Tiemann method, as pointed out by Heimovaara (1992) and Baker and Spaans (1993). Since then, the Giese-Tiemann method has become the standard equation for calculating EC from TDR measurements, and the EC obtained by Giese-Tiemann method can be formulated as:

$$\sigma_{GT} = \left(\frac{\varepsilon_0 c Z_p}{Z_s L}\right)\left(\frac{1-\rho_\infty}{1+\rho_\infty}\right) = \frac{K_p}{Z_s}\left(\frac{1-\rho_\infty}{1+\rho_\infty}\right) = \beta\left(\frac{1-\rho_\infty}{1+\rho_\infty}\right) \qquad [2\text{-}43]$$

where $K_p = (\varepsilon_0 c Z_p)/L$ is a geometric factor, $\beta = K_p/Z_s$ is defined as the probe constant, $\rho_\infty = (v_\infty - v_0)/v_0$, in which v_∞ is the steady state response of the TDR waveform and v_0 is the incident step (ideally equals twice the source voltage, v_s), Z_s is the source impedance.

The aforementioned methods did not consider the resistance effect, which can cause significant error in EC measurement when cable is long. Heimovaara et al. (1995) and Reece (1998) proposed a modified G-T method including the resistance effect. They first redefined the traditional G-T method that can be rewritten as:

$$\sigma_{TDR} = \frac{K_p}{R_L} \qquad\qquad \text{[2-44]}$$

where K_p is a geometric factor as shown in Eq. [2-43], the R_L is the load resistance measured by the TDR sampler, and it equals $Z_s (1 + \rho_\infty)/(1 - \rho_\infty)$. Heimovaara et al. (1995) indicated that the load resistance R_L measured by the TDR is the sum of sample impedance R_{sample} and a combined series resistance of cable, connectors, and cable tester R_{cable}, so that Eq.[2.44] should then be corrected for resistance as:

$$\sigma_{TDR} = \frac{K_p}{R_L - R_{cable}} \qquad\qquad \text{[2-45]}$$

in which $R_L = R_{sample} + R_{cable}$. Reece (1998) believed that the R_{cable} can be equal to R_L as the shorted waveguide case ($R_{sample} = 0$) in Eq. [2-45]. Therefore, R_{cable} can be directly determined from a measurement on a sample with known R_{sample}, as suggested by Reece (1998). In the limiting case of a sample with $R_{sample} = 0$ (i.e., TDR waveguide probe whose conductors are shorted together), the R_{cable} can be determined as

$$R_{cable} = \frac{R_s}{\left(\dfrac{1 - \rho_{\infty,SC}}{1 + \rho_{\infty,SC}} \right)} \qquad\qquad \text{[2-46]}$$

where $\rho_{\infty,SC}$ is the steady state reflection coefficient of the measurement in which the conductors are shorted together.

Castiglione and Shouse (2003) presented an alternative approach for taking cable resistance into account, however, in which the steady-state reflection coefficients are linearly

scaled between -1.0 and 1.0 with respect to the range expanded by the measurements in air (EC = 0) and the short-circuited condition (EC = ∞):

$$\rho_{scale} = 2 \frac{\rho_{sample} - \rho_{open}}{\rho_{open} - \rho_{short}} + 1 \qquad [2\text{-}47]$$

where ρ_{scaled} is the TDR measurement corrected for cable resistance by the scaling process; ρ_{open} and ρ_{short} are the reflection coefficients with the probe in open air and short-circuited, respectively. The value of ρ_{scaled} represents the TDR measurement as if there is no cable resistance, so the Giese–Tiemann equation (Eq. [2-43]) can be used for calculating the EC. Castiglione and Shouse (2003) claimed that the series resistors model is incorrect and Eq. [2-47] leads to better agreement with experimental results. It should be pointed out, however, that the scaling process is linear while the effect of cable resistance on the steady-state reflection coefficient will be shown to be nonlinear.

The TDR EC measurement is more straightforward, but methods accounting for the cable resistance remain controversial; and the effect of TDR recording time has been underrated when long cables are used. Therefore, one of objectives of this study attempts to develop a new model to show the correct method for taking account of cable resistance and guideline for selecting proper recording time.

2.3.4   TDR Waveform Modeling

Principle of TDR waveform modeling

Heimovaara (1994a) firstly developed the modeling process of single-section TDR response in 1994.   Subsequently, Feng et al. (1999) and Lin (2003a, and 2003b) provided the multi-section modeling processes of TDR response.   Lin (2003a) used the input impedance of

electrical circuit theory to model the multi-section transmission line system, as shown in Fig. 2-12. The input impedance at the TDR sampler can be determined by the following eqautions:

$$Z_{in}(z_n) = Z_L$$

$$Z_{in}(z_{n-1}) = Z_{c,n} \frac{Z_L + Z_{c,n} \tanh(\gamma_n l_n)}{Z_{c,n} + Z_L \tanh(\gamma_n l_n)}$$

$$Z_{in}(z_{n-2}) = Z_{c,n-1} \frac{Z_{in}(z_{n-1}) + Z_{c,n-1} \tanh(\gamma_{n-1} l_{n-1})}{Z_{c,n-1} + Z_{in}(z_{n-1}) \tanh(\gamma_{n-1} l_{n-1})} \qquad \text{[2-48]}$$

$$\vdots$$

$$Z_{in}(0) = Z_{c,1} \frac{Z_{in}(z_1) + Z_{c,1} \tanh(\gamma_1 l_1)}{Z_{c,1} + Z_{in}(z_1) \tanh(\gamma_1 l_1)}$$

where Z_L is the terminated impedance of the system, which is equal to zero with shorted-end and infinity with open-end (e.g. in air), $Z_{c,i}$ and γ_i are the characteristic impedance and propagation constant of i section, respectively, and the l_i is length of each i section. The characteristic impedance and propagations constant are the phasor form and depend on frequency. They can be determined by Eq. [2-34] and Eq. [2-35]

Based on the concept of input impedance, the solution of the sampling voltage $V(0)$ in frequency domain in Fig. 2-12 can be calculated according to the electric circuit theory as:

$$V(0) = \frac{Z_{in}(0)}{Z_{in}(0) + Z_S} V_S = HV_S \qquad \text{[2-49a]}$$

$$H = \frac{1 + S_{11}}{2} \qquad \text{[2-49b]}$$

where the V_s .and Z_S are the voltage source and source impedance of the cable tester,
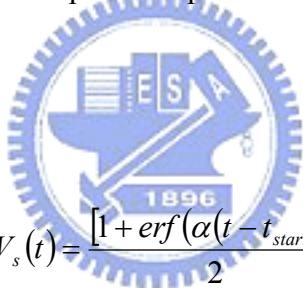
respectively. Z_S is typically equal to 50 Ω, but it depends on the TDR cable tester. *H* is the system function of TDR, and S_{11} is called the scattering function, which can be seen as the reflection coefficient of the whole transmission line.

Fig. 2-13 shows a flow chart of overall modeling process, we first obtain the source impulse v_s(t), and the transform v_s(t) to V_s(f) by using *Fast Fourier Transform* (FFT). Then, the output response *V(f)* in the frequency domain is obtained by evaluating the product *H(f)* with V_s(f). Finally, using *Inverse Fast Fourier Transform* (IFFT) to restore the output response *v(t)* in time domain.

Since the voltage source v_s(t) of the input function V_s(f) of the cable tester should be quantified before TDR modeling, several methods of treating the input function are available. Heimovaara (2001) proposed an empirical input function involving the error function *erf(t)* as:

$$V_s(t) = \frac{[1 + erf(\alpha(t - t_{start}))]}{2} \qquad [2\text{-}50]$$

where t_{start} is the beginning time of the input pulse rise, and *α* is related to the inverse of the rise time of the pulse. The parameters t_{start} and *α* can be estimated by fitting Eq. [2-50] to the measurement of the input pulse obtained by matching a 50 Ohms reference termination at cable tester.

Weerts et al., (2001) presented that the input function was chosen as the signal leaving the coaxial, and open and shorted-circuited voltages, V_{open} and V_{short}, were measured, respectively. By normalizing the absolute voltage values to the unity, the input signal is obtained from:

$$V_s(t) = \frac{\left(V_{open} - V_{short}\right)}{2} \qquad\qquad \text{[2-51]}$$

Lin (1999) indicated that the input pulse can be generated from electric circuit model, thus the equation of the normalized input pulse was formulated as:

$$V_s(t) = 1 - \exp(-\frac{t - \zeta}{\tau}) \qquad\qquad \text{[2-52]}$$

where τ= (rise time/α_r) is a parameter correlated with the specification of step pulse rise time of TDR cable tester, ζ is the lag time of step pulse rise.   The parameters α_r and ζ are also estimated by fitting Eq. [2-52] to the measurement of the input pulse obtained by matching a 50 Ohms reference termination at cable tester.

As regard for the complexity for practical calibrations of input function, Mattei et al., (2006) examined aforementioned methods and proposed a new approach, in which the input function is derived form the signal reflected at the end of the coaxial cable disconnected form the TDR probe, and the response function coincides with the input function.
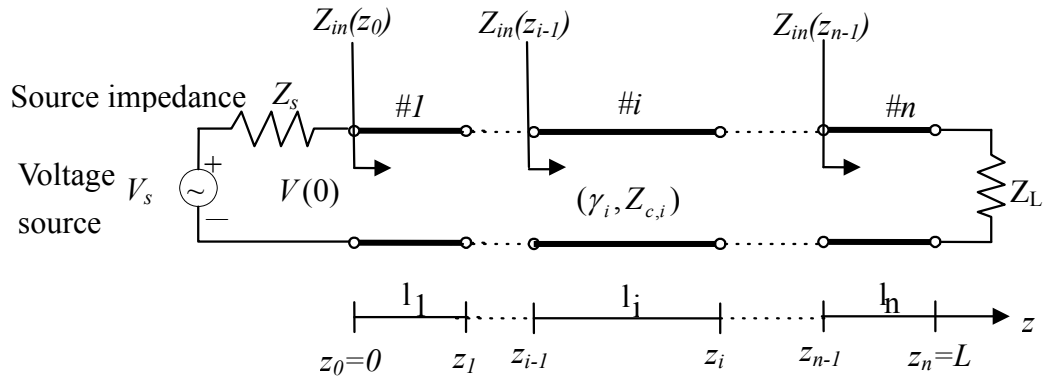
Fig. 2-12   Equivalent circuit of a cascade of uniform section for TDR system. (after Lin, 2003a)
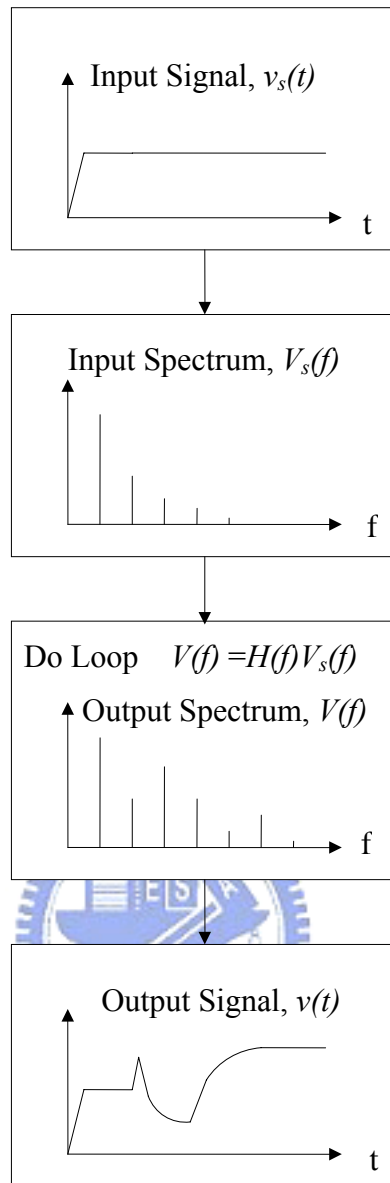
Fig. 2-13   The flow chart of the spectral algorithm (modified from Lin, 1999)

Comprehensive TDR modeling considering resistance effect

The transmission line parameters γ and Z_c in Eqs. [2-34] and [2-35] were derived by neglecting the effect of resistance of the waveguide (transmission line) conductors.   This is a typical assumption to simplify the derivation and be justified when cable length is not too long. However, when TDR measurements are used for field monitoring, long cable may be used. (Su, 1987; Heimovaara, 1993; Dowding et al., 2003).

Lin and Tang (2007) modified the TDR modeling process by considering the effect of resistance, and derived a complete form for the transmission line parameters. The characteristic impedance and propagation constant are parameterized as:

$$Z_c' = \frac{Z_p}{\sqrt{\varepsilon_r^*}} * A \qquad\qquad [2\text{-}53]$$

$$\gamma' = \frac{j2\pi f}{c}\sqrt{\varepsilon_r^*} * A \qquad\qquad [2\text{-}54]$$

$$A = \sqrt{1 + (1-j)\left(\frac{\eta_0}{Z_p}\right)\frac{\alpha_R}{\sqrt{f}}} \qquad\qquad [2\text{-}55]$$

where A is the (per-unit-length) resistance correction factor, $\eta_0 = \sqrt{\mu_0/\varepsilon_0} \approx 120\pi$ is the intrinsic impedance of free space, and α_R (sec$^{-0.5}$) is the resistance loss factor (a function of the cross-sectional geometry and surface resistivity due to skin effect). If cable resistance is ignored (i.e. $\alpha_R = 0$), A becomes 1.0 and γ and Z_c have expressions identical to the non-resistance formulations (Feng et al., 1999; Lin, 2003a).

Fig. 2-14 shows a TDR response under a long leading cable (30 m) and simulated TDR waveforms with/without consideration of cable resistance. The modeling with resistance effect can truly represent the dispersive characteristic in the reflected waveform when long cables are used.

This complete TDR model will be used to investigate the effect of cable resistance on the simplified analyses for determining apparent dielectric constant and electrical conductivity. Sensitivity analysis of dielectric spectroscopy and development of new spectral analysis technique will also utilize this complete model.
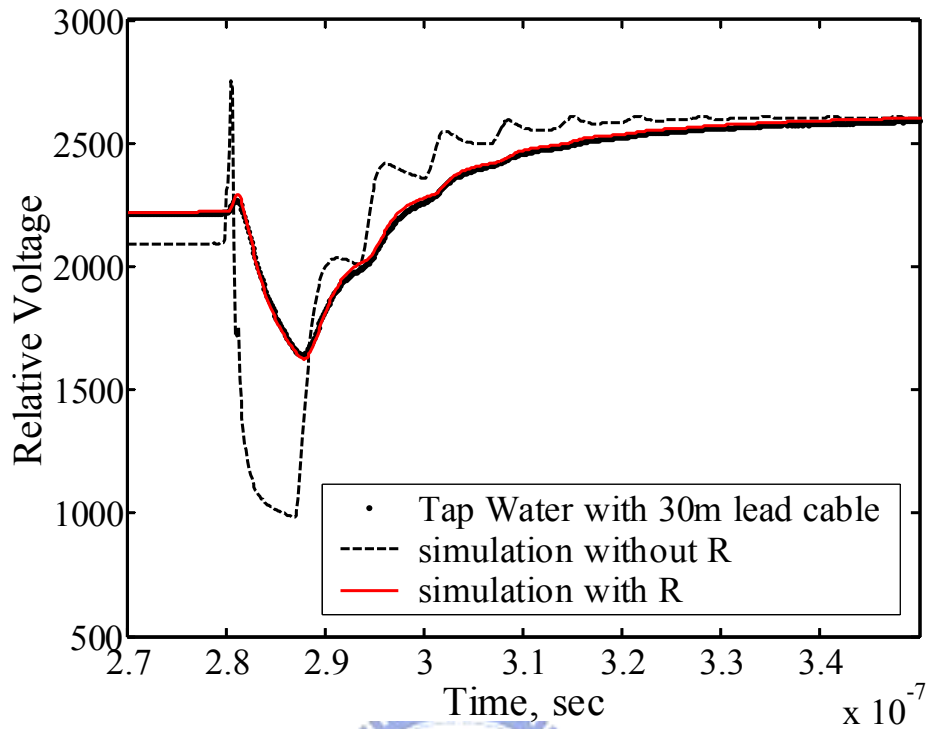
Fig. 2-14   The comparison of TDR modeling with and without consideration of cable resistance (after Lin and Tang, 2007)

2.3.5   Inverse Analysis of TDR Waveform for Dielectric Spectrum

Based on the TDR waveform modeling, the system function H or the S_{11} function can be experimentally determined by measured waveform v(t) and the known input step v_s(t). The system function contains the dielectric properties of a measured material. Heimovaara (2001) and Lin (2003a) used the simplex optimization algorithm [Nelder and Mead, 1965] to determine the optimal values to fit the measured waveform or S11 function at each frequency.

As discussed in section 2.2, the equivalent complex dielectric permittivity of materials can be expressed as a complex number in Eq. [2-15].   Therefore, dielectric permittivity of materials can be directly determined to fit the measured waveform or S_{11} function at each frequency.   This type of inversion of material dielectric properties is called "model free". Dielectric properties of material can be described as Debye's equation as Eq. [2-12].   An

adopted Debye's equation which is named "Cole-Cole equation" is more often used for describing the dielectric dispersive as (Hasted, 1973):

$$\varepsilon^*(f) = \left[\varepsilon_\infty + \frac{\varepsilon_s - \varepsilon_\infty}{1 + (if/f_{rel})^{1-\xi}} \right] - \frac{i\sigma_{dc}}{2\pi f \varepsilon_0} \qquad [2\text{-}56]$$

where f_{rel} is the relaxation frequency which defined as the frequency at which the permittivity equals $(\varepsilon_{dc} + \varepsilon_\infty)/2$, and ξ is a factor which accounts for a possible spread in relaxation frequency. Dielectric properties described by the model also can be determined to fit the measured waveform or S11 function using optimization. The type of this inversion is called "model fits".

However, the "model fits" method depends on the dielectric mixing model, which is hard to develop especially for the complex mixture. The inversion method of "model free" can not reliably obtain the dielectric permittivity at high frequency (> 200 MHz) (Lin, 1999 and 2003b), and this will be further discussed in section 3.2.1.

In order to obtain reliable dielectric spectrum of the measured material, several efforts on the TDR spectrum analysis have been proposed, but it still faces the problem of complexity and incompleteness. One of objectives in this study tries to establish a standard operation process (SOP) of TDR inversion analysis.

2.3.6   TDR Probe Development and Performance

There are two main issues for the TDR probe design or construction, one is the sample volume, and the other is the measurement sensitivity. Recently, many researches have examined these aspects through theoretical studies and laboratory experiments. The primary factors that affect the sample volume and the measurement sensitivity include the

configuration and length of the waveguide conductors.

Probe sample volume

The sample volume is considered in both the axial and cross sectional directions. The vertical sample volume along the axial direction of the probe increases when the probe length *L* increases, whereas the horizontal sample volume defined as the region of materials contributing to the measurement perpendicularly to the direction of the probe (Ferre et al., 1998) is affected by probe configuration.

The configuration of probe includes four factors: type of probe conductors (rods or plates), numbers of rods, spacing of rods, and the diameter (or thickness) of rods. Knight (1992) presented approximate analytical solutions for two-rod and multi-rod probes. The approach approximates the weighting of the energy density distribution, resulting from the solution to the two-dimensional electrostatic problem in the plane perpendicular to the rods. Knight et al. (1997) later presented the use of numerical methods to solve the Laplace equation in two dimensions to model the response of TDR probes. The numerical approach offers a powerful tool allowing the modeling of non-uniform probe geometries. Kirkby (1996) used Arbitrary Transmission Line Calculator (ATLC) program to estimate the relative energy storage density for a range of TDR probe configurations as shown in Fig. 2-15. The dark areas represented zones of greatest energy storage. From Fig. 2-15(a) to Fig. 2-15(d), it compared the commonly used probes constructed with rods, while Fig. 2-15(e) and (f) displayed cross sections for parallel plate geometries.

Due to the common practice in the field, probes with rod configuration would be much more acceptable compared to the plate types (Robinson et al., 2003). Ferre et al. (1998) compared two- and three-rods probes, and found that given an increase in rod diameter for the same center spacing provides a marginal improvement in the uniformity of the distribution of

the energy density within the sample area. But the three-rod probe had a reduced sample volume and more energy around the central rod.

However, the two-rod probe is an unbalanced line, in which voltages are unequal (e.g., +1V, 0V), while the three-rod probe is a balanced line.   A great influence of unbalance line is common mode noise rejection [Spaans and Baker, 1993]. They indicated that in the unbalanced configuration, common mode noise can affect the voltage of the signal, and decrease reproducibility of the analysis of the TDR waveform.   A balun, which converts electric field from unbalanced to balanced, is discussed in recent researches (Zegelin et al., 1989; Baker and Allmaras, 1990). Spaans and Baker (1993) used a simple 1:1 balun to minimize the signal loss in the antenna wire leading to the probe, and this simple balun performed at least as well as conventional one in soil water content and EC determination.

In spite of attempts that focus on the sample volume with a variety of TDR probe configurations mentioned above, there are still some new types of TDR probe, such as spiral waveguide [Vaz and Hopmans, 2001], whose sample volume would be more complex to determine by using conventional 2-dimensional numerical analysis.   Furthermore, for some special case, such as using TDR probe to determine the material properties in submerged condition, how electric field distributes in the probe head and rods is not yet revealed. Calculations of 3-dimentional electric field should be performed to investigate unconventional TDR probes.   Fortunately, existing software, such as Ansoft HFSS[®], provides 3D electromagnetic field simulation of high-frequency. The 3D electromagnetic field simulation software will be used to investigate probe performance in chapter 5.
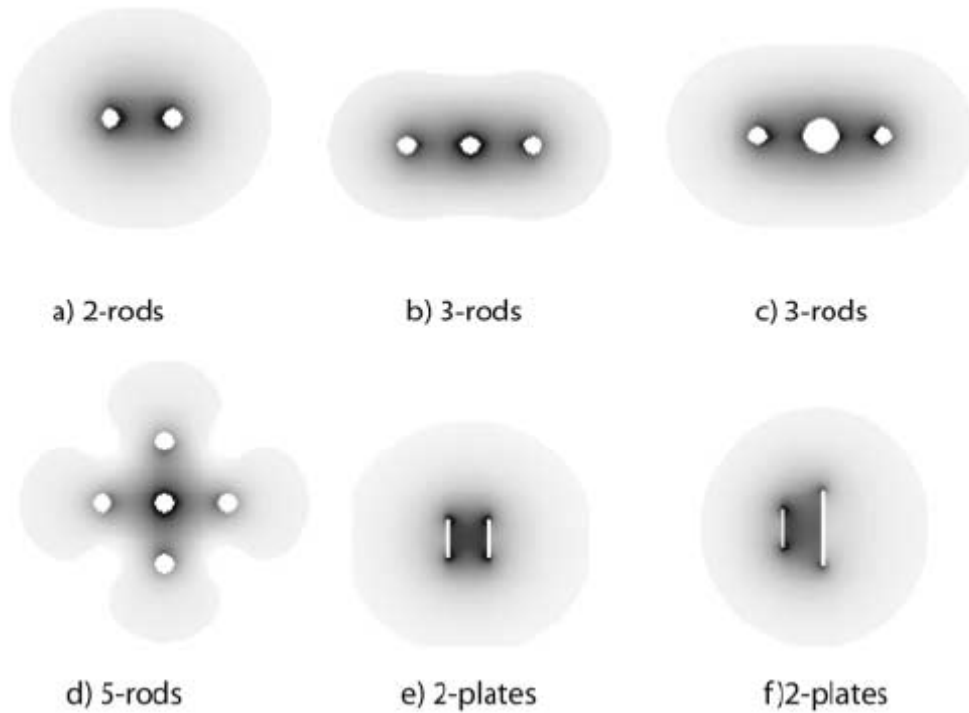
Fig. 2-15   Relative electric field intensity and energy storage density cross-sections for a variety of TDR probe designs. Configurations include (a) two rods, (b) three rods, (c) three rods with the center rod twice the diameter of the outer rods, (d) five rods, (e) parallel plates, and (f) parallel plates with the right-hand plate twice the length of the left-hand plate. (after Kirkby, 1996)

Measurement sensitivity

While the spatial sensitivity is related to the weighting of energy density, measurement sensitivity is defined as the change of the measurement value, such as travel time and steady state voltage, due to a unit change of the parameter, such as dielectric permittivity and EC. The normalized sensitivity evaluated at $m = \hat{m}$ is defined as:

$$S_{\hat{m}} = \left[\frac{\partial g / g}{\partial m / m} \right]_{\hat{m}} = \frac{\partial g}{\partial m} \frac{m}{g} \qquad [2\text{-}57]$$

where m denotes the physical parameters, and $g(m)$ represents the measured data (e.g. the TDR waveform or dielectric spectrum).   The measurement sensitivity may be evaluated

48

analytically (if the measured data g can be expressed analytically in terms of the physical parameter m and differentiable) or numerically. In this study, measurement sensitivity of dielectric permittivity and EC as a function of probe parameters will be discussed.

3   TDR Dielectric Permittivity Analysis and Influence Factors

3.1 Implication of Travel Time Analysis

Several methods were proposed for determining the apparent dielectric constant (K_a) from a TDR waveform. Their influencing factors have not been extensively investigated and the apparent dielectric constant and effective frequency obtained from different methods have not been critically compared. The objectives of this study are two folds: (1) to examine effects of electrical conductivity, dielectric dispersion, and cable length on apparent dielectric constant and effective frequency; and (2) to investigate whether effects of those factors on the apparent dielectric constant can be accounted for by the effective frequency.

3.1.1   Travel Time Calibration and Effective Frequency
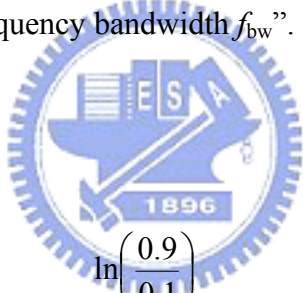
An arbitrary time in the reflection waveform was chosen as the reference time. The arrival time of the end reflection was determined by different methods including the single tangent, dual tangent, and derivative methods, as shown in Fig. 2-10. The time between these two points is denoted as $\Delta\tau$, which is a combination of the actual travel time in the sensing waveguide (t_s) and a constant time offset (t_0) between the reference time and the actual start point. The travel time t_p is related to the apparent dielectric constant (K_a) by Eq. [2-39] as suggested by Heimovaara (1993) in Eq. [2-42]. It should be noted that different values of system parameters (t_0 and L) may be obtained when different methods of travel time analysis are used.

Two methods have been used to investigate the "effective frequency" of the K_a measurement. One method compares the K_a from the travel time analysis with the permittivity obtained from the frequency domain dispersion curve (Or and Rasmussen 1999; Lin 2003b). The other method is based on the 10% to 90 % rise time of the end reflection (Logsdon 2000;

Robinson et al. 2005). To avoid confusion, the first approach is termed "equivalent frequency f_{eq}". It is determined by equating K_a to the frequency-dependent apparent dielectric permittivity $\varepsilon_a(f)$:

$$K_a = \varepsilon_a(f_{eq}) = \sqrt{\frac{\varepsilon_r'(f_{eq})}{2}\left(1+\sqrt{\left(\frac{\varepsilon_r''(f_{eq})+\frac{\sigma}{2\pi f_{eq}\varepsilon_0}}{\varepsilon_r'(f_{eq})}\right)^2}\right)} \qquad [3\text{-}1]$$

The apparent dielectric permittivity is used instead of the real part of dielectric permittivity to take into account effects of dielectric loss and electrical conductivity on phase velocity. The second approach is termed "frequency bandwidth f_{bw}". It is defined by the 10% to 90 % rise time (t_r) of the end reflection as

$$f_{bw} = \frac{\ln\left(\frac{0.9}{0.1}\right)}{2\pi\, t_r} \approx 0.35/t_r \qquad [3\text{-}2]$$

where t_r is measured in seconds.

3.1.2   Evaluation of Influence Factors

The wave phenomena in a TDR measurement include multiple reflections, dielectric dispersion, and attenuation due to conductive loss and cable resistance. A comprehensive TDR wave propagation model that accounts for all wave phenomena has been proposed and validated by Lin and Tang (2007). With the proved capability to accurately simulate TDR measurements, the TDR wave propagation model can be used to systematically investigate

effects of dielectric dispersion, electrical conductivity, and cable length on apparent dielectric constant and effective frequency. Synthetic TDR measurements (waveforms) were generated by varying the influential factors in a controlled fashion. The associated apparent dielectric constants and effective frequencies were calculated and compared.

The synthetic TDR measurement system is composed of a TDR device, a RG-58 lead cable, and a sensing waveguide. Possible mismatches due to connectors and probe head are neglected since the simplification will not affect the apparent dielectric constant. Tap water and a silt loam modeled by the Cole-Cole equation were used as the basic materials. It is understood that the Cole-Cole equation may not be perfect for modeling dielectric dispersion of soils, but it is used to parameterize the dielectric dispersion for the parametric studies. The transmission line parameters and dielectric properties used in the parametric study are listed in Table 3-1 and Table 3-2, respectively. Time interval $dt = 2.69 \times 10^{-11}$ sec and time window $0.5N \, dt = 8192 \times 40$ $dt = 8.8 \times 10^{-6}$ sec (slightly greater than the pulse length of 7×10^{-6} sec in a TDR 100) were used in the numerical simulations. The corresponding Nyquist frequency and frequency resolution are 18 GHz and 60 kHz, respectively. The Nyquist frequency is well above the frequency bandwidth of TDR 100 and the long time window ensures that the steady state is obtained before onset of the next step pulse.

Table 3-1　TDR system parameters

Section	Parameters	Reference value	Range
Sensing waveguide	EC σ, S m^{-1}	0.01	0.005 ~ 0.1
	Dielectric permittivity ε_r	Tap water, and Silt loam[†]	with varying f_{rel}
	Geometric impedance Z_p , Ω	300	300
	Length L, m	0.3	0.3
	Resistance loss factor α_R, sec$^{-0.5}$	0	0
Lead cable (RG-58)	EC σ, S m^{-1}	0	0
	Dielectric permittivity ε_r	1.95	1.95
	Geometric impedance Z_p , Ω	77.5	77.5
	Length L, m	10	1 ~ 50
	Resistance loss factor α_R, sec$^{-0.5}$	19.8	19.8

[†] Referring to the Cole-Cole parameters listed in Table 3-2

Table 3-2　Cole-Cole parameters for material used in numerical simulations (modified from Friel and Or, 1999)

Material	ε_{dc}	ε_∞	f_{rel}	ξ
Silt loam	26.0	18.0	0.2e9	0.01
Tap water	78.54[†]	4.22	17e9	0.0125

[†] Water temperature = 25°C

Effect of electrical conductivity

The electrical conductivity is well known for having a smoothing effect on the reflected waveform and hence affecting the K_a determination. However, the degree of influence may depend on dielectric dispersion and the method of travel time analysis. Varying the value of electrical conductivity in water (as a non-dispersive case) and silt loam (as dispersive case), Fig. 3-1 shows the effects of electrical conductivity on K_a for different methods of travel time analyses. In the non-dispersive case, only the single tangent method is slightly affected by the

electrical conductivity. Both the dual tangent method and derivative method are unexpectedly immune to changing electrical conductivity (see Fig. 3-1(a)). As the medium becomes dielectric dispersive within TDR bandwidth, the apparent dielectric constant becomes sensitive to changing electrical conductivity (see Fig. 3-1(b)). Among all methods, the dual tangent method is least affected by electrical conductivity. When EC is greater than 0.05 Sm^{-1}, the dual tangent method and derivative method suddenly obtains higher apparent dielectric constants as EC increases. The K_a may even become greater than DC electric permittivity due to significant contribution of EC at lower frequencies.

For each simulated waveform, the equivalent frequencies of different travel time analysis methods and the frequency bandwidth of the end reflection can be determined by Eq. [3-1] and Eq. [3-2], respectively. The equivalent frequencies and frequency band width associated with Fig. 3-1(b) (the dispersive case) is shown in Fig. 3-2. Only the dispersive case is shown since the equivalent frequencies in non-dispersive case is not meaningful. Against common perception, the frequency bandwidth is not significantly affected by electrical conductivity. The end reflection may appear smooth due do decreased reflection magnitude as electrical conductivity increases. The 10% to 90% rise time and hence the frequency bandwidth remains relatively constant. The equivalent frequencies decrease with increasing electrical conductivity as expected. The dual tangent method leads to the highest equivalent frequency while the derivative method, as also pointed out by Robinson et al. (2003), results in the lowest equivalent frequency, which is closer to the frequency bandwidth. The dual tangent is advantageous in this regard since, at higher frequency, the apparent dielectric permittivity is less affected by changing electrical conductivity. Unfortunately, its automation of data reduction is also most difficult.
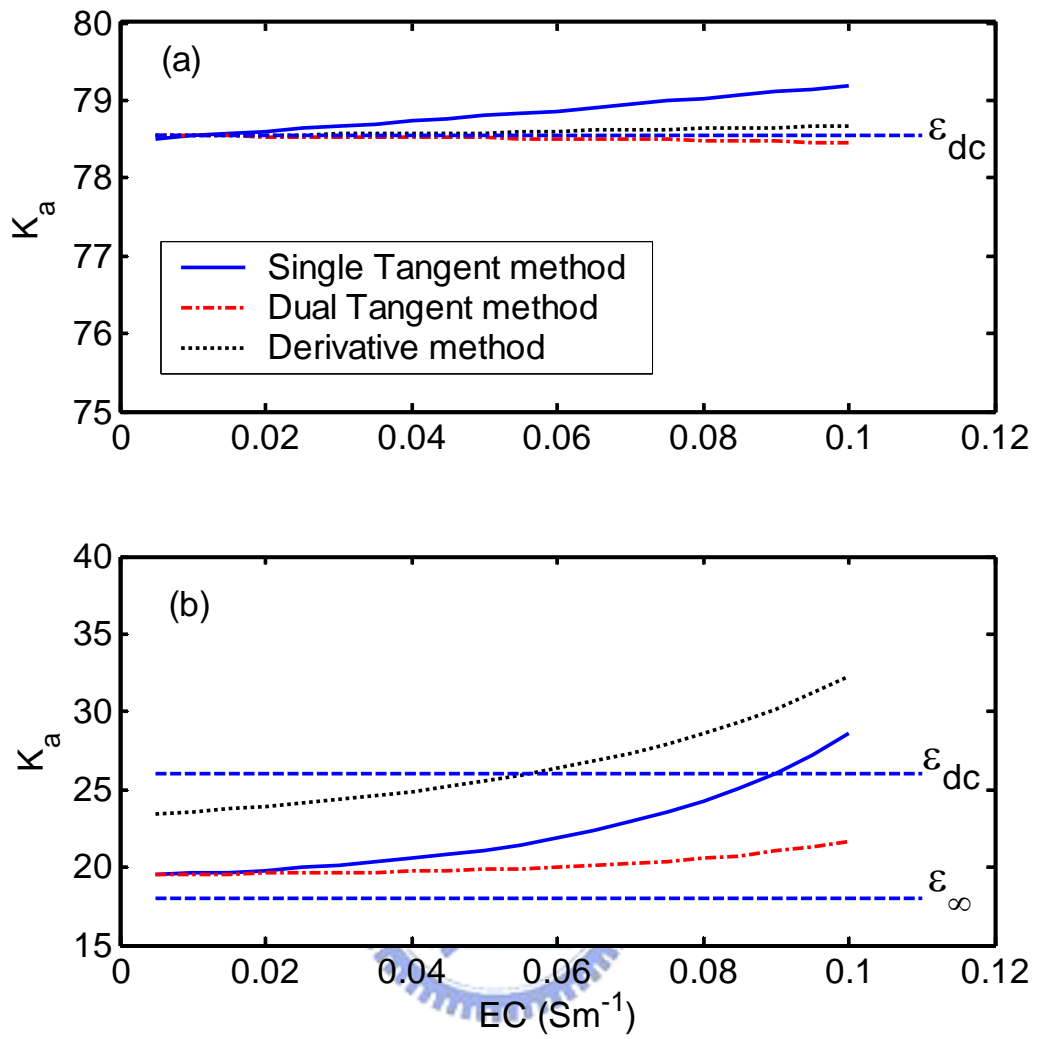
Fig. 3-1   The apparent dielectric constants as affected by electrical conductivity in (a) the non-dispersive case and (b) the dispersive case.
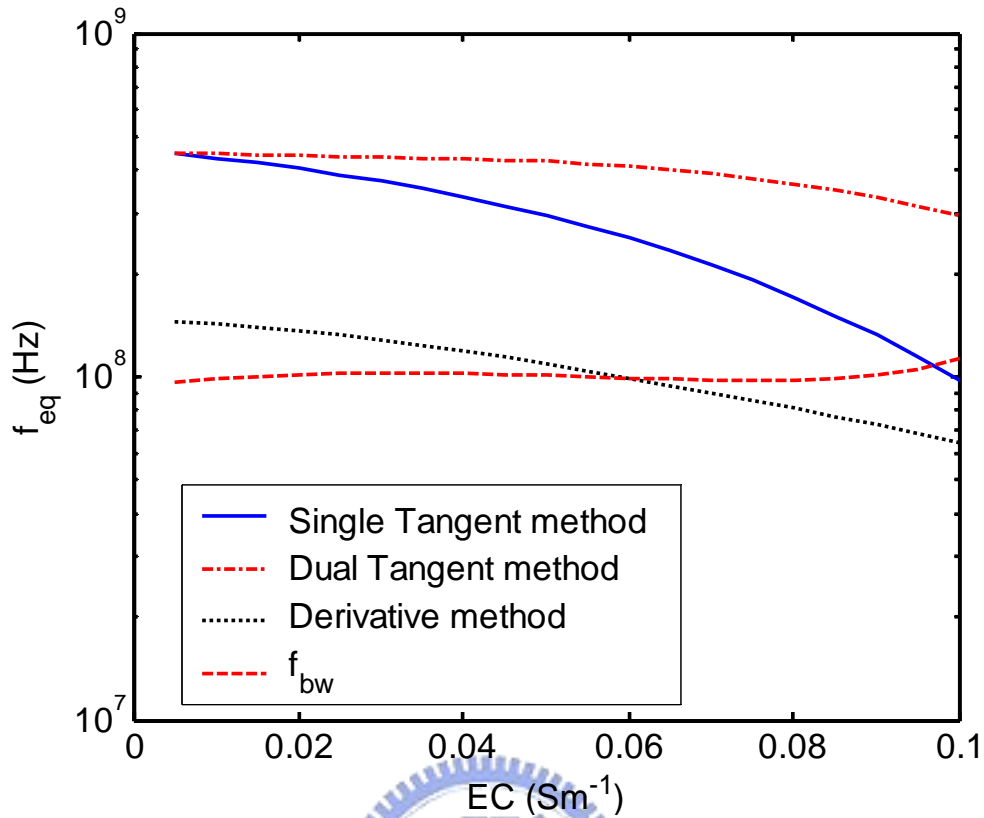
Fig. 3-2   The equivalent frequency and frequency bandwidth corresponding silt loam case

Effect of cable resistance

The per-unit-length parameters that govern the TDR waveform include capacitance, inductance, conductance, and resistance. The first three parameters are associated with electrical properties of the medium and cross-sectional geometry of the waveguide. The per-unit-length resistance is a result of surface resistivity and cross-sectional geometry of the waveguide (including cable, connector, and sensing probe), which is often ignored in early studies of TDR waveform by assuming a short cable. The cable resistance is practically important since significantly long cable is often used in monitoring (Lin and Tang 2007). Not only does it affect the steady-state response and how fast the TDR waveform approaches the steady state, the cable resistance also interferes with the transient waveform related to the travel time analysis, as shown in Fig. 3-3 for measurements in water with different cable lengths. The "significant length" in which cable resistance becomes unnegligible depends on the cable type,

which could range from lower quality RG-58, medium quality RG-8, to higher quality cables with solid outer conductor used in cable television (CATV) industry. The RG-58 cable is used for simulation in this study to manifest the effect of cable resistance and since it has been widely used for its easy handling.

The measurements of water and the silt loam with various cable lengths were simulated. As an attempt to counteract the effects of cable length, the system parameters (i.e. t_0 and L) were obtained by air-water calibration for each cable length. The calibrations of system parameters indicated that the L increases as cable length increases as shown in Table 3-3, except the case of using dual tangent method with 50m cable. Fig. 3-4 shows the effects of cable length on K_a for different methods of travel time analyses. In the non-dispersive case (Fig. 3-4 (a)), all methods are not affected by cable length if air-water calibrations are performed each cable lengths. As the medium becomes dielectric dispersive within TDR bandwidth, the apparent dielectric constant becomes quite sensitive to changing cable length (see Fig. 3-4 (b)), in particularly for the derivative method, even though the probe parameters have been calibrated by the air-water calibration procedure for each cable length. Fig. 3-4 suggests that the empirical relationship between K_a and soil water content would depends on cable length if the soil is significantly dielectric-dispersive. This is in agreement with the finding by Logsdon (2000). When studying the effect of cable length on TDR calibration for high surface areas soils (or called "dispersion material" in this study), Logsdon (2000) concluded that high surface area samples should be calibrated using the same cable length used for measurements. This is even more imperative if the derivate method is used.

Both the equivalent frequency and frequency bandwidth decreases with increasing cable length, as shown in Fig. 3-5. The single tangent and dual tangent methods have similar trends, while the derivative method is most sensitive to and results in the lowest effective frequency and frequency bandwidth. Therefore, the derivative method can leads to a K_a greater than DC

dielectric permittivity due to existence of electrical conductivity and low effective frequencies. It should be noted that, for the simulated RG-58 cable, the equivalent frequency corresponds to the frequency bandwidth only valid for cable length around 10~15 m. Although Robinson et al. (2005) concluded that the permittivity determined from the derivative method corresponds to the frequency bandwidth, but they made few account of the cable length effect, which may decrease the frequency bandwidth as the cable length increases. According to Fig. 3-5, this conclusion holds only for limited range of cable length.

Table 3-3   The calibrated probe length (m) obtained from the air-water calibration for different cable lengths and methods of travel time analysis

Methods	Cable Length			
	1 m	10 m	25 m	50 m
Single tangent method	0.2935	0.2968	0.3020	0.3049
Dual tangent method	0.2934	0.2968	0.3015	0.2993
Derivative method	0.3025	0.3062	0.3129	0.3352
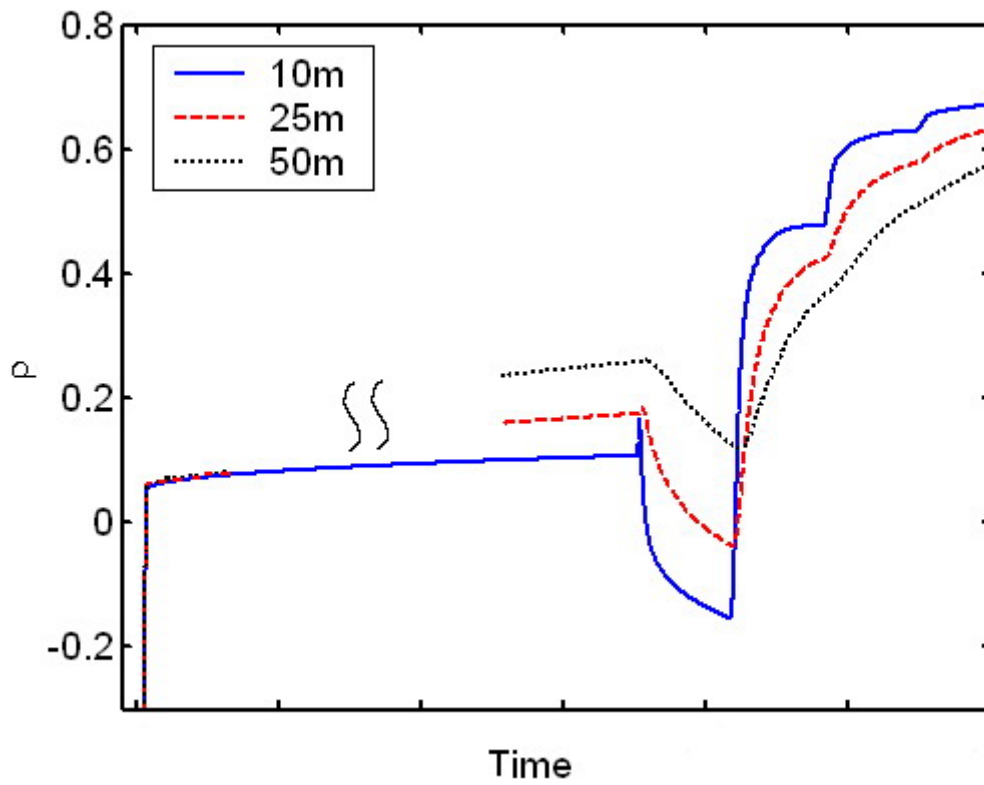
Fig. 3-3   Measurements in water with various cable lengths.
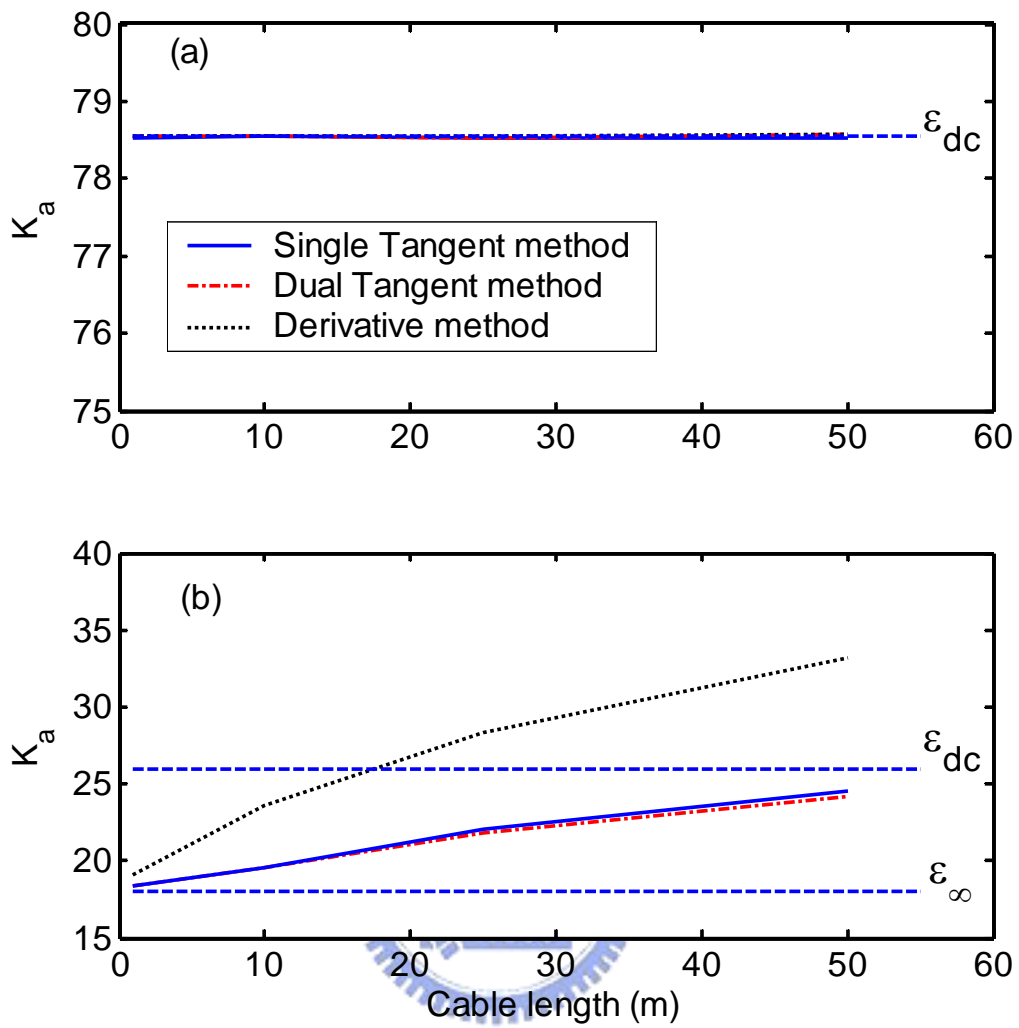
Fig. 3-4 The apparent dielectric constants as affected by cable length in (a) the non-dispersive case and (b) the dispersive case.
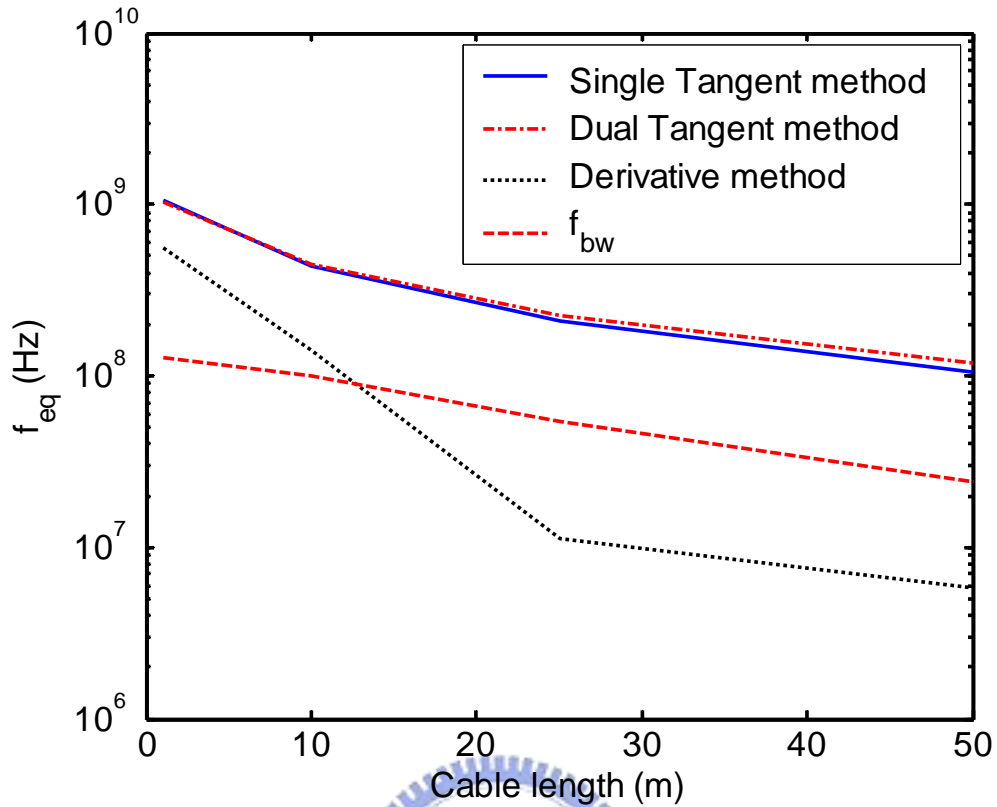
Fig. 3-5   The equivalent frequency and frequency bandwidth corresponding to silt loam case

Effect of dielectric relaxation frequency, f_{rel}

The apparent dielectric constant does not have a clear physical meaning when the dielectric permittivity is dispersive. Based on the Cole-Cole equation, the effects of dielectric relaxation frequency f_{rel} on K_a were investigated by varying f_{rel} in Table 3-2, while keeping other Cole-Cole parameters constant. The water-based cases represent cases with large difference between ε_∞ and ε_{dc} (defined as $\Delta\varepsilon = \varepsilon_{dc} - \varepsilon_\infty$), and the silt loam-based cases represent cases with relatively small $\Delta\varepsilon$. The apparent dielectric constants as affected by f_{rel} are shown in Fig. 3-6. The f_{rel} seems to have a lower bound frequency below which the dielectric permittivity is equivalently non-dispersive and equal to ε_∞, and a higher bound frequency above which the dielectric permittivity is equivalently non-dispersive and equal to ε_{dc}. As f_{rel} increases from the lower bound frequency to higher bound frequency, the apparent dielectric constant goes from ε_∞ to ε_{dc}. In these relaxation frequencies, the derivative method yields higher K_a than tangent

methods because its equivalent frequency is always lower than that of tangent methods, as shown in Fig. 3-2 and Fig. 3-5. Comparing Fig. 3-6a with Fig. 3-6b, the lower bound frequency seems to decrease as $\Delta\varepsilon$ increases. That is, the higher the $\Delta\varepsilon$, the wider the relaxation frequency range is affected by the dielectric dispersion.

Also depicted in Fig. 3-6 are the associated frequency bandwidths as affected by the relaxation frequency. When the relaxation frequency is outside the frequency range spanned by the aforementioned lower bound and higher bound, the dielectric permittivity does not show dispersion in the TDR frequency range, and hence the frequency bandwidths are similar. The frequency bandwidth decreases as the relaxation frequency becomes "active" and reaches the lowest point near the middle of the "active" frequency range spanned by the lower bound and higher bound.
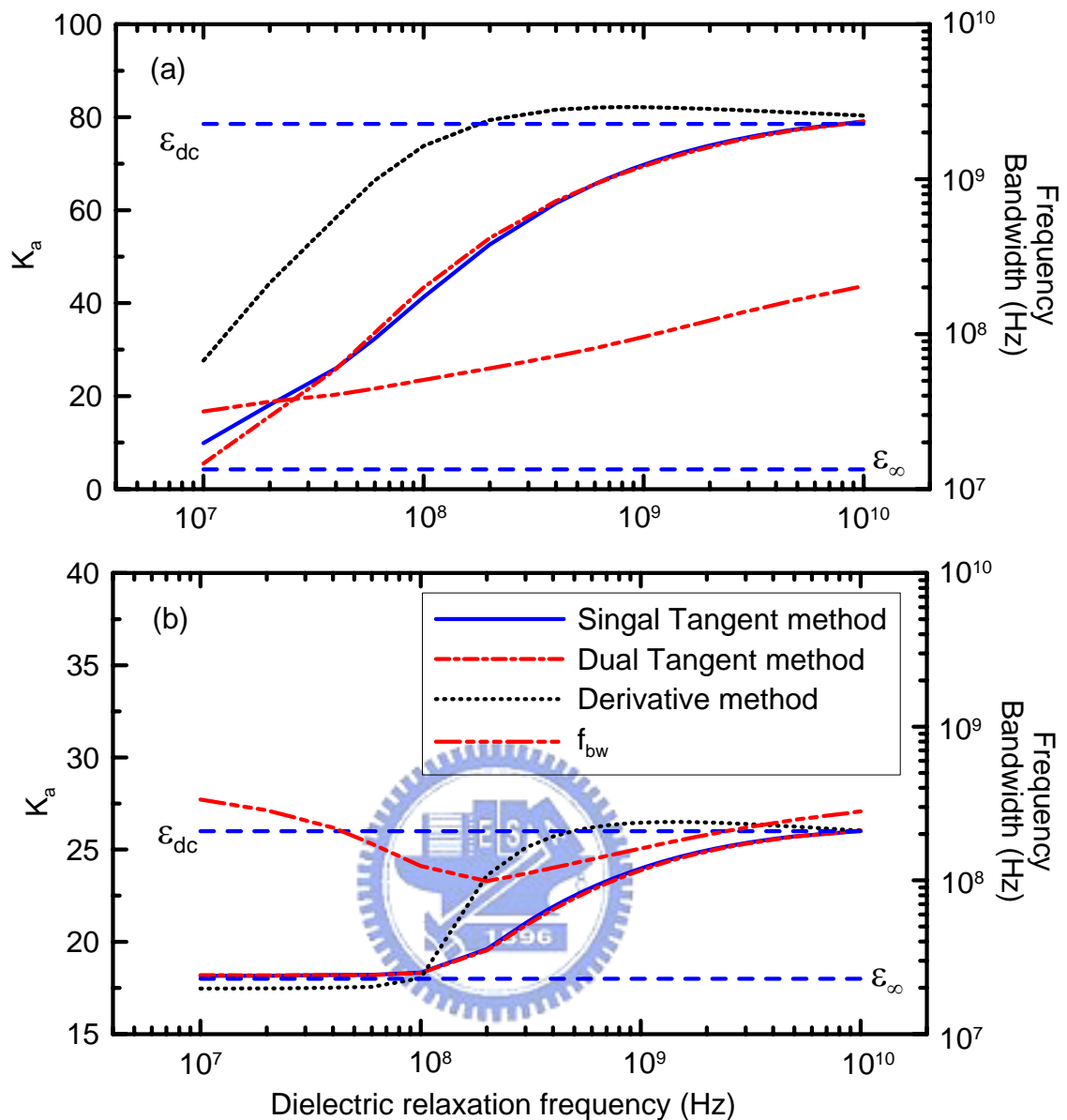
Fig. 3-6 The apparent dielectric constants and frequency bandwidth by changing the dielectric relaxation frequency while keeping other Cole-Cole parameters constant in (a) water and (b) silt loam.

Apparent Dielectric Constant vs. Frequency Bandwidth

The effects of electrical conductivity, cable resistance, and dielectric dispersion were systematically investigated. These factors can significantly affect the measured apparent dielectric constant. The equivalent frequency would give some physical meaning to the measured apparent dielectric constant, but no method is available for its direct determination. Even if the equivalent frequency of the apparent dielectric constant can be determined, it may

not correspond to the optimal frequency range for water content measurement, as shown in Fig. 2-11. The frequency bandwidth, sometimes referred to as the effective frequency, can be determined from the rise time of the end reflection. It was anticipated to correspond to the equivalent frequency of certain travel time analysis (i.e. the derivative method). However, this correspondence is not generally true. Besides, the derivative method is quite sensitive to electrical conductivity and cable resistance, and hence would not be a good alternative to the conventional tangent line methods. Nevertheless, the frequency bandwidth of the TDR measurement offers an extra piece of information. An idea has been proposed to incorporate frequency bandwidth into the empirical relationship between apparent dielectric constant and soil water content (Evett et al. 2005). To examine whether this idea is generally feasible, the relationship between apparent dielectric constant from the dual tangent method and frequency bandwidth is plotted in Fig. 3-7 using the data obtained from previous three parametric studies. The electrical conductivity, cable length, and dielectric dispersion apparently have distinct effects on the K_a-f_{bw} relationship. In fact, the change in apparent dielectric constant vs. the change in frequency bandwidth as the influencing factors vary is divergent. When measuring soil water contents, the same water content may measure different apparent dielectric constant due to different electrical conductivity (e.g. from water salinity), cable length, and dielectric dispersion (e.g. from soil structure). Since there is no consistent trend between the change in apparent dielectric constant and the change in frequency bandwidth, compensating the effects of electrical conductivity, cable length, and dielectric dispersion by the frequency bandwidth seem theoretically infeasible.
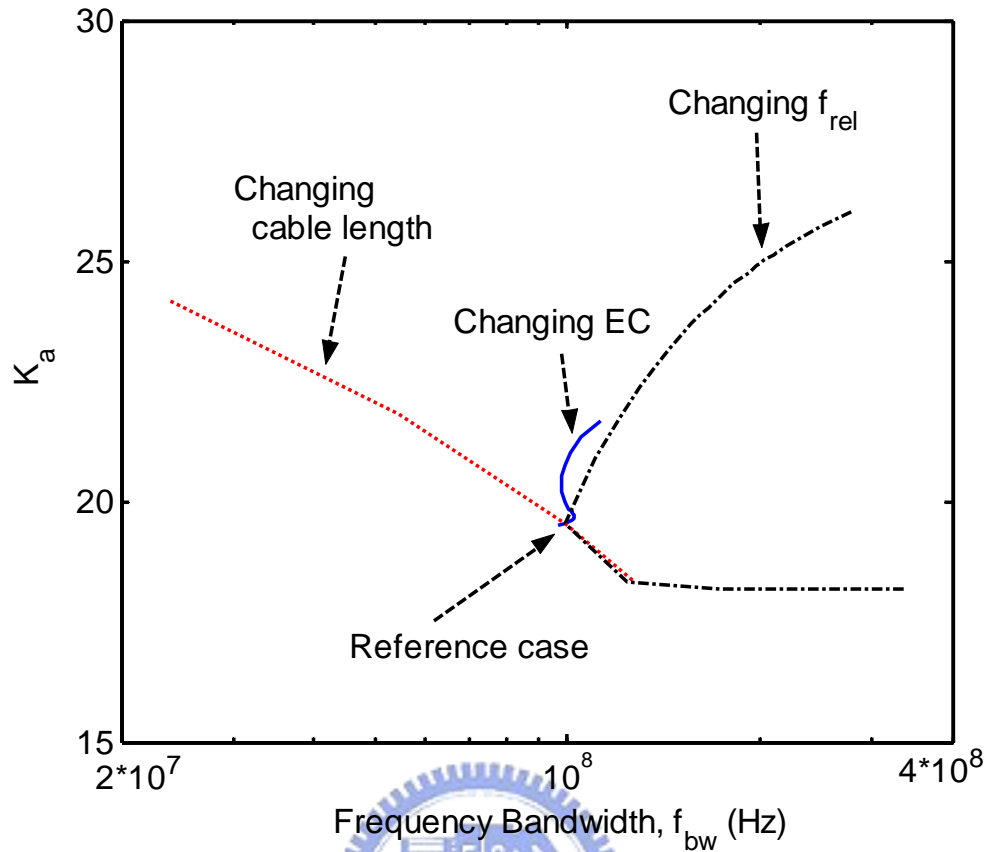
Fig. 3-7   The relationship between K_a from the dual tangent method and frequency bandwidth due to different influences

3.2 Dielectric Spectrum Analysis

Dielectric spectrum analysis by TDR provides extra information compared to the travel time and EC analysis. The study in the previous section has indicated that there is no consistent trend between the change in K_a and the change in the associated effective frequency as the influencing factors varies. Compensating the effects of electrical conductivity, cable length, and dielectric dispersion by the effective frequency seems theoretically infeasible.   To improve soil water content estimation considering the influence factors, dielectric spectrum analysis at least in the previously-found optimal frequency range between 500 MHz to 1 GHz seem inevitable. Besides, dielectric spectrum at low frequency provides information related to soil-water interactions. The dielectric spectrum, although more informative, is difficult to be

reliably obtained. The following study will investigate the sensitivity and reliability of dielectric spectroscopy to indentify the source of uncertainty and provide preferred guideline.

3.2.1   Sensitivity Analysis and Reliability of Dielectric Spectroscopy

Lin (2003b) preformed dielectric spectroscopy based on realistic modeling of the multi-section TDR system. An example is shown in Fig. 3-8 for a silt loam. The measured data was obtained by directly solving the S11 function for the dielectric permittivity. A reliable result could only be obtained below 200 MHz. Inversion based on a dielectric dispersion model is more reliable but requires a good dispersion model, which is not always available for many composite materials.

Errors in high frequency are possibly affected by signal to noise ratio (SNR), imperfect TDR system calibration, and the fringing effect. The decreased SNR in high frequency range is due to lower high frequency energy of step input and greater signal loss at high frequencies in wave propagation. The calibration of the multi-section TDR measurement system is a delicate work. The connector and the probe head may have several mismatched that may not be perfectly considered in system calibration. Imperfect calibration of these mismatches may affect the dielectric spectroscopy in the high frequency range.   The fringing effect occurs at the open end of the sensing waveguide, it may be treated as an equivalent end fringing capacitance C_f, as illustrated in Fig. 3-9.   The equivalent end fringing capacitance causes a phase shift which results in the trace not being coincident with the open point after mathematical correction of equivalent extra line of length (L_{eo}), as shown in Fig. 3-9.   The end fringing capacitance is not difficult to be modeled and neglected in the current TDR model. This assumption may be another source of error for high frequency measurements.

Fringing effect can be avoided by using a probe with shorted end. de Loor et al. (1972) and Cereti et al. (2003) presented the TDR travel time analysis using shorted-end probe. On

an attempt to reduce error in the high frequency range, a shorted-end probe was also used to overcome the fringing effect in dielectric spectroscopy. Fig. 3-10 (Tang, 2007) displays the comparison of estimated dielectric spectrum of tap water from open-end and shorted-end coaxial probe. The shorted-end probe does not seem to improve the accuracy much in the high frequency range. On the other hand, great deviation form the theoretical values exist in the low frequency is observed. This result is unexpected and remains to be explained.

Since the shorted-end probe does not improve the estimated dielectric spectrum, an alternative approach which focuses on the sensitivity analysis is used to discover the source of error. The TDR scatter function (S_{11}) is taken as the frequency response for the sensitivity analysis. The S_{11} is the reflection spectrum of the whole TDR system as shown in Eq. [2-49b], thus it is influenced by several factors, including the dielectric constant of the material, length and impedance of the probe, and even the cable resistance. The investigation of S_{11} sensitivity is based on the TDR modeling whose basic parameters can be referred to the Table 3-1 and Table 3-2, thus the S_{11} can be estimated by these parameters using Eq. [2-49b]. Fig. 3-11 shows the abs(S_{11}) response with different cable length as measuring the tap water and silt loam. Beyond 1MHz, the magnitude of S_{11} is decreased due to cable resistance.

To discuss the sensitivity of S_{11} to the measured dielectric permittivity and calibration parameters (probe length and Z_p), the normalized sensitivity of S_{11} is formulated as:

$$S_{\hat{m}} = \left[\frac{\partial[abs(S_{11})]/abs(S_{11})}{\partial m/m} \right]_{\hat{m}} = \frac{\partial[abs(S_{11})]}{\partial m} \frac{m}{abs(S_{11})} \qquad [3\text{-}3]$$

where m indicates the influence factors. Since there is no efficient way to derive the analytical formulation of sensitivity, the numerical derivative method is used in this study to obtain the sensitivity function. The influence factors include the dielectric constant of the material,

length and impedance of the probe, and the boundary condition of probe.

Fig. 3-12 to Fig. 3-16 are the normalized sensitivity of S_{11} due to ε_{dc}, ε_{∞}, probe length L, and impedance Z_p, respectively. Each of these figures has the S_{11} normalized sensitivity of tap water and silt loam in open and shorted boundary conditions. The results of all cases indicate that the sensitivity function of S_{11} in the shorted-end condition is much lower than in the open-end condition at frequency below 50 MHz. This may explain why the dielectric spectroscopy can yield reasonable result at low frequencies.

The shorted-end probe does not significantly improve the measurements in the high frequency range and yield poor results in the low frequency range. Therefore, the fringing effect is not the source for the large deviation in the high frequency range, and the shorted-end probe is not recommended to replace open-end probe. The large deviation in the high frequency should be attributed to low energy of signal is the high frequency range and imperfect calibration of the TDR system.
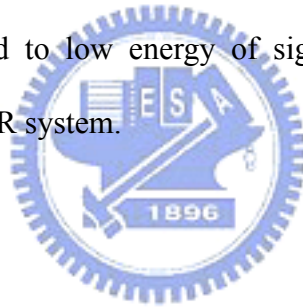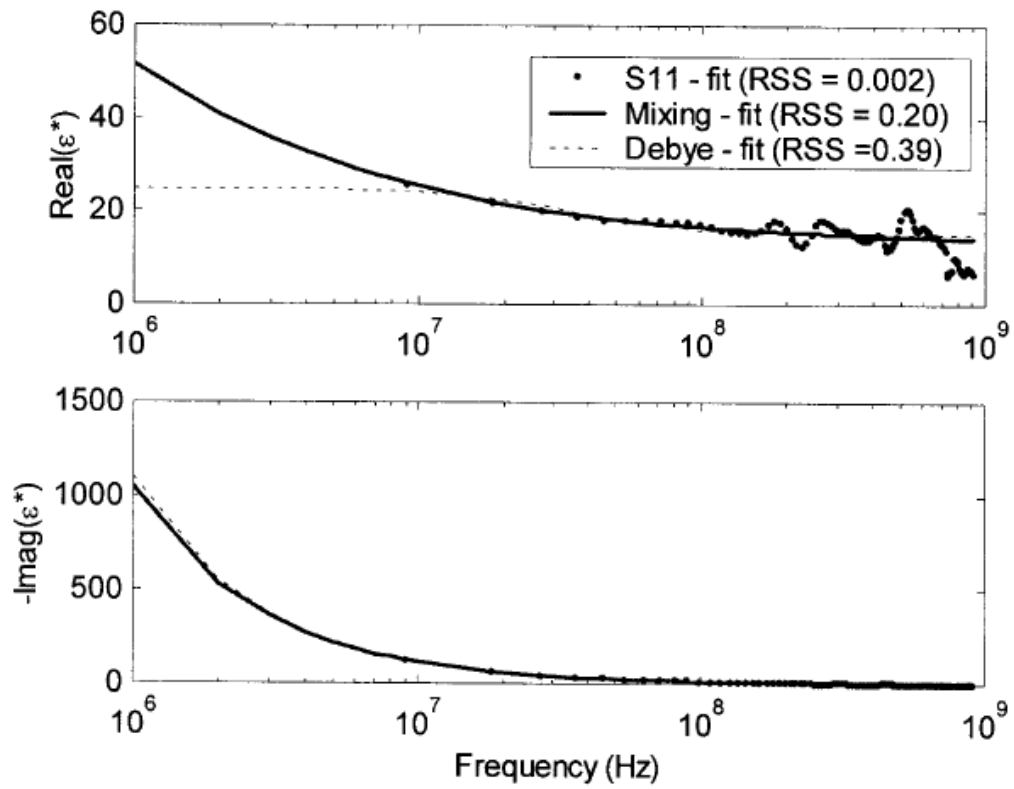
Fig. 3-8   Estimated frequency-dependent dielectric properties of a silt loam (after Lin, 2003b)
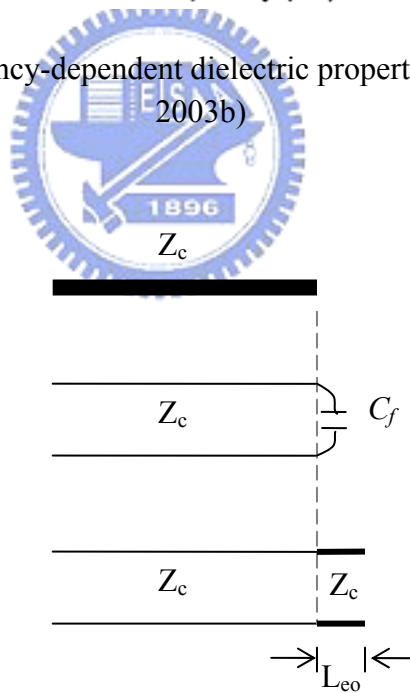
Fig. 3-9   Equivalent capacitance and extra length for fringing effect
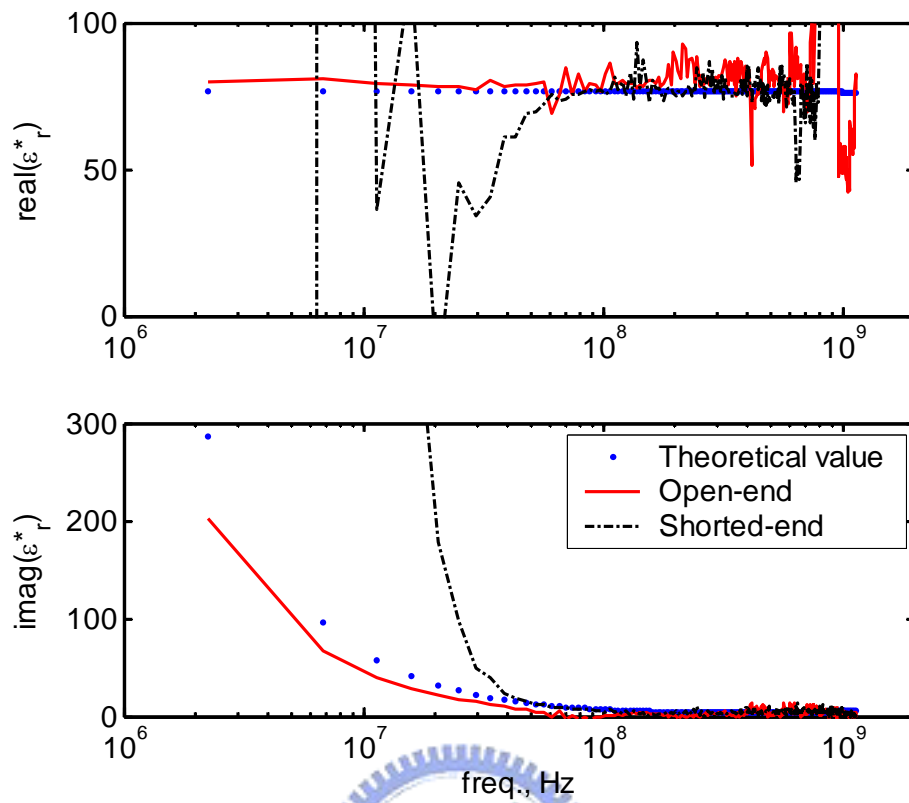
Fig. 3-10   Estimated dielectric spectrum of tap water from open-end and shorted-end coaxial probe (modified after Tang, 2007)
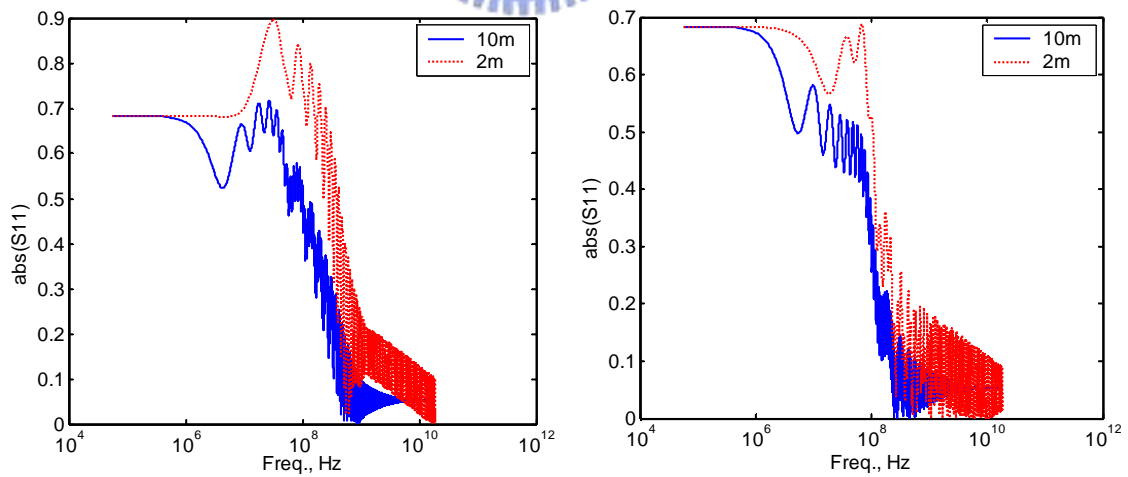
Fig. 3-11   TDR abs(S_{11}) response with different cable length as measuring the (left) tap water and (right) silt loam
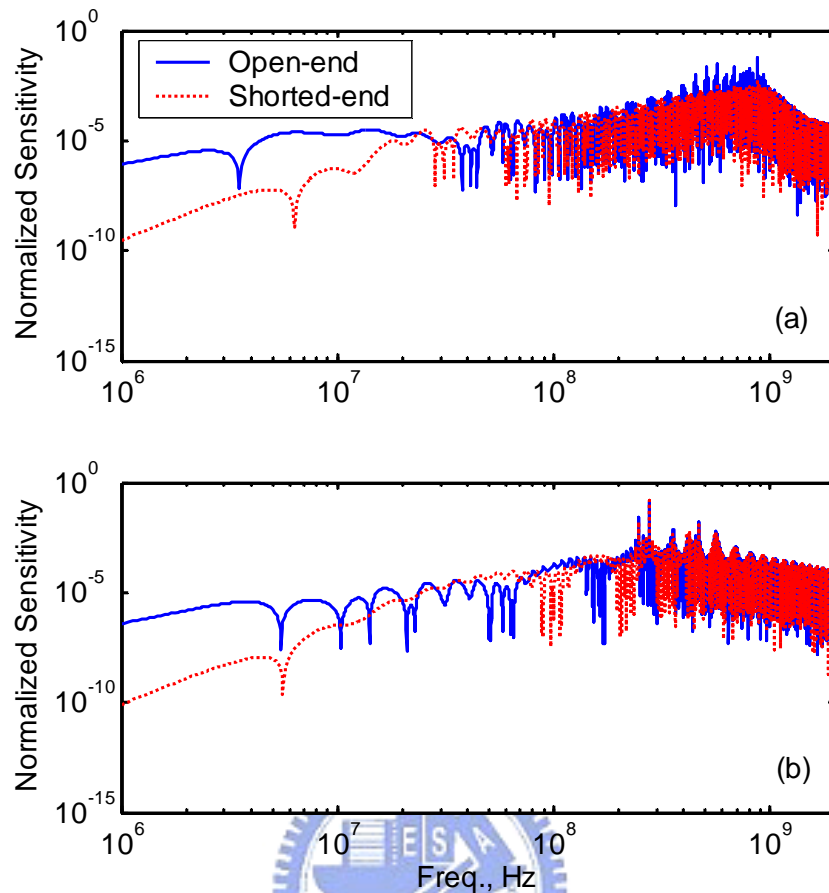
Fig. 3-12   Normalized sensitivity of abs(S_{11}) due to ε_{dc} as measuring the (a) tap water and (b) silt loam
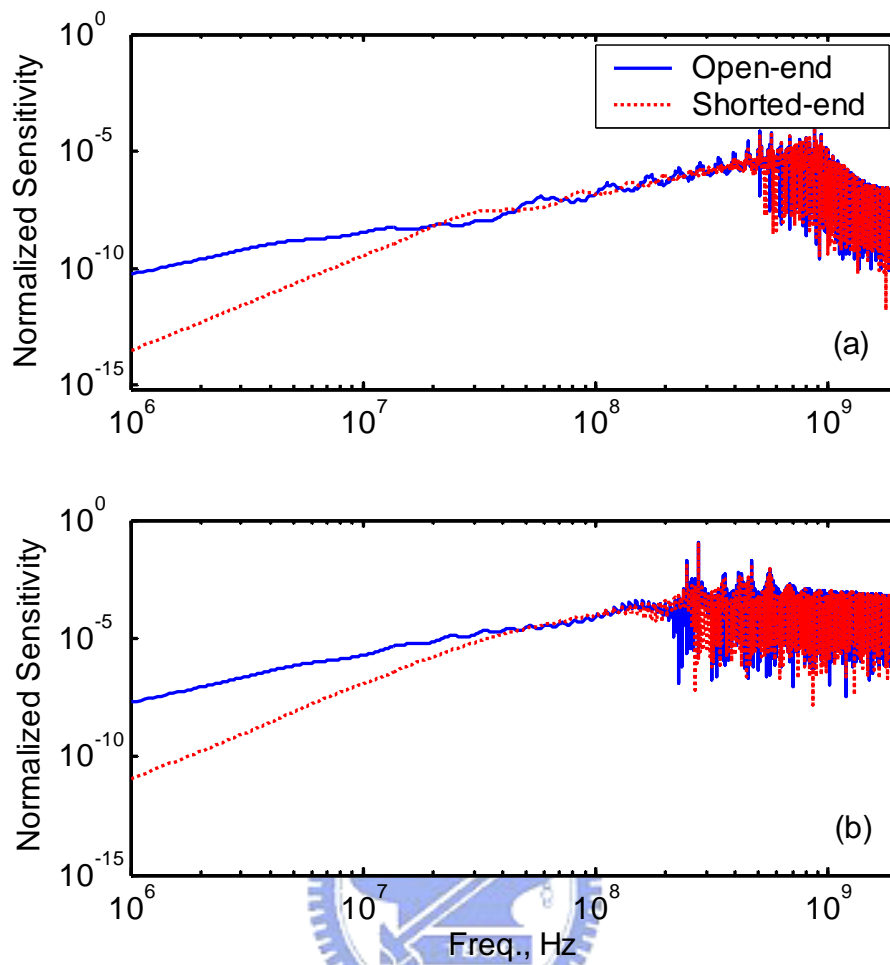
Fig. 3-13 Normalized sensitivity of abs(S_{11}) due to ε_∞ as measuring the (a) tap water and (b)
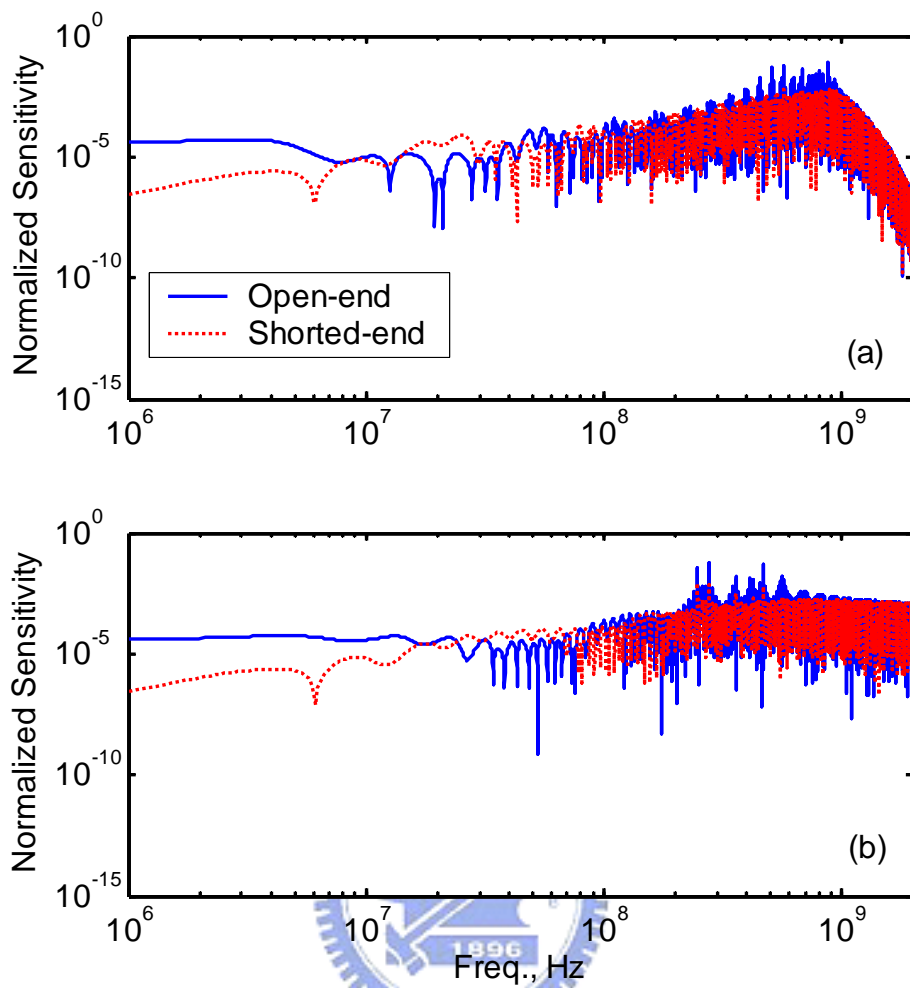
silt loam

Fig. 3-14 Normalized sensitivity of abs(S_{11}) due to length of probe (*L*) as measuring the (a)

tap water and (b) silt loam
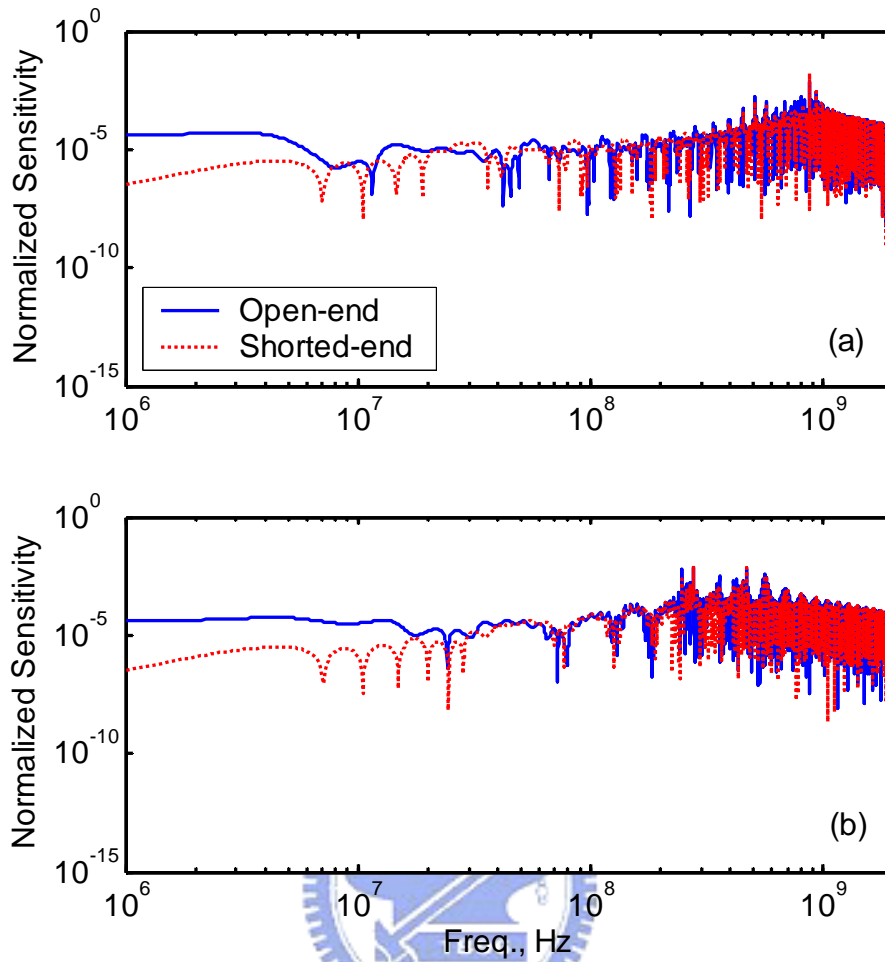
Fig. 3-15　Normalized sensitivity of abs(S_{11}) due to impedance of probe (Z_p) as measuring

the (a) tap water and (b) silt loam

3.2.2　Frequency Domain Phase Velocity Method

The applicability and limitations of travel time analysis were revealed in previous, which

suggested the importance of dielectric spectroscopy. The dielectric spectrum, however, is still

difficult to obtain reliable measurements at frequency at present. A novel approach to obtain

dielectric permittivity at high frequencies is proposed here based on the frequency domain

phase velocity. The proof of the concept will be introduced in this section.

3.2.2.1 Principle of Frequency Domain Analysis of Phase Velocity

The idea stems from the spatial analysis of surface wave method (SASW), which is a widely-used nondestructive method for measurements of shear wave velocity in situ (Foti, 2000). Surface waves in a typical SASW test are generated by an impact source, detected by a pair of geophones (receivers), and recorded on an appropriate recording device as shown in Fig. 3-16 (Foti, 2000). The phase velocity of each frequency component is determined by the difference between the phase angles of the two signals recorded by geophones ($\Delta\phi = \phi_2 - \phi_1$) is equal to the phase angle of the average cross-spectral density CSD(u1,u2):

$$\Delta\phi(f) = \phi_2(f) - \phi_1(f) = Angle\big[CSD\big(u_1(t), u_2(t)\big)\big] \qquad [3\text{-}4]$$

Following Eq. [3-4], the apparent phase velocities of each frequency component can be determined as:

$$v_a(f) = \frac{2\pi f}{\dfrac{\Delta\phi(f)}{L}} = \frac{2\pi f L}{\Delta\phi(f)} \qquad [3\text{-}5]$$

where L is the geophone spacing. The actual phase difference $\Delta\phi$ increases with frequency, but the angle of the cross-spectral density oscillates between $-\pi$ and π by definition. Thus, the angle of cross-power spectrum has to be unwrapped before applying it to Eq. [3-5], as shown in Fig. 3-17.

Based on the principle of SASW method, a similar approach of determining the frequency domain phase velocity of TDR is proposed here. Fig. 3-18(a) shows a typical TDR waveform, in which the start reflection and end reflection form the sensing waveguide are clearly shown. Two characteristic pulses (pulse 1 and pulse 2) in Fig. 3-18(b) are separated

into two independent signals, and treated as the measurements of the two geophones in a SASW test, as shown in Fig. 3-19. According to Eq. [3-5], the TDR frequency domain phase velocity (V_{ph}) can be estimated from the phase angle of the cross-spectral density of two characteristic signals, and it is formulated as:

$$V_{ph} = \frac{2\pi f(2L)}{\Delta \phi(f)}$$ [3-6]

where the $2L$ is the round trip distance in the TDR probe.

In chapter 2, the phase velocity (V) of an electromagnetic wave as a function of dielectric property is derived as Eq. [2-37]. This analytical expression will be used to verify the feasibility of the frequency domain phase velocity method. The proof of the concept is conducted in the following using TDR waveform simulations as described in section 2.3.4.
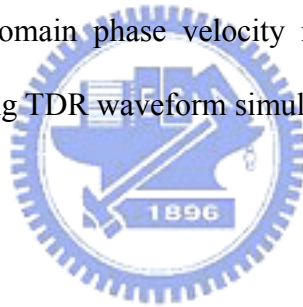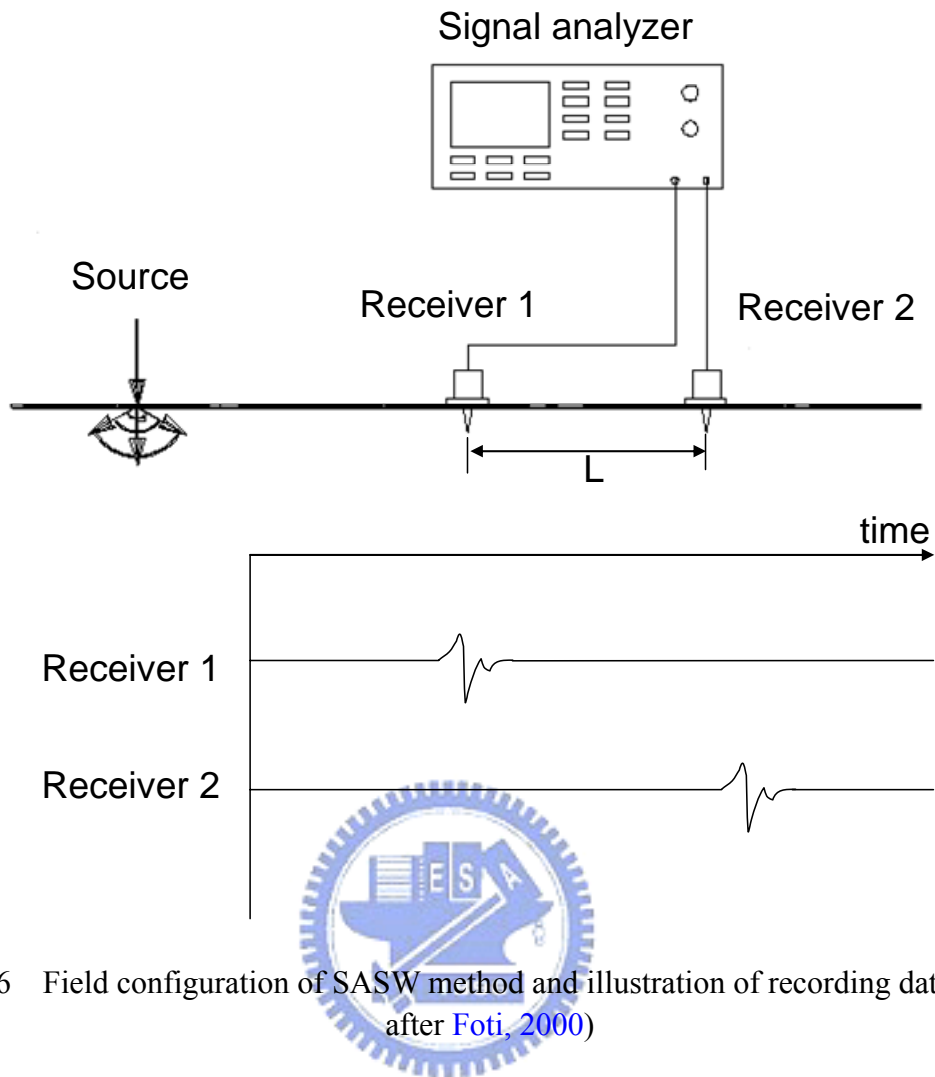
Fig. 3-16 Field configuration of SASW method and illustration of recording data (modified after Foti, 2000)
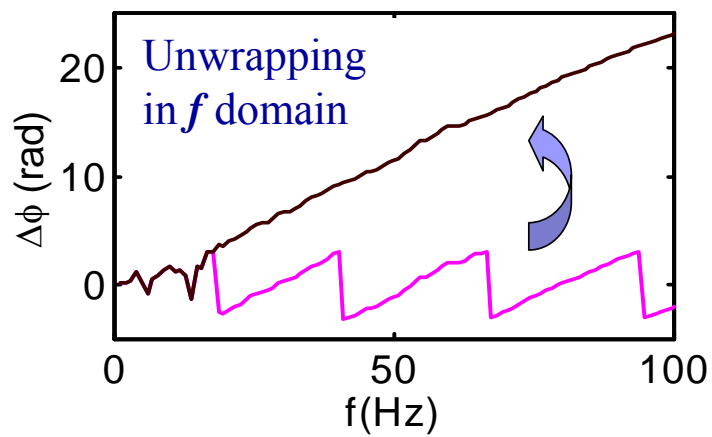
Fig. 3-17 Unwrapping process of the angle of cross-power spectrum for the SASW method
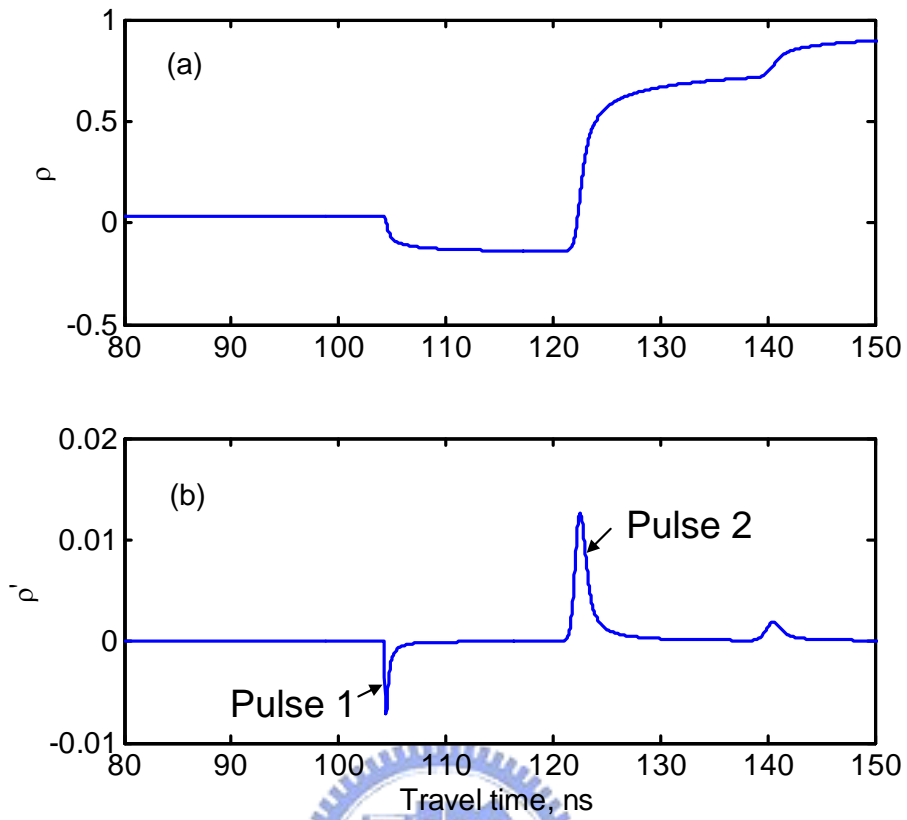
Fig. 3-18   (a) typical TDR waveform, and (b) its derivative
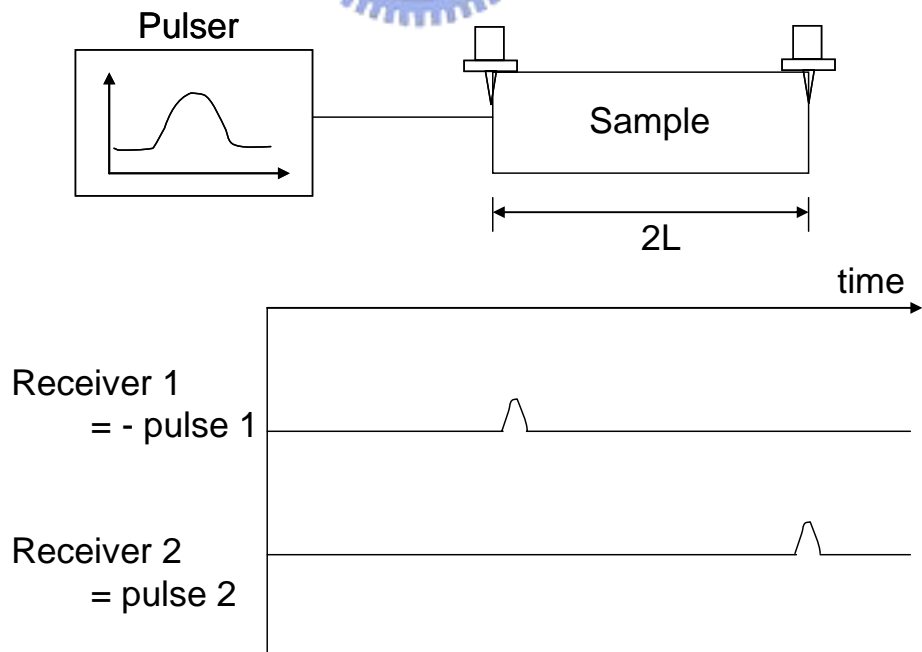
Fig. 3-19   The TDR frequency domain phase velocity method analogous to the SASW method

3.2.2.2 Proof of Concept

The synthetic TDR measurement system is composed of a TDR device, a RG-58 lead cable, and a sensing waveguide. The transmission line parameters listed in Table 3-1 were used, except that the geometric impedance Z_p of probe is set as 50 Ω to ensure negative first reflection for all cases. Tap water modeled by the Cole-Cole equation was used as one of the testing materials (as listed in Table 3-2). To modeling dielectric dispersion of soils, a four-component dielectric mixing model (Lin, 2003b) referred to Eq. [2-33] was used in this study. The associated parameters of four-component dielectric mixing are listed in Table 3-4. Time interval $dt = 2.69\times10^{-11}$ sec and time window $0.5N\ dt = 8192\times40\ dt = 8.8\times10^{-6}$ sec (slightly greater than the pulse length of 7×10^{-6} sec in a TDR 100) were used in the numerical simulations. The corresponding Nyquist frequency and frequency resolution are 18 GHz and 60 kHz, respectively. The Nyquist frequency is well above the frequency bandwidth of TDR 100 and the long time window ensures that the steady state is obtained before onset of the next step pulse.
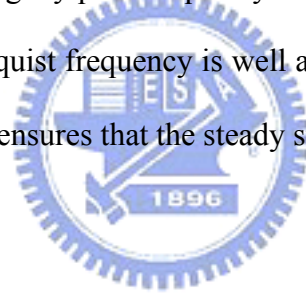
Table 3-4　Volumetric mixing parameters

Volumetric Mixing Parameters	Range	Reference value
Soil physical parameters		
volumetric water content θ, %	5 ~ 40	5 & 40
volumetric soil content θ_s, %	60	60
effective specific surface A_s, m^2g^{-1}	50 ~ 400	200
Dielectric parameters of air		
constant ε	1	1
Dielectric parameters of soil particles		
constant ε	4.7	4.7
Dielectric parameters of free water		
static value ε_{dc}	80	80
high frequency value ε_∞	4.22	4.22
Relaxation frequency f_{rel}, GHz	17.4	17.4
Conductivity σ_{fw}, S m^{-1}	0 ~ 0.5	0.02
Dielectric parameters of bound water		
static value ε_{dc}	80	80
high frequency value ε_∞	4.22	4.22
Relaxation frequency f_{rel}, kHz	9	9
Conductivity σ_{bw}, S m^{-1}	5	5
Empirical Parameter		
Fitting Parameter α	0.5	0.5

A typical waveform for the tap water is shown in Fig. 3-18. This simple case (with electrical conductivity = 0.02 S/m) is firstly applied to verify the principle of TDR frequency domain phase velocity method.

Fig. 3-20(a) shows the phase angle of the cross-spectral density ($\Delta\phi$) from two characteristic signals before unwrapping, and Fig. 3-20(b) shows the result after unwrapping with comparison to the theoretical values. Fig. 3-20 (c) compares the measured frequency domain phase velocity (V_{ph}) with the theoretical values obtained from Eq. [2-37]. Both Fig. 3-20(b) and (c) show that measured $\Delta\phi$ and V_{ph} are in good agreement with the theoretical values in the frequency range from 0.1 GHz to the upper bound of TDR frequency bandwidth (1.5 GHz). The disagreement at frequency below 0.1 GHz may be resulted from leakage due to truncations of the two characteristic signals. Fortunately, the frequency range where the

frequency domain phase velocity method works happens to be where dielectric spectroscopy does not perform well. Therefore, these two techniques seem to be in good complement.

The effect of EC on the apparent dielectric constant has been fully discussed in Chapter 3. Due to the EC effect, apparent dielectric constants estimated by the single tangent method and derivative method are increasingly overestimated as EC increases. Similarly, simulations were conducted to investigate the EC effect on the TDR frequency domain phase velocity method. Fig. 3-21(a) shows the error percentage of the phase angle of the cross-spectral density ($\Delta\phi$) and Fig. 3-21 (b) shows the error percentage of the phase velocity compared with theoretical values with a variety of EC values. This result indicates that the TDR frequency domain phase velocity method is practically not affected by the EC at the frequency range from 0.1 GHz to 1GHz for the tap water case.
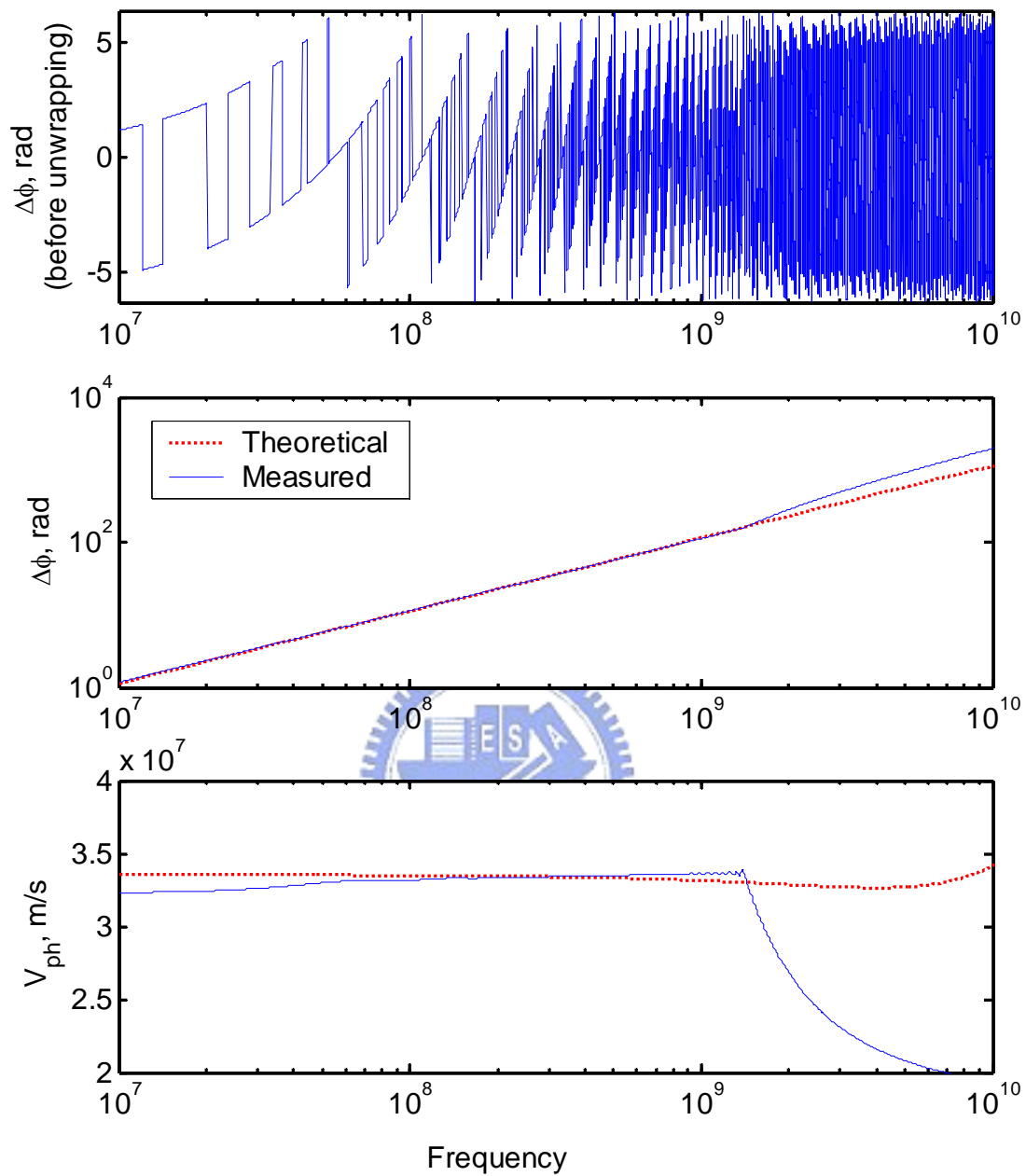
Fig. 3-20 (a) The phase angle of the cross-spectral density ($\Delta\phi$) of two characteristic signals before unwrapping, (b) the results after unwrapping compared with theoretical values, and (c) the measured frequency domain phase velocity (V_{ph}) compared with the theoretical values
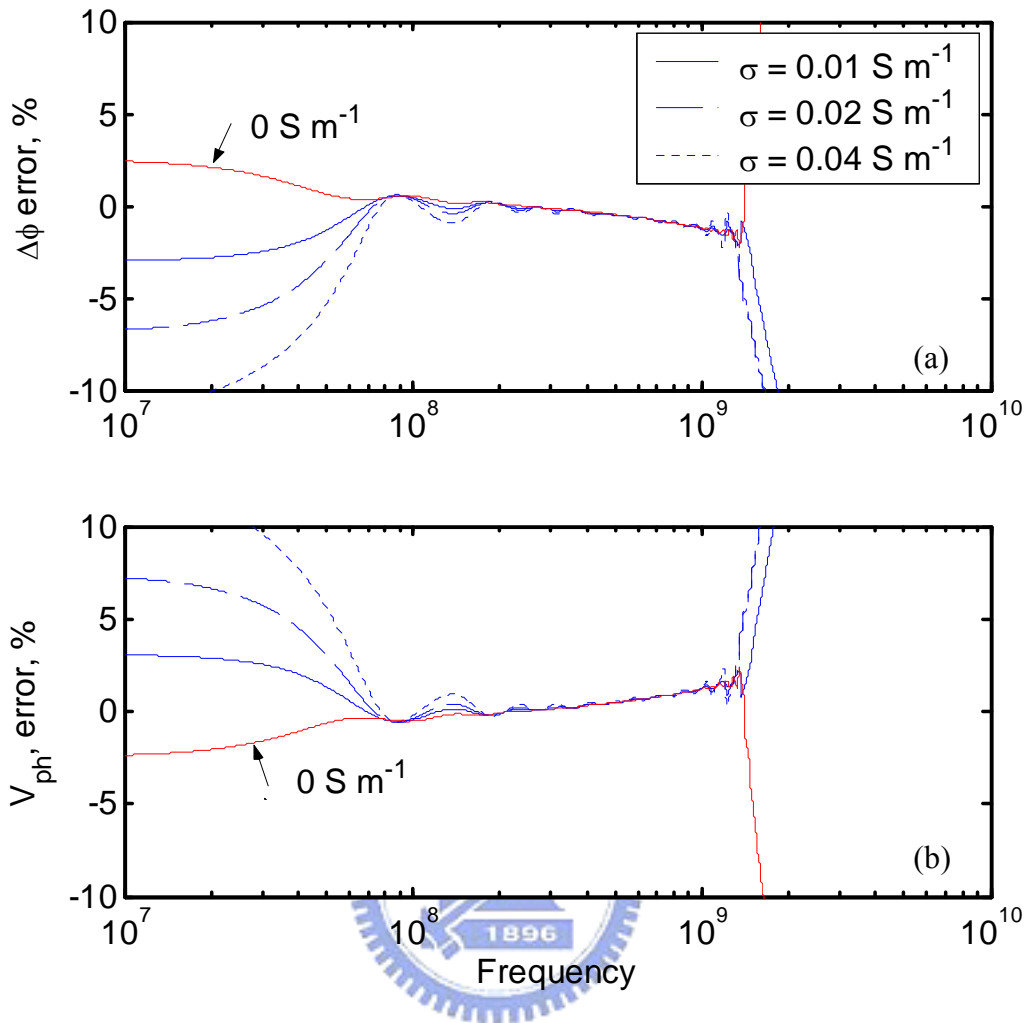
Fig. 3-21　(a) The error percentage of phase angle of the average cross-spectral density ($\Delta\phi$) and (b) the error percentage of phase velocity compared with the theoretical one as a variety of EC.

The four-component dielectric mixing model (Lin, 2003b), as shown in Eq. [2-33], was further used to examine the feasibility of the TDR frequency domain phase velocity method on soils. The modeled dielectric dispersion (in term of the apparent dielectric constant K_a using Eq. [2-38]) due to soil-water interaction (in cases with effective specific surface $A_s = 50$, 200, and 400 m^2g^{-1}) and soil water content θ using four-component dielectric mixing model is shown in Fig. 3-22, in which frequencies near 1 GHz are least affected by soil type (As) and considered as the optimal frequency for water content measurement (Lin, 2003b). The

apparent dielectric constants are accordingly determined by the frequency domain phase velocity method at 1GHz for a variety of soil water content, as shown in Fig. 3-24. Also shown in Fig. 3-24 are the theoretical values of the volumetric mixing model and the apparent dielectric constant of single tangent method from the simulated waveforms. The measured values by the frequency domain phase velocity method agree well with the theoretical values, which shows invariance with soil types. On the contrary, the apparent dielectric constant of the single tangent method depends on the soil type, especially for high As. This result inspires a new approach for soil water content estimation because that the dielectric constant estimated by the frequency domain phase velocity method is less influenced by low-frequency dispersion and provide a actual dielectric constant in particular frequency range, whereas the dielectric constant estimated by the travel time analysis method are greatly effected by low-frequency dispersion and lacks actual physical meaning.

The frequency domain phase velocity method is further examined for the effects of electrical conductivity and cable length, which cause series problems for the tangent line method in dispersive materials, as discussed in Chapter 3. Fig. 3-24 shows the estimated apparent dielectric constant (K_a) at 1GHz from the frequency domain phase velocity analysis for As = 200, and the apparent dielectric constants estimated by the single tangent method as affected by EC of free water (σ_{fw}). The results from frequency domain phase velocity method at 1GHz remains relatively constant in the entire EC range. The dielectric constants estimated by the single tangent method, on the other hand, show dependency on the EC in high soil water content. Furthermore, Fig. 3-25 shows that dielectric constants estimated by single tangent method are dramatically influenced by the cable length, as also shown in Fig. 3-4. The dielectric constants estimated by the frequency domain phase velocity method, however, still remain relatively regardless of the cable length.

When measuring soil water contents using the travel time analysis, the same water content

may measure different apparent dielectric constant due to different electrical conductivity (e.g. from water salinity), cable length, and dielectric dispersion (e.g. from soil texture). The soil water contents estimated by the frequency domain phase velocity method at 1GHz are less affected by the aforementioned factors. Therefore, the frequency domain phase velocity method not only provides good estimations of dielectric permittivity at high frequency, it also shows great promise of providing a universal correlation with soil water content. Laboratorial tests are suggested to further verify the feasibility of the frequency domain phase velocity method.
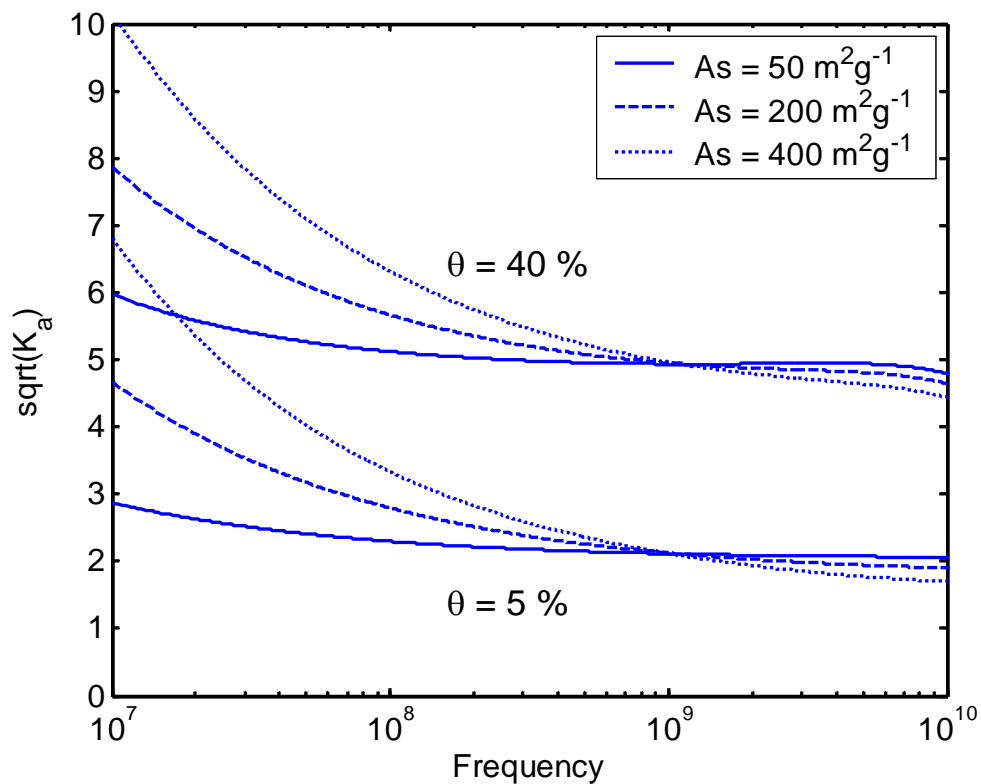
Fig. 3-22   The synthetic dielectric dispersion due to soil-water interaction and soil water content using four-component dielectric mixing model
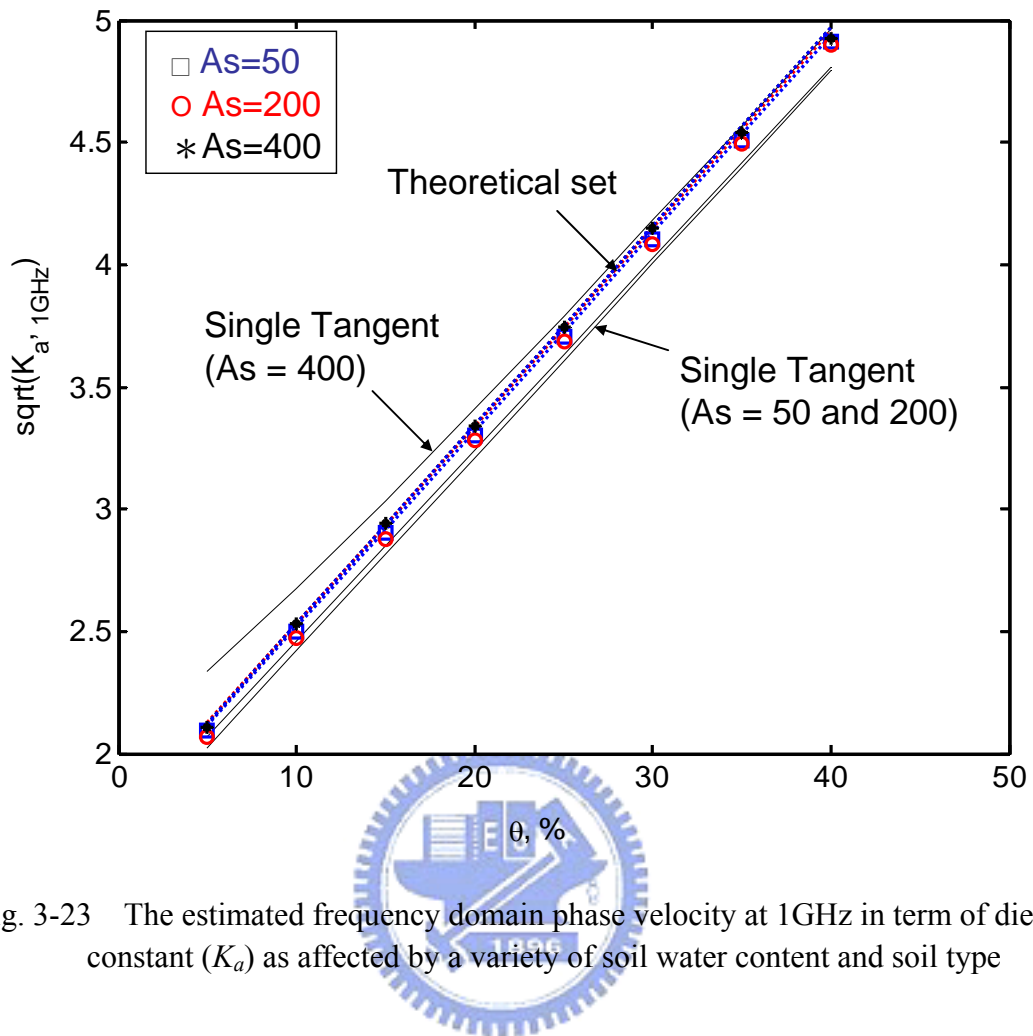
Fig. 3-23 The estimated frequency domain phase velocity at 1GHz in term of dielectric constant (K_a) as affected by a variety of soil water content and soil type
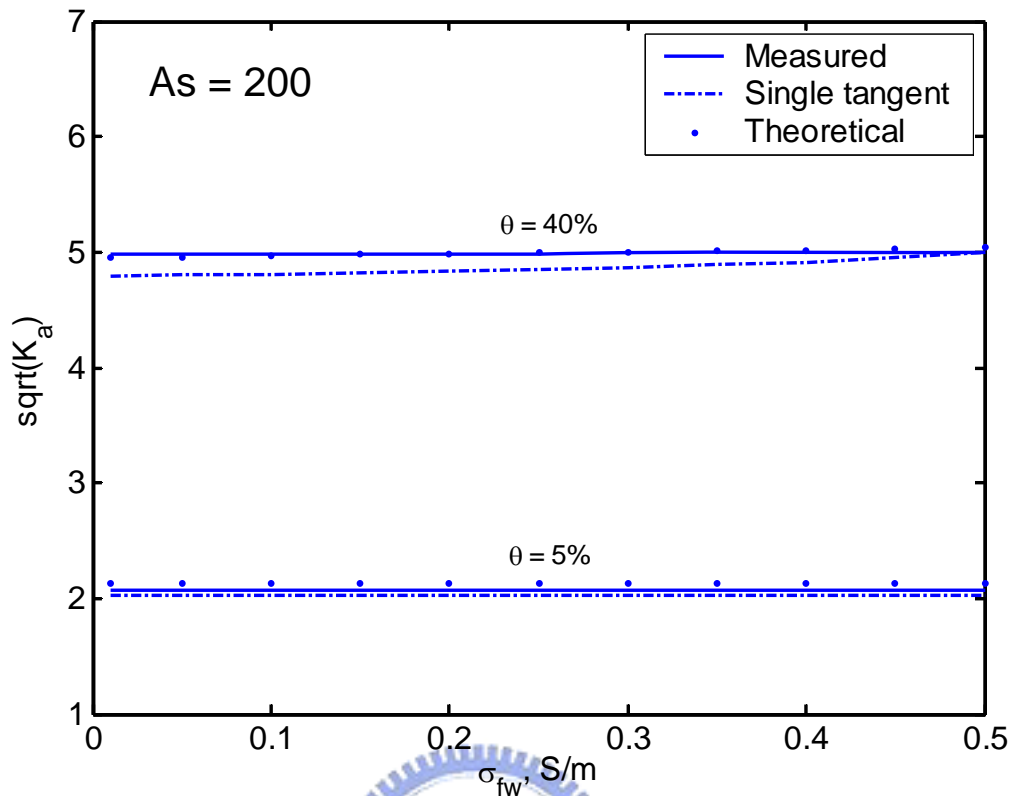
Fig. 3-24   The estimated apparent dielectric constant (K_a) at 1GHz from frequency domain phase velocity analysis for As = 200 and the apparent dielectric constants estimated by the single tangent method as affected by EC of free water (σ_{fw}) and soil water content
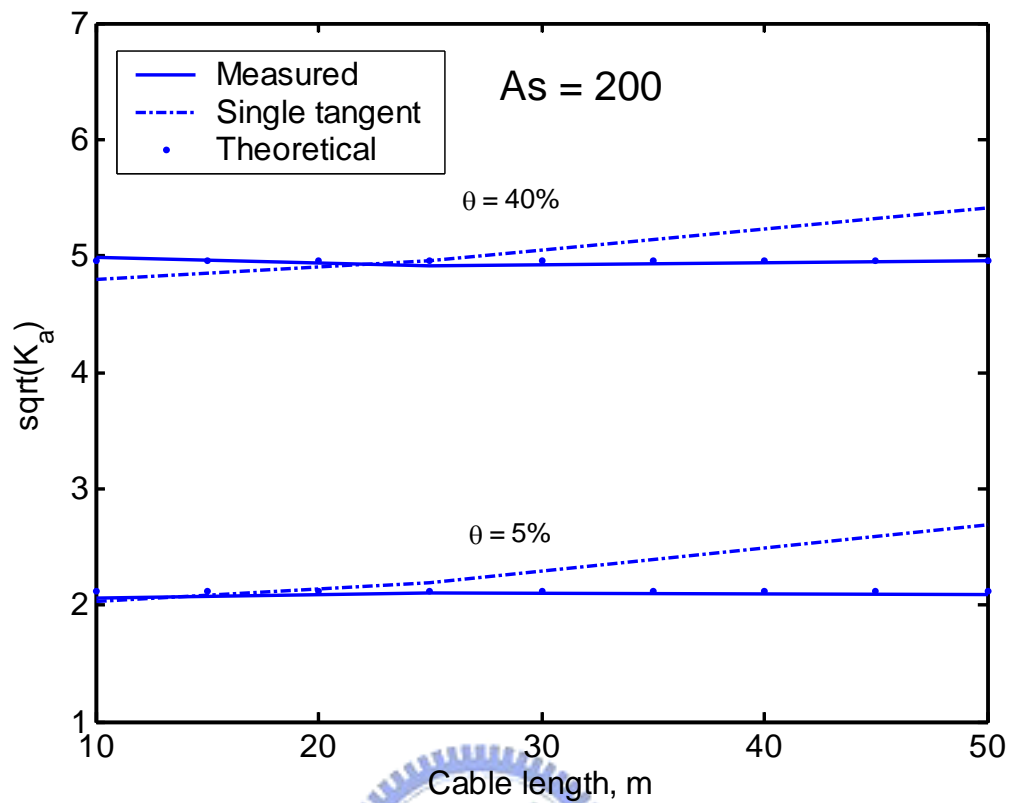
Fig. 3-25   The estimated apparent dielectric constant (K_a) at 1GHz from frequency domain phase velocity analysis for As = 200 and the apparent dielectric constants estimated by the single tangent method as affected by cable length and soil water content

4 TDR EC Analysis

4.1 Comprehensive Method of EC Analysis

4.1.1 DC Lumped Circuit Model

From basic circuit theory, the transmission line can be modeled as a lumped circuit when the wavelength is significantly greater than the electrical length. At zero frequency, the lumped circuit is shown in Fig. 4-1b, equivalent to the assumptions made by Heimovaara et al. (1995) and Reece (1998). The DC lumped circuit model includes the voltage source v_s (double of the pulse step v_0), the inner resistance R_S (equal to the source impedance Z_S), and cable resistance R_{cable} (in fact, the combined series resistance of probe, cable, connector, and cable tester) and soil sample resistance R. The steady state reflection voltage can be derived from circuit theory as

$$v_\infty = \frac{R + R_{cable}}{R + \left(R_S + R_{cable}\right)} v_S \qquad [4\text{-}1]$$
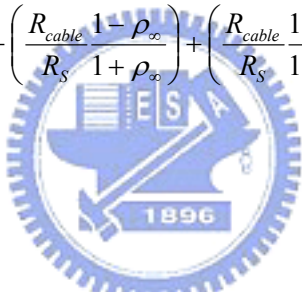
where the sample resistance is related to the EC by

$$R = \frac{K_p}{\sigma} \qquad [4\text{-}2]$$

in which K_p is a geometric factor as shown in chapter 2. Substituting Eq. [4-1] into Eq. [4-2] and noting $\rho_\infty = \left(v_\infty - v_0\right)/v_0$, in which $v_0 = 2\,v_s$ since the source impedance is typically designed to be identical to the characteristic impedance of the connected transmission line as shown in Lin (2003), the EC of the sample can be derived as a function of the steady state reflection coefficient ρ_∞:

$$\sigma = \frac{K_p}{R_S}\left(\frac{1-\rho_\infty}{1+\rho_\infty}\right)\left(\frac{1}{1-\left(\dfrac{R_{cable}}{R_S}\dfrac{1-\rho_\infty}{1+\rho_\infty}\right)}\right) = \beta\left(\frac{1-\rho_\infty}{1+\rho_\infty}\right)k\left(R_{cable},\rho_\infty\right) \qquad [4\text{-}3]$$

where β $(= K_p / R_s)$ is a probe constant and k is the correction factor for cable resistance, named as cable correction factor.   The term $R_{cable}/R_s*(1-\rho_\infty)/(1+\rho_\infty)$ is equal to or less than 1 (can be proved by substituting R_{cable} from Eq. [2-46]), so cable correction factor k can also be written as a power series:

$$k = \frac{1}{1-\left(\dfrac{R_{cable}}{R_S}\dfrac{1-\rho_\infty}{1+\rho_\infty}\right)} = \left[1+\left(\frac{R_{cable}}{R_S}\frac{1-\rho_\infty}{1+\rho_\infty}\right)+\left(\frac{R_{cable}}{R_S}\frac{1-\rho_\infty}{1+\rho_\infty}\right)^2+\left(\frac{R_{cable}}{R_S}\frac{1-\rho_\infty}{1+\rho_\infty}\right)^3+\dots\right]$$

$$[4\text{-}4]$$

It should be noted that the cable correction factor k depends not only on the R_{cable} but also on the EC of the sample since it is a function of ρ_∞.   The effect of cable resistance increases with increasing EC (i.e. as ρ_∞ decreases).
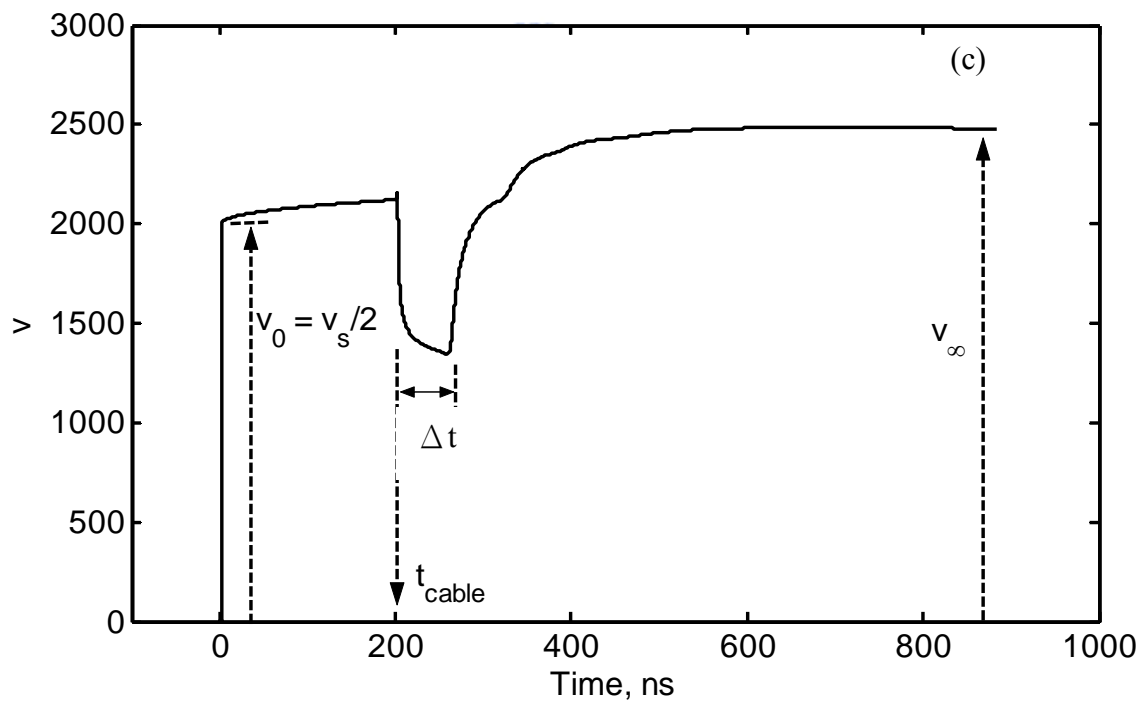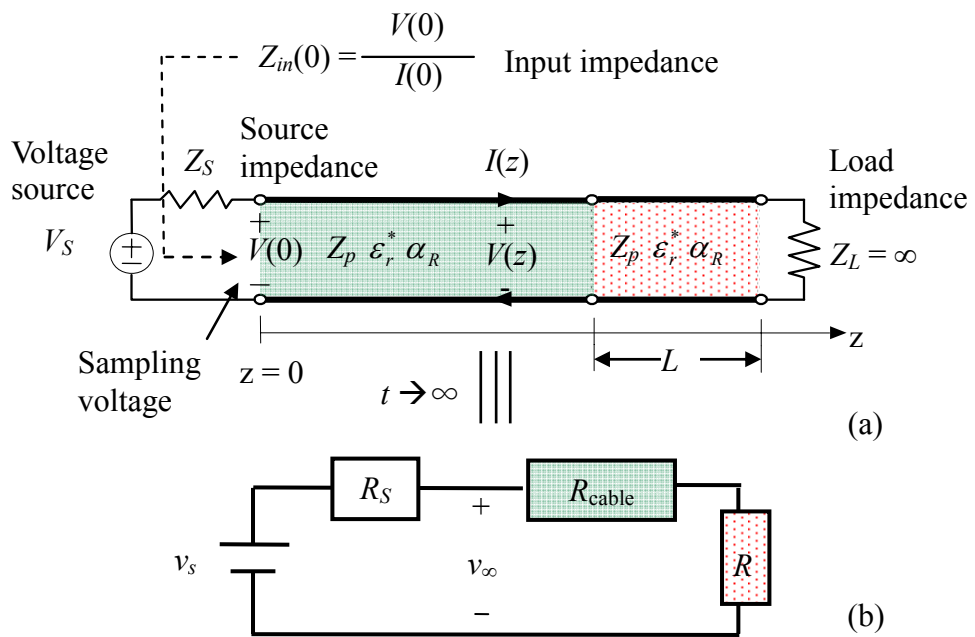
Fig. 4-1 (a) The mutli-section transmission line model of the TDR measurement system, (b) the associated DC circuit model, and (c) a typical TDR waveform showing definition of reflection coefficient ρ.

4.1.2   Theoretical Assessment of EC Measurement

Material and method

The ability of the TDR wave propagation model to capture the resistance effect was first verified by several TDR measurements with a 30-m RG58A/U cable.   TDR measurements were made by attaching the TDR probe (12-cm two rod probe with conductors 3 mm in diameter and 20 mm in spacing) to a Campbell Scientific TDR 100 via the 30m-long lead cable and a SDMX multiplexer.   Any uniform transmission line section can be parameterized by the length (L), geometric impedance (Z_p), dielectric permittivity (ε_r^*), and resistance loss factor (α_R).   One of the three parameters (L, Z_p, ε_r^*) needs to be known so that the other two parameters and α_R can be calibrated from a measured TDR waveform (Lin and Tang, 2007). With known lengths, the transmission line parameters (Z_p, ε_r^*, and α_R) of the lead cable and multiplexer section were calibrated by a measurement with the lead cable open-ended.   The transmission line parameters (Z_p, L, and α_R) of the TDR probe were then calibrated by a measurement with the probe immersed in de-ionized water, whose dielectric property is known.   Using the calibrated transmission line parameters, TDR waveforms were simulated and compared with measured waveforms for the probe open in air, immersed in tap water, and short-circuited.   Time interval dt = 2.5×10^{-11} sec and time window $0.5N$dt = 8192×40 dt = 8.2×10^{-6} sec (slightly greater than the pulse length of 7×10^{-6} sec in a TDR 100) were used in the numerical simulations.   The corresponding Nyquist frequency and frequency resolution are 20 GHz and 60 kHz, respectively.   The Nyquist frequency is well above the frequency bandwidth of TDR 100 and the long time window ensures that the steady state is obtained.

Using the verified TDR wave propagation model, the theoretical validity of the series resistors model and Castiglione-Shouse method can be examined.   The electrical conductivity is numerically controlled and compared with that estimated from the synthetic waveforms using the Giese-Tiemann method, series resistors model, and Castiglione-Shouse

method. The time window used for above numerical simulations is excessively large to ensure that the steady state is obtained and DC analysis is examined. As will be seen, the cable resistance can have a great effect on how the reflection approaches the steady state. Intermediate reflection plateaus at long times may be mistakenly taken as the steady state reflection coefficient. The effect of recording time on the series resistors model and the Castiglione-Shouse method is investigated through a parametric study. Factors considered include lead cable length, probe length, probe impedance, and electrical properties of the material under test. The simulation parameters used in the parametric study are listed in Table 4-1 and Table 4-2. The resistance loss factor (α_R) of the waveguide is set as 0.0 for all cases since it has a negligible effect on the TDR waveform due to the short probe length.

The numerical findings were verified by experimental data. Time domain reflectometry measurements were made on 7 $NaCl$ electrolytic solutions, with σ varying from 0 to 0.15 S/m, using the 30-m RG58A/U cable and 12-cm two-rod probe. The electrical conductivity was measured independently with a standard EC meter (YSI-32 Yellow Spring Int. Inc., Yellow Spring, OH). When directly determining R_{cable} using Eq. [2-46], the measurements were performed by shorting the cable end with a short wire. The resistance in the probe section was found negligible from Eq. [2-45] and theoretical α_R value computed from the probe geometry and conductor property. The cross section of the probe is much larger than that of the coaxial cable. Shorting the probe end with a wire may introduce extra resistance. It is suggested to shorten the cable end with a short wire or the probe end with a metal plate.

Table 4-1   Simulation parameters

Section	Parameters	Range
Waveguide	σ, S m^{-1}	0.005 ~ 0.2
	ε_r	Tap water, Ethanol alcohol, and Silt loam[†]
	Geometric impedance Z$_p$, Ω	150 ~ 300
	Length L, m	0.1 ~ 0.3
	α_R , sec$^{-0.5}$	0
Lead cable	σ, S m^{-1}	0
	ε_r	1.95
	Geometric impedance Z$_p$, Ω	77.5
	length, m	0 ~ 200
	α_R , sec$^{-0.5}$	0, 19.8

[†] Referring to the Cole-Cole parameters listed in Table 2

Table 4-2   Cole-Cole parameters for material used in numerical simulations

Material	ε_{dc}	ε_∞	f_{rel}	ξ
Tap water	79.9	4.22	17*10^9	0.0125
Ethanol alcohol	25.2	4.5	0.78*10^9	0.0
Silt loam	26.0	18.0	0.2*10^9	0.01

Effect of Cable Resistance on TDR Waveforms

The effect of cable resistance on TDR waveform is illustrated by TDR measurements with a 30-m RG58A/U cable and modeled by the full waveform analysis.   The characteristics of the lead cable (Z_p = 77.5 Ω, ε_r^* = 1.95, and α_R = 19.8 sec$^{-0.5}$) were back calculated from the measured waveform with the lead cable open-ended, while the characteristics of the probe (Z_p = 290 Ω, L =0.126 m, and α_R =153 sec$^{-0.5}$) were obtained from a measurement with the probe immersed in de-ionized water.   Fig. 4-2(a) shows the measured waveforms and predicted waveforms using the back calculated parameters for the probe open in air, immersed in tap

water, and short-circuited. The full waveform analysis takes into account the multiple reflections, dielectric dispersion, and attenuation due to conductive loss and cable resistance altogether. The excellent match between the measured and predicted waveforms validates the TDR wave propagation model and the calibration by full-waveform inversion. The predicted waveforms in which cable resistance is ignored are also shown in Fig. 4-2(a) for comparison. Of most importance to EC measurements is how cable resistance affects the steady state response. As depicted in Fig. 4-2(a), cable resistance gives rise to an increase in the steady state response, causing an underestimation of EC if cable resistance is not taken into account. The amount of increase in the steady state response depends on the EC, with no increase when EC = 0 (i.e. probe open in air) and maximum increase when EC = ∞. Therefore, the TDR EC measurements are increasingly underestimated as EC increases, as also observed by Heimovaara et al. (1995) and Reece (1998). This monotonic behavior is different from that revealed by Castiglione and Shouse (2003) in their Fig. 5(b), reproduced in Fig. 4-2(b) for comparison. The reflection coefficient in air (i.e. EC = 0) should be 1.0 regardless of the lead cable length, as also suggested by Eq. [4-3]. The data shown in Castiglione and Shouse (2003) seems abnormal. The error was most likely caused by the data acquisition program, and was overlooked due to the misconception that long-time reflection coefficient is reduced in absolute value due to cable attenuation (i.e. positive long-time reflection coefficient decreases at low EC, while negative long-time reflection coefficient increases at high EC, as shown in Fig. 4-2(b)).

In addition to the steady state response, it is also interesting to note how cable resistance affects the time required to reach the steady state. The characteristic impedance of the cable used is actually 55 Ω, not precisely 50 Ω. The unmatched cable gives rise to multiple reflections within the cable section, as can be observed from the reflections around 560 ns in Fig. 4-2(a). Even if the cable has a nominal characteristic impedance perfectly matched with

the source impedance of the TDR device (typically 50 Ω), the characteristic impedance of the cable is in fact a function of frequency and cable resistance as suggested in Eq. [2-51]. This is evidenced by the rising step pulse, as shown in Fig. 4-2(a) and illustrated in Fig. 4-1. Therefore, the multiple reflections within the cable section are inevitable. The magnitude of the multiple reflections within the cable depends not only on cable resistance but also on the electrical conductivity. It is most prominent when the probe is open in air or shorted. The rising plateau of the step pulse and the rise time of the reflected pulse increase as α_R or cable length increases. Hence, it takes much longer time to reach steady state for long cables. The reflection coefficient beyond 400 ns may be mistakenly taken as the steady state if the waveform is not recorded long enough, as shown in Fig. 4-2(a). This problem has been overlooked and may have significant effect on TDR EC measurements.
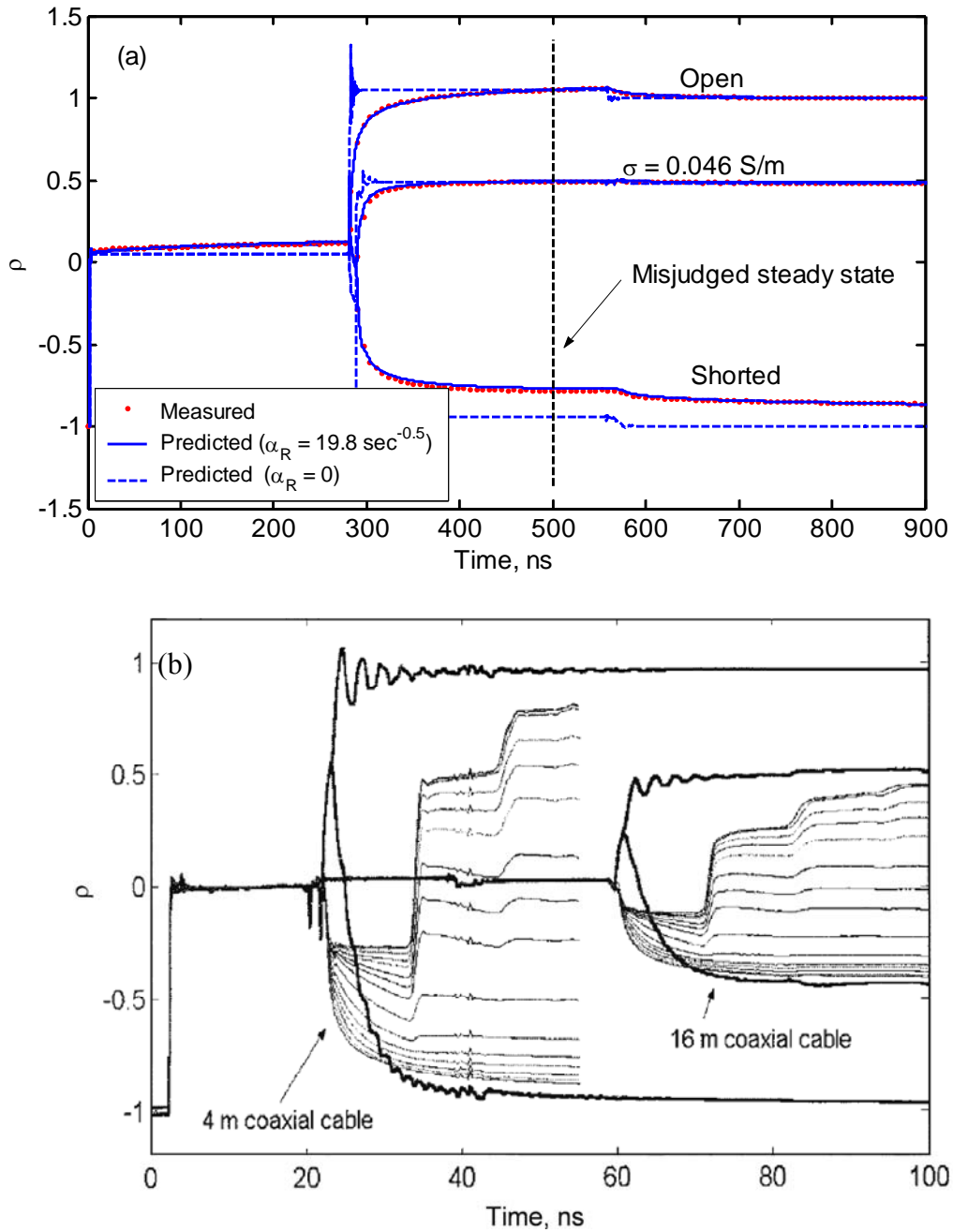
Fig. 4-2   Effect of cable resistance on TDR waveforms: (a) measured TDR waveforms compared with that predicted by the full waveform model in this study; (b) measured TDR waveforms in Fig. 5b of Castiglione and Shouse (2003).

Theoretical Assessment of DC Analysis Methods (Without Time Error)

Using the verified TDR wave propagation model, the theoretical validity of the series resistors model and the Castiglione-Shouse method can be examined. A very long time (8.2×10^{-6} sec) was used in the numerical simulations to ensure that the assessment is performed under the true steady state responses. The deficiency of the scaling process proposed by Castiglione and Shouse (2003) is illustrated in Fig. 4-3. To enhance visual illustration, a long RG-58 cable (200 m) was used for the numerical simulation. The steady state reflection coefficient with 200-m RG-58 cable (α_R = 19.8 sec$^{-0.5}$) is plotted against that without cable loss (α_R = 0 sec$^{-0.5}$), as shown by the solid line in Fig. 4-3. This curve is not a linear line and the scaled line by applying Eq. [2-46] is a nonlinear line rather than the 1:1 linear line. This disparity reveals that the Castiglione-Shouse method is correct only for EC = 0 and EC = ∞ since the effect of cable resistance on the steady state reflection coefficient is nonlinear while the scaling process is linear.

In Fig. 4-4, the electrical conductivity in the measurement system was numerically controlled and compared with that estimated from the synthetic waveforms using three different DC analysis methods. The result shows that the series resistor model is theoretically correct (if the true steady state response is obtained). While the Giese-Tiemann method and Castiglione-Shouse method result in underestimation and overestimation, respectively. The overestimation by the Castiglione-Shouse method linearly increases with EC, while the underestimation by the Giese-Tiemann method nonlinearly increases with EC. In Fig. 4-4, the probe constant β is only a function of probe geometry and independent of cable resistance. If the probe constant β is obtained using least square fitting of TDR EC measurements in salt solutions of different concentrations to conductivity measurements made with a conventional conductivity meter, the result becomes that shown in Fig. 4-5. The linear overestimation by the Castiglione-Shouse method is completely compensated for by the fitted

probe constant, while the nonlinear underestimation by the Giese-Tiemann method is only minimized in least square sense resulting in slight overestimation at low EC and underestimation at high EC in the fitting range.   It should be noted that the fitted probe constant depends not only the probe geometry but also the cable resistance.   Hence, probes with the same probe geometry but different cable length should be individually calibrated when the Castiglione-Shouse method and the Giese-Tiemann method are used.   This is not very practical for field monitoring with many probes.   In practice, the series resisters model should be used.   It has a unique probe constant for each type of probe.   The cable resistance can be easily determined by Eq. [2-46] without further calibrations.
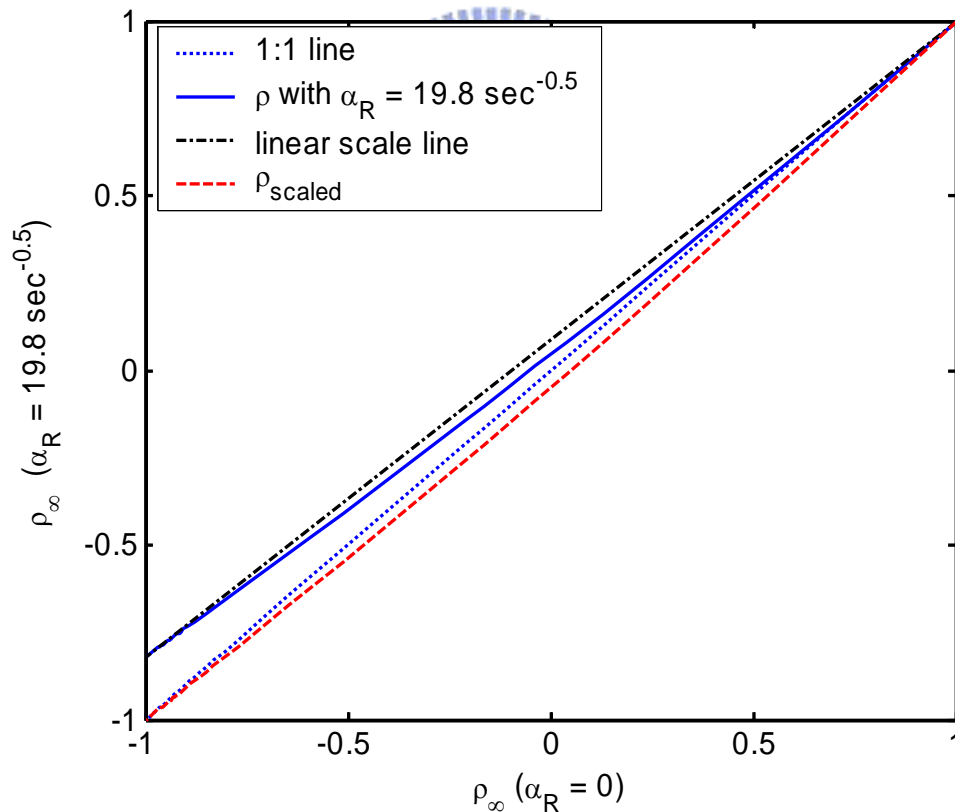
Fig. 4-3   Illustration of the nonlinear relationship between the steady state reflection coefficient with 200-m RG-58 cable and that without cable resistance.
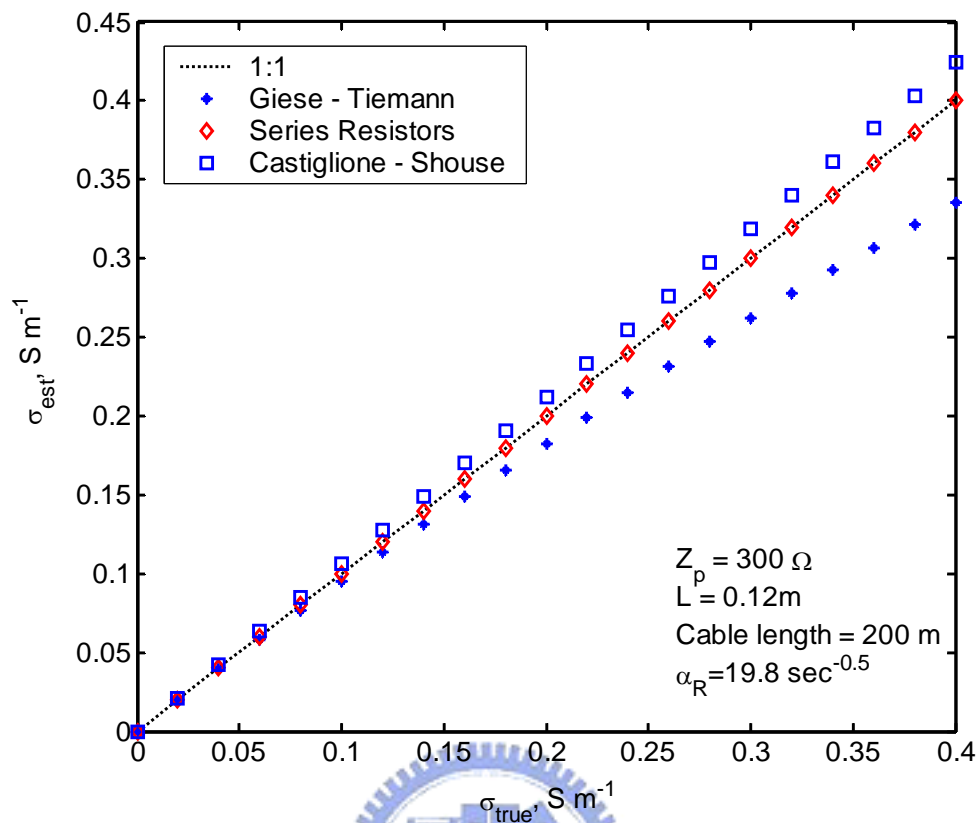
Fig. 4-4　The estimated EC using the actual probe constant in three different methods compared with the numerically-controlled true EC.
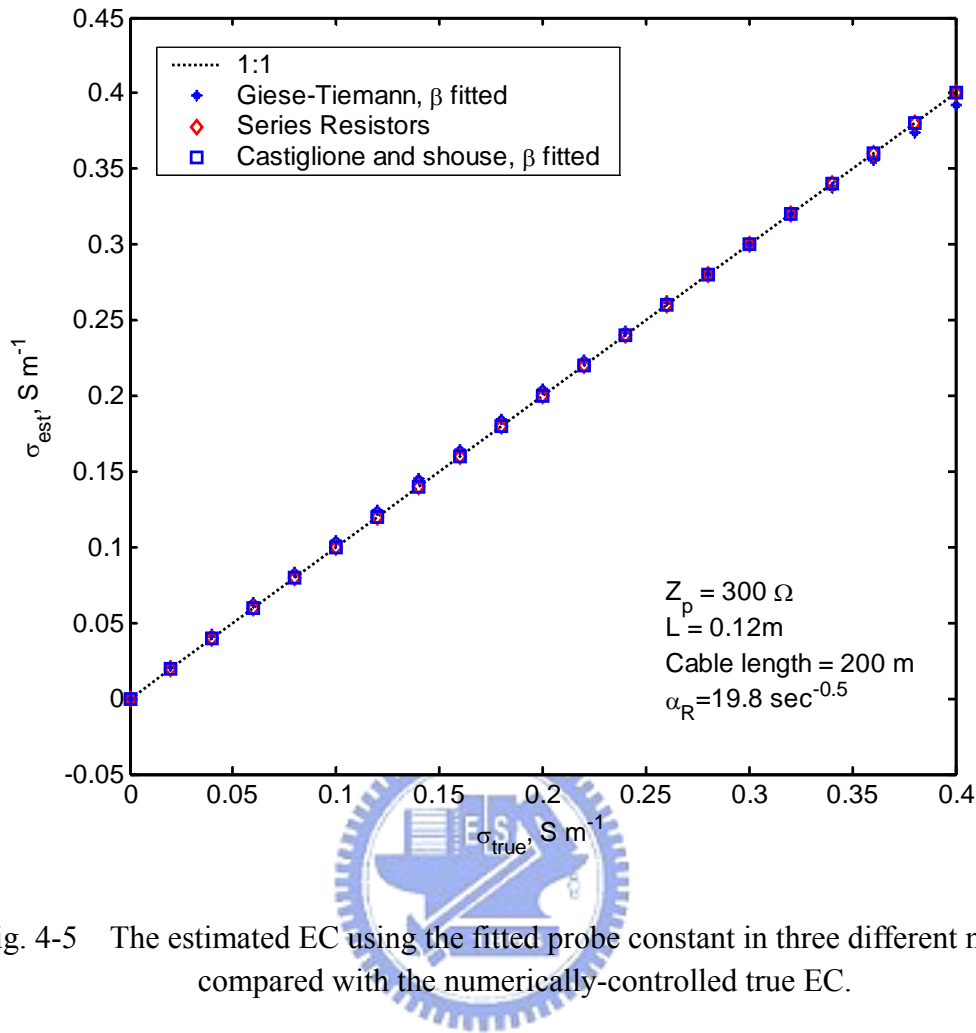
Fig. 4-5   The estimated EC using the fitted probe constant in three different methods compared with the numerically-controlled true EC.

4.1.3   Effect of Recording Time

The assessment of DC analysis methods assumes that steady state is obtained. In practice, an arbitrary "long" time is usually assumed for the steady state without close examination of its legitimacy. The parametric study shows that the time required to reach the steady state depends on the cable resistance, electrical properties of the medium, and probe characteristics. In the case of negligible cable resistance, Fig. 4-6 shows how EC, probe characteristics, and dielectric permittivity affect the time required to reach the steady state. The recording time is expressed as the time that includes multiples of roundtrip travel time in the probe section (Δt). The reflection voltage at a very long time (8.2×10^{-6} sec, slightly greater than the pulse length of 7×10^{-6} sec in a TDR 100) was used to represent v_∞.

The time required to reach the steady state increases with decreasing EC, decreasing characteristic impedance, and increasing dielectric constant. But without cable resistance, reflection coefficients all converge to the steady state ($v_t/v_\infty = 1$) in less than 10 multiple reflection within the probe, a time often used to represent the steady state in practice.

For the 12-cm probe, Fig. 4-7 shows the effect of recording time for different lengths of RG58 cable and electrical conductivities. The time required to reach the steady state increases with cable resistance. But the way reflection coefficient approaches the steady state strongly depends on the EC, as also suggested by Fig. 4-2. Two extreme cases, probe open in air (i.e. EC =0) and probe with conductors shorted together (EC = ∞), are shown in Fig. 4-7a and Fig. 4-7c. Fig. 4-7b shows the results for two electrical conductivities in between the two extreme cases. At high EC, the ratio v_t/v_∞ decreases monotonically and gradually approaches the steady state, while at low EC, v_t/v_∞ increases slightly over 1.0 and then quickly approaches the steady state. The medium EC is least affected by the recording time. The definition of "high", "medium", and "low" EC here means EC that results in reflection coefficient near -1.0, 0, and 1.0, respectively. This property depends on the probe characteristics (i.e. geometric impedance and probe length). For example, the EC may be considered "high" for a long probe but is considered "medium" for a short probe. When the waveguide is short-circuited, it takes much longer time to reach the steady state even with small cable resistance, as shown in Fig. 4-7a. Hence, cautions should be taken when determining the cable resistance from the TDR measurement of short-circuited probe using Eq. [2-46].

Four approaches may be used to determine the TDR EC from the steady state response: (a) using the series resistor model with cable resistance directly measured by the short-circuited probe and probe constant fitted to calibration tests, (b) using the series resistor model with both cable resistance and probe constant fitted to calibration tests, (c) using the

Castglione-Shouse method with actual probe constant or calibrated with a very short cable, and (d) using the Castiglione-Shouse method with probe constant fitted to calibration tests. Fig. 4-8 reveals the effect of recording time on estimated EC using four different approaches, in which the estimated EC of any recording time is expressed as σ_t. In this illustration, calibrations were performed with EC ranging from 0 to 0.2 S/m with 0.02 S/m spacing. The fitted probe constant is the probe constant that results in minimum least square error between estimated EC and actual EC in the fitting range. It coincides with the theoretical probe constant only when the series resisters model is used and the recording time is representative of the steady state. As shown in Fig. 4-8, the estimated EC by the series resisters model eventually converges to the true value, but the rate of convergence depends on calibration method, cable length, and EC. The results by fitting both probe constant and cable resistance (Fig. 4-8b) increase the estimation accuracy slightly for each recording time, but the convergence trend is similar to that by fitting only the probe constant with cable resistance directly measured by the short-circuited probe (Fig. 4-8a). The time window required to have accurate estimation of EC increases with cable length as expected, and is generally less than that required to reach the steady state due to the fitted probe constant. However, unlike what Fig. 4-7b may suggest, high EC converges to the true value faster than low EC does. This is due to the fact that TDR EC measurements are affected by the recording time not only when making measurements but also when fitting probe constant and cable resistance. As shown in Fig. 4-7, TDR response approaches to the steady state in different ways for different electrical conductivities. Depending on the fitting range and data sampling, the fitted probe constant may work in favor of some electrical conductivity. But of most importance is how to obtain accurate estimation for all electrical conductivities. The recording time is expressed as the time that includes multiples of roundtrip travel time in the probe section (Δt) in Fig. 4-8. The same result is plotted in Fig. 4-9 with recording time expressed as multiples

of roundtrip travel time in the lead cable (t_{cable}).   Except for the case of very short lead cable, accurate estimation of EC can be obtained with recording time as long as TDR equipment can serve, regardless of the fitting range for probe constant.   The characteristic impedance of the lead cable increases with increasing cable length, giving rise to multiple reflections within lead cable, as shown in Fig. 4-2a.   The convergence of EC estimation is governed by multiple reflections in the sensing probe for short lead cable, while it becomes dominated by multiple reflections in the lead cable for long lead cable.   A simple guideline for selecting an appropriate recording time can be drawn from the parametric study.   To determine the EC accurately, the recording time should be taken after 10 multiple reflections within the probe and 3 multiple reflections within the lead cable as shown in this case; however, it urgently suggest that take recording time as long as pulse can provide as measuring EC.   Errors found in the literature using the series resister model with cable resistance directly measured by the short-circuited probe may be explained by the time effect, imperfect shorting element, or wrong acquisition program.
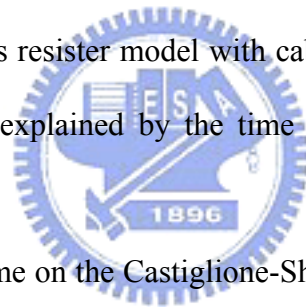
The effect of recording time on the Castiglione-Shouse method is shown in Fig. 4-8 (c,d) and Fig. 4-9(c,d) for comparison.   If the probe constant is fitted (Fig. 4-8d and Fig. 4-9d), the estimated EC by the Castiglione-Shouse method also converges to the true value with reduced time effect.   But if the actual probe constant is determined and used (Fig. 4-8c and Fig. 4-9c), it takes much longer time for the estimated EC by the Castiglione-Shouse method to become invariant with time.   When the recording time is greater than $6t_{cable}$, the estimated EC still gradually decreases with time.   The asymptotic value overestimates the EC.   The overestimation increases with cable length and the asymptotic σ_t/σ_{true} is independent of the EC, as also suggested in Fig. 4-4.

In other words, the effect of recording time, expressed as multiples of roundtrip travel time in the lead cable, on the estimated probe constant β using series resisters model, and

Castiglione-Shouse method is illustrated in Fig. 4-10. The probe constants β estimated by resistors method converge regardless the cable length as recording time is greater than $4t_{cable}$, while the probe constants β estimated by Castiglione-Shouse method are not the same due to cable length, and it means that probe constants β estimated by Castiglione-Shouse is not consistent with actual probe constant.
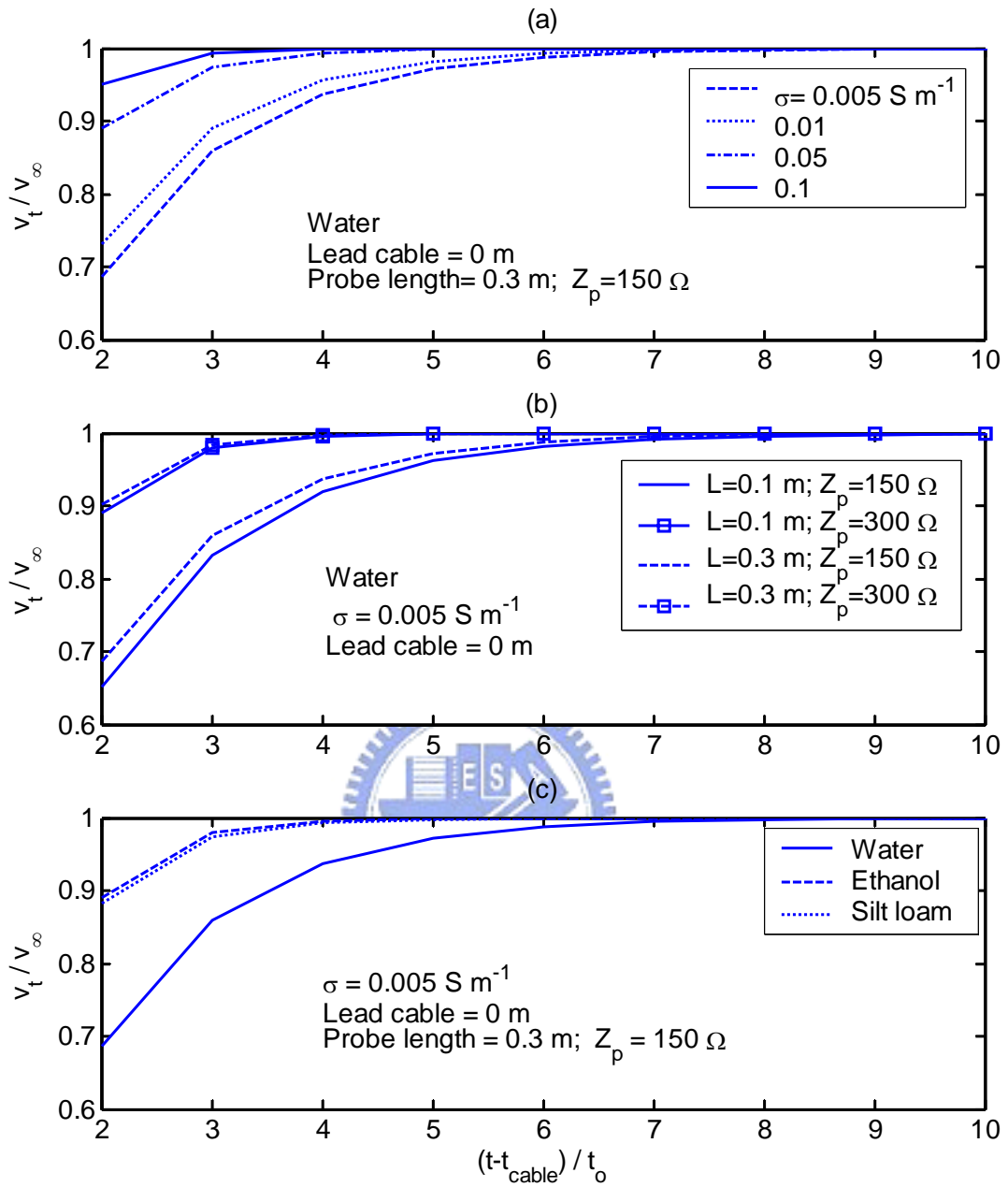
Fig. 4-6 Examples showing how (a) EC, (b) Z_p and L of waveguide, and (c) dielectric permittivity affect the time required to reach the steady state, with time expressed as the time that includes multiples of roundtrip travel time in the probe section (t_0)

.
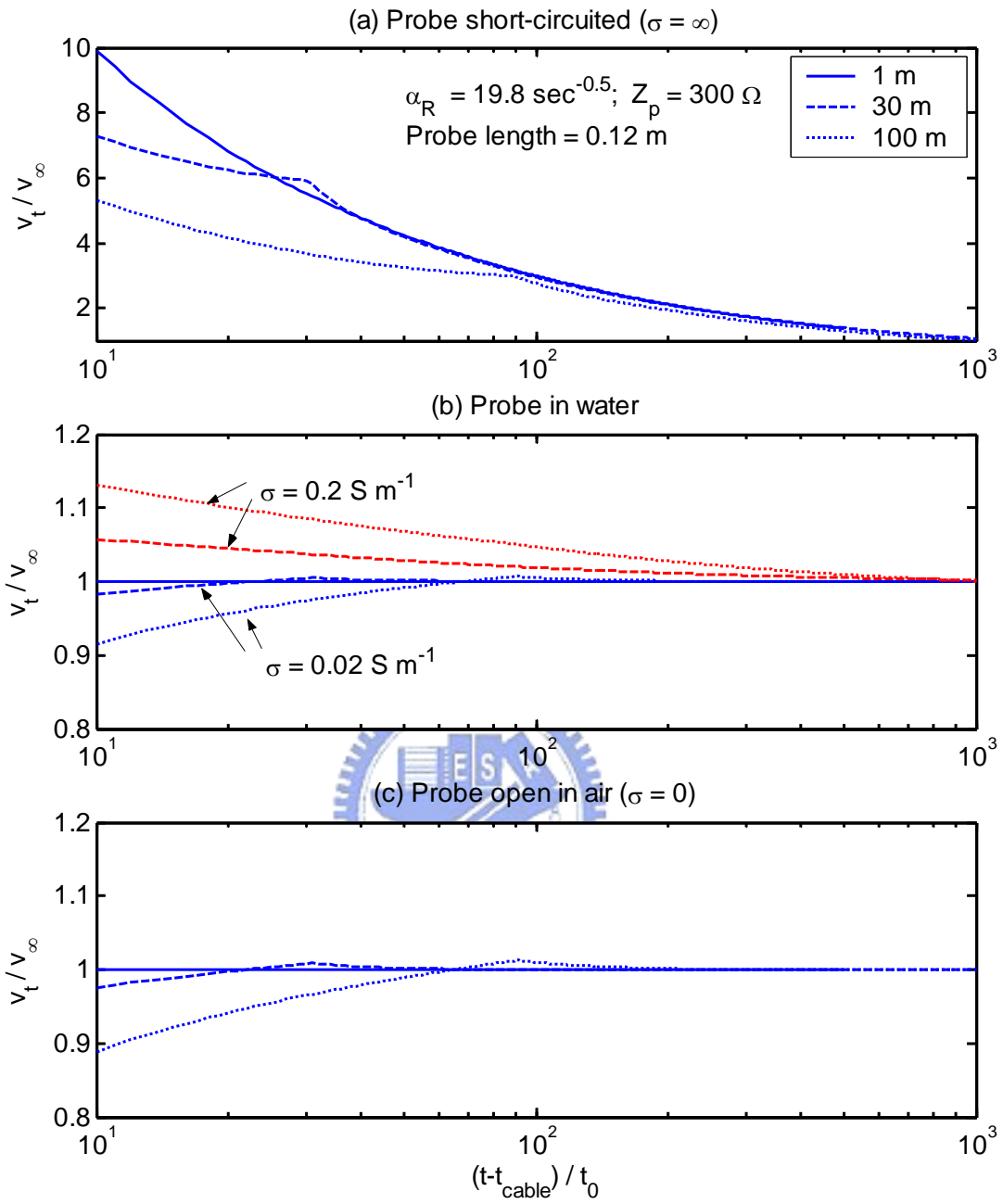
Fig. 4-7   Recording time required to reach the steady state for probes (a) short-circuited, (b) in water of two electrical conductivities, and (c) open in air.
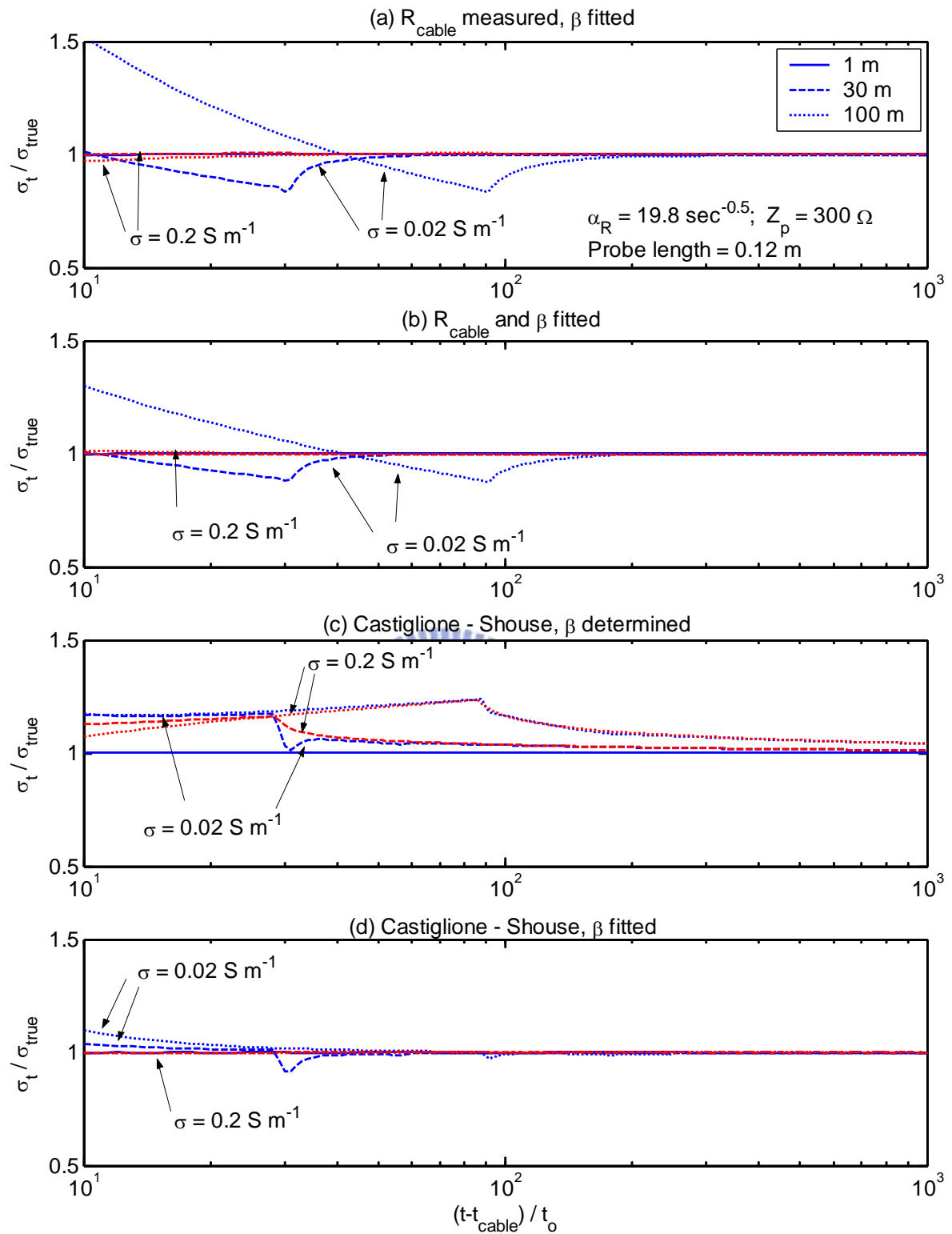
Fig. 4-8   The effect of recording time, expressed as the time that includes multiples of roundtrip travel time in the probe section, on the estimated EC using series resisters model with (a) R_{cable} measured and β fitted, (b) R_{cable} and β fitted, (c) Castiglione-Shouse method with actual β determined, and (d) Castiglione-Shouse method with β fitted.
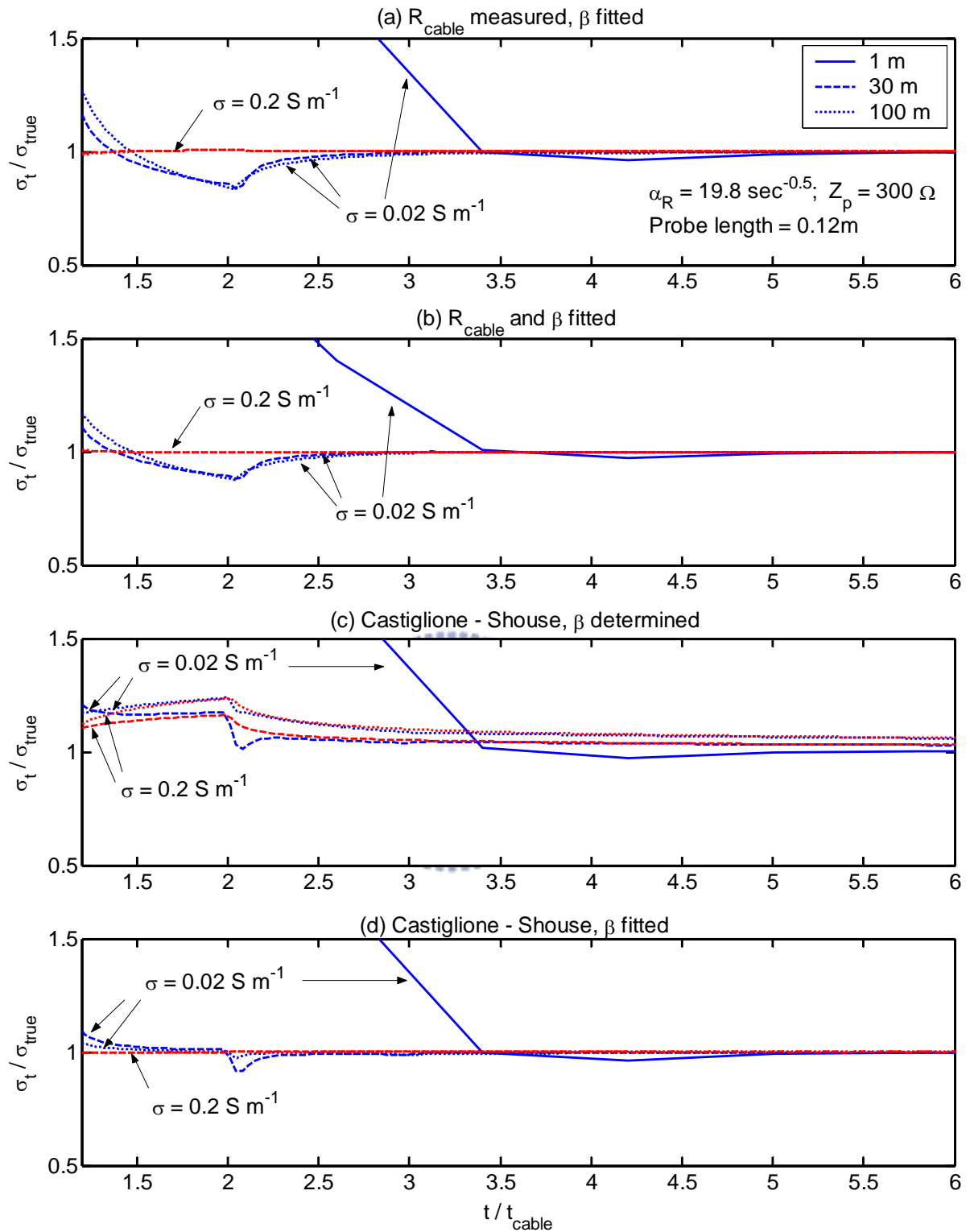
Fig. 4-9   The effect of recording time, expressed as multiples of roundtrip travel time in the lead cable, on the estimated EC using series resisters model with (a) R_{cable} measured and β fitted, (b) R_{cable} and β fitted, (c) Castiglione-Shouse method with actual β determined, and (d) Castiglione-Shouse method with β fitted.
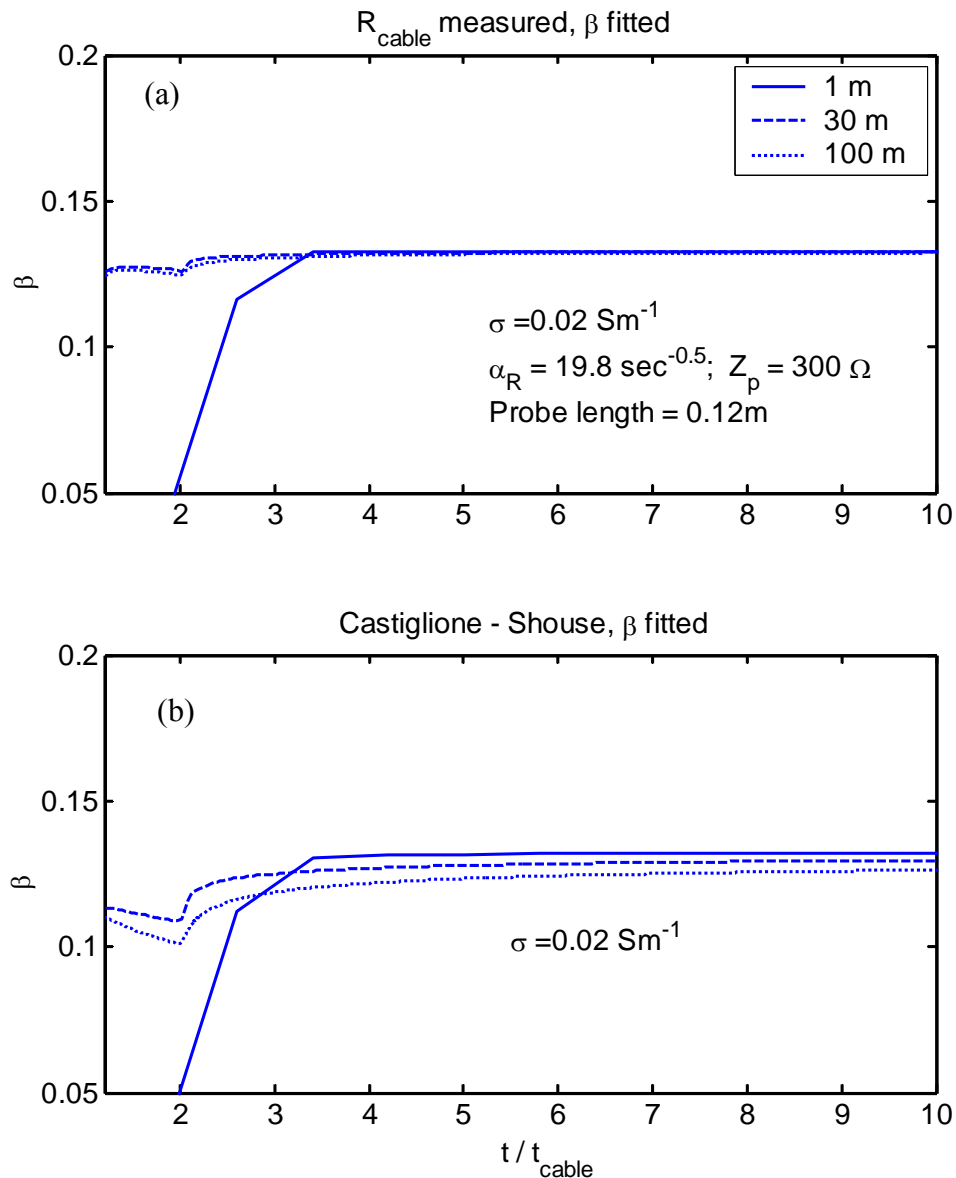
Fig. 4-10   The effect of recording time, expressed as multiples of roundtrip travel time in the lead cable, on the estimated probe constant β using (a) series resisters model, and (b) Castiglione-Shouse method

4.1.4   Experimental Verifications

To further verify the numerical findings, a few TDR measurements were made on *NaCl* electrolytic solutions, with σ varying from 0 to 0.15 S/m, using the 30-m RG58A/U cable and 12-cm two-rod probe.   TDR measurements were interpreted by the Giese-Tiemann method, Castiglione-Shouse method, and the series resisters model with cable resistance directly

measured by the short-circuited probe. The steady state responses were recorded at the time around 4.5 t_{cable} that includes 80 multiple reflections within the probe, satisfying the criteria for the steady state. The same data was used for calibrating the probe constant. Fig. 4-11 compares the TDR EC with that measured by a conventional EC meter. The results are in good agreement with that found in Fig. 4-4 and Fig. 4-5. When the probe constant is fitted, both the series resisters model and Castiglione-Shouse method provide accurate EC measurements in the full EC range, while the Giese-Tiemann method slightly overestimates at low EC and underestimates at high EC in the fitting range. The fitted probe constants are equal to the actual probe constant when the lead cable is very short. For long lead cables, the fitted probe constant is identical to the actual one only in the series resisters model. If the actual probe constant is used, linear overestimation by the Castiglione-Shouse method and non-linear underestimation by the Giese-Tiemann method are obvious, agreeing well with the numerical findings.
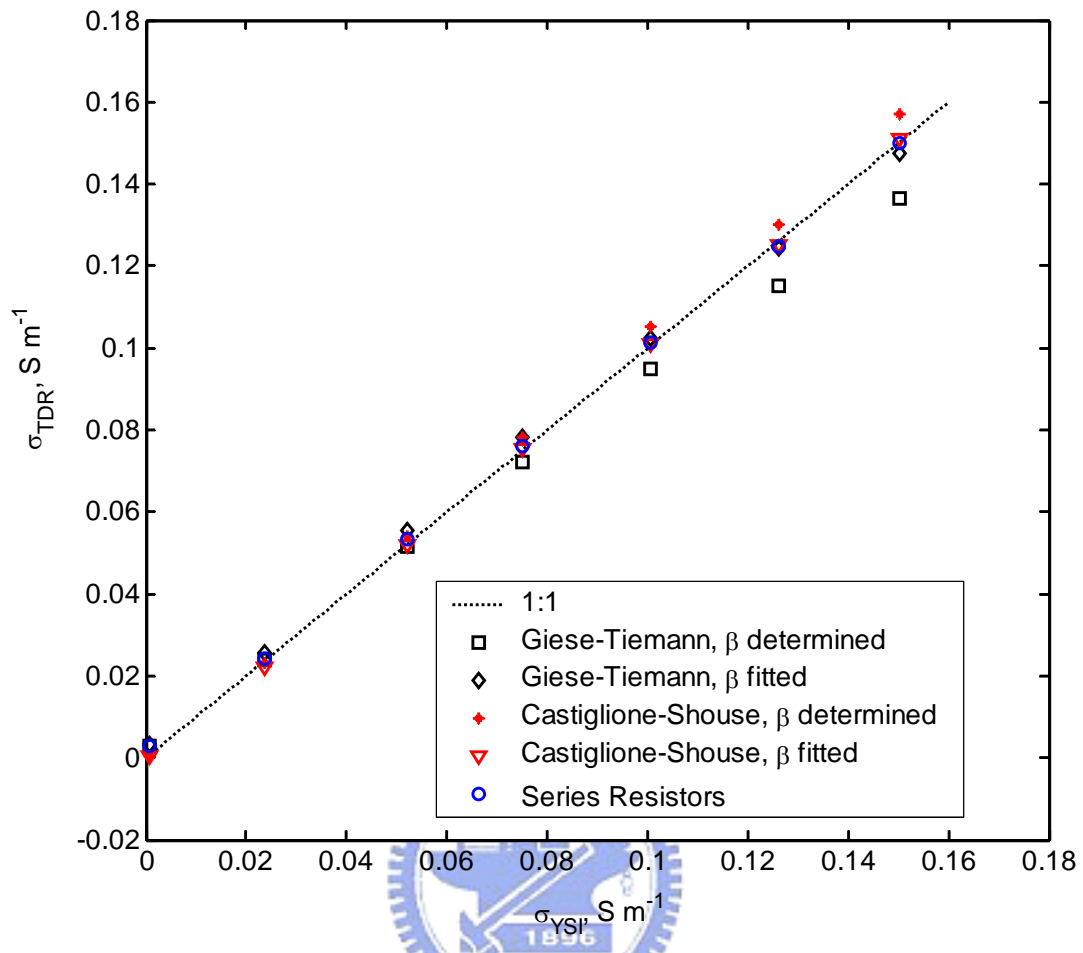
Fig. 4-11　Electrical conductivity measured by TDR compared with that measured by YSI conductivity meter.
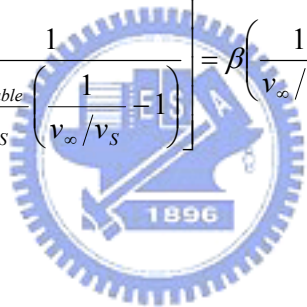
4.2　Calibration of EC Measurement

4.2.1　Clarification of Reflection Coefficient in EC Measurement

The ρ_∞ of a measurement in air (i.e. open circuit without any conduction) is theoretically 1.0 regardless of the cable length. However, this is not the case for many TDR devices, resulting in non-zero EC at the zero-EC condition.　For example, the ρ_∞ of our TDR100 units open in air range from 0.95 to 0.97. Typical fluctuations between 0.96 and 1.00 are the best the manufacturer can do with the technology they are using (Campbell Scientific Inc., personal communication).　Therefore, the objective is to clarify that the series resistors

model is indeed accurate and that the non-zero EC problem in air is due to something else instrument error in defining the reflection coefficient for TDR EC measurement. A calibration (correction) method is proposed, leading to an accurate and theoretically sound procedure for TDR EC measurement.

The steady state voltage of a TDR signal is related to the DC electrical conductivity of the material in the probe. At zero frequency ($t \to \infty$), the transmission line can be modeled as a lumped circuit composed of the voltage source v_S, the inner resistance R_S, cable resistance R_{cable}, and soil sample resistance R, as shown in Fig. 4-1. Hence, the soil bulk EC can be written as a function of the steady-state voltage as

$$\sigma = \frac{K_p}{R_S}\left(\frac{1}{v_\infty/v_S}-1\right)\left[\frac{1}{1-\frac{R_{cable}}{R_S}\left(\frac{1}{v_\infty/v_S}-1\right)}\right] = \beta\left(\frac{1}{v_\infty/v_S}-1\right)\left[\frac{1}{1-\frac{R_{cable}}{R_S}\left(\frac{1}{v_\infty/v_S}-1\right)}\right] \qquad [4\text{-}5]$$

where cable resistance can be calibrated along with the probe constant by measurements made in liquids with known EC or directly determined from the TDR measurement with the probe short-circuited as

$$R_{cable} = \frac{R_S}{\left(\frac{1}{v_{\infty,SC}/v_S}-1\right)} \qquad [4\text{-}6]$$

where $v_{\infty,SC}$ is the steady state voltage of the short-circuited probe.
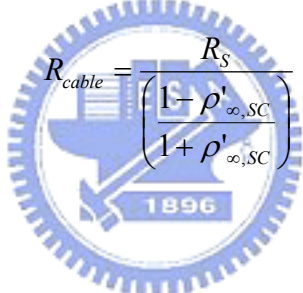
In theory, it is the ratio of the steady state voltage to the source step voltage that determines the TDR EC measurement. Let $v_0 = v_S/2$ be the ideal incident voltage, the reflection

coefficient for TDR EC measurement (ρ') is defined as

$$\rho' = \frac{v - v_0}{v_0} \qquad\qquad \text{[4-7]}$$

The TDR EC measurement (Eq. [4-5] and [4-6]) can be written in the more familiar form as

$$\sigma = \frac{K_p}{R_S}\left(\frac{1 - \rho'_\infty}{1 + \rho'_\infty}\right)\left[\frac{1}{1 - \dfrac{R_{cable}}{R_S}\left(\dfrac{1 - \rho'_\infty}{1 + \rho'_\infty}\right)}\right] \qquad\qquad \text{[4-8a]}$$

$$R_{cable} = \frac{R_S}{\left(\dfrac{1 - \rho'_{\infty,SC}}{1 + \rho'_{\infty,SC}}\right)} \qquad\qquad \text{[4-8b]}$$

the steady state reflection coefficient ρ'_∞ indicates how conductive the medium is. According to Eq. [4-8a], ρ'_∞ is a function of R_S but independent of Z_c and impedance mismatches in the probe head. Fig. 4-12 shows theoretical values of ρ'_∞ for three distinct electrical conductivities, $\sigma = 0$, $\sigma = K_p/R_S$, and $\sigma = \infty$. At constant EC, ρ'_∞ increases as the cable resistance increases. The amount of increase in ρ'_∞ due to cable resistance decreases as EC decreases. In a non-conductive medium ($\sigma = 0$), the steady state reflection coefficient ρ'_∞ is 1.0 regardless of cable resistance.
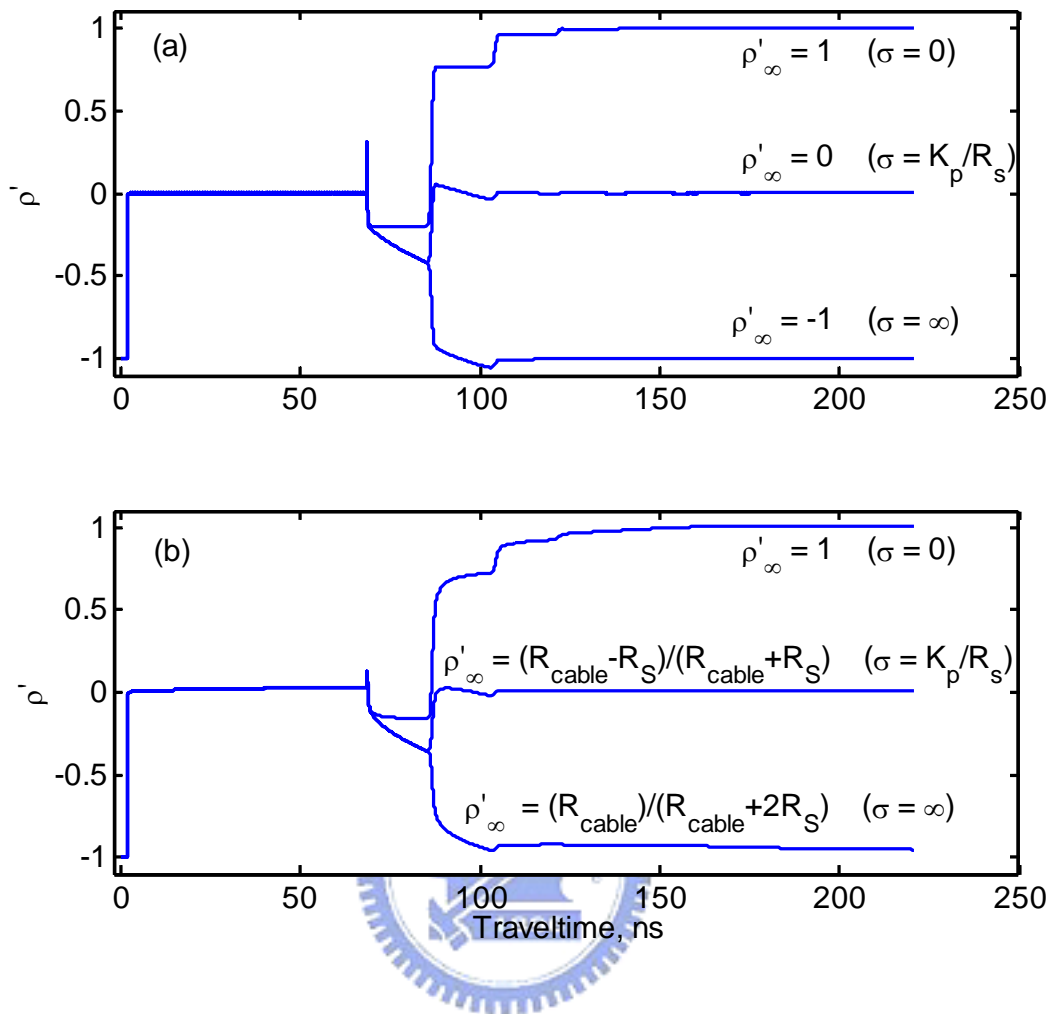
Fig. 4-12   Theoretical values of EC-associated reflection coefficient ρ'_∞ for three distinct electrical conductivities in the case of (a) zero cable resistance and (b) non-zero cable resistance.

4.2.2   TDR System Error

It should be noted that $\rho_\infty = \rho'_\infty$ only when $v_i = v_0$. Unfortunately, small differences between v_i and v_0 often occur in practice due to imperfect amplitude calibration at the 50 Ω level. Although the small error is insignificant when the reflection coefficient is used as an indication of the quality of the transmission system, it may introduce significant errors in TDR EC measurements at low electrical conductivities. Let $v_i = v_0 + \delta$, in which δ is a small error. The relationship between the instrument (measured) reflection coefficient ρ and the EC-associated

reflection coefficient ρ' can be written as.

$$\rho = \frac{v - v_i}{v_i} = \frac{v - (v_0 + \delta)}{v_0 + \delta} = \left(\frac{v_0}{v_0 + \delta}\right)\rho' - \frac{\delta}{v_0 + \delta} \qquad [4\text{-}9]$$

The relationship is graphically shown in Fig. 4-13a, in which the $\rho_{\infty,air}$ = 0.95. The instrument reflection coefficient ρ underestimates the EC-associated reflection coefficient ρ'. The underestimation linearly decreases with decreasing reflection coefficient and vanishes at ρ' = -1. The underestimation is maximal at zero EC (e.g. TDR probe open in air) when ρ' = 1. This phenomenon is often mistakenly interpreted as the effect of cable resistance. The effect of instrument error on the estimated TDR EC is shown in Fig. 4-13b and Fig. 4-13c for high EC and low EC, respectively. Using the actual probe constant (e.g. K_p = 8.93 for the probe used in this study) and condition of zero cable resistance in Eq. [4-8], the instrument error results in an overestimation of EC. This is particularly evident in the low EC range. The overestimation may be minimized by fitting the probe constant instead of using the actual probe constant. However, the fitted K_p will now depend on the EC range used for calibration (see Fig. 4-13b and 4-12c). Although the fitted K_p is only slightly lower than the actual one and small errors of the estimated TDR EC are not noticeable in the high EC range, the fitted K_p is significantly lower and errors of the estimated TDR EC are obvious in the low EC range. Typically, one would determine the K_p with the high EC measurements (e.g. K_p = 8.62) and apply it also to the low EC data, resulting in considerable errors in the low EC range as shown in Fig. 4-13c.

From Eq. [4-8a], the EC-associated reflection coefficient ρ'_∞ in the case of zero EC should be 1.0 regardless of cable resistance. Therefore, the zero-EC ρ_∞ obtained by a measurement with the TDR probe in air or simply disconnected, denoted by $\rho_{\infty,air}$, can be used to correct the instrument reflection coefficient. The calibration equation to transform

instrument reflection coefficients into EC-associated reflection coefficients can be derived from Fig. 4-13 as

$$\rho' = 2\frac{\rho - \rho_{\infty,air}}{\rho_{\infty,air} + 1} + 1 \qquad [4\text{-}10]$$

Assuming a cable resistance equal to that of a 20 m long RG58 cable (e.g. $R_{cable} = 0.723$ Ω) and no instrument error ($\rho'_\infty = \rho_\infty$), Fig. 4-14a shows the effect of cable resistance on ρ'_∞ and the scaled steady-state reflection coefficient by the Castiglione-Shouse method and the series resistors model. To enhance visual illustration, Fig. 4-14 plots deviations from the expected values on the y axis in stead of absolute values as in Fig. 4-13. In contrast to the instrument error due to imperfect amplitude calibration, the cable resistance causes an increase in ρ'_∞. However, the amount of increase reduces nonlinearly with increasing ρ'_∞ and vanishes at zero EC ($\rho'_\infty = 1$). This nonlinear effect cannot be correctly accounted for by the linear scaling method proposed by Castiglione and Shouse (2003). Fig. 4-14b shows the deviation of estimated EC from true EC for the Castiglione-Shouse method and series resistors model using the actual probe constant (e.g. $K_p = 8.93$). The linear scaling method proposed by Castiglione and Shouse (2003) overestimates the EC by a constant rate, the magnitude of which depends on cable resistance. As pointed out earlier, a linear overestimation by the Castiglione-Shouse method can be completely compensated for if the probe constant is adjusted (e.g. the fitted K_p becomes 8.78 in this case) such that calculated TDR EC matches the known EC. However, the fitted probe constant will depend not only on the probe geometry but also on the cable resistance. Hence, probes with different cable lengths should be individually calibrated when the Castiglione-Shouse method is used. The series resistors model is more consistent. It has a unique probe constant for each type of probe

regardless of the cable length.
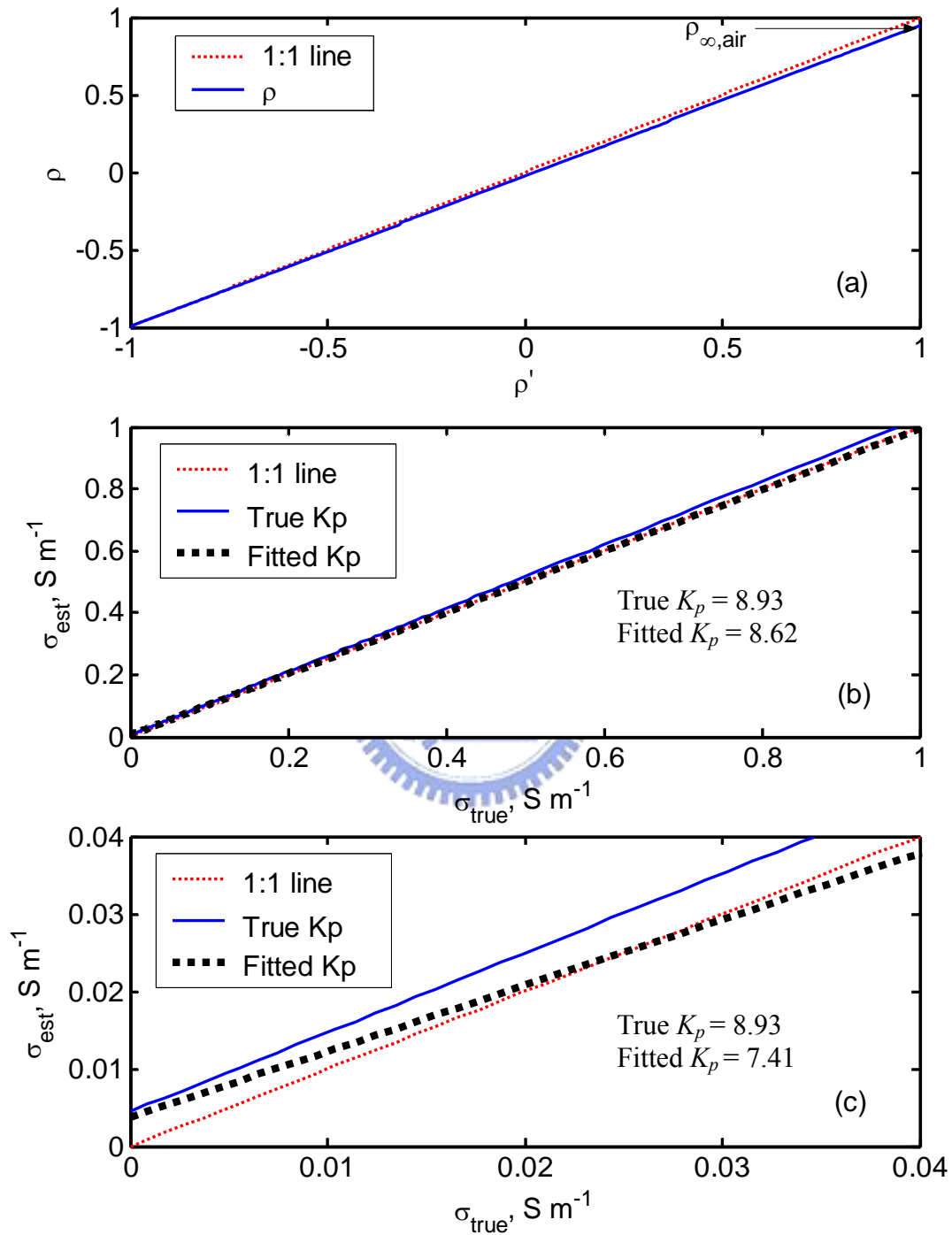
Fig. 4-13   (a) The relationship between instrument reflection coefficient ρ and EC-associated
reflection coefficient ρ' when incident voltage $v_i \neq v_0$ (half of the source voltage) due to
imperfect amplitude calibration at the 50 Ω level; (b) the effect of instrument error on TDR
EC in high EC range and (c) in low EC range
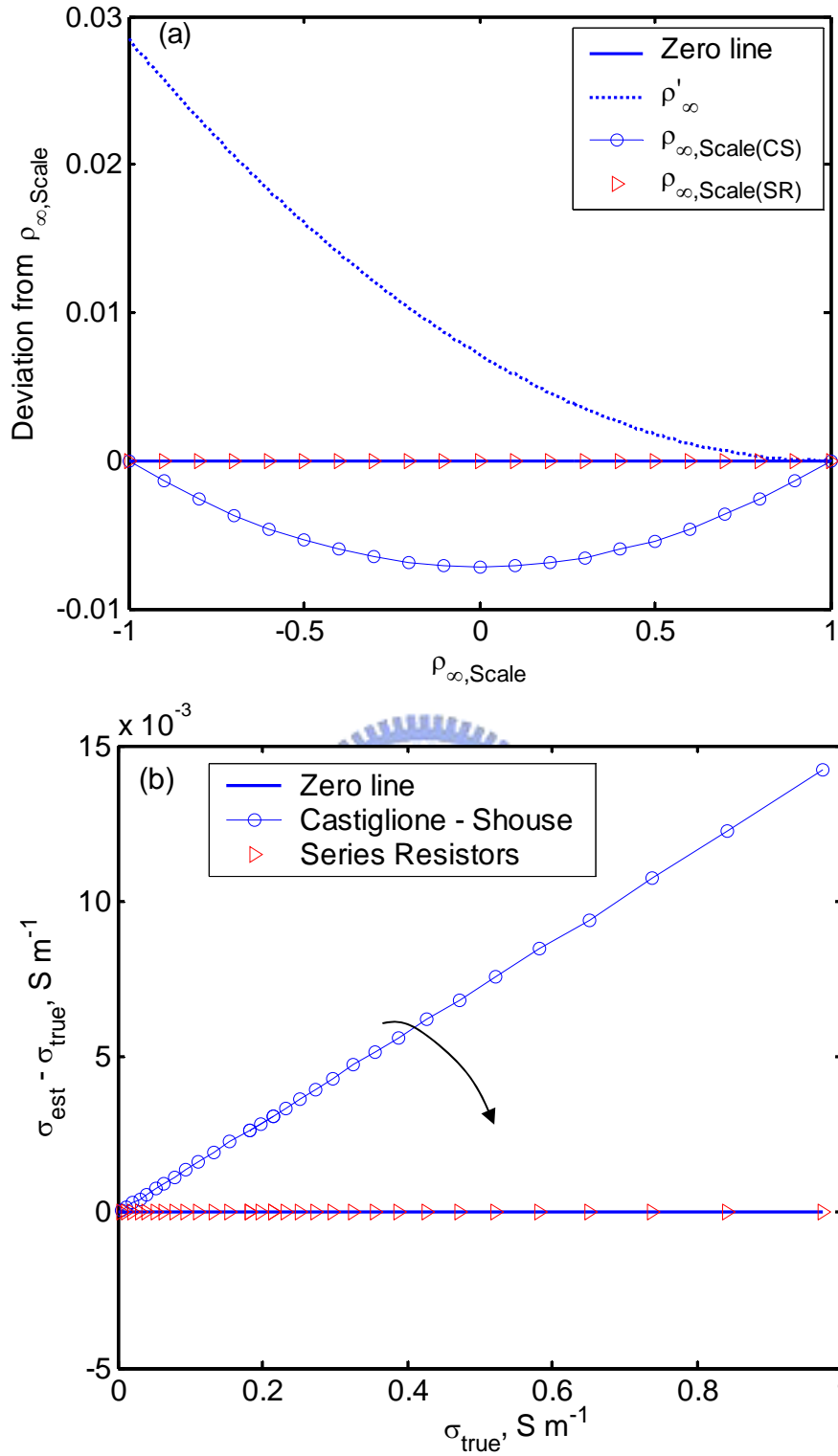
Fig. 4-14 (a) Effect of 20m RG-58 cable resistance on steady-state reflection coefficient ρ'_∞ and the scaled steady-state reflection coefficient by the Castiglione-Shouse method and series resistors model; (b) deviation of the estimated EC from true EC for the Castiglione-Shouse method and series resistors model using actual probe constant

4.2.3   Calibration Method and Verification

Material and method

The instrument errors due to imperfect amplitude calibration were examined for a Campbell Scientific TDR100 and a Tektronix 1502C. Three measurements were taken in which the front panel connector was open, shorted, and terminated by a 50 Ω block, respectively. To further demonstrate that the instrument error is not related to cable resistance, the three measurements were repeated with a 10 m RG58 cable connected to the TDR devices.

To experimentally investigate the effect of the imperfect amplitude calibration, TDR EC measurements were made on 7 *NaCl* solutions, with EC varying in the low EC range from 0 to 0.04 Sm^{-1}. The low EC range was used to clearly illustrate the effect of instrument error due to imperfect amplitude calibration. The measurements were conducted using a TDR probe (10-cm two rod probe with conductors 4 mm in diameter and 20 mm in spacing) connected to a Campbell Scientific TDR100 via a 2m-long RG-58 cable. The electrical conductivity of each electrolytic solution was measured independently with a standard EC meter (YSI-32 Yellow Spring Int. Inc., Yellow Spring, OH). When determining the R_{cable} using Eq. [4-8b], the measurements were performed by shorting the cable end with a short wire. The steady state responses were recorded near the end of the TDR pulse to better approximate the steady state. This is in fact mandatory for measurements in the high EC range or for the short-circuited probe. The computation of TDR EC involves Eq. [4-8], and Eq. [4-9] successively for the series resistors model and Eq. [2-43] and Eq. [2-47] for the Castiglione-Shouse method. To calculate the TDR EC using Eq. [2-43], the probe constant β is first obtained using least square fitting of TDR EC to EC measurements made with the conventional conductivity meter. TDR EC measurements of electrolytic solutions were repeated using a 20m-long RG-58 cable to show the effect of cable resistance on the fitted

probe constants.

Results and discussions

A TDR device may output voltage (e.g. a Tektronix 1502C) or reflection coefficient (e.g. a Campbell Scientific TDR100). To determine EC, v_∞ / v_S in Eq. [4-5] or ρ'_∞ in Eq. [4-8a] should be known. The source step voltage v_{S0} of a voltage-output TDR device is simply equal to the v_∞ when the TDR probe is open in air, which then serves as the reference voltage for computing the electrical conductivity. The original TDR waveform $v(t)$ of a voltage-output TDR device is often converted to $\rho(t)$, in which the incident step v_i is determined by using a 50-Ω cable or terminating block as the impedance reference and for amplitude calibration. Fig. 4-15a shows a group of TDR waveforms $\rho(t)$ from the 1502C device, in which the front panel and a 10-m lead cable are shorted, open, and terminated with a nominal 50-Ω terminating block. The front panel terminated with a 50-Ω terminating block was used for amplitude calibration such that its reflection coefficient at long times is equal to 0.0. In this case, the steady-state reflection coefficient ρ_∞ is 0.995 for the probe open in air, regardless of the cable length. It is not precisely 1.0 due to imperfect match between the source impedance and the terminating block. This reflection coefficient corresponds to 0.0045 dSm^{-1} for the TDR probe used in this study, a small EC error in the condition of zero EC.   The ρ_∞ for the shorted front panel not being -1.0 is attributed to some internal resistance. The ρ_∞ for a shorted cable increases as cable length increases. The amount of increase in ρ_∞ due to cable resistance reduces nonlinearly with increasing ρ_∞ and vanishes at $\rho_\infty = 1$. Applying the calibration equation Eq. [4-10], the corrected reflection coefficient $\rho'_\infty(t)$ can be obtained as shown in Fig. 4-15b. The corrected ρ'_∞ becomes 1.0 in the condition of zero EC. The degree of imperfect match between the source impedance and the terminating block is indicated by

ρ'_∞ =0.0025 in Fig. 4-15b. A TDR device that outputs reflection coefficient uses the nominal 50-Ω internal cable as the impedance reference and for amplitude calibration. Analogous to Fig. 4-15, Fig. 4-16 shows a group of TDR waveforms $\rho(t)$ from the TDR100 device. The mismatch between the reference impedance and source impedance in the TDR100 is more significant, leading to ρ_∞ = 0.950 (corresponding to EC = 0.046 dSm^{-1}) for the open front panel and ρ_∞ = 0.961 for the probe open in air as shown in Fig. 4-16a. The amplitude calibration error in a TDR100 seems to depend on whether the front panel is connected to a cable, a phenomenon which may be related to the fringing field of the open front panel. The apparent error can be corrected by applying the calibration equation Eq. [4-10], as shown in Fig. 4-16b.

Fig. 4-17 shows the results of several TDR EC measurements in the low EC range using the TDR100 device with 2 m and 20 m of RG-58 lead cable. The probe constant K_p was fitted as described before. Table 4-3 lists the fitted K_p using the Castiglione-Shouse method and the series resistors model. The percentage errors between the TDR EC measurements and conductivity meter EC measurements are listed in Table 4-4. As shown in Fig. 4-17, the Castiglione-Shouse method inherently corrects the instrument error and provides accurate TDR EC measurements when the probe constants are fitted. But the fitted probe constant K_p varies with cable length, as shown in Table 4-3. The fitted probe constant decreases as cable resistance increases, as also suggested in Fig. 4-14.

If the measured reflection coefficient is not corrected for instrument error, the actual reflection coefficient is underestimated especially in low EC range as shown in Fig. 4-13a. This will have an effect on the estimated EC using the series resistors model.   Depending on the EC data range, the fitted K_p is lower than the actual K_p to some degree. As a consequence, the TDR EC by the series resistors model overestimates at lower EC and underestimates at higher EC, as shown in Fig. 4-17a and Table 4-4. This experimental result exactly agrees with

the theory illustrated in Fig. 4-13c. The results of the series resistors model with TDR100 reflection coefficient corrected by Eq. [4-10] are shown in Fig. 4-17b and Table 4-4. The large percentage error for the lowest EC in Table 4-4 can be attributed to the conductivity meter resolution and TDR quantization resolution. Except for the lowest EC (0.00039 Sm^{-1}), both the corrected series resistors model and the Castiglione-Shouse method give TDR EC measurements in precise agreement with that measured by the conventional EC meter. But the fitted probe constant K_p can be considered independent of the cable length only in the case of the series resistors model, as shown in Table 4-3.

To accurately determine TDR EC, both the instrument error due to imperfect amplitude calibration and cable resistance should be properly addressed. The instrument error results in an underestimation of reflection coefficient, which linearly decreases with decreasing reflection coefficient and vanishes at reflection coefficient = -1.0. In contrast, the effect of cable resistance leads to overestimation of reflection coefficient, which nonlinearly decreases with increasing reflection coefficient and vanishes at reflection coefficient = 1.0. The combined effect of instrument error and cable resistance on the steady-state reflection coefficient is nonlinear, so the Castiglione-Shouse method is incorrect, although the error can be compensated by adjusting the probe constant. The series resistors model is theoretically sound and precise if the reflection coefficient is properly calibrated to account for the instrument error.
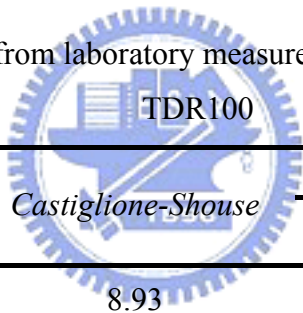
The instrument error can be calibrated by the steady-state reflection coefficient at the zero-EC condition, while the cable resistance can be determined by the steady-state reflection coefficient when the probe is short-circuited. A calibration equation is derived to correct the measured reflection coefficient for instrument error. The corrected reflection coefficient can then be used in the series resistors model (Eq. [4-8]) for reduction of electrical conductivity considering the effect of cable resistance. To keep the usual practice and simplicity, the effect

of instrument error and cable resistance can be addressed in one step. An equation replacing the Castiglione-Shouse equation is suggested here:

$$\rho_{\infty,Scale} = 2\frac{(\rho_{\infty,air} - \rho_{\infty,SC})(\rho - \rho_{\infty,air})}{(1 + \rho_{\infty,SC})(\rho - \rho_{\infty,air}) + (\rho_{\infty,air} - \rho_{\infty,SC})(1 + \rho_{\infty,air})} + 1 \qquad [4\text{-}11]$$

where $\rho_{\infty,Scale}$ is the scaled reflection coefficient to be used in the usual Giese-Tiemann equation, ρ is the steady-state reflection coefficient of the sample under measurement, $\rho_{\infty,air}$ is the steady-state reflection coefficient when the probe is open in air, and $\rho_{\infty,SC}$ is the steady-state reflection coefficient when the probe is short-circuited.

Table 4-3   Fitted K_p (m^{-1}) from laboratory measurements using a Campbell Scientific TDR100

| Cable length (m) | Castiglione-Shouse | Series Resistors | |
		Uncorrected	Corrected[†]
2	8.93	7.58	8.93
20	8.78	7.56	8.92

[†]Corrected using Eq. [4-10]

124

Table 4-4   Percentage errors between the TDR EC measurements and conductivity meter EC measurements

Error (%) $\sigma_{YSI}(Sm^{-1})$	Series Resistors (Uncorrected)		Series Resistors (Corrected)		Castiglione-Shouse	
	2m	20m	2m	20m	2m	20m
0.00039	818.81	849.88	-6.23	68.29	-6.09	68.28
0.00529	46.64	47.07	-1.92	1.01	-1.78	1.01
0.01183	13.41	14.19	-0.80	0.93	-0.66	0.93
0.01525	7.80	7.64	-0.12	0.24	0.03	0.23
0.02014	2.14	2.45	-0.65	0.00	-0.51	0.00
0.03003	-2.55	-2.73	0.11	-0.07	0.25	-0.07
0.04015	-5.22	-5.02	0.18	0.33	0.33	0.33
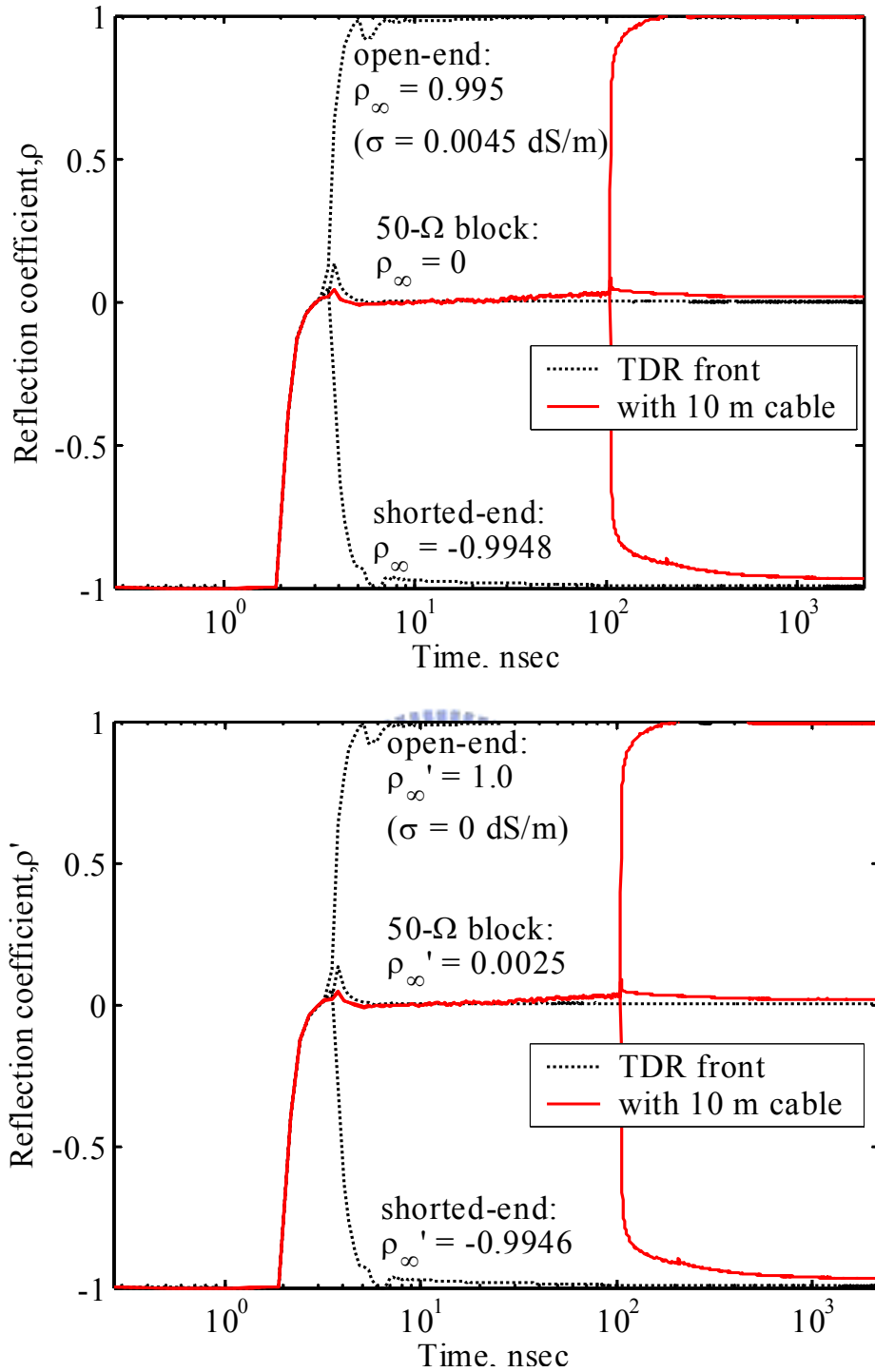
Fig. 4-15 (a) Original TDR waveforms from a Tektronix 1502C and (b) the associated corrected waveforms using calibration equation Eq. [4-10].
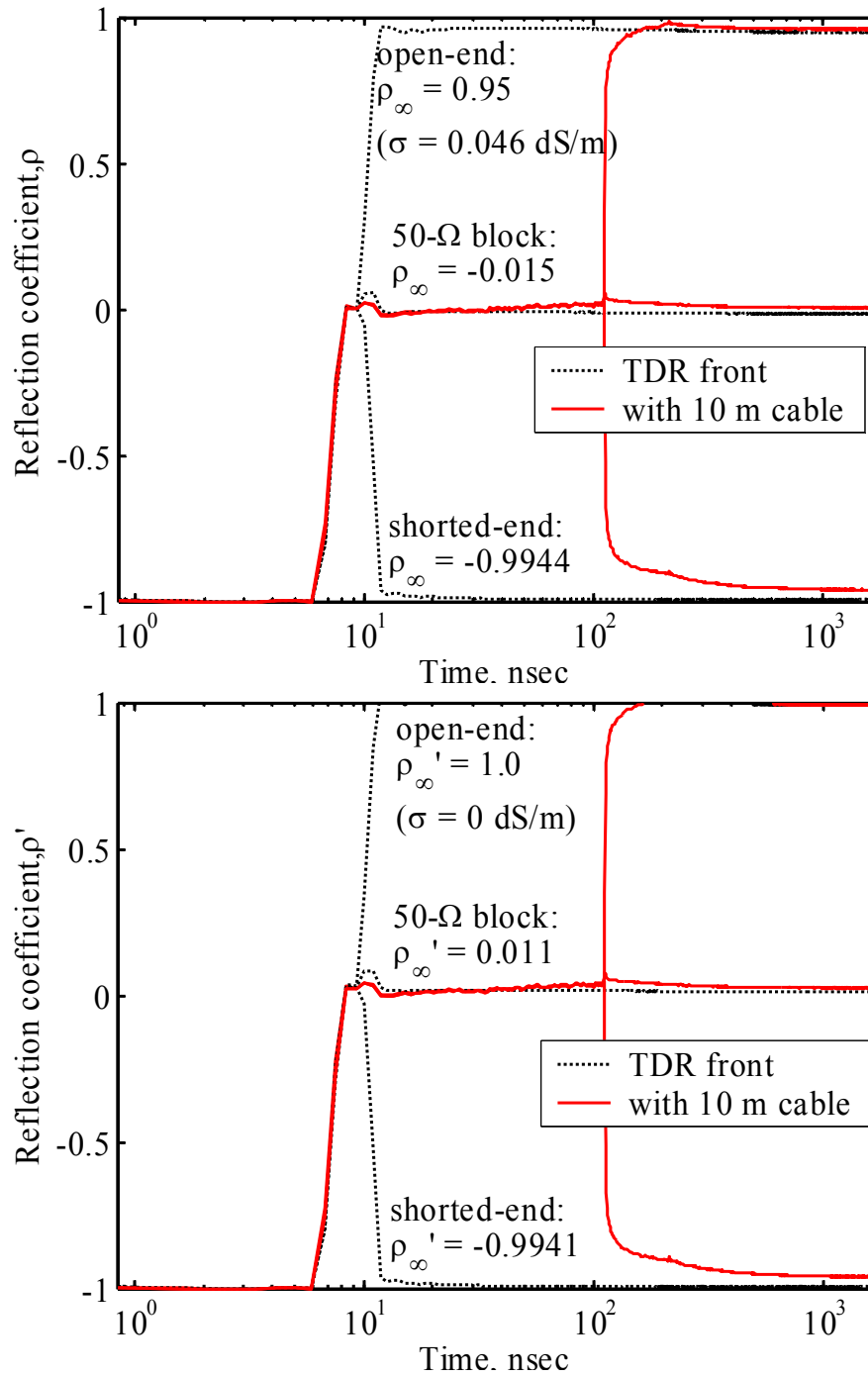
Fig. 4-16   (a) Original TDR waveforms from a Campbell Scientific TDR100 and (b) the associated corrected waveforms using calibration equation Eq. [4-10].
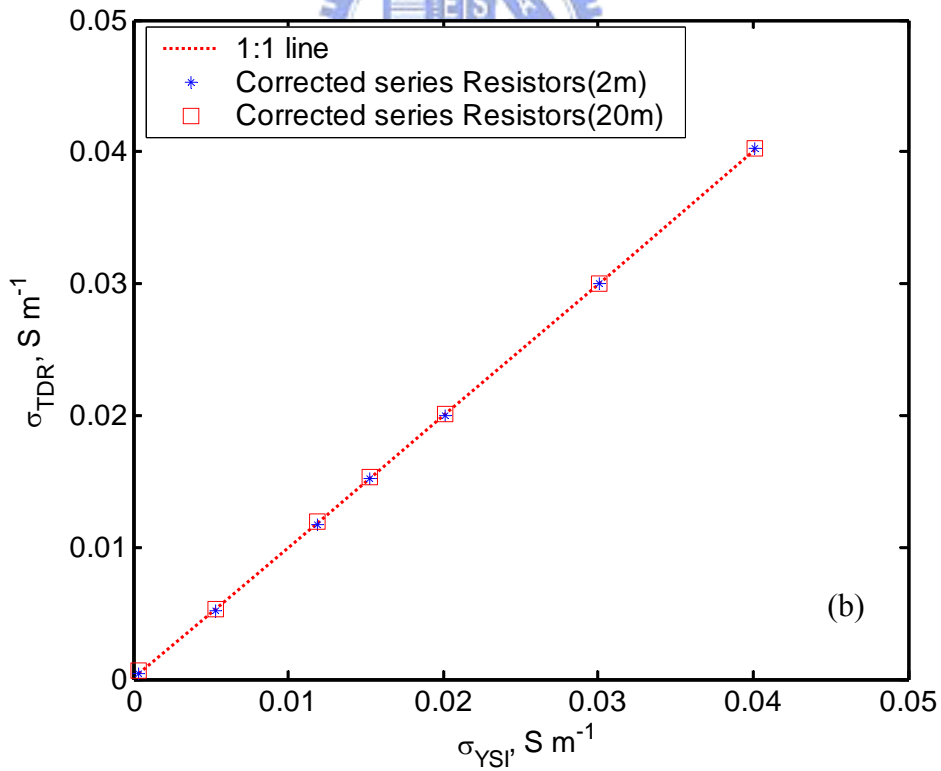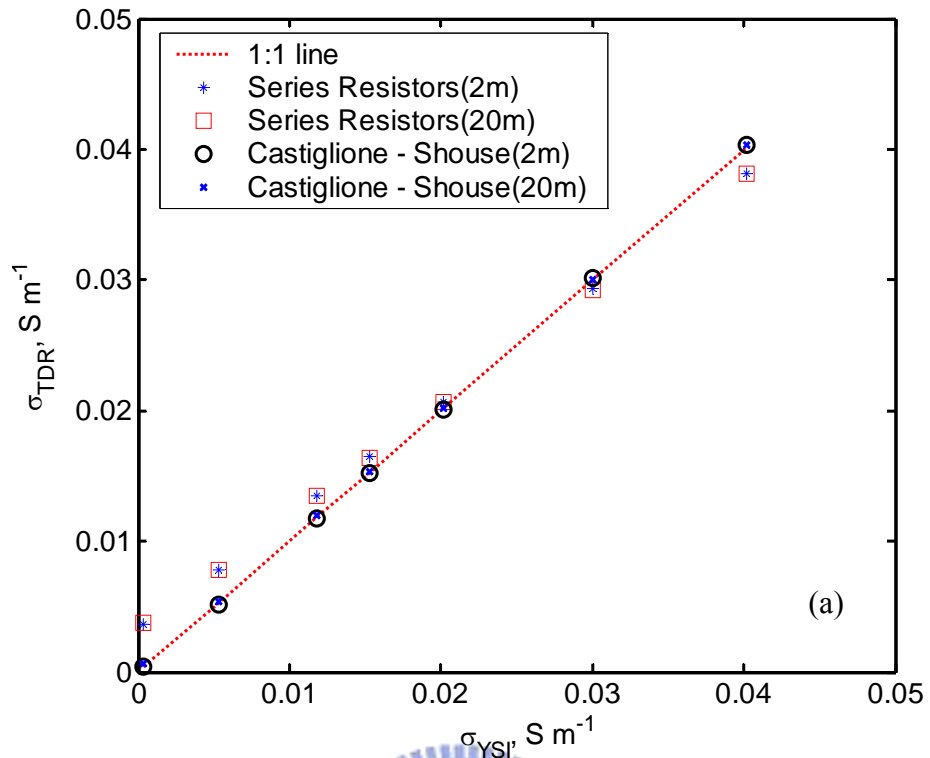
Fig. 4-17 TDR EC measurements made by a Campbell Scientific TDR100 (a) without reflection coefficient calibration and (b) with reflection coefficient calibration.

5 TDR Probe Design

There are two main aspects of the TDR probe design that will be discussed in this chapter: the effects of probe rods configuration and boundary condition, and the measurement sensitivity of TDR travel time and EC measurement.

As mentioned in Chapter 2, the spatial EM density distribution has been investigated by analytical solution and numerical approaches for common probe configurations in the context of spatial sample volume. However, these early studies do not apply to some TDR probe types. Advanced 3D EM field simulation software will be demonstrated to be useful for investigation of probe rod configuration and boundary effect.

Moreover, measurement sensitivity which is defined as the change of the measurement data due to variations of physical parameter is investigated to provide guidelines for probe design.

A development of a new type of TDR probe, TDR penetrometer, is included in this chapter to meet need of in-depth characterization of soil or soil-water mixtures. Due to the complexity of TDR penetrometer, this study will provide calibration methods for the TDR penetrometer and experimentally evaluate its measurement performance.

5.1 Probe Rods Configuration and Boundary Effect

Advanced 3D EM field simulation software is recommended for the further investigation of TDR probes. Using Ansoft HFSS®, one can simulate the EM field around TDR probes in 3D, which relates the measurement performance. Fig. 5-1 shows the basic setup of 3D solid models, boundary conditions, and excitation for a three-rod TDR probes in Ansoft HFSS®. All details of the 3D solid models can be accurate captured as shown in Fig. 5-2. All the electric fields are solved by HFSS using the finite element method (FEM) at 1 GHz roughly

corresponding to the effective frequency of common TDR devices.

Influence factors including two-rod or three- rod configuration, shielded or unshielded in probe head, and open-end or shorted-end boundary, are investigated through the Ansoft HFSS$^{®}$ simulation.

From Fig. 5-3 (only the yz place is shown for convenience), it can be found that the input energy is shielded well by the coaxial cable. After propagating into the probes, part of the energy is confined in the metal cup (shielded case), while the rest is guided by the three-rod probes toward the probe ends. It is clear from the figure that a strong radiation exists at probe ends and around the outer probes, where the surrounding material (e.g. water or soil) can be considered as a capacitive load for the probe antenna. The result of shorted-end, as shown in the right of Fig. 5-3, indicates much energy is confined among rods compared to the result of open-end probe. However, using shorted-end probe has disadvantage related to low sensitivity in the low frequency range as revealed in Chapter 3.

Since the TDR signal experiences an abrupt impedance change from the coaxial cable to the probes, there is also a strong radiation near the coax-probe transition. If the transition is not shielded by a metal cup (as shown in Fig. 5-4), there will be stray energy radiated into the surrounding material. Consequently, not all energy is consumed to detect the TDR impedance change by the measured material of the probe section. The metal cup can be considered as a reflector for directing the main beam of the probe antenna into measured material. Therefore, the shielded probes can better resolve the impedance variation in TDR due to measured material. Based on the same reasoning, for the special condition as emerged in the water, the L-shaped probes with shield, as shown in Fig. 5-5, will provide an effective solution.

Comparing Fig. 5-3 and Fig. 5-6, one can tell the two-rod probe is more effective spatially in detecting material properties than the three-rod one because the fields are not bounded in between probes. However, Fig. 5-7 shows that the main beams of radiation are not well directed

into the water in absence of the metal cup.

From the above comparison, the two-rod shielded probe in Fig. 5-6 has a greater sample volume than the three-rod shielded probe, which the electric field is symmetric and well distributed at the vicinity of the rods. However, the three-rod probe is more sensitive to slight changes in material properties than the tow-rod one because of the former has closely spaced rods with higher capacitance per unit length. For both configurations, the metal cups ensure that backward radiation is minimized and the radiated energy is directed into measured material.

These simulations help to design appropriate submerged probe for measurements of soil-water mixtures.
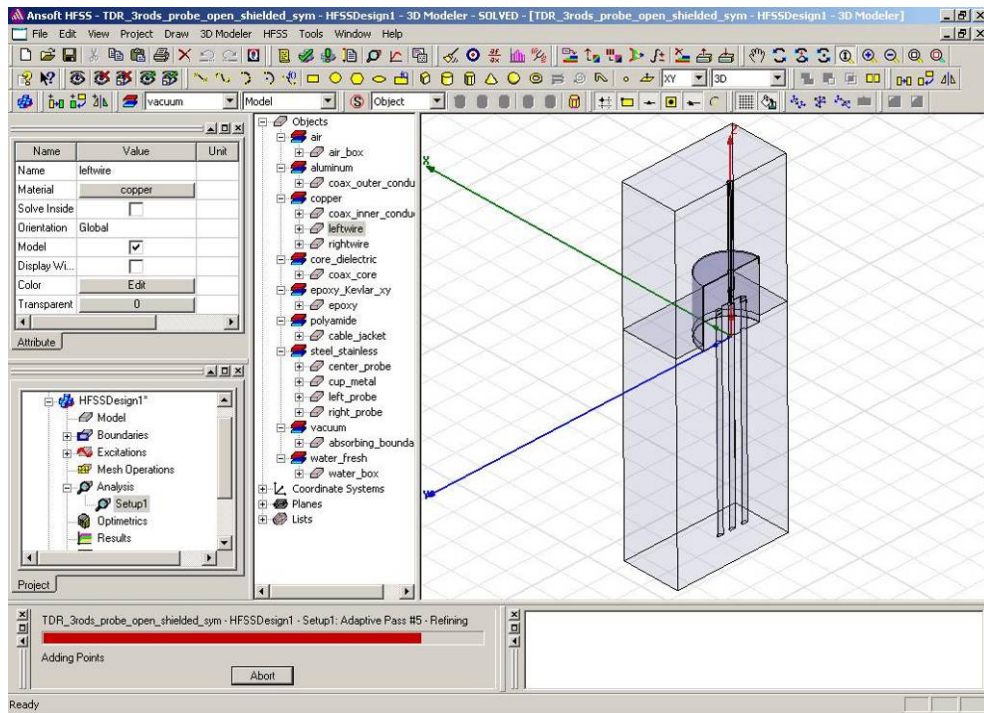
Fig. 5-1　Setup of the electromagnetic simulation in Ansoft HFSS® for a three-rod TDR probe.
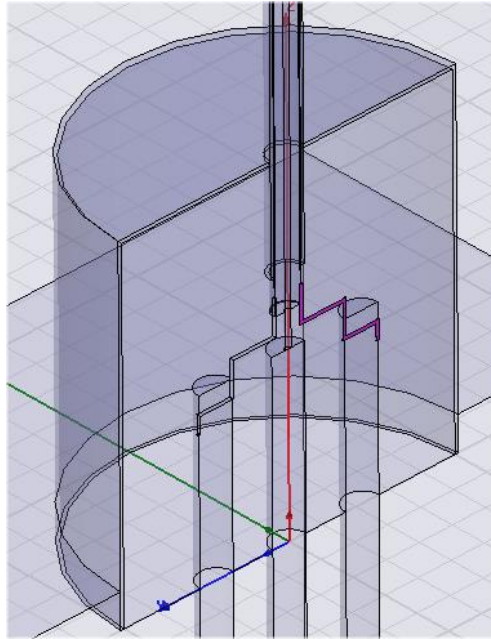
Fig. 5-2   Details of the metal wires connecting the probes and the coaxial cable.
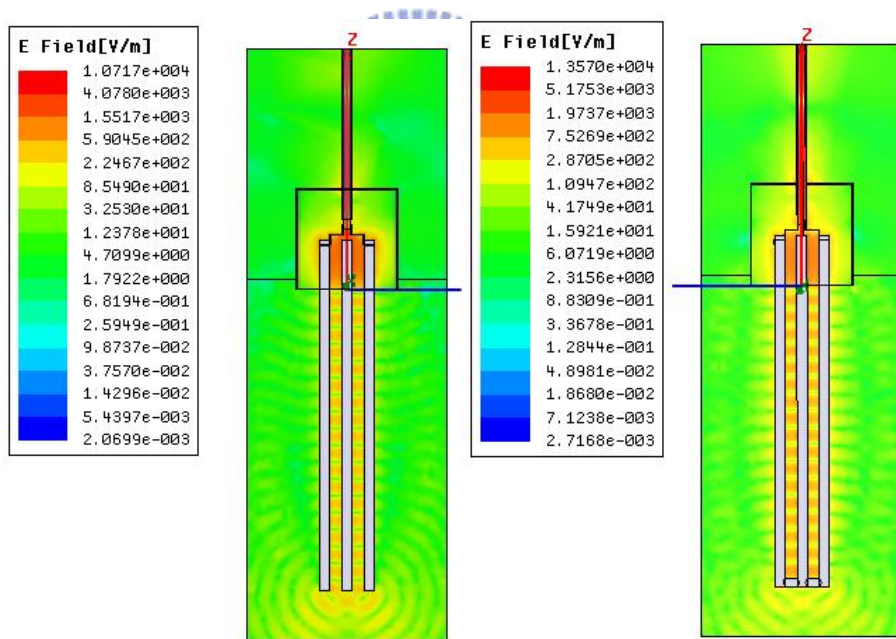
Fig. 5-3   E-field plots of a three-rod shielded TDR probe on the yz plane with probe ends open (left) and shorted (right).
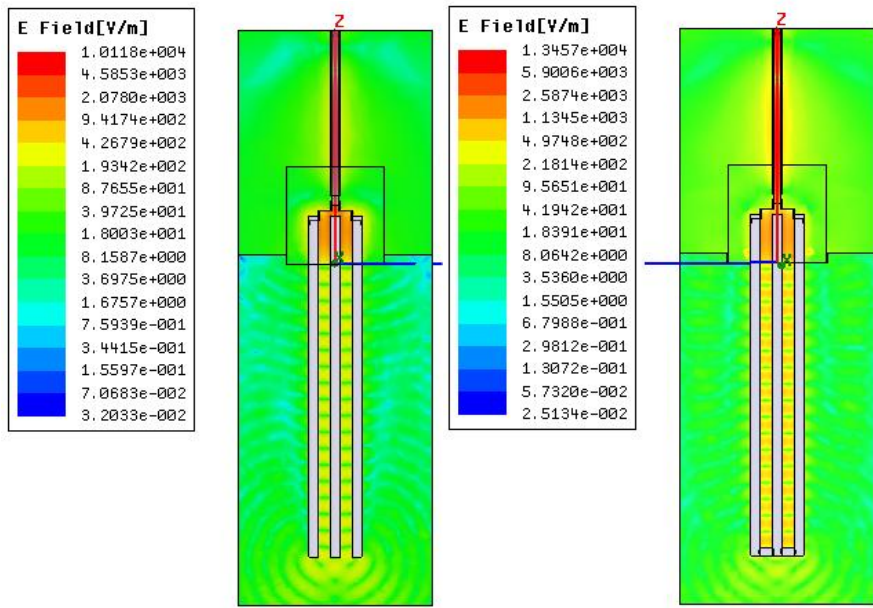
Fig. 5-4   E-field plots of a three-rod unshielded TDR probe on the yz plane with probe ends open (left) and shorted (right).
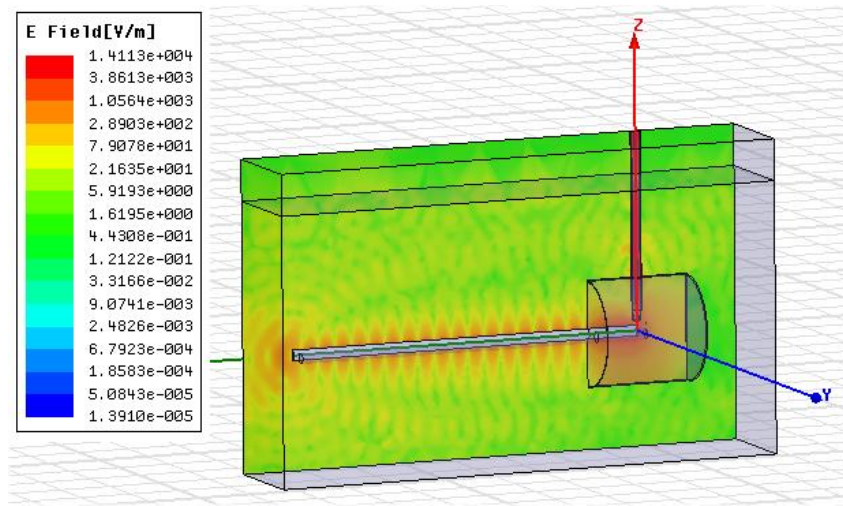
Fig. 5-5   E-field plot of the L-shaped three-rod shielded TDR probe on the xz plane.
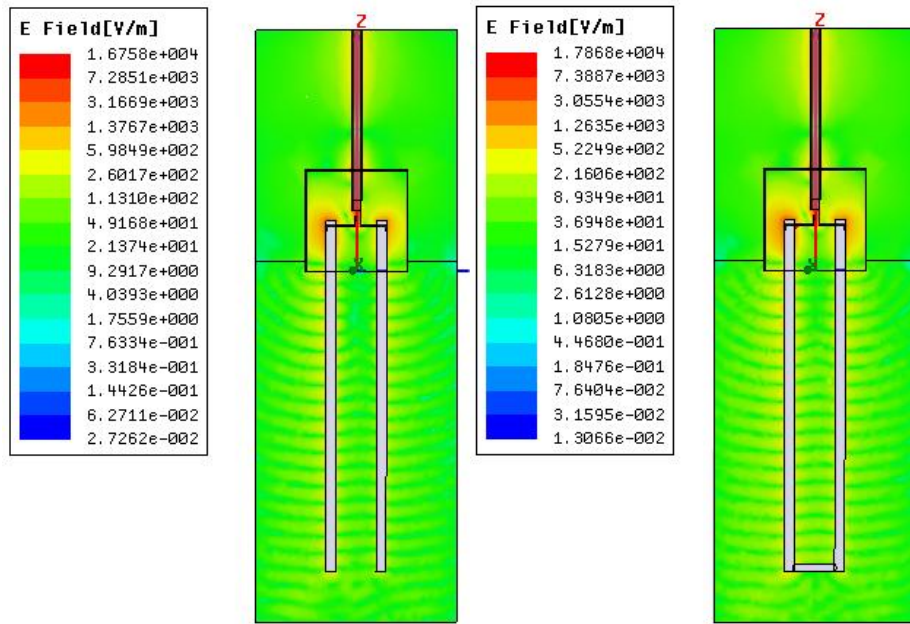
Fig. 5-6   E-field plots of a two-rod shielded TDR probe on the yz plane with probe ends open (left) and shorted (right).
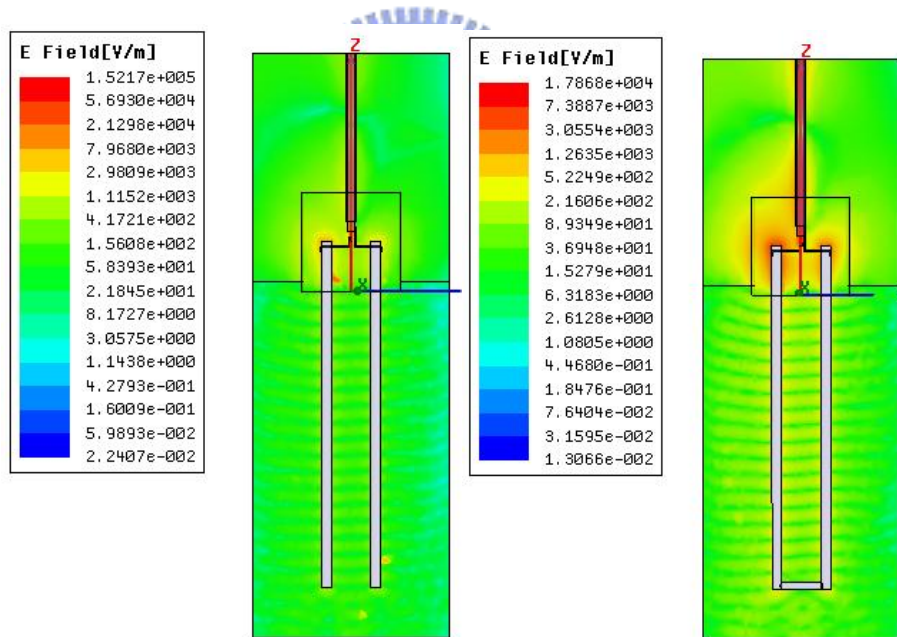
Fig. 5-7   E-field plots of a two-rod unshielded TDR probe on the yz plane with probe ends open (left) and shorted (right).

5.2 Sensitivity of Travel Time and EC Measurement

TDR probe contains two main geometric parameters: probe length L and impedance Z_p, which control the measurement of travel time and EC.   As mentioned above, measurement

sensitivity which is defined as the change of the measurement data due to variations of physical parameters, therefore, their effects on the sensitivity provide information for guidelines of probe design.

Sensitivity of Travel Time

According to the definition of the measurement sensitivity, the measurement sensitivity of travel time Δt can be derived from Eq. [2.38] as:

$$S_{traveltime} = \frac{d(\Delta t)}{dK_a} = \frac{L}{c\sqrt{K_a}}$$ [5-1]

From this equation, the measurement sensitivity of travel time is mainly controlled by the probe length L. Fig. 5-8 shows that the measurement sensitivity of travel time increases linearly with increasing probe length L, while it decreases as K_a increases. Therefore, it is obviously that increasing probe length helps hence the measurement sensitivity of travel time, and hence increase the resolution of K_a measurement; however, long probe will experience greater signal loss due to EC and may leads to the difficult for determining the end reflection Besides, longer probe has a greater sample volume along the probe direction, which implies lower spatial resolution. Therefore, aforementioned tradeoff should be considered for specific applications.
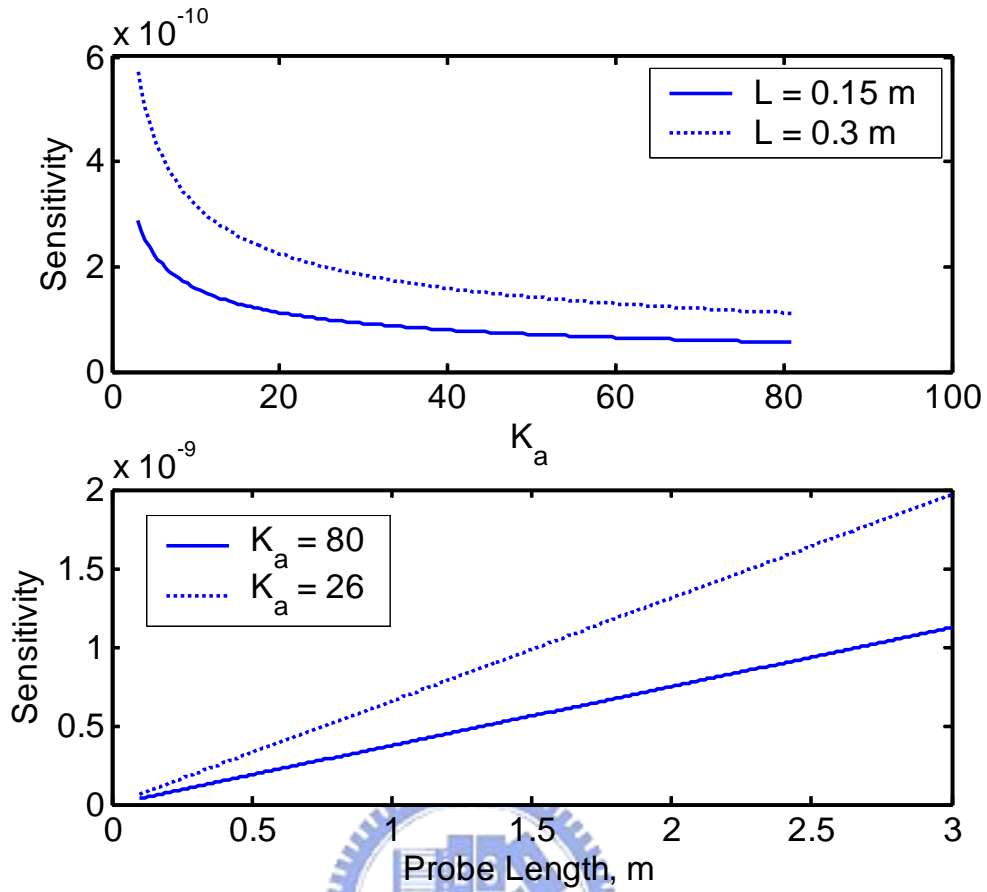
Fig. 5-8　The sensitivity of the travel time due to K_a and probe length

Sensitivity of EC

The TDR EC is determined by the reflection at steady state, thus the measurement sensitivity of EC can be derived by the derivative of the steady state reflection coefficient to the EC. According to the improved EC measurement equation as shown in Eq. [2-43], the measurement sensitivity of EC can be formulated as:

$$S_{EC} = \frac{d(\rho_{\infty,Scale})}{dEC} = \frac{-2\beta}{(EC+\beta)^2}$$

[5-2]

where the $\beta = K_p/Z_s$ is the probe constant, and $K_p = (\varepsilon_0 c Z_p)/L$.

As shown in the Eq. [5-2], both the probe length L and the geometric impedance Z_p plays

important roles on the EC measurement sensitivity. Fig. 5-9 shows the EC measurement sensitivity with a variety of probe length L and the geometric impedance Z_p, and the sensitivity is normalized by letting the sum of sensitivity vector be 1. Two conclusions can be drawn from Fig. 5-9 : (1) the EC measurement sensitivity monotonically decreases as EC increases, and (2) the EC measurement sensitivity increases as probe length increases (and Z_p decreases) when EC is below 0.005 S/m, but the trend switch a rough when EC is higher than 0.005 S/m. Therefore, the probe design for EC measurement should depend on the target range of EC measurements.
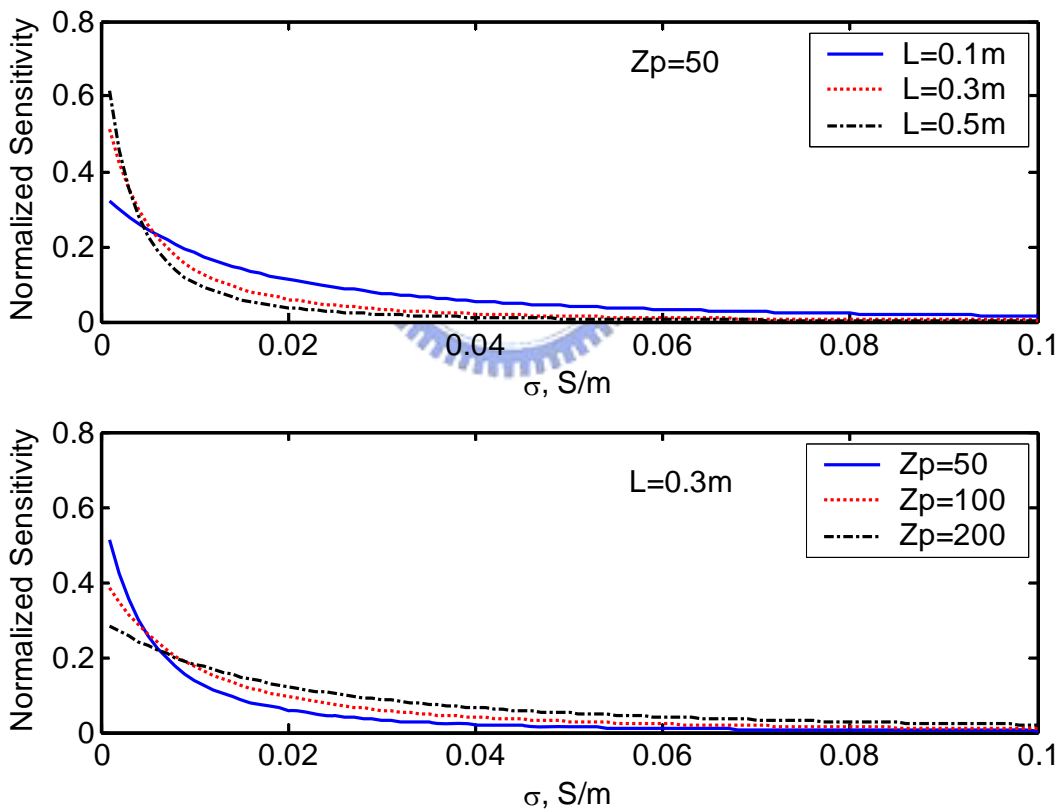
Fig. 5-9   The sensitivity of the EC due to probe length and impedance

5.3 Development of TDR Penetrometer

Electrical properties of a material include its electrical conductivity and frequency-dependent dielectric permittivity. Much laboratory and theoretical work has been done on the relation between soil electrical and physical parameters (Santamarina et al. 2001). These results encourage further development of field measurement techniques and more effective homogenization model for electrical properties of media. While laboratory and theoretical development continues to advance, electrical characterization in situ lags behind. Campanella and Weemees (1990) developed an electrical resistivity module in CPT using the four-electrode array under low frequency excitation. Several similar modules are now commercially available. However, interpretation of the resistivity alone for soil properties is difficult because it is sensitive to many factors, such as water content, soil type and ground water characteristics. CPT dielectric modules have been reported more recently for soil moisture measurements based on resonant frequency modulation or time domain reflectometry (Knowlton et al. 1995; Singh et al. 1997; Shinn et al. 1998; Young et al. 1999; Vaz and Hopmans 2001). On the contrary, these probes measure only the dielectric constant in a certain frequency range. To better characterize the soil electrically, both the resistivity (reciprocal of electrical conductivity) and dielectric permittivity in a wide band are desired. The spatial sensitivity and penetration effect of both resistivity and dielectric penetrometer should also be studied.

5.3.1   Probe Design of TDR Penetrometer
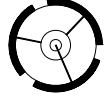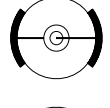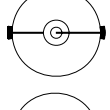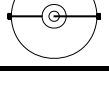
Standard waveguides or probes for TDR measurements are primarily of two types: coaxial type and multi-conductor type, as shown in Fig. 5-10(a) and Fig. 5-10(b). The coaxial type of probe is composed of a cylinder (C) acting as the outer conductor and a rod along the centerline of the cylinder acting as a central conductor. The multi-conductor type of probe is composed

of one or more rods acting as the outer conductors and a center rod as the inner conductor. The coaxial type of probe is adopted for laboratory measurements such as in the compaction mold or in a Shelby tube, using the cylinder as the outer conductor with the inner conductor being a steel rod inserted along the centerline of the soil in the mold. The multi-conductor probes can be used for in-place measurements. Conventional multi-conductor probes are 30 cm long and therefore difficult to insert at depths below one meter. In order to adapt the TDR technique to a cone penetrometer application, a new design is required for the probe. The multiple conductors are placed around a non-conducting shaft to form a TDR probe as shown in Fig. 5-10(c).

Also shown in Fig. 5-10 are the electrical potential distributions corresponding to the cross-sections of different probe types. The electrical field is contained in the C for a coaxial probe while it is open in a multi-conductor probe. Placing multiple conductors around a non-conducting shaft allows the waveguide to sense the material around the shaft. It should be noted that the material inside the shaft of the TDR cone penetrometer is different from the surrounding material to be measured by the probe design. Therefore, a new calibration procedure is requiredfor measurements of the apparent dielectric constant and electrical conductivity using the TDR penetrometer. Previous studies on two-conductor probes have shown that the unequal spatial weighting in the plane transverse to the probe is inherent in the TDR measurement and cannot be eliminated (Baker and Lascano, 1989; Knight, 1992). Hence, the probe should be designed to minimize the effect of the material inside the shaft and maximize the influence zone in the surrounding medium. A series of trial probes were constructed in the laboratory to determine the optimal configuration for the waveguide. The variables considered included the number of conductors and conductor width (or spacing). The PVC tubes were used as the shaft and copper strips as the waveguide conductors. The configurations of the trial probes are summarized in Table 5-1. A later section will present the

performance of these probes through laboratory investigations

Table 5-1   Probe types with different conductor configurations.

Type No.	Copper width (mm)	Copper length (mm)	No. of copper	Probe type
T1	20	200	4	
T2	30	146	3	
T3	20	200	2	
T4	10	200	2	
T5	3	200	2	
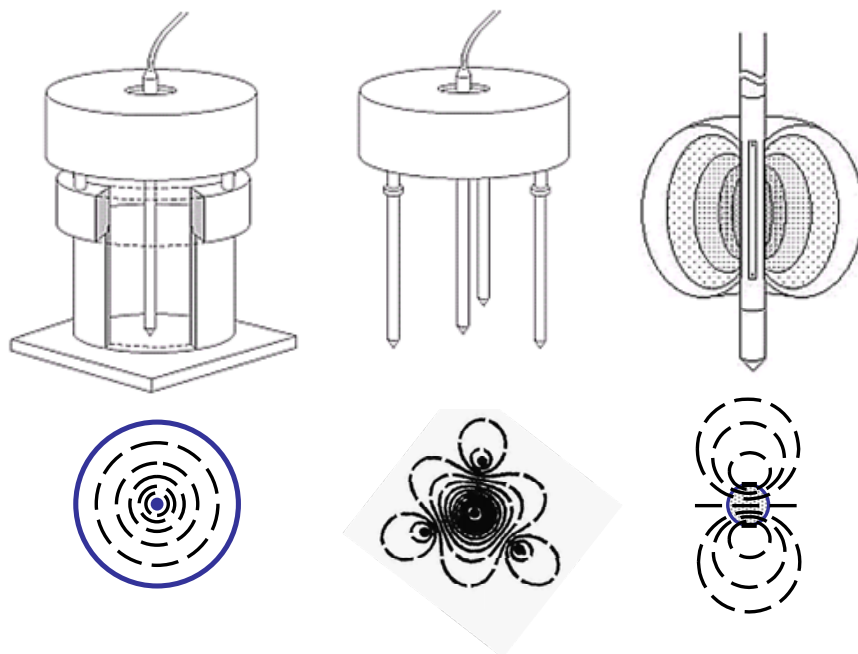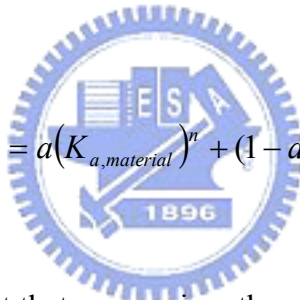
Fig. 5-10   Interpretation of the TDR waveform to determine apparent dielectric constant.

140

5.3.2 Calibration Method for K_a and EC

The dielectric constant measured by the penetrometer probe is a weighted average of the soil water medium dielectric constant and the dielectric constant of the probe material (derlin® and air)between the conductors. A new calibration equation was formulated to determine the dielectric constant of the surrounding material from travel time analysis of the waveform measured by TDR penetrometer. The derivation of the new calibration equation is based on a homogenization model proposed by Birchak et al. (1974). Using Birchak's exponential model, the effective (or measured) apparent dielectric constant ($K_{a,eff}$) may be written as a function of the measured material dielectric constant ($K_{a,material}$) and probe dielectric constant ($K_{a,probe}$). We have

$$\left(K_{a,eff}\right)^n = a\left(K_{a,material}\right)^n + (1-a)\left(K_{a,probe}\right)^n \qquad [5\text{-}3]$$

where n is an empirical constant that summarizes the geometry of the medium with respect to the applied electric field and a is a weighting factor of the surrounding soil. $K_{a,eff}$ in Eq. [5-3] is determined from TDR penetrometer measurement. The last term in Eq [5-3] can be lumped as an empirical parameter b, since the dielectric permittivity of the probe is a constant. Hence, the measured material dielectric constant may be determined from the TDR penetrometer measurement as
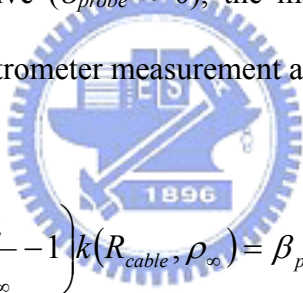
$$K_{a,material} = \left(\frac{\left(K_{a,eff}\right)^n - b}{a}\right)^{1/n} = \left(\frac{\left(\frac{cT}{2L}\right)^{2n} - b}{a}\right)^{1/n} \qquad [5\text{-}4]$$

where *n, a* and *b* are calibration parameters for the measurement of apparent dielectric constant using the TDR penetrometer.

Similarly, the probe material between the conductors affects the effective electrical conductivity. Following the same homogenization formulation, the effective (measured) electrical conductivity (σ_{eff}) is related to the material electrical conductivity ($\sigma_{material}$) and probe electrical conductivity (σ_{probe}) as

$$\left(\sigma_{eff}\right)^n = a\left(\sigma_{material}\right)^n + (1-a)\left(\sigma_{probe}\right)^n \tag{5-5}$$

According to the series resistors model and considering that the probe material between the conductors is not conductive ($\sigma_{probe} \approx 0$), the material electrical conductivity may be determined from the TDR penetrometer measurement as

$$\sigma_{material} = \frac{\left(\sigma_{eff}\right)}{a^{1/n}} = \frac{\beta}{a^{1/n}}\left(\frac{2}{\rho_\infty}-1\right)k\left(R_{cable},\rho_\infty\right) = \beta_{penetrometer}\left(\frac{2}{\rho_\infty}-1\right)k\left(R_{cable},\rho_\infty\right)$$

$$\tag{5-6}$$

where $\beta_{penetrometer}$ is the calibration parameter for the measurement of electrical conductivity using the TDR penetrometer. The new calibration equations (Eq [5-4] and Eq [5-6]) will be verified by experimental data.

5.3.3   Evaluation of TDR Penetrometer Performance

TDR Waveforms and Measurement Sensitivity

Time domain reflectometry measurements were made by attaching the TDR probe to a Tektronix 1502C via 2 m of 50-ohm coaxial cable fitted with 50-ohm BNC connectors at each

end. The multi-conductor penetrometer waveguides were submerged in a large tank (100cm*100cm*50cm) filled with tap water. Fig. 5-11 shows the TDR waveforms in water for waveguides with different numbers of conductors. Similarly, the waveforms in water for 2-conductor waveguides with different conductor width are shown in Fig. 5-12. The waveform of a coaxial probe is also shown in Fig. 5-11 and Fig. 5-12 for comparison. The length of the coaxial probe was 116 mm and the length of T2 was 146mm. All other probes were 200 mm. The TDR sends a step pulse down the cable and some of the wave energy is reflected from both the beginning and end of the probe as shown in Fig. 5-11 and Fig. 5-12. The first positive reflection is due to the impedance change at the connector between the cable and the probe. The sudden drop of the waveform resulting from the negative reflection occurs when the pulse enters the probe section. The second positive reflection occurs at the end of the probe. From a practical perspective, the data shown in Fig. 5-11 and Fig. 5-12 suggest any of the 5 probe configurations can be used to identify reflection points. However, as the number of conductors and conductor width increases, the impedance of the probe decreases and the negative reflection at the beginning of the probe increases, causing the waveform to drop down to a lower level. Hence, the reflection points in probe T1 are clearest. This becomes more obvious especially when the dielectric constant of the surrounding medium decreases (e.g. soils with low water contents).

The travel time T of the penetrometer probe is about 70% of that of the coaxial probe with the same length. All penetrometer probes perform similarly in this aspect. The effective dielectric constants ($K_{a,eff}$) measured by the probes listed in Table 5-1 are all near 41, which is approximately equal to ($K_{a,water}$+$K_{a,probe}$)/2, in which $K_{a,water}$ = 80 and $K_{a,probe} \approx 2$. $K_{a,probe}$ is the combination of dielectric constant of probe material, derlin® and air. Considering the theoretical value n=1.0, Eq. [5-3] can be simplified as

$$K_{a,eff} \cong \frac{K_{a,material} + K_{a,probe}}{2} \qquad \text{[5-7]}$$

for all probe configurations. Regardless of the waveguide configuration, the material inside the probe weights the same as the material surrounding the probe in K_a measurements.

Unlike the traveltime measurement, the asymptotic value of the reflection coefficient ρ_∞ depends on the impedance of the probe. As the number of conductors and conductor width increases, the impedance of the probe decreases and ρ_∞ decreases. Therefore, the effective electrical conductivity (σ_{eff}) can not be determined unless the constant α in Eq. [5-5] is known for the multi-conductor probe with conductor arrangement identical to the TDR penetrometer but without the cone shaft. However, the relationship between the effective electrical conductivity and electrical conductivity of the surrounding medium can be revealed by comparing the ρ_∞ value of the TDR penetrometer with that of the probe with the same conductor arrangement but without the cone shaft. The measurements in tap water showed that $\sigma_{eff} = 0.5 \; \sigma_{Tap\ water}$ and $\sigma_{probe} = 0$ (derlin® and air are nonconductive) for all probe types listed in Table 5-1. Considering the theoretical value $n = 1.0$, Eq. [5-5] can be simplified as

$$\sigma_{eff} \cong \frac{\sigma_{material} + \sigma_{probe}}{2} \qquad \text{[5-8]}$$

Regardless of the waveguide configuration, the material inside the probe also weights the same as the material surrounding the probe in σ measurements.

The material surrounding the TDR penetrometer contributes 50% to the effective dielectric constant and electrical conductivity. This percentage can not be increased by changing the conductor configuration. Placing multiple conductors around a non-conducting shaft allows the waveguide to sense the material around the shaft at depths, but decreases the

sensitivity of dielectric and conductivity measurements. The measurement sensitivity is defined here as the derivative of the TDR response (i.e. the T or ρ_∞) with respect to the dielectric constant or electrical conductivity of the material under test. The sensitivity of the TDR penetrometer is about 70% of the coaxial or conventional multi-conductor probes. This reduction in sensitivity is acceptable in practice.
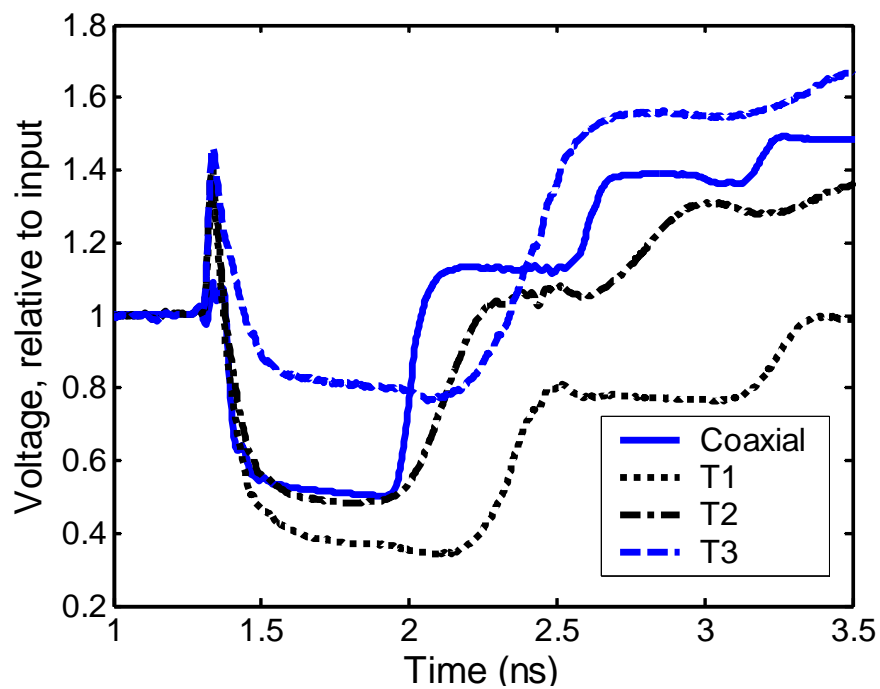
Fig. 5-11   The TDR waveforms of probes with different number of conductors.
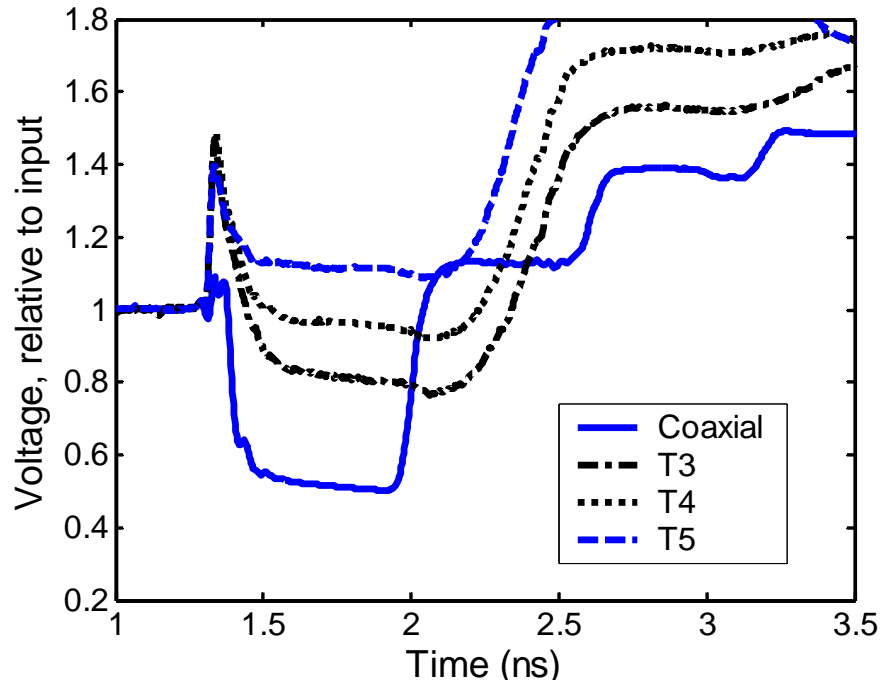
Fig. 5-12   The TDR waveforms of probes with different conductor spacing (width).

Weighting function for travel time and EC measurements

The radial sampling of TDR measurements using the TDR penetrometer may be investigated using electromagnetic field theory.   Alternatively, an experimental approach was taken since the theoretical derivation is complicated and also needs to be verified experimentally.   In order to investigate the radial sampling of the TDR penetrometer, the trial probes were submerged in water-filled PVC tubes of different diameters.   Fig. 5-13 illustrates the cross section of the testing arrangement in the plane transverse to the probe.   The material surrounding the TDR penetrometer is a composite medium with tap water located concentrically around the center rod and air outside the PVC pipe.   The dielectric constant of the PVC material is close to that of air, so the inner diameter of the PVC tube can be considered as the boundary between tap water and air.   Since the dielectric constants of water and air lie in the two opposite extremes ($K_{a,wate}$=80 and $K_{a,air}$= 1.0) the "spatial weighting function" for K_a and σ may be defined experimentally as

146

$$F(r) = \frac{K_{a,r}}{K_{a,eff}} \times 100\% \qquad\qquad [5\text{-}9a]$$

$$F(r) = \frac{\sigma_r}{\sigma_{eff}} \times 100\% \qquad\qquad [5\text{-}9b]$$

where $K_{a,r}$ and σ_r the effective dielectric constant and electrical conductivity measured in a water-filled PVC tube with inner diameter r, respectively, and $K_{a,eff}$ is the effective dielectric constant measured in a large water-filled tank. $K_{a,eff}$ is representative of the effective dielectric constant measured in a water-filled PVC tube with inner diameter $r = \infty$. It is applicable for electrical conductivity.

The K_a spatial weighting functions for different probe configurations are also shown in Fig. 5-13. The effective dielectric constant approaches an asymptotic value at a distance of 100 mm and greater. The majority of the electromagnetic response occurs within the first several centimeters in the radial direction. The four-conductor probe (T1) and three-conductor probe (T2) have similar spatial weighting functions; and the spatial weighting appears to be insensitive to the conductor width for the two-conductor configuration (see T3, T4, and T5). In K_a measurements, the radial sampling of the four-conductor probe (T1) and three-conductor probe (T2) is more focused on the vicinity of the probe than that of the two-conductor probes (T3, T4, and T5).

Unlike dielectric permittivity, effective electrical conductivity is a directional and conductive parameter that depends on current flow paths and distribution of conductivity variation. Defining a unique radial sampling function for the electrical conductivity measurement is not possible. To compare the radial sampling of different probes, a spatial weighting function for electrical conductivity analogous to Eq. [5-9b] was experimentally defined using the same PVC-tube experiments depicted in Fig. 5-14. The tap water inside the

PVC tube was conductive with σ = 0.67 dS/m and the PVC material and air were considered non-conductive (σ = 0 dS/m). The σ spatial weighting functions for different probe configurations are shown in Fig. 5-14. In this case, the radial sampling is even more biased towards the probe for σ measurements than for K_a measurements. On the contrary to dielectric measurement, theσ radial sampling of the four-conductor probe (T1) and three-conductor probe (T2) is less focused on the vicinity of the probe than that of the two-conductor probes (T3, T4, and T5). Observations from Fig. 5-13 and Fig. 5-14 raise the concern for the penetration (disturbance) effect on K_a and σ measurements in soils. The soil displaced by the penetrometer may change the density of soil adjacent to the penetrometer, and hence the dielectric constant and electrical conductivity. The penetration effect appears to be a common problem to all electrical probes, and the degree of its influence should be quantified.
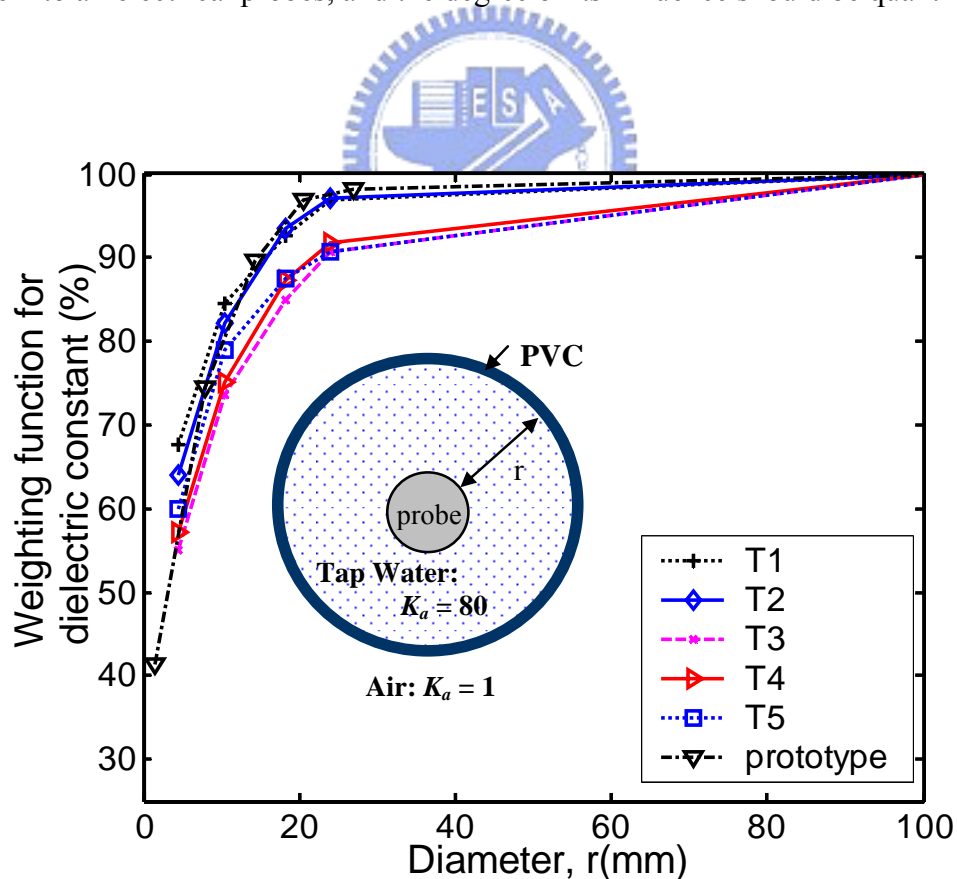
Fig. 5-13   Spatial weighting function for dielectric constant K_a.
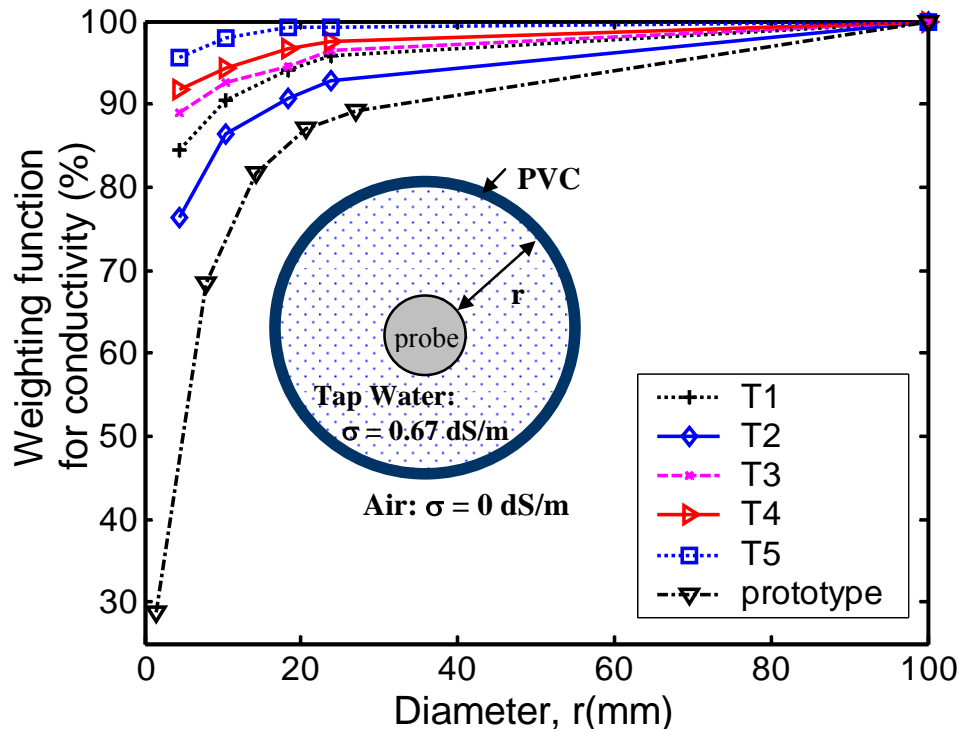
Fig. 5-14   Spatial weighting function for electrical conductivity σ.

TDR penetromter Prototype

The spatial weighting functions of different probe types have different trends in dielectric constant and conductivity measurements, as shown in Fig. 5-13 and Fig. 5-14.   There is a tradeoff between selecting an optimum probe design for dielectric measurements and that for conductivity measurements.   A TDR dielectric penetrometer was actually fabricated using the design similar to probe T1.   It was selected at the time when the major concern was to have TDR reflection that can be identified most easily for all cases (i.e. from dry to wet soils).   Fig. 5-15 shows the design and a photo of the probe.   The diameter of the prototype is the same as a standard CPT module (35 mm) and the sensing waveguide is 20 cm long.   The probe consists of four arc-shape stainless steel plates and a Delrin® shaft.   The thickness of the stainless steel was maximized to increase the axial strength of the probe.   The stainless steel plates were fit into four grooves in the Delrin® shaft and fastened with screws.   This probe was used to

perform simulated penetration tests in a calibration chamber.
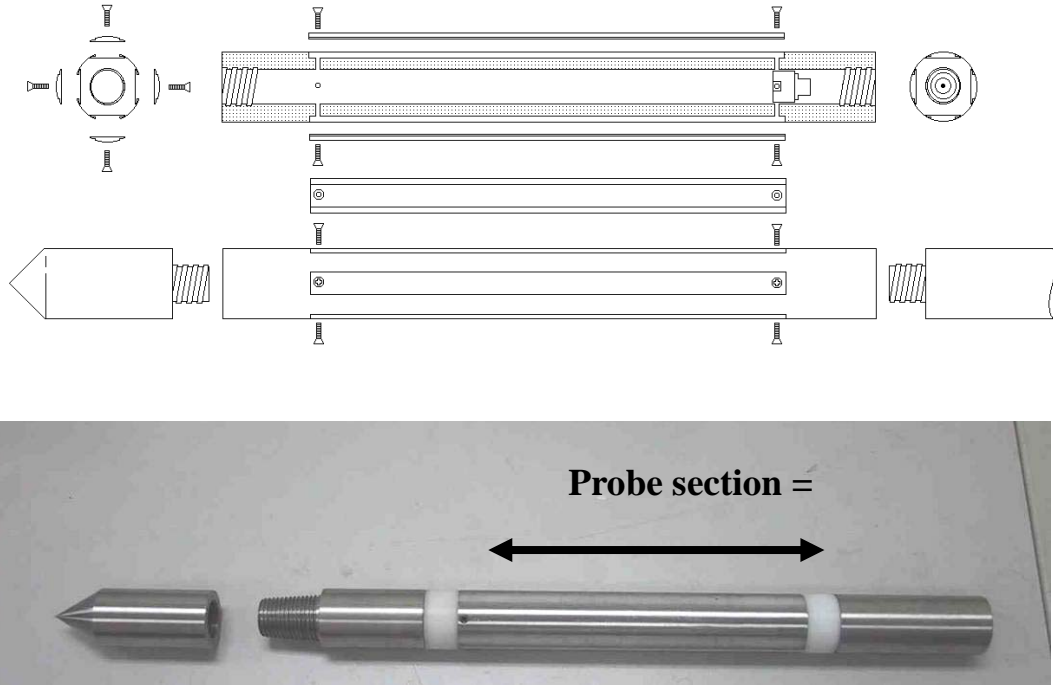
Fig. 5-15   Prototype of the TDR penetrometer

Calibration of the Prototype

The TDR penetrometer shown in Fig. 5-15 differs slightly from probe T1 in that thick conductors are embedded in a dielectric shaft instead of thin conductors bonded to the surface of the dielectric shaft. Calibration tests need to be carried out before it can be used for measurements of dielectric constant and electrical conductivity. Several liquids of known dielectric constants and electrical conductivities were used for calibrating the probe using Eqs. [5-4] and [5-6]. The materials used for calibrating dielectric measurements were air, butanol, ethanol, and water; while NaCl solutions of different concentrations were used for calibrating electrical conductivity measurements. According to Birchak et al. (1974), the theoretical value of *n* is 1.0 for the probe design. Assuming theoretical value *n* =1.0, the calibrated parameters *a* = 0.34 and *b* = 1.91 were obtained through linear regression. If *n* remained

unknown during calibration, the calibrated parameters are $a = 0.35$, $b = 1.78$, and optimal $n = 0.96$. Note that the a value is smaller than 0.5 (suggested by Eq. [5-7]), because the prototype used thick conductor plates fit into Delrin® grooves rather than thin conductor plates stick on the surface of a dielectric shaft. Using the calibrated parameters, the apparent dielectric constants of the calibrating liquids are plotted against their known values in Fig. 5-16. Both calibrated results provide fairly good fit. The theoretical value $n = 1.0$ is verified, as can be inferred from Fig. 5-16. For simplicity, $n = 1.0$, $a = 0.34$, and $b = 1.91$ are used. Similarly, the calibration constants for electrical conductivity were obtained as $\beta_{penetrometer} = 0.0362$. The estimated electrical conductivities using the calibrated parameters are shown in Fig. 5-17 to fit the known values very well. These results prove the new calibration equations (Eqs. [5-4] and [5-6]) to be extremely accurate.
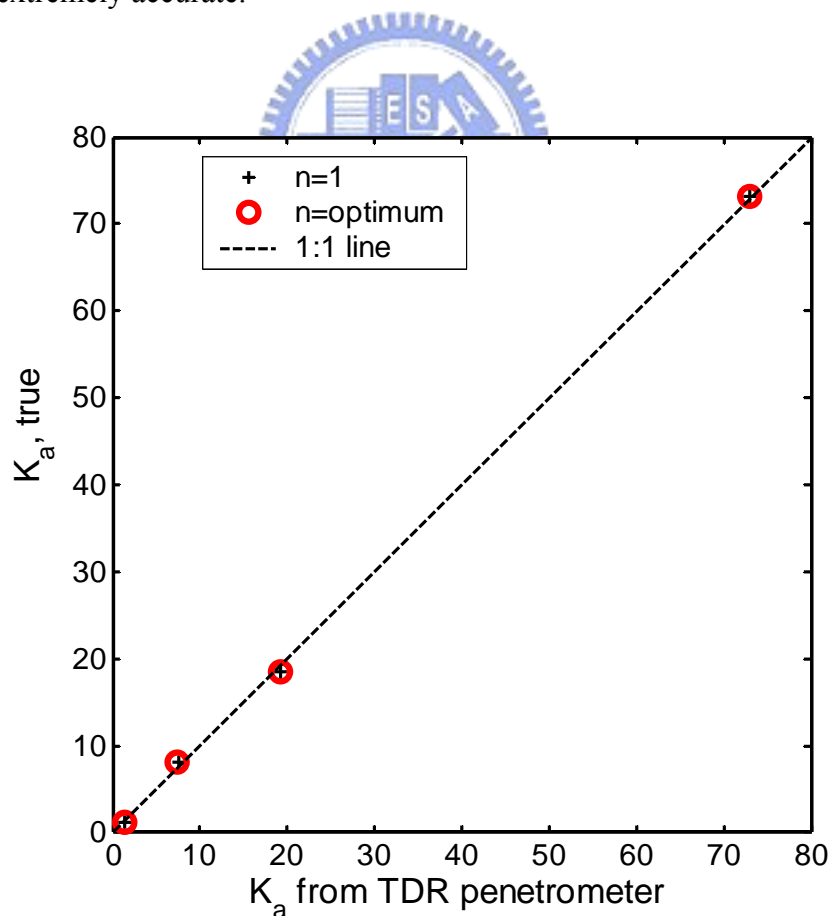
Fig. 5-16 K_a calibration of TDR penetrometer with known values materials
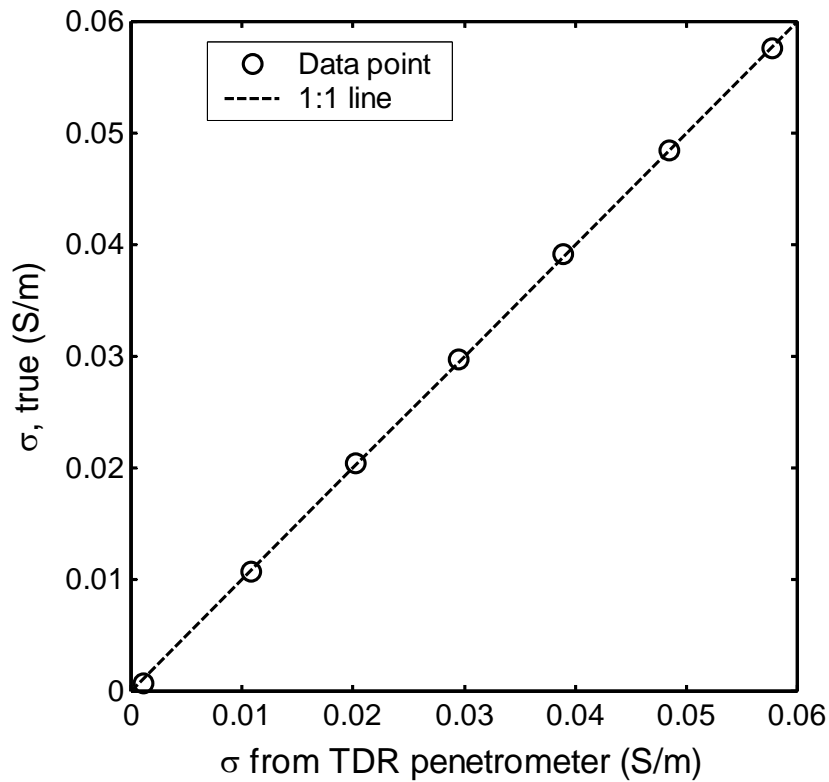
Fig. 5-17 σ calibration of TDR penetrometer with known EC liquids

Spatial Weighting Function of the Prototype

To quantify the spatial weighting function of the prototype, the aforementioned radial sampling experiment was carried out on the prototype.   The spatial weighting function of the prototype is also shown in Fig. 5-13 for K_a measurements and in Fig. 5-14 for σ measurements. The K_a radial sampling characteristic of the prototype is similar to that of the trial probes T1 and T2.   However, the σ radial sampling of the prototype is much less focused on the vicinity of the probe than that of all trial probes (T1-T5).   This may be attributed to the fact that the prototype used thick conductor plates fit into grooves of a dielectric shaft rather than thin conductor plates attached to the surface of a dielectric shaft.   This configuration alters the distribution of the electromagnetic response, further decreasing the measurement sensitivity but making the σ radial sampling less biased towards the probe.

5.3.4   Simulated Penetration Tests

To test the penetrometer and study the penetration effect, simulated penetration tests were performed in the laboratory using a calibration chamber and hydraulic loading frame. The chamber was 45 cm in inner diameter and 40 cm in height. A silty sand (SM) was used for the simulated penetration tests. Seven different gravimetric water contents were used to prepare samples in the chamber. The soil and water were mixed thoroughly to obtain the desired water content. The mixed soil was sealed with plastic wrap and allowed to equilibrate for more than 24 h, to yield a uniform soil specimen. The soil was then compacted in the calibration chamber in layers and the total mass of the soil and chamber was measured. The gravimetric water content of the soil specimen ranged from 2% to 10% and the dry density ranged from 1.58 to 1.67 g/cm^3.

Two TDR measurements were taken. Simulated penetration test was first conducted by penetrating the TDR penetrometer at the center of the chamber. No surcharge was applied to the soil specimen but a cap was placed on top of the chamber to prevent the soil from heaving during penetration. Hence, the soil around the penetrometer was slightly densified during penetration. After the penetrometer was retracted, another TDR measurement was taken at the location between the penetrated hole and the chamber cylinder using a conventional multi-rod probe (MRP) similar to Fig. 5-11b. The diameter of the multiple rods is 9.5 mm and the spacing between the center conductor and outer conductors is 65 mm. The MRP mimics a coaxial probe in which the electromagnetic field is concentrated around the central rod. The effect of penetration on TDR measurements using the MRP is considered negligible (Siddiqui et al., 2000). Comparing the measurements of TDR penetrometer with that of MRP can reveal the effect of penetration. After all the TDR measurements were taken, samples of the soil were oven-dried to determine the gravimetric water content. The volumetric water content (θ) of each soil sample was determined from the total density and gravimetric water content.

Dielectric properties - θ relationship

TDR measurements show that both dielectric constant and electrical conductivity increase with water content. A good linear relationship between $\sqrt{K_a}$ measured by the TDR penetrometer and the volumetric water content (θ) exists as Fig. 5-18 shows. The $\sqrt{K_a}$-θ relationship was shown by Topp et al. (1980) to be relatively independent of soil type and electrical conductivity of pore water. The correlation between $\sqrt{\sigma}$ and θ also shows great linearity. But the $\sqrt{\sigma}$-θ relationship is greatly affected by soil type and pore water electrical conductivity. Therefore, apparent dielectric constant can be used for measuring volumetric water content (or void ratio when the soil is saturated). The electrical conductivity can then provide additional information for determining the characteristic of the pore water. The correlation between $\sqrt{\sigma}$ and θ also shows great linearity in Fig. 5-19. Unlike the $\sqrt{K_a}$-θ relationship, the intercept and slope of the $\sqrt{\sigma}$-θ relationship depend on the soil type and electrical conductivity of pore water. Soil water content can be estimated by the K_a measurement alone, electrical conductivity and future study on dielectric dispersion can provide extra information for characterizing soil type and pore water.
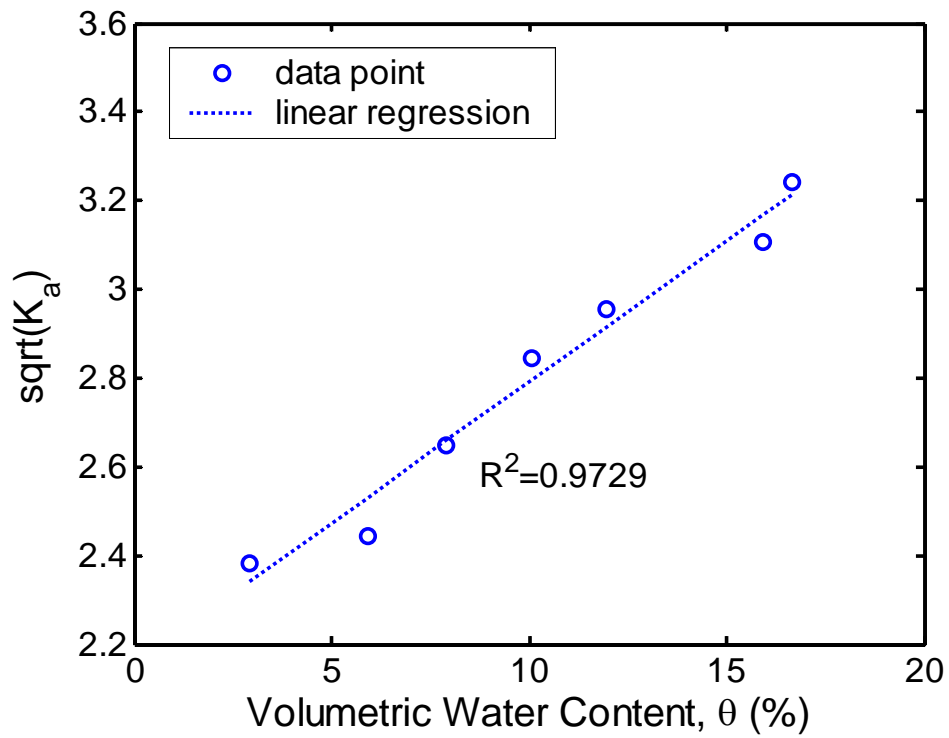
Fig. 5-18   Correlation between $\sqrt{K_a}$ and volumetric water content
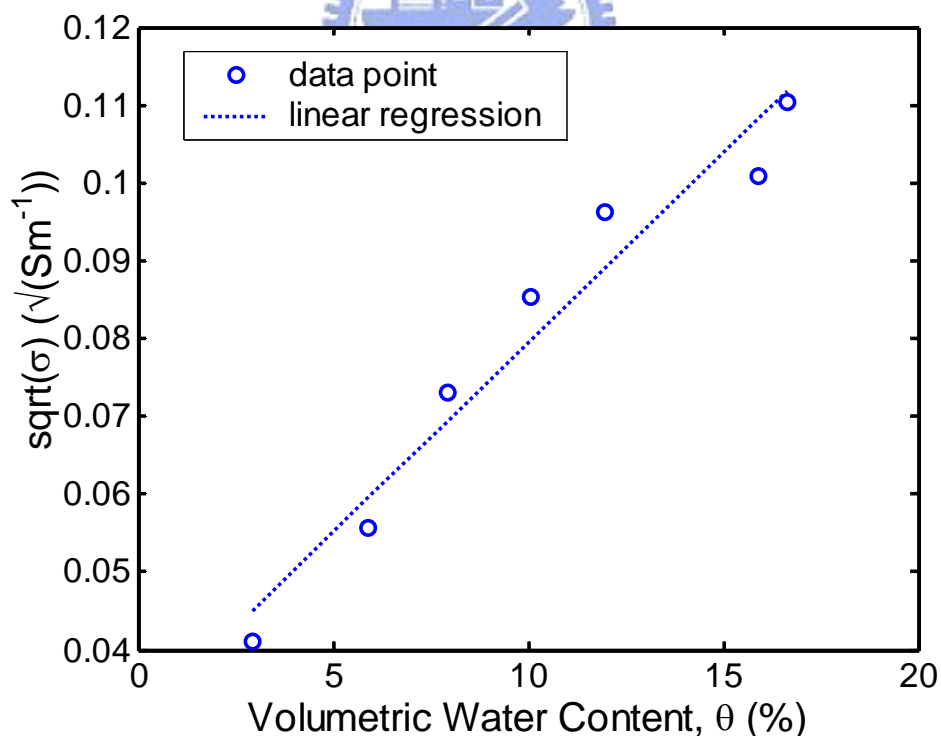
Fig. 5-19   Correlation between $\sqrt{\sigma}$ and volumetric water content

Penetration Effect

In addition to measurements using the TDR penetrometer, TDR measurements were also performed using a 4-rod MRP probe (measurements which were much less disturbed). Fig. 5-20 shows the comparison for K_a measurements. The effect of penetration can be noticed in K_a measurements as expected. K_a increases as soil density increases due to penetration because the volumetric water content increases with density when gravimetric water content remained unchanged. This increase in apparent dielectric constant depends on the degree and extent of the soil densification. As the original soil density increases, the densification due to penetration is less significant but the disturbed zone becomes larger. Therefore, the K_a measurement is less affected by the penetration effect for dense soil than for loose soil. This can explain the effect of penetration shown in Fig. 5-20. The soil samples prepared for the simulated penetration tests were compacted at dry side of optimum. At dry side, the density increases as gravimetric water content, and hence the apparent dielectric constant, increases. Therefore, the penetration effect is more pronounced for the soil with lower K_a, as Fig. 11 shows. In summary, the penetration effect induces a coherent K_a error which increases with decreasing soil density. For the soils tested (dry density ranging from 1.58 to 1.67 g/cm3), this error is within the uncertainty associated with the $\sqrt{K_a}$-θ correlation. But caution should be taken when performing tests in looser soils.

Fig. 5-21 compares electrical conductivity measured by the prototype TDR penetrometer with that by the MRP probe. Unexpectedly, coherent errors due to penetration effect are not noticeable in σ measurements. The radial sampling is less focused on the vicinity of the probe for σ measurements, as shown by comparing Fig. 5-14 to Fig. 5-13. However, this difference can only partly explain the unnoticeable penetration effect. The σ spatial weighting function was experimentally defined by the PVC-tube experiment. This spatial weighting function was valid strictly only for the condition shown in Fig. 5-14. In actual soil measurements, the

conductivity variation due to penetration is smooth. It is believed that the actual radial sampling is much greater than that shown in Fig. 5-14, resulting in an unnoticeable penetration effect
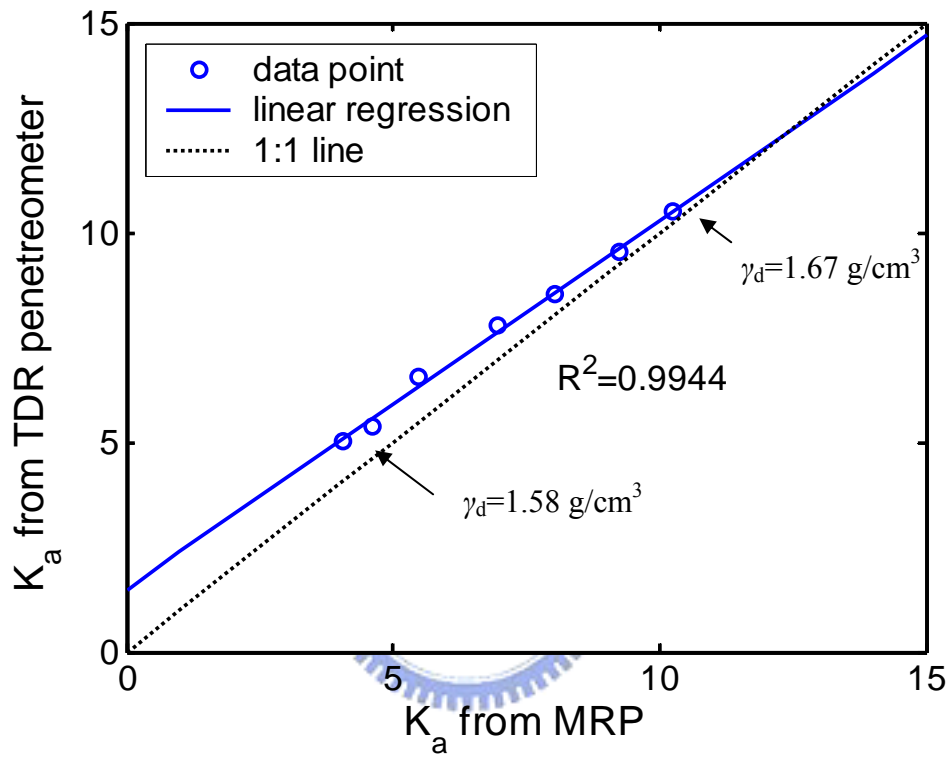
Fig. 5-20 The K_a obtained from TDR penetrometer vs. that from MRP
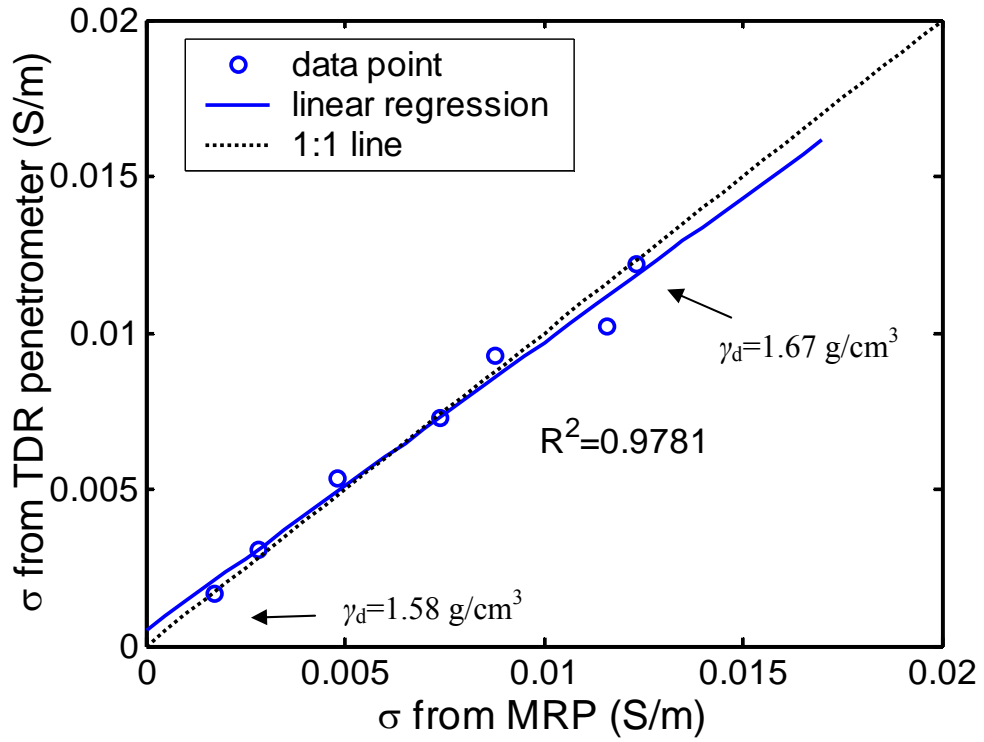
Fig. 5-21   The electrical conductivity obtained from TDR penetrometer vs. that from MRP

6 Applications: Characterization of Soil-water Mixture

6.1 Introduction

Shihmen Reservoir is a multi-purpose water resources project, for irrigation, power generation, water supply, flood control and tourism.   The Shihmen Dam is an earth-filled dam situated at approximately 50 km south east of Taipei.   Since plugging of the diversion tunnel in May, 1963, the hydro-project has made significant contributions to northern Taiwan in agricultural production, industrial and economic developments, as well as alleviating flood or drought losses.   The watershed of Shihmen Reservoir has characteristics of being steep in slopes and weak in geologic formations.   As a result, during heavy storms, severe surface erosions coupled with land slides often occur.   Since its completion in 1963, reservoir siltation has gradually increased, in spite of measures taken on dredging and construction of sediment retention structures.   The reservoir was designed to have a total storage of 309 million m^3 (volume of water that can be stored in the reservoir) and an effective storage of 252 million m^3 (volume of water above the intake level).   As of March of 2004, the total storage had been reduced to 253 million m^3 and the effective storage was 238 million m^3.   Aere Typhoon invaded northern Taiwan in August, 2004.   The event caused an average rainfall of 973 mm in the watershed which resulted in a total landslide area of 854 hectares, and an estimated inflow of approximately 28 million m^3 of sediments into the Reservoir.

Due to aforementioned risks of sedimentation in Shihmen reservoir, there are two problems occur after by.   The first one is that the intake valve of the hydro power plant was covered by 10 m of sediment.   The other is the requirement of monitoring for suspended sediment concentration during typhoon or deluge.   However, the traditional techniques for such purposes are limited in measurement range and durability, such as optical and acoustic sensors, while TDR provides an alternative solution, especially on the soil-water mixture

characterization. Therefore, two applications of soil-water mixture characterization using TDR are presented in this chapter, and the objectives are listed as: (1) Establishing the relationships between electrical properties and sediments concentration with TDR technique, and evaluate the TDR penetrometer performance for basal sediment characterization; (2) Development a high resolution method for monitoring suspended sediment concentration in reservoir area.

6.2 Characterization of Basal Sediment

The intake valve with its center at approximately 70 m below design water surface level was originally designed to be operated in clean water. In order to evaluate if the control mechanism had sufficient power to safely lift the intake valve, it was necessary to know the density state of the sediment and the lateral pressure exerted on the intake valve. Because of the significant amount of revenue involved in power generation, the reservoir operator was eager to obtain the necessary parameters for their decision making.

The bottom mud was expected to have consistencies ranging from close to liquid to as stiff as medium dense silt. The Marchetti dilatometer (DMT) (Marchetti, 1980) with its pointed blade can easily penetrate into the bottom mud, using the weight of the drill rods. The material density and its ratio to that of water, γ or γ/γ_w can be inferred through DMT modulus (E_D) and material index, I_D as shown in Fig. 6-1. The time domain reflectometry (TDR) on the other hand, can be used to estimate the concentration of sediment (or density of the bottom mud) through dielectric constant and electrical conductivity measurements. The correlation between TDR readings and concentration of sediment is most desirable when γ/γ_w is less than 1.5. Thus, a combination of DMT and TDR should compliment each other and serve the purpose as a hybrid testing device.

After a brief description on the principles of TDR, the study presents field set up of the

TDR/DMT probe, the test results and their interpretation.

SOIL DESCRIPTION
and ESTIMATED γ/γ_w
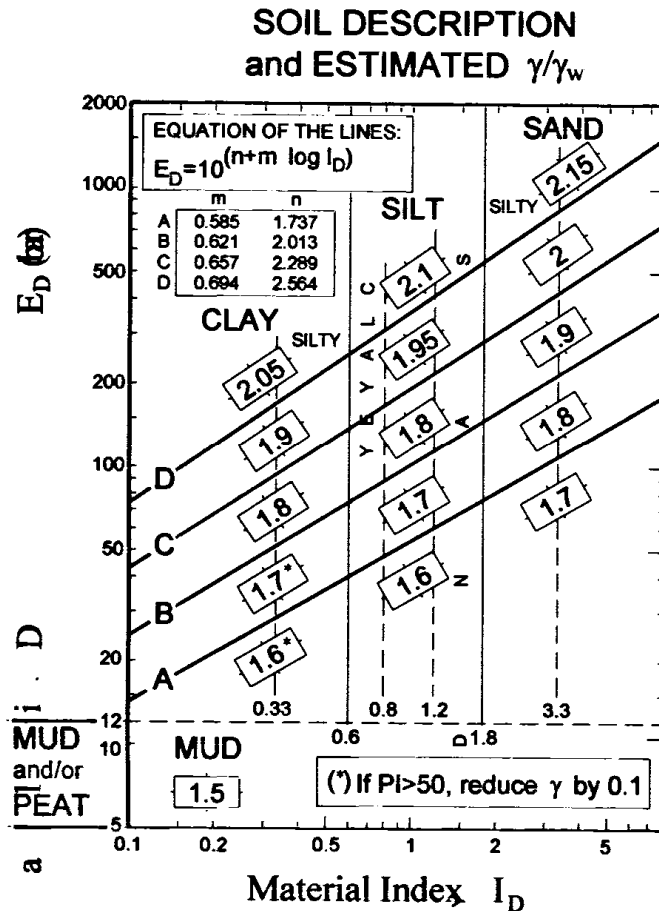
Fig. 6-1   Soil classification and density estimation based on DMT (after Marchetti and Crapps, 1981)

6.2.1 K_a/EC─Sediment Concentration Relationship by TDR Penetrometer

Sediment concentration may be measured electrically based on the relationship between the sediment concentration and electrical properties.   Because of the permanent dipole of the water molecule, the dielectric constant of water is very high.   Dry soil is only polarizable by atomic and electronic polarization, leading to a low dielectric constant.   This difference makes it possible to measure the sediment concentration by determining the dielectric constant of the soil-water mixture.   Sediment samples were taken from the Shihmen reservoir to conduct calibration tests for sediment concentration.   Fig. 6-2 shows the relationship between the K_a and sediment concentration in ppm (parts per million or mg/l).   The dielectric constant method

161

is more suitable for determining high sediment concentration. When the sediment concentration is below 30,000 ppm, the K_a readings tend to fluctuate significantly. A more sensitive and consistent relationship between the electrical conductivity and sediment concentration can be found, but the relationship is affected by water salinity. The experimental results reveal a unique relationship between the electrical conductivity and sediment concentration if the electrical conductivity of water phase (σ_w) is subtracted from the electrical conductivity of the soil-water mixture (σ), as shown in Fig. 6-3. The gaining EC may be due to the surface conduction, or diffusion double layer, of sediment particle as the sediment concentration increases (Mitchell, 1993). For better sensitivity, the sediment concentration is determined from electrical conductivity in this study. As shown in Fig. 6-3, however, when sediment concentration exceeds 10,000 ppm, there is no linear correlation between sediment concentration and electrical conductivity.
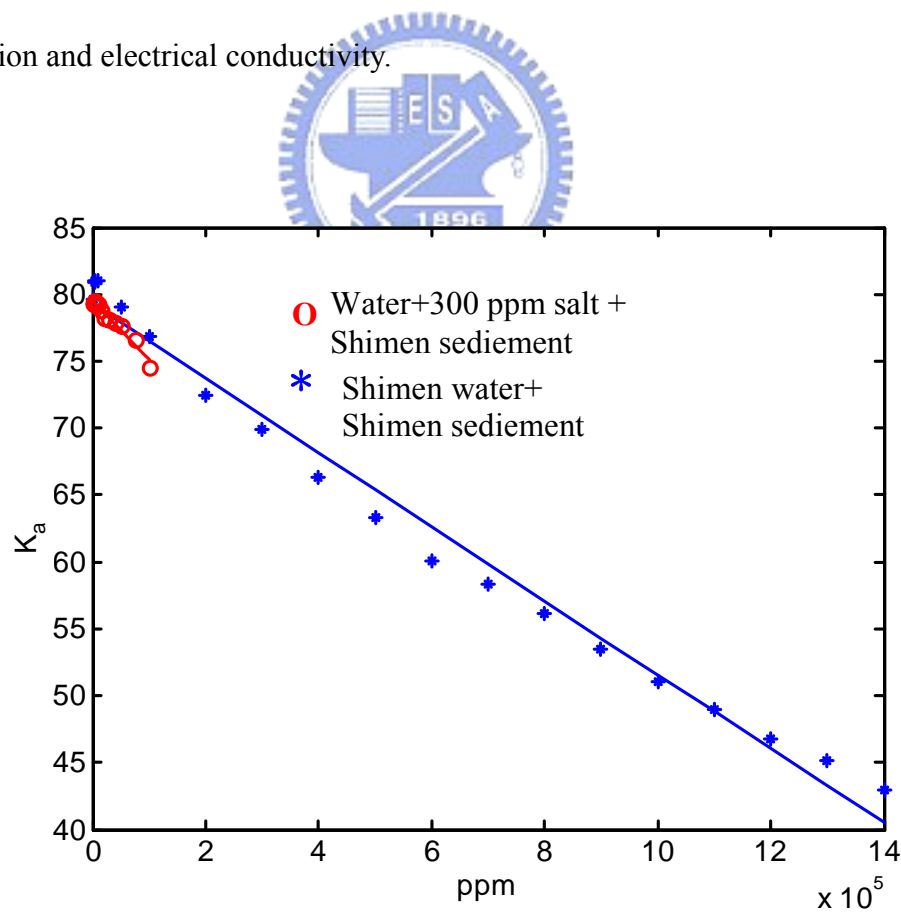
Fig. 6-2   Relationship between dielectric constant and sediment concentration
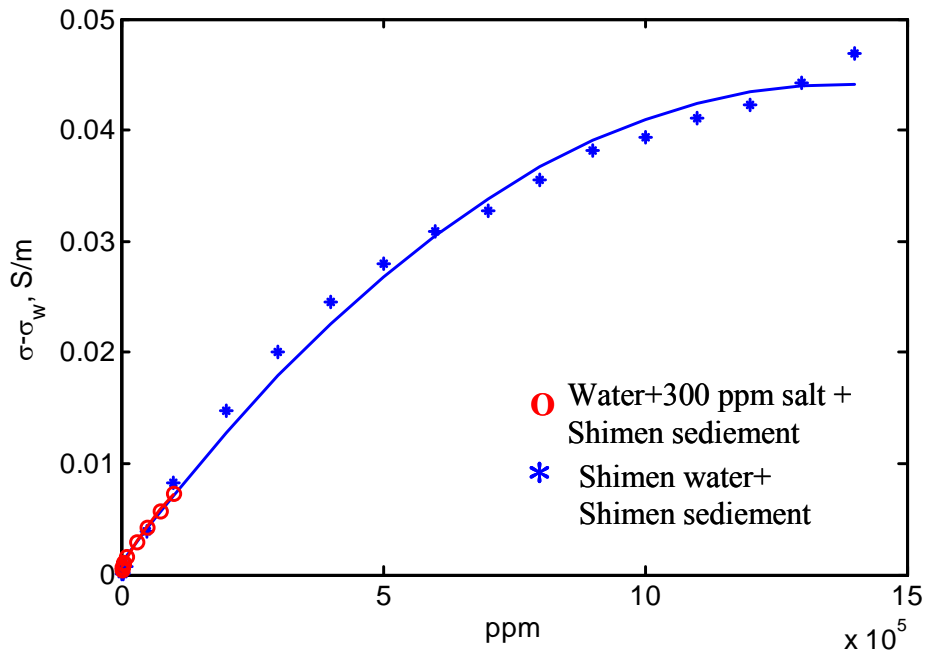
Fig. 6-3   Relationship between electrical conductivity and sediment concentration

6.2.2   Field Testing

Field Operation of TDR/DMT

In this study the TDR penetrometer waveguide was fitted immediately behind the DMT blade as shown in Fig. 6-4.   The DMT electric/pneumatic tubing passed through the inside of the hollow TDR penetrometer waveguide. The TDR/DMT probe was attached to 90 m long A rods.   The A rods had a total weight of approximately 900 kg, enough to offset the buoyancy and provide reaction force to penetrate the TDR/DMT probe 10 m into the sediment.   A portable drill rig mounted on a barge was used to hold the drill rods from the water surface as shown in Fig. 6-5.   The DMT tubing along with the TDR co-axial cable were threaded to the outside of the A rods through an adaptor and then connected to their respective control unit on the barge.   The function of the drill rig was to hang the drill rods and passively let them be lowered instead of pushing the drill rods.   Thus, the arrangement should avoid the potential problem of buckling the drill rods.   The relative position of the drill rig in relation to a

reference point on the dam crest was determined with a total station.   The barge was fixed to a rather massive dredging boat which was in turn fixed to the shore with cables.   All drainage tunnels of the reservoir were shut down during TDR/DMT tests to prevent fluctuation of the water surface elevation.   With these arrangements, the barge vertical movement during a single DMT is expected to be less than 30 mm.

The water surface was at an elevation of 244 m at the time of field testing.   A total of 10 profiles were conducted, five of them used the TDR/DMT probe (numbered TDR/DMT-1 to TDR/DMT-5), and the other five profiles used DMT only (numbered DMT-1 to DMT-5).   Fig. 6-6 presents a location diagram of all the DMT and TDR/DMT operations.   In plan view and at water surface level, the test locations were at 50 m to as much as 130 m from the shore line. The power plant inlet was located on the surface of a natural rock formation with a slope of approximately 2 (vertical):1 (horizontal).   The DMT readings started at elevation 185 m, TDR tests began at elevation 235 m, all tests ended at elevation 160 m.   Thus, the bottom of the penetration could be as close as 10 m from the rock surface.   The test interval varied from 5 m in clean water to 20 cm in dense sediment.   This arrangement prevented any possibility of water leakage and provided an opportunity to calibrate the DMT p_o readings against the hydrostatic pressure (u_o) in clean water while lowering the DMT.
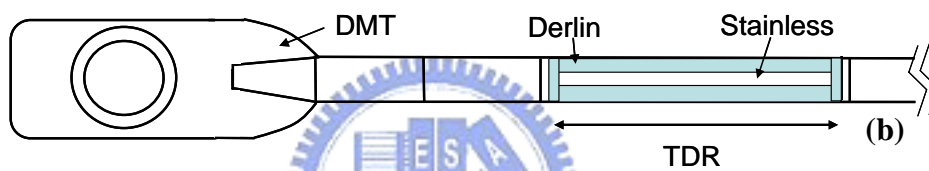
Fig. 6-4   (a) The photo of TDR/DMT probe and (b) the schematic illustration of TDR/DMT probe

Fig. 6-5   Operation of TDR/DMT from a barge
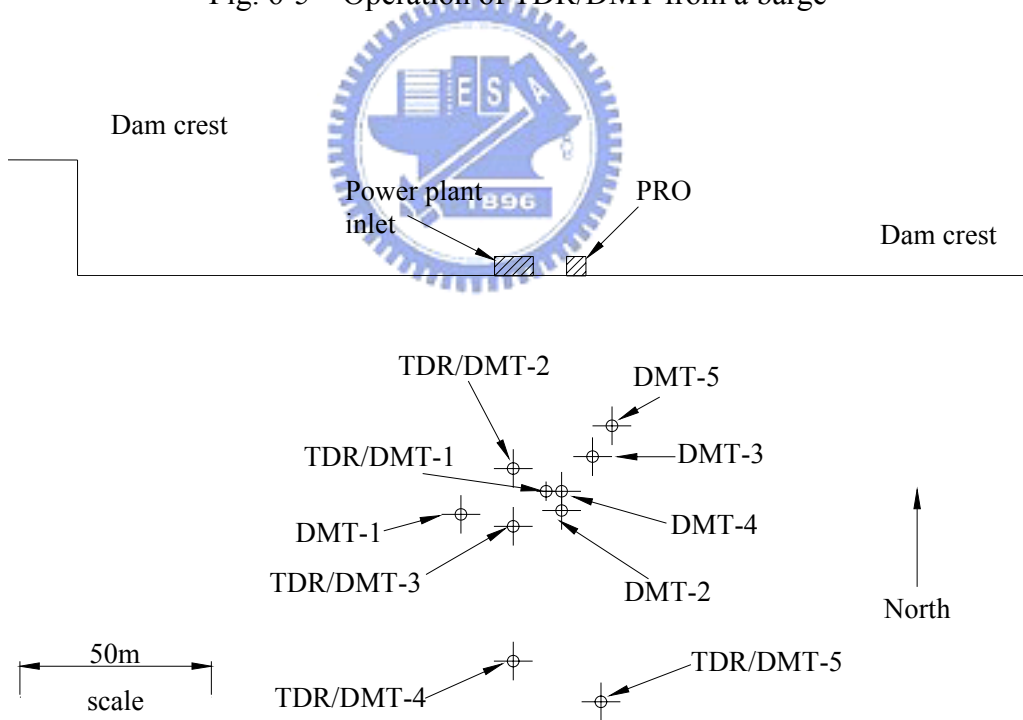
Fig. 6-6   The test locations

Interpretation of Test Results

Fig. 6-7 shows a series of waveforms recorded in TDR/DMT-3, of reflection coefficient versus the sequential number of data points.   At elevation 212.5 m, TDR was in clean water, the waveform at elevation 182.5 m indicated that the TDR had entered bottom mud.   The depth or elevation of all the TDR and DMT was referred to the center of the DMT blade.   The reflection coefficient towards the end of the record where the reading had reached a stable value was referred to as the terminal value, $V_{r, \infty}$.   A laboratory calibration between $V_{r, \infty}$ and (σ-σ_w) at various sediment concentrations was conducted using the sediment and water collected from the test location.   With the $V_{r, \infty}$ - (σ-σ_w) correlation and relationship between (σ-σ_w) and sediment concentration as shown in Fig. 6-3, the sediment concentration in terms of ppm is inferred from $V_{r, \infty}$.   The solid concentration by volume (θ_s) and thus the density ratio of bottom mud over water (γ_t / γ_w) can then be calculated based on the specific gravity of the solid.

Fig. 6-8 shows the results from the interpretation of all the TDR readings.   Except for TDR/DMT-1, the tests indicated a water/mud inter-face at elevation 183 m where solid concentration had a significant increase to 4×10^5 ppm.   At elevation 171 m, the γ_t / γ_w reached approximately 1.4.   Below elevation 171 m, the TDR readings became unstable.   This is likely due to the fact that the bottom mud had become solid below that elevation, and the inevitable waving of the barge caused disturbance or cavitations within the solid mud around the TDR waveguides.

The original plan of using the chart Marchetti and Crapps (1981) to determine the bottom mud density could not materialize as in most cases, p_o was very close to u_o, and that resulted in unreason-able material index, I_D.   Thus, the interpretation of DMT results was mostly based on p_o and p_1.   In diluted bottom mud, where the strength was close to zero, p_o should represent the ambient total stress.   Thus a comparison between the increase of p_o and that of hydrostatic pressure with depth should reveal the presence of mud.   As the solid content continued to

increase and the mud turned into solid, there should be significant differences between p_o and p_1 and thus the E_D values can be inferred.   The results of DMT-1 to DMT-5, following the above concept are shown in Fig. 6-9.   Significant differences between p_o and u_o could not be identified until elevation 176 m, which was 7 m lower than the TDR prediction.
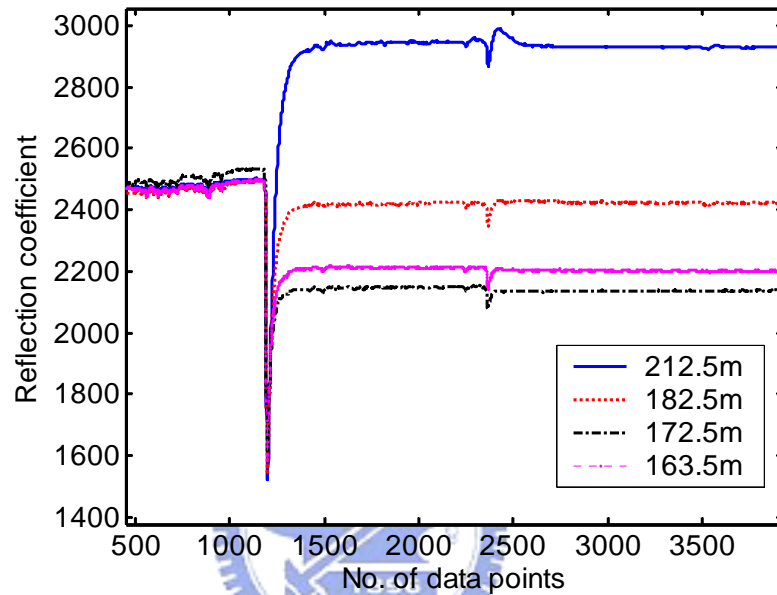
Fig. 6-7   TDR waveforms from TDR/DMT-3.
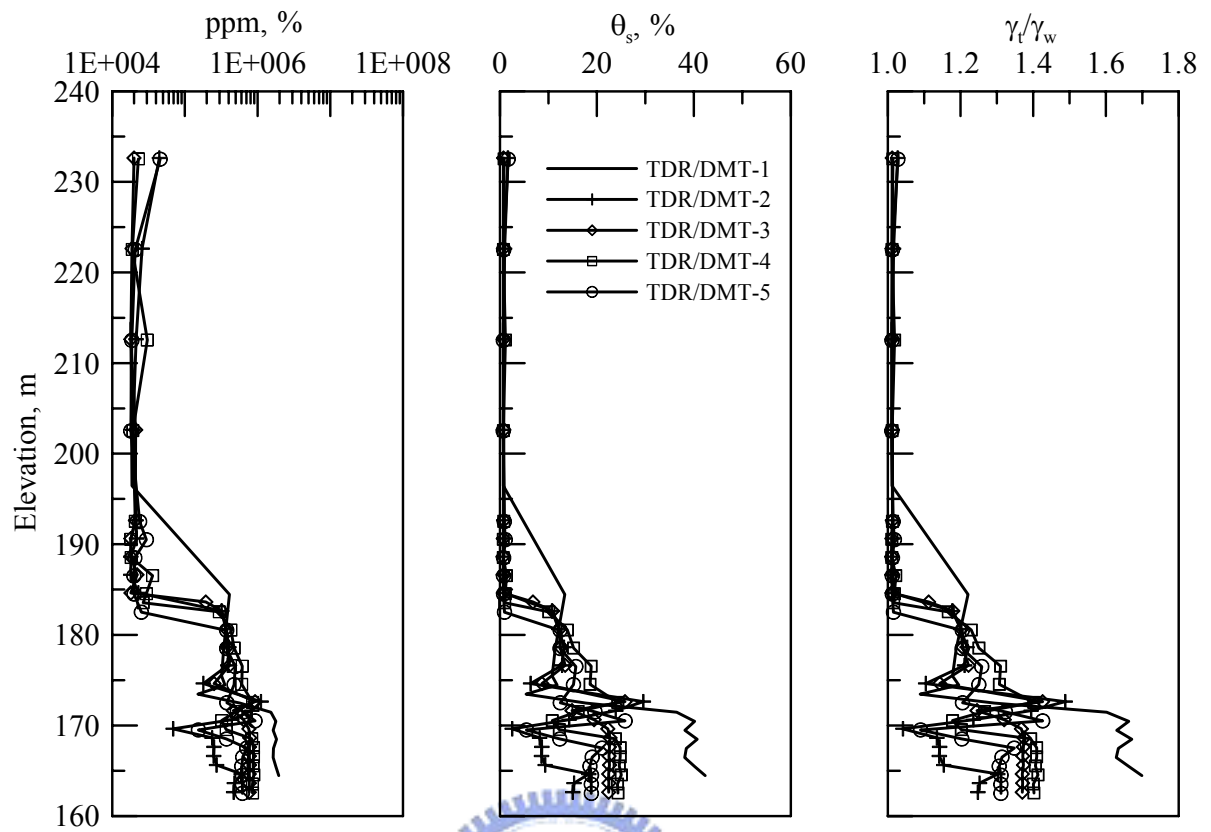
Fig. 6-8   The interpreted TDR test results
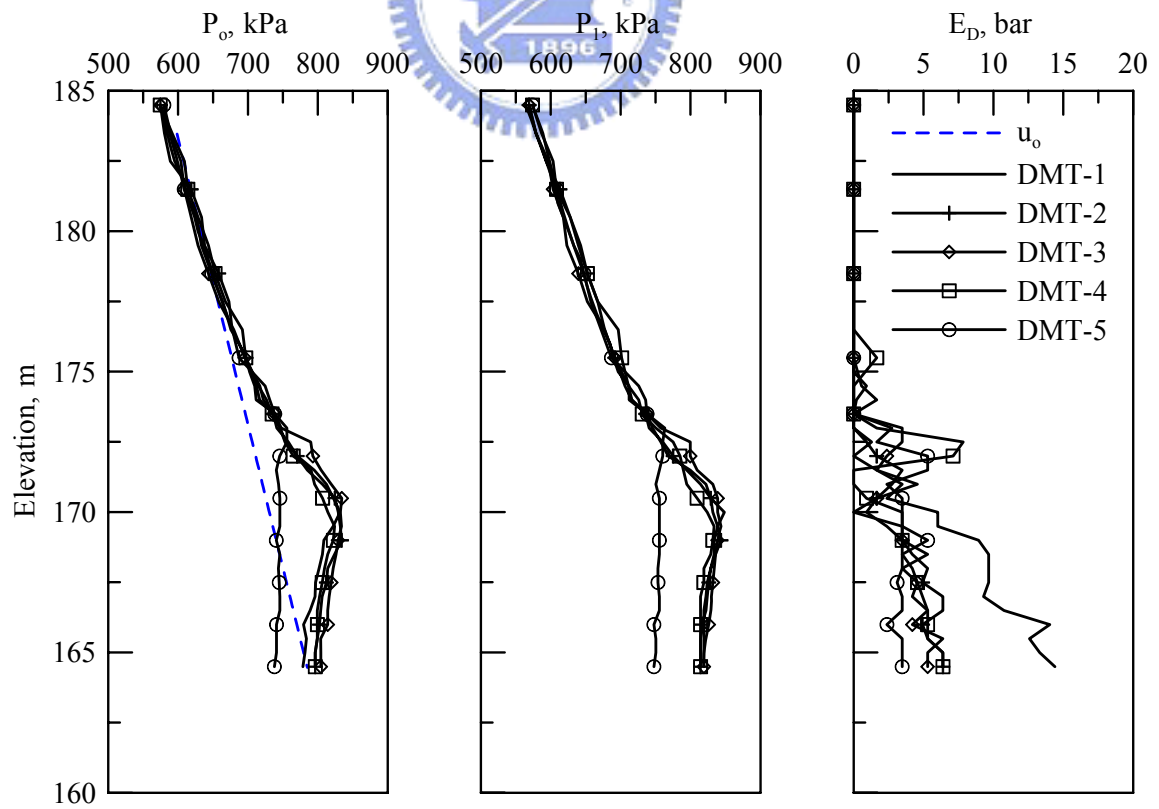
Fig. 6-9   The DMT test results

6.3 Characterization of Suspension

The in-situ monitoring of suspended sediment concentration (SSC) provides information of sediment yield and suspended sediment transportation, and this information may furnish the strategy establishment of flood discharge and sluicing operations for the river or reservoir administration (Bournet et al., 1999; Gessler et al., 1999). The SSC can be determined by directly taking samples for direct measurements or by using existing automated measuring techniques, such as optical and acoustic methods (Wren and Kuhnle, 2002). Of all in-situ monitoring methods, direct sampling is the most straightforward, wherein samples are taken manually or with a pump and then weighed and dried for further tests. Nevertheless, direct sampling incurs a high cost in time and manpower. Samples may also be disturbed and therefore lose their local representativeness.

Commercial automated measuring methods for SSC monitoring are generally categorized into three types: optical, sonic wave-based and laser-based (Wren and Kuhnle, 2002). However, optical methods are strongly affected by soil particle size, even also by the sediment color (Sutherland, 2000); furthermore, a measurement inconsistency for different types of the optical sensor exists (Anderson, 2005). The acoustic methods translate the acoustic attenuation into SSC (Derrow and Kuhnle, 1996), but it is even more sensitive to the grain size of suspended solids (Thorne, 2002). The laser diffraction method can avoid the effect of soil particle size, but it has a limited measurement range and is unreliable for its nearly point sample volume (Wren and Kuhnle, 2002).

The instrumental measurements carried out by these methods are easily affected by particle sizes of suspended solids or are limited to a narrow range of measurement. Therefore, these methods are not suitable for an environment where particle sizes change with time and SSC values vary in a wide range, such as the rivers and reservoirs in areas with erosion

problems. Moreover, while the major time points for monitoring SSC values in river are during floods, the sophisticated instruments used in the automated methods are easily damaged during such periods by the speedy flows and the rocks and debris entrained thereby. And what is worse, the main components of existing instruments for automated measurement are for being submerged in water and therefore hard to maintain. Still further, the instruments are often too expensive to also deal with wide spatial coverage.

TDR is a monitoring technique based on the transmission line. It can be multiplexed and sensing waveguides submerged in water do not have any electronic components, hence quite suitable for field monitoring.

In view of the above, this study tries to develop a TDR-based method to improve the shortcomings of the prior methods and apparatuses for SSC measurement.

6.3.1 Dielectric Spectrum Analysis of Suspended Sediment

The accuracy requirement of SSC measurement is much higher than that of soil moisture measurement. Chapter 3 revealed that the apparent dielectric constant is affected by the electrical conductivity and cable length when the measured material shows significant dielectric dispersion. In other words, only as the dielectric permittivity of the suspension is not significant dispersive, accurate SSC measurements using TDR travel time analysis can be made. Thus, this study first investigates the dielectric characteristics of suspended sediment.

The configuration of TDR system in this test is composed by coaxial probe and Tektrnoix 1502C TDR device. Parameters of TDR system, such as probe impedance and resistance of the leading cable, are calibrated beforehand to process the TDR inversion analysis.   Suspensions of Shihmen reservoir sediment are prepared as three concentrations: 0 ppm (or mg/l), 30000 ppm, and 60000 ppm in tap water.   TDR measurements with different SSC were recorded and subsequent TDR inverse analyses for SSC dielectric spectrum were

conducted.

Fig. 6-10 (modified from Tang, 2007) shows the model-free based inversion results of dielectric permittivity from model free inversion with a variety of SSC.   The result of the 0 ppm case represents the dielectric permittivity of water (with no sediment). Despite the fluctuation at high frequencies due to low signal-to-noise ratio (SNR), the trend of the real part of dielectric permittivity exhibits insignificant dispersion characteristic, while the rise of imaginary part of water dielectric permittivity at low frequencies is caused by EC. Fig. 6-10 also shows that dielectric spectra of other cases (30000 ppm and 60000 ppm) are almost parallel to the water case, indicating that the suspended sediment dose not exhibit significant dielectric dispersion.

Since the suspended sediment is relatively non-dispersive, the SSC measurement based on the travel time analysis may be feasible without interference by the EC and cable resistance. Therefore, measurement of SSC by TDR will be realized by the travel time analysis in this study.
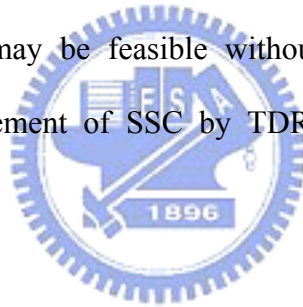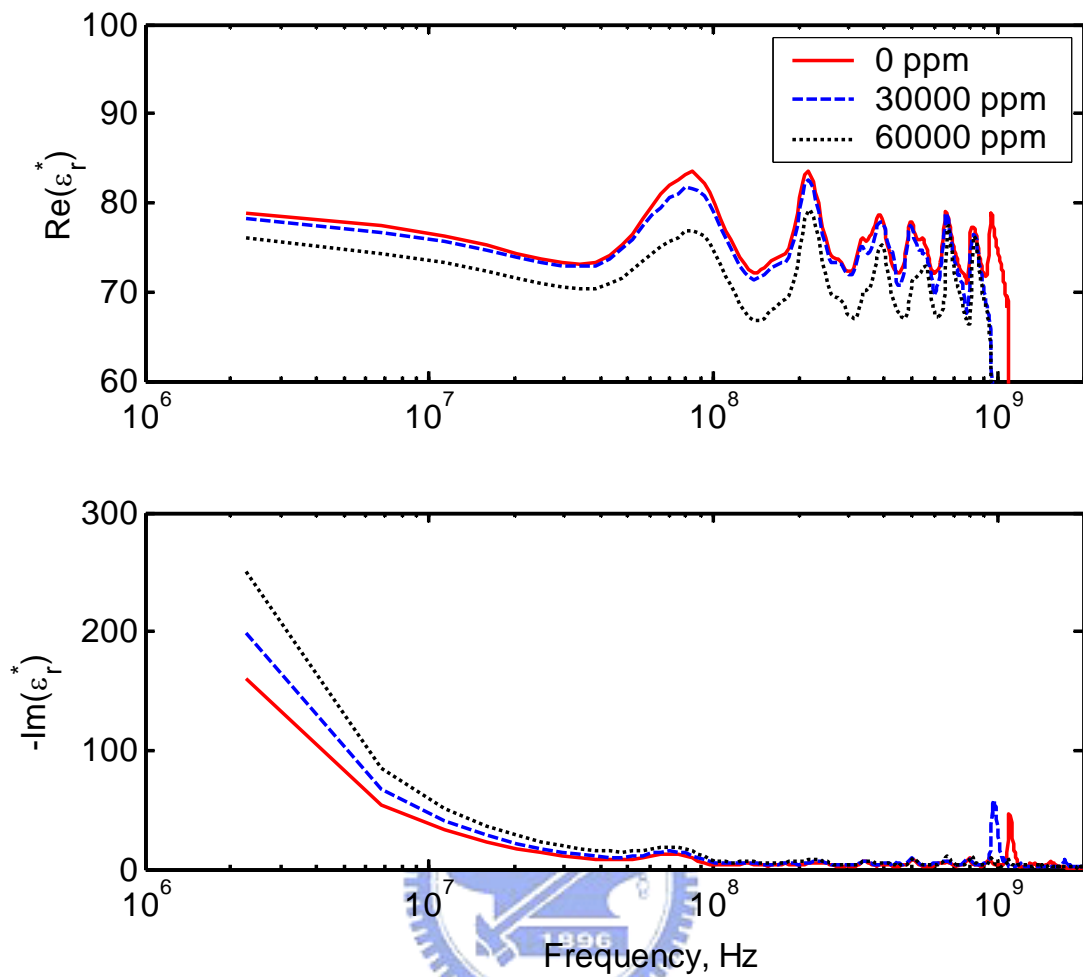
Fig. 6-10   The inversion result (model free) of dielectric spectrum of a variety of suspended sediment concentration (modified after Tang, 2007)

6.3.2   Theoretical Development of TDR SSC Measurement

6.3.2.1   Dielectric Mixing Model for Suspended Sediment

The bulk dielectric permittivity of suspended sediment may be expressed as a function of SSC by the volumetric mixing model (Dobson et al., 1985; Sihvola, 1999; and Starr, 2005). According to the principle of the volumetric mixing model, the dielectric mixing model of water with suspended sediment can be described as:

$$\sqrt{K_a} = (1 - SS)\sqrt{K_w} + SS\sqrt{K_{ss}}$$

[6-1]

where K_a is bulk apparent dielectric constant of the sediment suspension, SS is the volumetric percentage of suspended sediment, which ranges from zero to 1, K_w ($\fallingdotseq$ 80) is the apparent dielectric constant of the water, and K_{ss} (equals 3 ~ 10) is the apparent dielectric constant of the suspended sediment.   According to the definition of the apparent dielectric constant in Eq. [2-39], with known probe length L, Eq. [6-1] can be expressed in terms of TDR travel time as:

$$\Delta t = (1 - SS)(\Delta t_w) + (SS)(\Delta t_{ss}) \qquad [6\text{-}2]$$

where Δt is travel time in the suspended sediment, Δt_w and Δt_{ss} are the TDR travel times when measured materials are entirely water and suspended sediment, respectively.   Based on Eqs. [6-1] and [6-2], the volumetric percentage of sediment concentration (SS) can be determined by the measured travel time Δt in the sediment suspension if the dielectric properties of water and sediment are known by calibration:

$$SS = \frac{\sqrt{K_w} - \sqrt{K_a}}{\sqrt{K_w} - \sqrt{K_{ss}}} = \frac{\Delta t_w - \Delta t}{\Delta t_w - \Delta t_s} \qquad [6\text{-}3]$$

The SS can be transferred into the unit of ppm (or milligram per liter, mg/l), which is commonly used in hydraulic engineering, as:

$$ppm(mgl^{-1}) = \frac{SS \cdot G_s}{1 - SS} 10^6 \qquad [6\text{-}4]$$

where G_s is the specific gravity of the suspended sediment.

6.3.2.2 Sensitivity-Resolution Analysis

SSC measurement requires much higher resolution and accuracy than water content measurement. A sensitivity – resolution analysis of SSC measurement as function of acquisition and probe parameters will be carefully examined first.

The measurement sensitivity SSC is defined as the change of travel time due to unit change of *SS*

$$Sensitivity\ of\ SSC = \frac{\partial \Delta t}{\partial SS} = \frac{2L}{c}\left(\sqrt{K_{ss}} - \sqrt{K_w}\right) \qquad \text{[6-5]}$$

The measurement sensitivity of SSC is a function of apparent dielectric constants of water and suspended sediment, and more importantly the probe length (*L*). The measurement sensitivy of SSC linearly increases with increasing probe length. The resolution of TDR SSC measurement is defined as the relative SS change for each sampling interval (*dt*) of the TDR device. From Eq. [6-5], the resolution of TDR SSC measurement can be written as:

$$Resolution = \frac{dt}{\frac{2L}{c}\left(\sqrt{K_{ss}} - \sqrt{K_w}\right)} \qquad \text{[6-6]}$$

The unit of the TDR SSC measurement resolution is originally presented as volumetric percentage of sediment concentration (SS) or it can be transferred into mg/l or ppm by Eq. [6-4]. The resolution of SSC measurement is proportional to the sampling interval (*dt*), and inversely proportional to the probe length. The sampling interval is limited by the TDR device and the length of probe that can be used is restrained by the signal loss due to EC. To improve

the resolution of SSC measurement, the sampling interval should be minimized and the probe length should be maximized.

To perform a travel time analysis, a recorded TDR waveform should contain the start and the end reflection of the probe. If the TDR waveform is recorded with N discrete sampling points, the time window is Ndt. For the purpose of TDR SSC measurement, the recorded time showed at least equal the travel time of the probe in water. Take Campbell Scientific TDR100 device for example, the required recorded travel time Ndt is difined as

$$Ndt \geq \text{constant} + \frac{2L}{c}\left(\sqrt{K_w}\right) \qquad [6\text{-}7]$$

where the maximized N is 2048 for TDR100 device, and the shortest sampling time interval dt is 12.2 ps [Campbell Scientific, 2004]. The constant term in Eq. [6-7] represents sometime required before the start reflection and after the end reflection. For a fixed N, the shortest time interval that can be used according to the inequality of Eq. [6-7] increases as the probe length increases. Since the resolution is proportional and inversely proportional to dt and L, respectively, the optimal resolution may be obtained by Eq. [6-6] and Eq. [6-7], if EC does not dominate the constant of probe length.

6.3.2.3 TDR Probe Design for SSC Measurement

Since SSC measurement requires much higher accuracy than water content measurements, special attention is paid for the design of TDR SSC probe.

TDR SSC probe used a metallic shield head, as suggested in the Chapter 5, to prevent the leakage of electromagnetic wave. In addition, a balanced configuration of probe conductors is proffered compared to the unbalanced type to increase the repeatability of measurements. In addition, an electrical marker on the cable near the probe head is used to have a precision

time reference for the travel time analysis.

To optimize the probe length and sampling interval, Fig. 6-11 shows the SSC resolution as a function of the probe length L and sampling interval dt, in which the time constant in the Eq. [6-7] is set t as the travel time of 1m cable. The area satisfying the constraint of Eq. [6-7] is illustrated in double shaded are to the left side of Fig. 6-11. The optimal SSC resolution lies in the lower boundary of the constraint. This optimal curve (the interface between the two difference shaded area in Fig. 6-11) monotonically decreases wit some combined increase in L and dt. However, the probe cannot be infinitively long due to the existence of EC. The appropriate probe length should be experimentally evaluated.
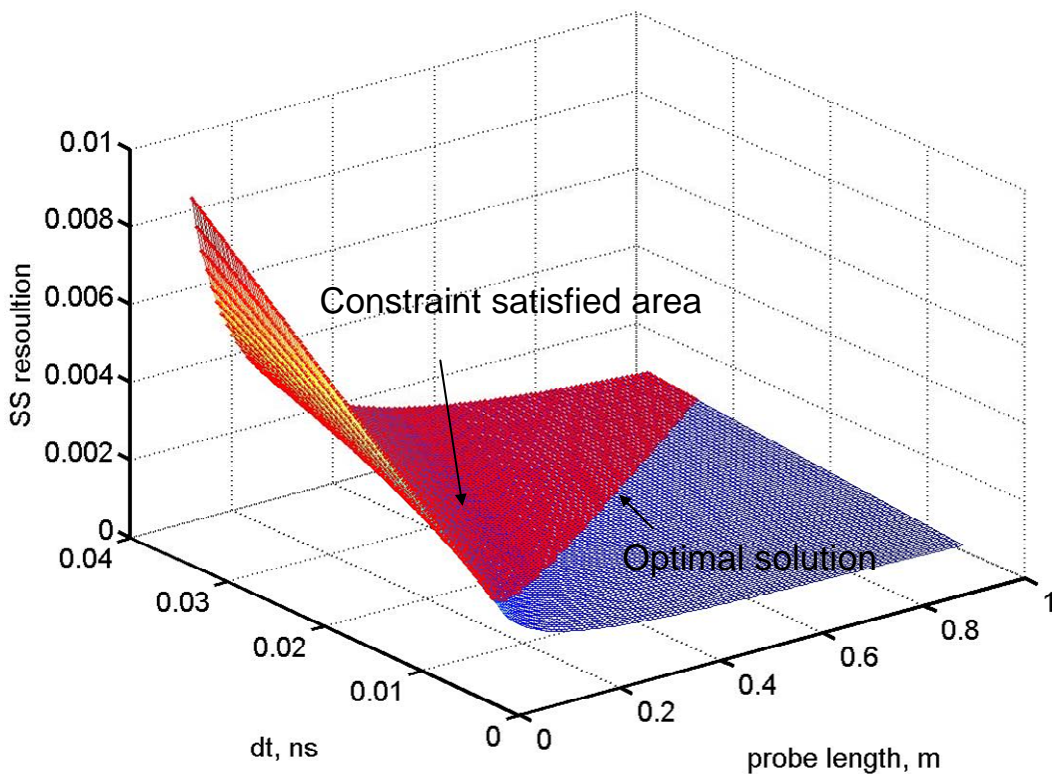
Fig. 6-11   Theoretical measurement resolution of soil volume affected by sampling interval (dt) and probe length (L)

6.3.2.4 Temperature Effect and Correction Method

The dielectric permittivity of water is temperature dependent, as shown in Eq. [2-19]. To obtain accurate SSC measurements, the temperature effect should be considered. Using TDR waveform analysis as shown in Fig. 2-10 and Eq. [2-42] (Heimovaara, 2003), the TDR travel time in a sediment suspension (Eq. [6-2]) at certain temperature can be rewritten as:

$$\Delta\tau(T^{o}C) = t_0 + t_s = t_0 + \left(\frac{2L}{c}\right)\left[\sqrt{K_w(T^{o}C)}(1-SS) + \sqrt{K_{ss}}(SS)\right] \qquad [6\text{-}8]$$

in which the TDR travel time $\Delta\tau$ (T ^{o}C) is composed of travel time between the electrical marker and start point of sensing waveguide t_0 and the actual travel time t_s in the probe section. The dielectric constant of water (K_w) as affected by temperature T can be expressed as Eq. [2-19].

Therefore, a temperature-corrected method of TDR SSC measurement has the following steps:

1. To calibrate the system parameters L and t_0 of the TDR sensing waveguide:

   Water and air are accessible and have known values of apparent dielectric constant. The apparent dielectric constant of air (K_a) is 1 and the apparent dielectric constant of water (K_w) can be expressed as Eq. [2-19]. According to the theory of Heimovaara (1993), a TDR travel time in air ($\Delta\tau_a$) and a TDR travel time in water ($\Delta\tau_w$) can be expressed, respectively, as:

$$\begin{cases} \Delta\tau_a = t_0 + \dfrac{2L}{c}\sqrt{K_a} \\ \Delta\tau_w = t_0 + \dfrac{2L}{c}\sqrt{K_w(T)} \end{cases} \qquad [6\text{-}9]$$

Then L and t_0 can be solved by measuring TDR travel times along the TDR sensing waveguide in air and in water and the water temperature.

2. To calibrate the dielectric permittivity of suspended solids (K_{ss}):

    Several suspensions with different and known concentrations are prepared, and TDR travel times $\Delta\tau$ therein and corresponding temperatures are measured. K_{ss} is then calibrated using Eq. [6-8] and the least square method.

3. To determine SSC

    Once the system parameters L and t_0 and the respective values of dielectric permittivity of suspended solids (K_{ss}) are known after calibration, the TDR sensing waveguide and a temperature sensor are used to measure the TDR travel time $\Delta\tau$ in a suspension with an unknown SSC and the temperature, respectively. The SSC can be determined by the equation:

$$SS_{estimated} = \frac{\left(\Delta\tau(T^0C) - t_0\right) - \frac{2L}{c}\sqrt{K_w(T°C)}}{\frac{2L}{c}\left(\sqrt{K_{ss}} - \sqrt{K_w(T°C)}\right)}$$

[6-10]

Since the TDR travel time $\Delta\tau$ is as function of temperature T, the error resulted from temperature error can be determined analytically. Le $\Delta\tau_1$ be the TDR travel time corresponding to the actual temperature T and $\Delta\tau_2$ corresponds to the temperature with an error T+ΔT, the resulting error in SSC can be determined from Eq. [6-6] and Eq. [6-8]:

$$SS \text{ error} = \frac{\Delta\tau_2 - \Delta\tau_1}{\text{Sensitivity}} = \frac{(1 - SS)\left(\sqrt{K_w(T + \Delta T)} - \sqrt{K_w(T)}\right)}{\left(\sqrt{K_{ss}} - \sqrt{K_w(T)}\right)}$$

[6-11]

The SSC error due to temperature error is also a function of the dielectric constants of water and suspended solid, and the volumetric sediment concentration.   Assuming typical value (SS =0, T = 25 in Celsius degree, and K_{ss} equals 4), the SS error per Celsius degree is about 0.3 % volumetric sediment concentration ($\fallingdotseq$ 8000 ppm, if Gs = 2.7).

6.3.3   Evaluation of Measurement Performance

To evaluate the performance of TDR SSC measurement, varies influence factors, such as water salinity, soil type or particle size, and cable length, are systematically examined.   A Campbell Scientific TDR100 device with SDMX50 multiplexer were used as typical TDR measurement system, and several trial TDR probes as shown in Fig. 6-12 were connected via 25m CommScope QR320 cable to the SDMX50 multiplexer. A submerged temperature sensor with $\pm$ 0.1 ^{o}C accuracy was also used.   All the probes shown in Fig. 6-12 are made with metallic shield head. The selection of the trial probes include difference in probe configuration (balanced vs. unbalanced), boundary condition (open-end vs. shorted-end), and probe length. U-shape probe are also evaluated to reduce the probe size while maintaining the desired sensing length.   In addition, the sampling interval dt of each probe is chosen for the greatest resolution as possible.

To provide a precise time reference for determining TDR travel time $\Delta\tau$, a QR320 cable connector was used as a electrical to generate a clear mark before the EM wave enters the probe. At least 10 repeated waveforms were recorded for each measurement to estimate standard deviation of measurements.   Probe parameters (t_0 and L) of each probe were calibrated through by the procedure introduced in the previous section.

Effect of water salinity was examined for all probes.   Probes were immersed into water (SSC = 0) with various electrical conductivity (EC) from 5 ~ 600 µs/cm. Both dual tangent

method and the derivative method were used and evaluated. The water temperature is recorded with submersible temperature sensor with accuracy of ± 0.1 Celsius degrees. The SSC error and variation due to EC were examined for each probe. Eq. [6-10] to check the variation caused by EC effect, then a probe with lowest error and least affected by EC is selected for further evaluations.

Three types of sediments were selected for tests, including natural sediments from Shihmen and ChiChi reservoir area in Taiwan, namely Shihmen clay (relative density Gs = 2.73) and ChiChi silt (Gs = 2.71), and one man-made silica silt (Gs = 2.67) grinded from glass materials. The particle size distributions of these three sediment were shown in Fig. 6-13. The particle size of Shihmen clay is the finest. The mean particle size of ChiChi silt and silica silt are most identical, except that the ChiChi silt is composed of some sand and clay size particles. Calibration tests for the travel time – SSC rating curve were conducted on sediment suspensions with various SSC from 0 ~ 150,000 ppm. At least ten TDR waveforms are taken for variation calculation. The calibrated K_{ss} is determined by regression analysis. For one of the sediment (silica silt), different cable length (2m, 15m, and 25m) were used to evaluate the effect of cable resistance. For each cable length, the probe constants are individually calibrated.
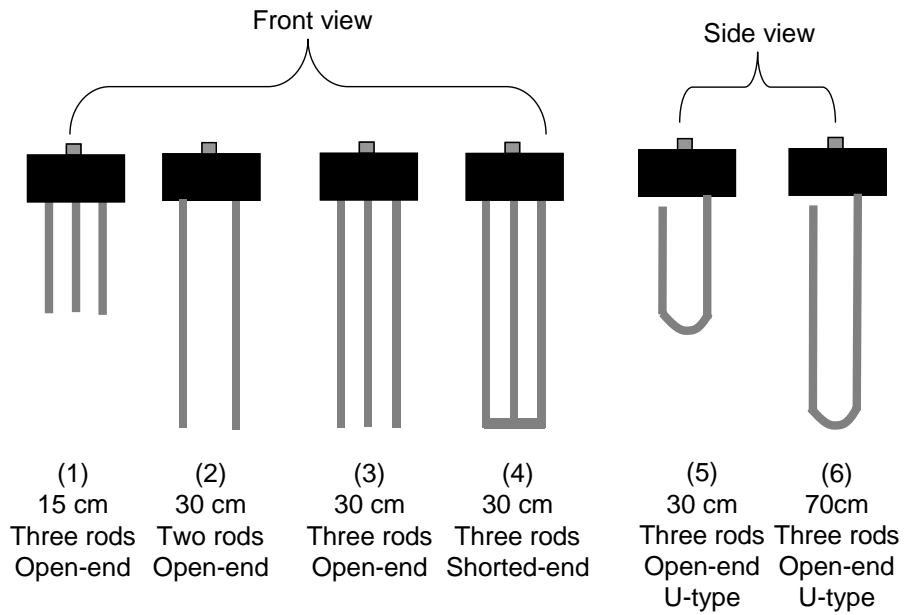
Fig. 6-12   Six types of TDR probe for SSC measurement
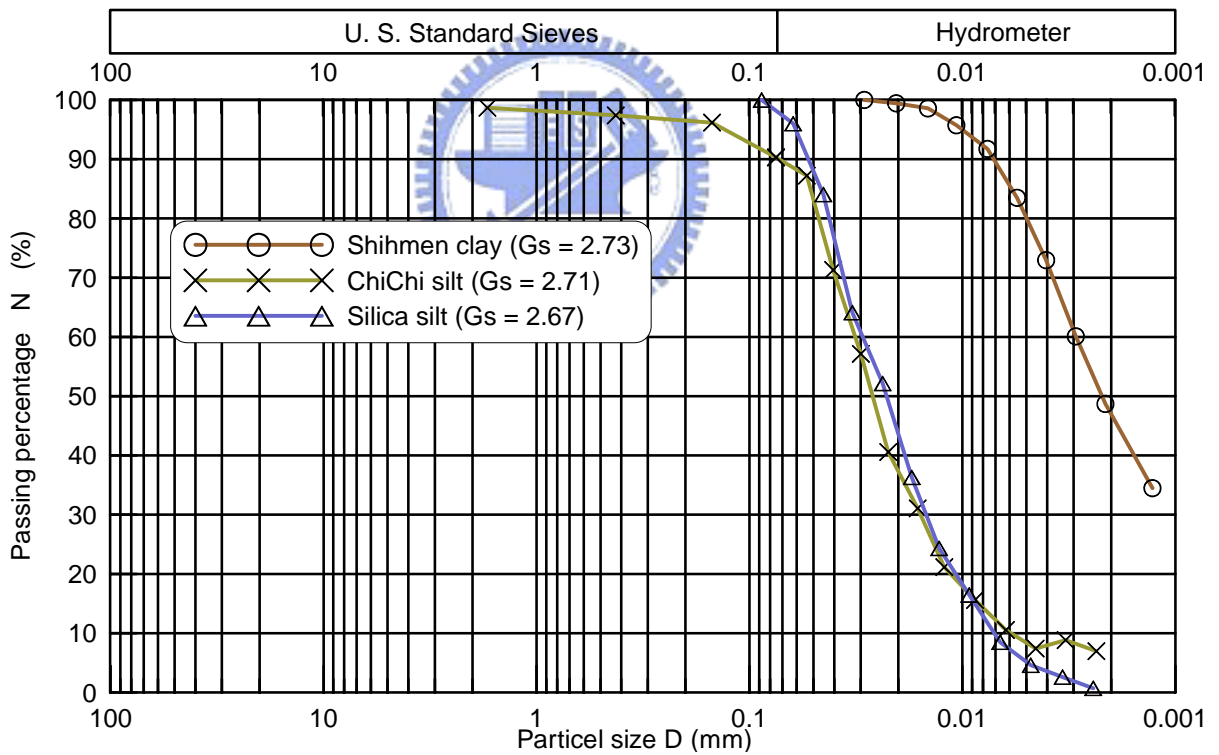
Fig. 6-13   Particle size distribution and relative density (Gs) of Shihmen clay, ChiChi silt, and silica silt

6.3.3.1 Effect of Water Salinity

In the measurements in water with different salinity, the range of variation in the TDR travel time is transferred to variation of SSC (by assuming Gs = 2.75 and K_{ss} = 4). The resolution and variation range due to water salinity are shown in

Table 6-1 For all probes, the derivative method of travel time analysis performs significantly better than the dual tangent method. The three-rod probe performs much better than the two-rod probe, suggesting the importance of balanced configuration. The shorted-end probe does not show improvement over open-end probe, and the U-shape dose not affect the measurement performance.

For the same or similar resolution, accuracy seem to increases with measuring probe length, waveform examination revealed that the reflections form electrical marker or mismatch in the probe head may interfere with the end reflection in short probes. Therefore, a pure and clear end reflection is important and should be ensured by placing the electrical marker at an appropriate location relative to the probe length and minimizing the reflection in the probe head. Among all the probes, the 70 cm U-shape probe with the derivative method of travel time analysis is least affected by water salinity, This probe will be used for further evaluations.

TDR travel times with different water salinity are corrected to the 25 Celsius degree. The measured travel time and corresponding SSC of the 70 cm open probe using the derivative method is shown in Fig. 6-14. Fig. 6-14a shows the mean value and error bar of travel time $\Delta \tau$. Using the case of 5 μs/cm as the reference, the SSC calculated form the TDR travel time in water with different salinity are considered as error due to water salinity, as shown in Fig. 6-14b. The mean error is less than 2100 ppm, better than the measurement resolution. This may be explained by the interpolation of the derivative method for determining the point of the end reflection.

Although temperature of laboratory did not vary signification while performing test with various water salinity, the greatest difference between each measurement is about 1 Celsius degrees which may result in 8,000 ppm error without temperature correction according to the Eq. [6-11].   Since changes of temperature were recorded for each test, the average error from the 70cm open probe is less than 1500 ppm after temperature correction.   This result verifies the applicability of temperature correction method in Eq. [6-11].

Table 6-1   Comparisons of derivation range due to salinity effect for each probe types

Deviation Range (ppm) Probe type	(1) 15 cm Three rods Open-end	(2) 30 cm Two rods Open-end	(3) 30 cm Three rods Open-end	(4) 30 cm Three rods Open-end U-type	(5) 30 cm Three rods Shorted-end	(6) 70 cm Three rods Open-end U-type
Resolution	7000	3200	3200	3200	3200	2500
Dual tangent (derivation range / resolution)	29,700 (4.2)	27,000 (8.4)	12,000 (3.8)	22,000 (6.9)	11,000 (3.4)	7000 (2.8)
Derivative (derivation range / resolution)	14,700 (2.1)	16,800 (5.3)	5200 (1.6)	4600 (1.4)	7300 (2.3)	2100 (0.84)
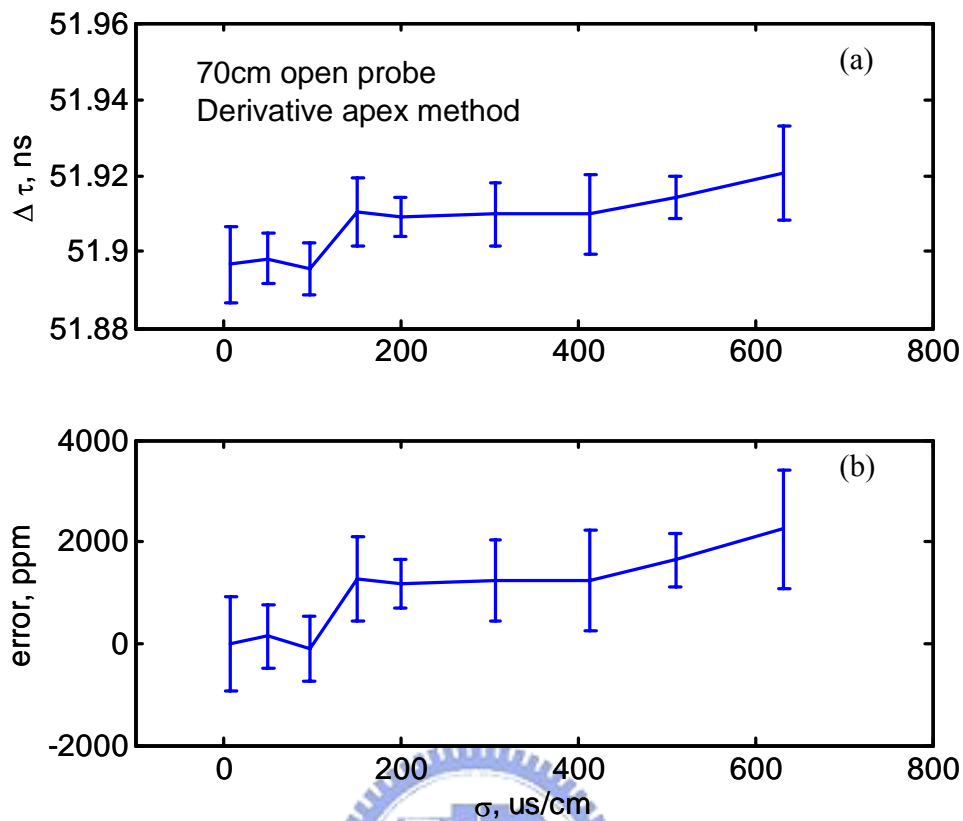
Fig. 6-14   The salinity effect for (a) travel time $\Delta\tau$ and (b) estimated error of the 70cm open probe using the derivative method

6.3.3.2   Travel time - SSC Rating Curve

At travel time – SSC rating curve of Shihmen clay is first established with the 70 cm probe.   TDR waveforms are recorded with various SSC from 0 to 150,000 ppm in water with two different EC (σ = 200, and 400 µs/cm), and the ravel times were determined by the derivative method.

The temperature corrected travel time $\Delta\tau$ (corrected to T = 25 $^{\circ}$C) are shown in Fig. 6-15. The dielectric constant of the sediment estimated by regression has similar value for the two cases with different water salinity (K_{ss} = 8.47 for σ = 200 µs/cm, and K_{ss} = 7.53 for σ = 400 µs/cm). The difference in the resulting slopes of the rating curves is less than 3 percent,

showing the insignificant influence by the water salinity as suggested by Fig. 6-14. The measurement accuracy of both cases is about 1500 ppm, which is close to the half of theoretical resolution.

Figure 6-16 shows mean errors estimated from the difference between measured data and the regression line within background water with two salinity contents as shown in the Fig. 6-15. Most of mean errors were under ±2000 ppm, indicating the TDR SSC measurement method provides high measurement accuracy compared to the basal sediment concentration measurement.

Fig. 6-15   Rating curve of travel time $\Delta\tau$ and Shihmen clay volumetric volume (SS) within background water with two salinity contents, and error bar represents experimental data with 2 standard deviation

Fig. 6-16   The measurement error from rating curve of travel time Δτ and Shihmen clay volumetric volume within background water with two salinity contents
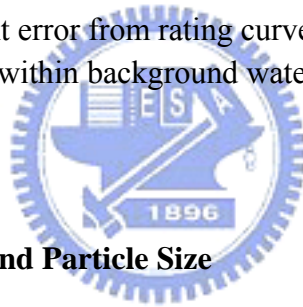
6.3.3.3   Effect of Soil Type and Particle Size

Using the water with EC = 400 μs/cm, the travel time – SSC rating curves for the silica silt and ChiChi silt were also performed. Due to limit amount of samples, the highest SSC for ChiChi silt was only 0.02 (50000 ppm). Fig. 6-17 shows the travel time – SSC rating curves for the three types of sediments, and Fig. 6-18 shows mean errors estimated from the difference between measured data and the regression lines of three different types of measured samples.   The rating curve of ChiChi silt almost overlaps with that of Shihment clay, showing no signs of particle size effect. However, the calibrated K_{ss} of silica silt is 3.61, significantly different for that of ChiChi silt and Shihmen clay, resulting in almost 14% difference in the slop of the travel time – SSC rating curve. This significant difference may be attributed to the apparently different mineralogy for the silica from natural soils. It is believed

that the bulk dielectric permittivity of the natural sediments does not vary significantly with time. Hence, it can be calibrated with a few actual SSC measurements. A major advantage of TDR SSC method over optical and acoustic methods is its invariance to the particle size.

Fig. 6-17   Rating curve of travel time $\Delta\tau$ with Shihmen clay, silica silt and ChiChi silt, and error bar represents experimental data with 2 standard deviation
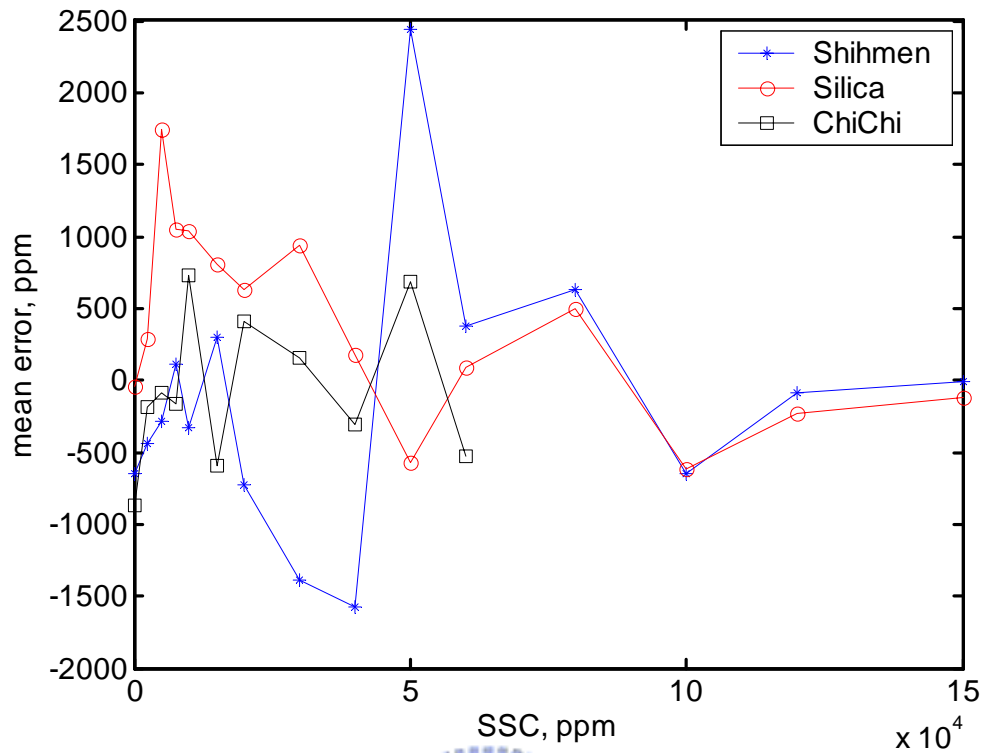
Fig. 6-18   The measurement error from rating curve of travel time Δτ with Shihmen clay, silica silt and ChiChi silt

6.3.3.4   Effect of Lead Cable Length

The travel time – SSC rating curve for three different length of leading cables are shown in Fig. 6-19 for the silica silt.   Due to the effect of cable length, the travel time of the three cases at 0 ppm (SS=0) is not the same. However, with individual calibration for the probe parameters (t_0 and L) for each case, slopes of the three travel time – SSC rating curves with different leading cable lengths are approximately parallel, and calibrated K_{ss} remains similar (K_{ss} = 3.61 for 25 m cable, K_{ss} = 3.72 for 15 m cable, and K_{ss} = 3.99 for 2 m cable). Therefore, these results show that, although the cable length affects the TDR travel time $\Delta\tau$, the effect of cable resistance can be taken into account through calibration of system parameters.
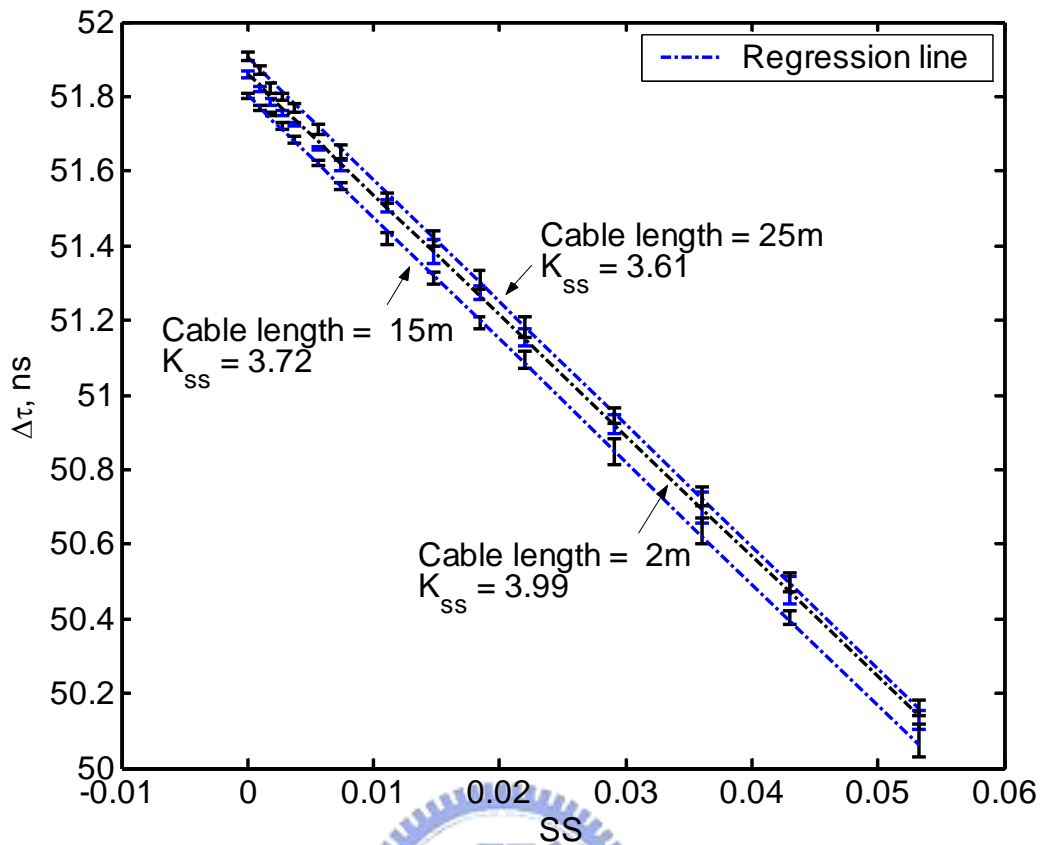
Fig. 6-19 Rating curve comparison for silica silt with QR320 lead cable length = 2m, 15m, and 25m

6.3.4 SSC Measurements using Frequency Domain Phase Velocity Method

The principle and proof of concept of TDR frequency domain phase velocity method have been shown in section 3.2.2, This new method can give reliable phase velocity estimates in the high frequency range (>100 MHz). As an alternative to the travel time method, application of the frequency domain phase velocity method to determine the SSC is investigated in this section.

K_a - SSC rating curve

The measured data from the preceding section were re-analyses using the frequency domain phase velocity method. The probe length was first calibrated by the water

measurement by comparing the measured phase velocity to the theoretical phase velocity in the high frequency range. Fig. 6-20 shows the rating curve between the K_a estimated from the frequency domain phase velocity and the volumetric volume (SS) of Shihmen clay in background water with different salinity. The calibrated K_{ss} of both cases are relatively closed to those estimated by the travel time analysis method in section 6.3.3.1, and the measurement errors, as shown in Fig. 6-21 are similar to the results of the travel time analysis method.
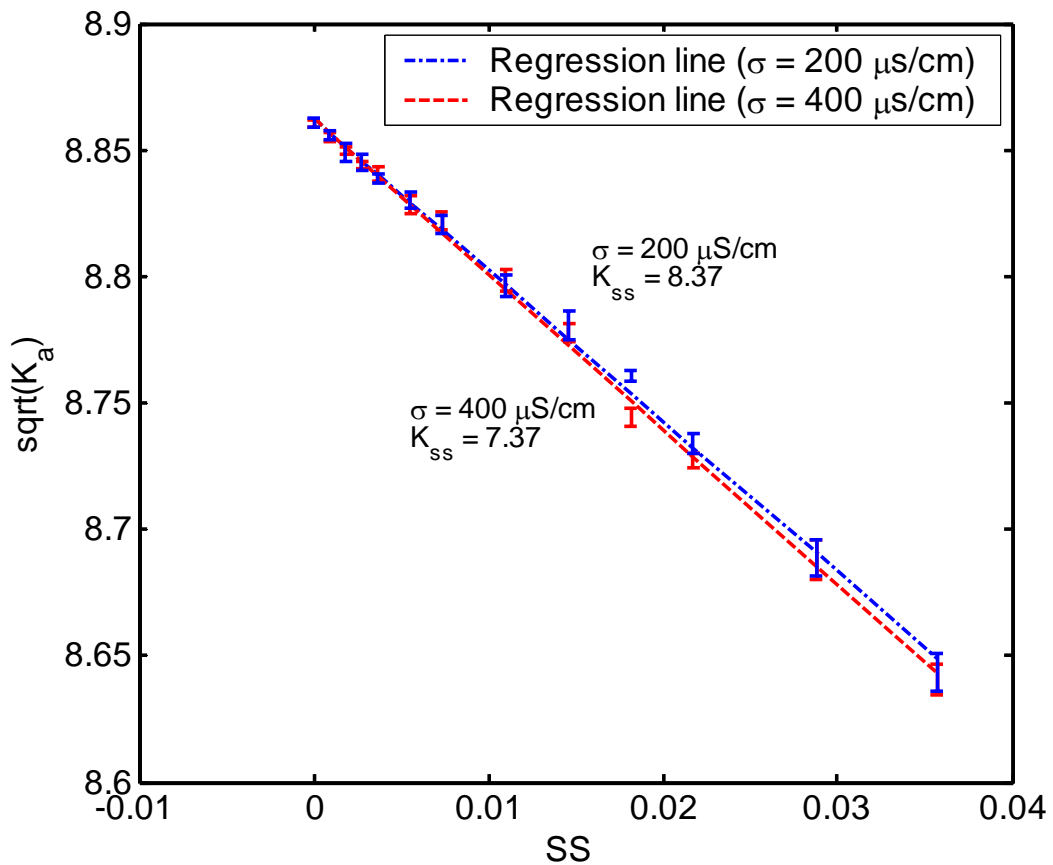
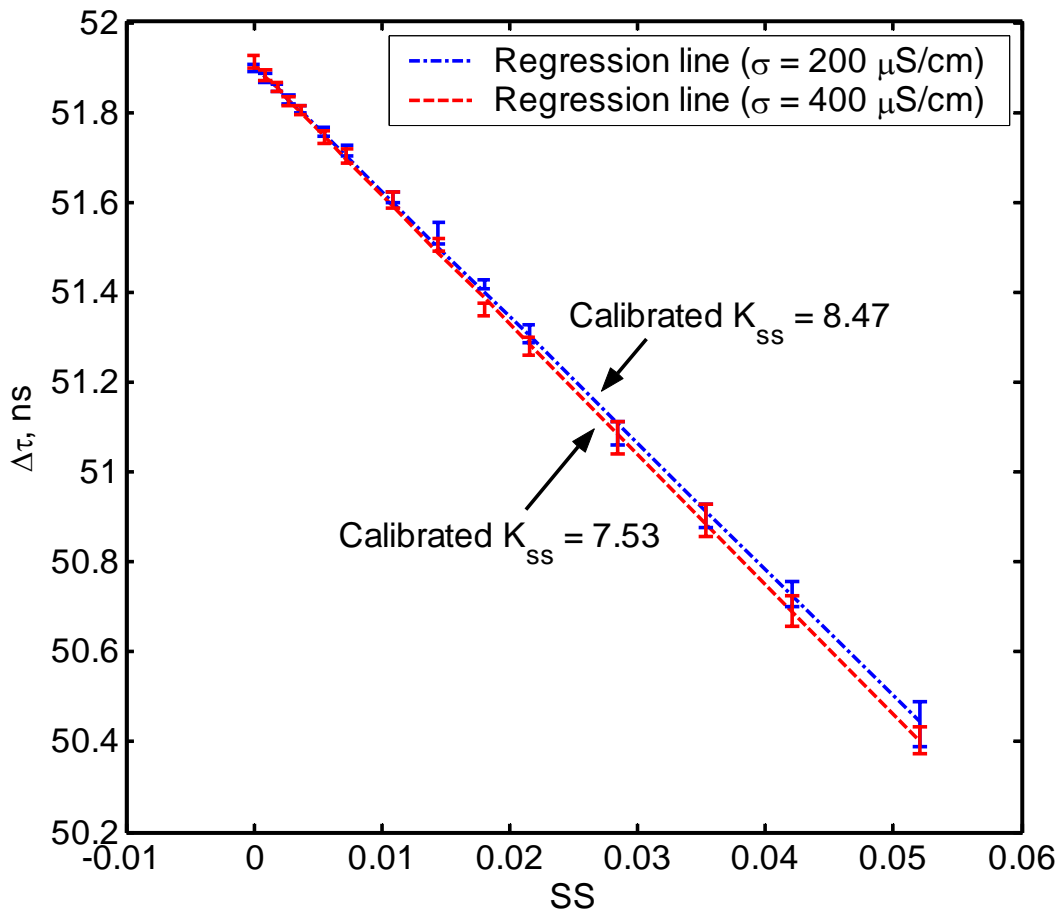Fig. 6-20   Rating curve of K_a and Shihmen clay volumetric volume (SS) within background water with two salinity contents, and error bar represents experimental data with 2 standard deviation
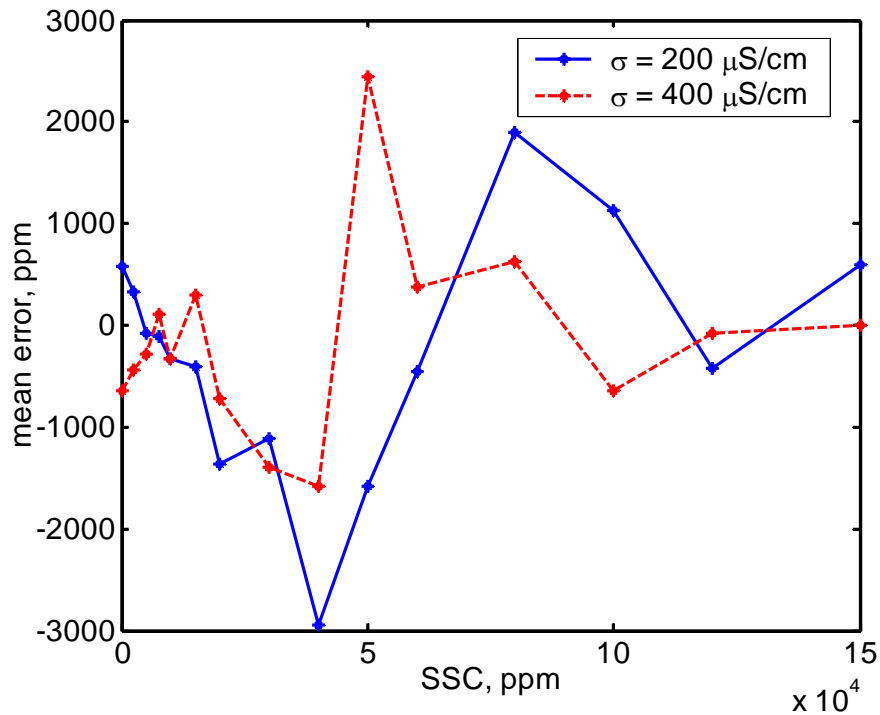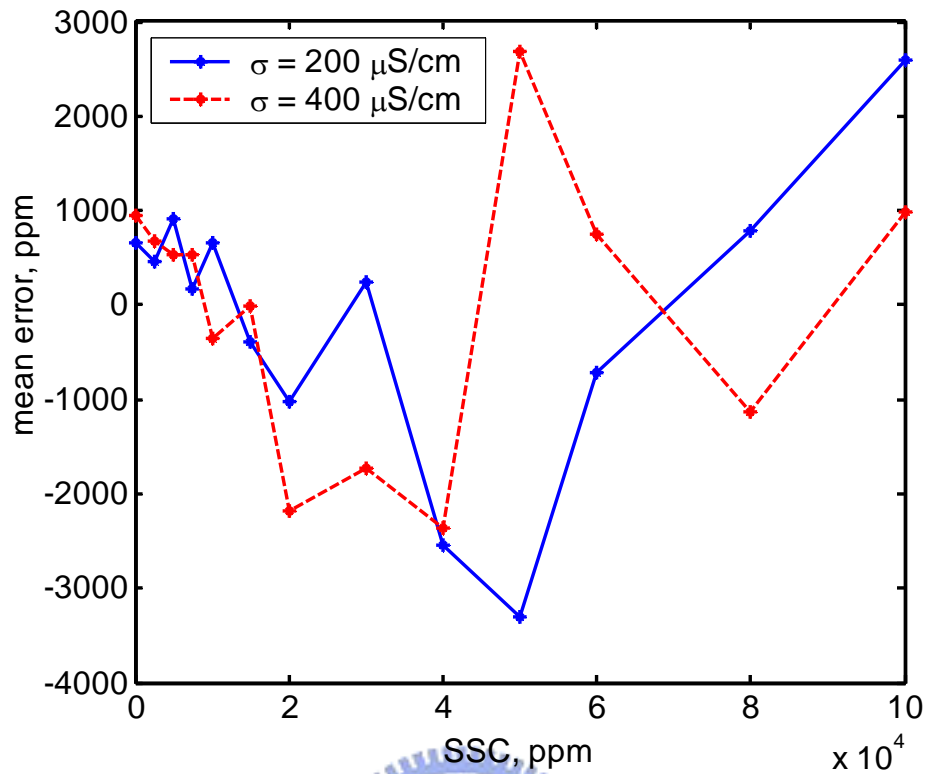
Fig. 6-21　The measurement error from rating curve of K_a and Shihmen clay volumetric volume within background water with two salinity contents
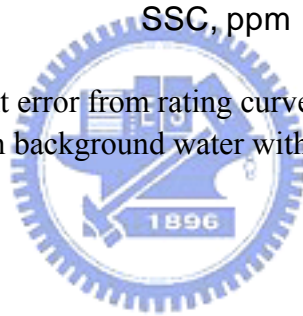
Effect of soil type and particle size

　　By re-analyzing the measured data in the section 6.3.3.2 using the TDR frequency domain phase velocity method, Fig. 6-22 shows the K_a – SSC rating curves for the three types of sediments, and Fig. 6-23 shows the mean errors estimated from the difference between measured data and the regression lines.　The similar results of rating curves and measurement errors indicate that the SSC estimated by the TDR frequency domain phase velocity method shows no signs of soil type and particle size effect.
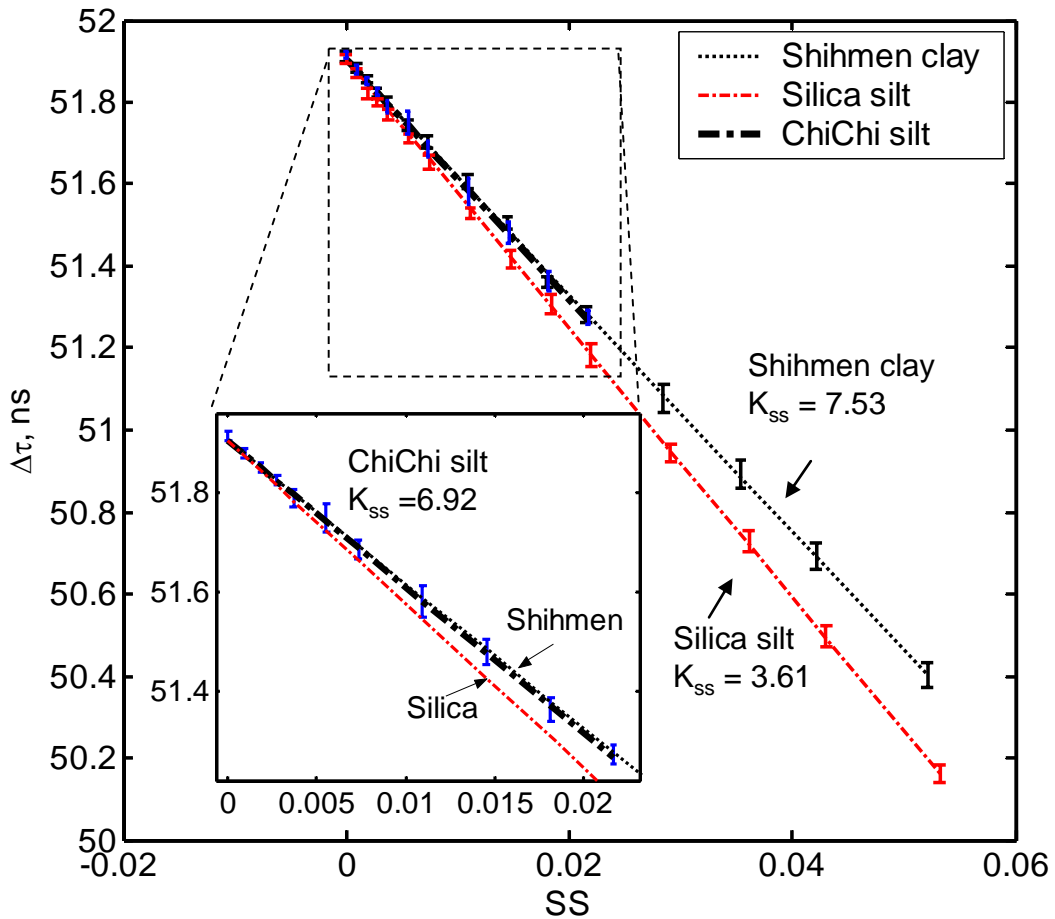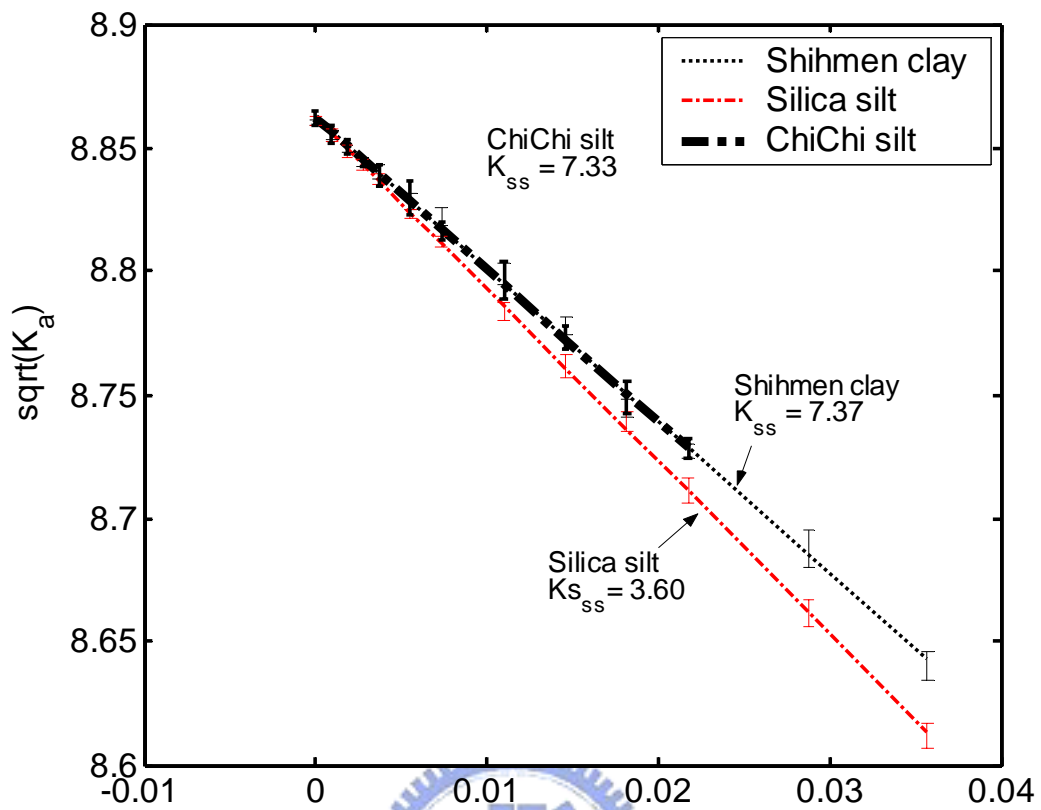
Fig. 6-22 Rating curve of K_a with Shihmen clay, silica silt and ChiChi silt, and error bar represents experimental data with 2 standard deviation
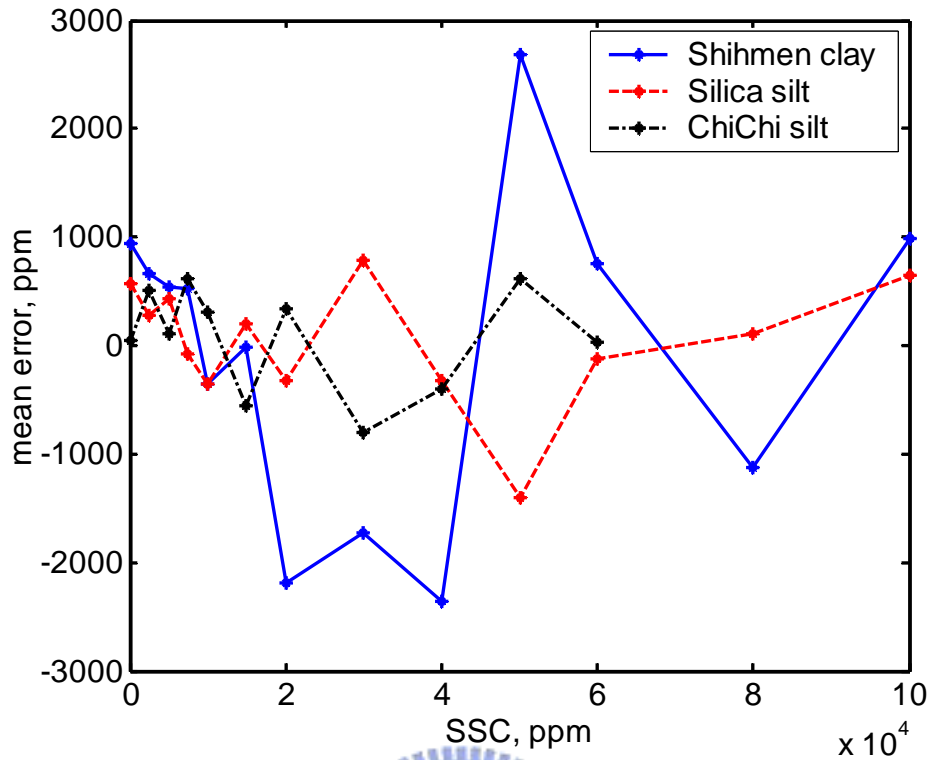
Fig. 6-23   The measurement error from rating curve of K_a with Shihmen clay, silica silt and ChiChi silt

Effect of cable length

The K_a – SSC rating curve for three different lengths of leading cables are shown in Fig. 6-24.   Unlike the results of the travel time analysis method, the estimated K_a of three cases at 0 ppm (*SS* = 0) are almost the same after the probe length calibration for each case, and slopes of the three K_a – SSC rating curves with different leading cable lengths are approximately the same.   Therefore, these results show that the effect of cable resistance can be well taken into account through probe length calibration using the frequency domain phase velocity method.
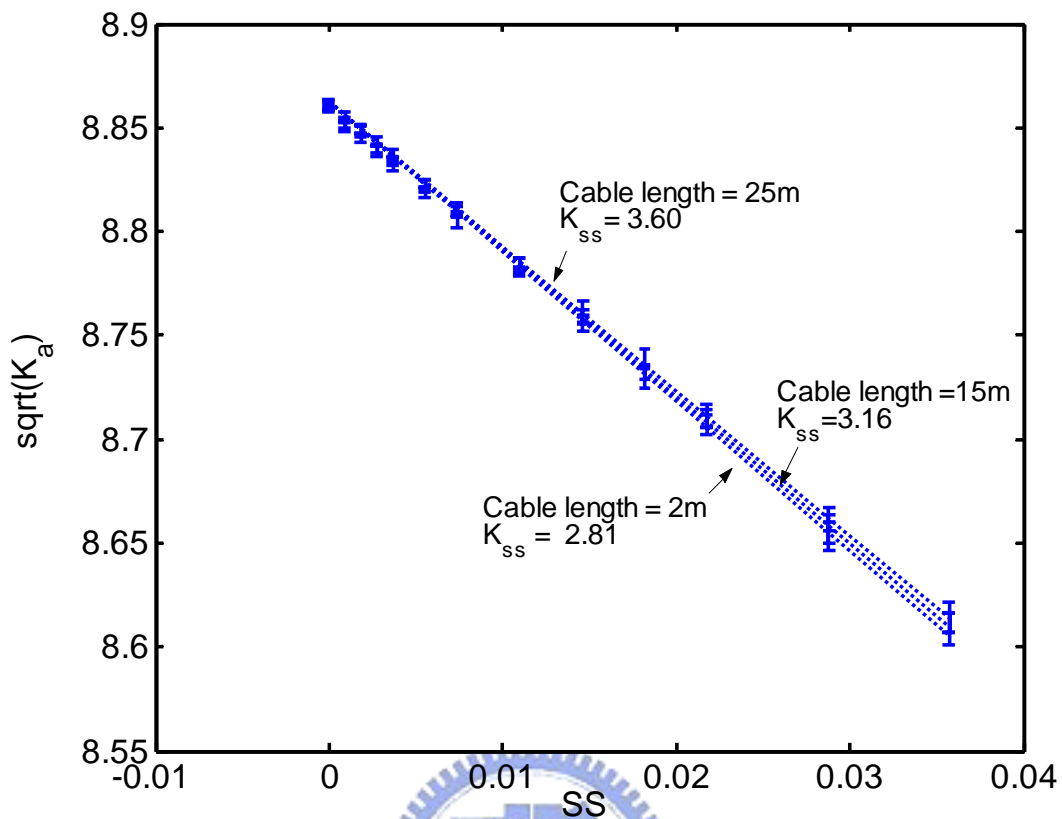
Fig. 6-24   Rating curve comparison for silica silt with QR320 lead cable length = 2m, 15m, and 25m

According to the previous results, the TDR frequency domain phase velocity method has shown its feasibility on the SSC measurements. The major advantages of using the frequency domain phase velocity method are its noise control in the frequency domain and no need for an electrical marker.   Unlike the travel time analysis method, the frequency domain phase velocity method does not require signal filtering and possible distortion of the electrical marker is not an issue.

7 Conclusions

Time domain reflectometry (TDR) can be used to measure apparent dielectric constant, electrical conductivity (EC), and dielectric permittivity as a function of frequency. Due to its versatility and applicability in field measurements, this relatively new technique is gaining popularity in characterization of engineering materials, such as suspended sediment, soil, concrete. The objectives of this study were to investigate and improve the TDR measurement techniques, provide guidelines for TDR probe design, and, as an application example, apply TDR to characterization of soil-water mixture.

Major conclusions drawn from studies on dielectric measurements include:

1. Not only does the dielectric dispersion significantly affect the apparent dielectric constant (Ka) measured by travel time analysis, it also plays an important role on how the Ka is affected by electrical conductivity and cable length. For materials with significant dielectric dispersion, Ka becomes dependent on EC, in particularly at high EC, and cable length, regardless of the effort of air-water calibration for each cable length.

2. There is no consistent trend between the change in Ka and the change in effective frequency as the influencing factors vary. Compensating the effects of electrical conductivity, cable length, and dielectric dispersion by the effective frequency seems theoretically infeasible. To improve the accuracy of TDR soil water content measurements in the existence of these influencing factors, TDR dielectric spectroscopy or developing signal processing techniques for determining dielectric permittivity near the optimal frequency range are suggested.

3. Current practice of TDR dielectric spectroscopy using open-end probe does not give reliable measurements at frequencies higher than 200 MHz. Using the shorted-end

probe to avoid fringing effect does not show significant improvement at high frequencies and contrarily degrades performance at low frequencies.

4. A novel approach for reliably estimating the dielectric permittivity in the high frequency range was proposed based on the frequency domain phase velocity method, analogous to the spectral analysis of surface wave (SASW). The proof of concept was given with numerical examples. This new approach provides accurate measurement of dielectric permittivity at frequencies higher than 200 MHz and has a great potential to improve water content measurements. Experimental studies were suggested for future study.

Major points related to improvement of TDR EC measurement are summarized as follows:

1. The TDR EC measurement requires the knowledge of the source step voltage, which is often implicitly accounted for in the measured reflection coefficient. However, it was found that errors may arise from imperfect amplitude calibration when transforming the voltage signal into the reflection coefficient signal. The instrument error commonly results in an overestimation of electrical conductivity.

2. On the other hand, neglecting cable resistance leads to an underestimation of electrical conductivity. To account for cable resistance, the series resisters model is proven to be theoretically sound and should be used.

3. A calibration (correction) method for the measured reflection coefficient is proposed to account for both the instrument error and the effect of cable resistance, leading to a simple, accurate and theoretically sound procedure for TDR electrical conductivity measurements.

4.   The effect of TDR recording time has been underrated when long cables are used.   To determine the electrical conductivity accurately, the recording time approximating the steady state should be taken after 10 multiple reflections within the probe and 3 multiple reflections within the lead cable. An even longer time (near the end of the TDR step pulse) is required if cable resistance is directly measured by short circuiting the probe.

Issues related to probe design were also investigated. Results revealed:

1.   3D EM field simulations help understand how EM field distribution is affected by the configuration of probe rods. Numerical simulations showed a strong backward radiation near the coax-probe transition, which may be confined by shielding the probe head with a metal cup.

2.   The measurement sensitivity of Ka and EC were derived as a function of the probe parameters (i.e. probe length and geometric impedance), providing guidelines for probe design.

3.   A novel TDR penetrometer probe to allow simultaneous measurements of dielectric permittivity and electrical conductivity at depths during cone penetration was developed.

The above advancement was applied to characterization of basal sediment and suspended sediment. TDR penetrometer was integrated with the Marchetti dilatometer (DMT) and the TDR/DMT probe was used to characterize the bottom mud in Shihmen reservoir. To meet the requirement of higher accuracy in characterizing suspended sediment, a TDR probe and a measurement procedure based on travel time analysis and the frequency domain phase velocity method were further developed for monitoring of suspended sediment concentration

(SSC) in fluvial and reservoir environment. Both methods for SSC measurements were found not affected by particle sizes of sediments and water salinity. Furthermore, the major advantages of using the frequency domain phase velocity method are its noise control in the frequency domain and no need for an electrical marker. Unlike the travel time analysis method, the frequency domain phase velocity method does not require signal filtering and possible distortion of the electrical marker is not an issue. The submerged TDR probes do not have any electronic components and can be multiplexed for multi-point measurements, posting great advantages for field monitoring. Field testing and possible further improvement by replacing the travel time analysis with the frequency domain phase velocity method are suggested for future studies.

Reference

Anderson, C. W., 2005, *Handbooks for Water-Resources Investigations, Section A6.7 – Turbidity*, USGS, USA.

Antoniadis, A., and Oppenheim, Eds. G., 1995, *Wavelets and Statistics, 103, Lecture Notes in Statistics*, Springer Verlag.

Bagchi, S., and Mitra, S. K., 1999, *The Nonuninform Discrete Fourier Transform and its Application in Signal Processing*, Kluwer Academic Publisher.

Baker, J. M., and Allmaras, R. R., 1990, System for automating and multiplexing soil moisture measurement by time-domain reflectometry, Soil Sci. Soc. Am. J., Vol. 54, pp.1-6.

Baker, J. M. and Lascano, R. J., 1989, The spatial sensitivity of time-domain reflectometry, Soil Science, Vol. 147, pp. 378-384.

Baker, J. M., and Spaans, E. J. A., 1993, Comments on "time domain reflectometry measurements of water content and electrical conductivity of layered soil columns", Soil Sci. Soc. Am. J., Vol. 57, pp. 1395-1396.

Ball, J. A. R., 2002, Characteristic impedance of unbalanced TDR probes, IEEE Transactions on Instrumentation and Measurement, Vol. 51, pp. 532-536.

Birchak, J. R., Gardner, C. G., Hipp, J. E., and Victor, J. M., 1974, High dielectric constant microwave probes for sensing soil moisture, Proc. IEEE, Vol. 62, pp. 93-98.

Bournet, P. E., Dartus, D., Tassin, B., and Vincon-Leite, B., 1999, Numerical investigation of plunging density current, Journal of Hydraulic Engineering, Vol. 125, pp. 584-594.

Campanella, R.G.., and Weemees, I., 1990, Development and use of an electrical resistivity cone for groundwater contamination studies, Canadian Geotechnical Journal, Vol. 27, pp. 557-567.

Campanella, R.G., Davies, M.P., Boyd, T.J., and Everard, J.L., 1994, In-situ testing methods for groundwater contamination studies, Symposium on Developments in Geotechnical Engineering, From Harvard to New Delhi, 1936-1994, Balkema.

Campbell Scientific, 2004, *TDR100 instrument manual*, Campbell Scientific, Inc, Utah, USA.

Castiglione, P., and Shouse, P. J., 2003, The effect of ohmic cable losses on time-domain reflectometry measurements of electrical conductivity, Soil Sci. Soc. Am. J., Vol. 67, pp.

414-424.

Cereti, A., Pettinelli, E., Galli, A., and Bella, F., 2003, Shorted-end probes for accurate permittivity measurements with time domain reflectometry, Applied Physics Letters, Vol. 83, pp. 1050-1052.

Chan, C. Y., and Knight, R. J., 1999, Determining water content and saturation from dielectric measurements in layered materials, Water Resources Research, Vol. 35, No. 1, pp. 85-93.

Chan, C. Y., and Knight, R. J., 2001, Laboratory measurements of electromagnetic wave velocity in layered sands, Water Resources Research, Vol. 37, No. 4, pp. 1099-1105.

Cheng, D. K., 1989, *Field and Wave Electromagnetics 2nd Edtion*, Addison-Wesley, US.

Clarkson, T. S., Glasser, L., Tuxworth, R. W., and Williams, G., 1977, An appreciation of experimental factors in time-domain spectroscopy, Adv. in Mol. Relax. Processes, Vol. 10, pp. 173-202.

Cole, R. H., 1976, Time-domain spectroscopy of dielectric materials, IEEE, Trans. Instrum. Meas., Vol. IM-25, pp.371-375.

Cole, R. H., Berberian, J. G., Mashimo, S., Chryssikos, G., Burns, A., and Tombari, E., 1989, Time domain reflection methods for dielectric measurements to 10 GHz, J. Appl. Phys., Vol. 65, pp. 2211-2215

Collins, B.D., and Znidarcic, D., 2004, Stability analysis of rainfall induced landslides, ASCE Journal of Geotechnical and Geoenvironmental Engineering, Vol.130, No.4, pp.362-372.

Dalton, F.N., Herkelrath, W. N., Rawlins, D. S., and Rhoades, J. D., 1984, Time-domain reflectometry: simultaneous measurement of soil water content and electrical conductivity with a single probe, Science, Vol. 224, pp. 989-990.

Dasberg, S., and Hopmans, J. W., 1992, Time domain reflectometry field measurements of soil water content and electrical conductivity, Soil Sci. Soc. Am. J., Vol. 56, pp. 1341-1345.

Davis, J. L. and Annan, A. P., 1977, Electromagnetic detection of soil moisture: progress report 1, Can. J. Remote Sensing, Vol. 3, pp. 76-86.

Dean, T. J., Bell, J. P., and Baty, A. B. J., 1987, Soil moisture measurement by an improved capacitance technique: I. Sensor design and performance, J. Hydrol., Vol. 93, pp. 67-78.

de Loor, G. P., Van Gemart, M. J. C. and Gravesteyn, H., 1973, Measurement of dielectric

permittivity with time domain reflectometry extension of the method to lower relaxation frequencies, Chemical Physics Letters, Vol. 18, pp. 295-299.

Derrow, R. W., and Kuhnle, R. A., 1996, Preliminary analysis of the NCPA-NSL suspended sediment calibration system, Paper present in Proc., 6th Fed. Interagency Sedimentation Conf. 1996, Federal Interagency Sedimentation Project, vol. 2, pp. 58–65, St. Anthony Falls Lab., Minneapolis, Minn.

Dobson, M. C., Ulaby, F. T., Hallikainen, M. T., and EL-Rayes, M. A., 1985, Microwave dielectric behavior of wet soil part II: dielectric mixing models, IEEE Trans. Geoscince and Remote sensing, Vol. GE-23, pp. 35-46.

Dowding, C. H., Dussud, M. L., Kane, W. F., and O'Connor, K. M., 2003, Monitoring deformation in rock and soil with TDR sensor cables, Geotechnical News, pp. 51-59.

Duan, Q., Gupta, V. K. and Sorooshian, S., 1992, Effective and efficient global optimization for conceptual rainfall-runoff models, Water Resour. Res., Vol. 28, pp. 1015-1031.

Edwards, T. C., and Steer, M. B., 2000, *Foundations of Interconnect and Microstrip Design, 3rd Edition*, Jown Wiley & Sons.

Evett, S.R., Tolk, J. A., and Howell, T. A., 2005, Time domain reflectometry laboratory calibration in travel time, bulk electrical conductivity, and effective frequency, Vadose Zone Journal, Vol. 4, pp. 1020–1029.

Fellner-Feldegg, H., 1969, The Measurement of Dielectrics in Time Domain, Journal of Physical Chemistry, Vol.73, pp. 616-623

Feng, W., Lin, C. –P., Deschamps, R. J., and Drnevich, V. P., 1999, Theoretical model of a multisection time domain reflectometry measurement system, Water Resources Research, Vol. 35, No. 8, pp. 2321-2331.

Ferré, T. P. A., Knight, J. H., Rudolph, D. L., and Kachanoski, R. G., 1998, The sample areas of conventional and alternative time domain reflectometry probes, Water Resources Research, Vol. 34, pp.2971-2979.

Ferré, T. P. A., Knight, J. H., Rudolph, D. L., and Kachanoski, R. G., 2000, A numerical based analysis of the sensitivity of conventional and alternative time domain reflectometry probes, Water Resources Research, Vol. 36, pp. 2461-2468.

Ferré, T. P. A., Nissen, H. H., Knight, J. H., and Moldrup, P., 2003, Transverse sample area of

two- and three-rod time domain reflectometry probes: electrical conductivity, Water Resources Research, Vol. 39, 1261, doi:10.1029/2002WR001572.

Friel, R. and Or, D., 1999, Frequency analysis of time-domain reflectometry with application to dielectric spectroscopy of soil constituents, Geophysics, Vol. 64, pp. 707-718.

Friedman, S. P., 1998, A saturation degree-dependent composite spheres model for describing the effective dielectric constant of unsaturated porous media, Water Source Research, Vol. 34, pp. 2949-2961.

Friedman, S. P., and Seaton, N. A., 1998, Critical path analysis of the relationship between permeability and electrical conductivity of three-dimensional pore network, Water Resources Research, Vol. 34, pp. 1703-1710.

Foti, S., 2000, *Multistation Method for Geotechnical Characterization using Surface Waves*, Ph. D. thesis, Politecnico di Torino.

Gessler, D., Hall, B., Spasojevic, M., Holly, F., Pourtaheri, H., and Raphelt, N., 1999, Application of 3D mobile bed hydrodynamic model, Journal of Hydraulic Engineering, Vol. 125, pp. 737–749.

Giese, K. and Tiemann, R., 1975, Determination of the complex permittivity from thin-sample time domain reflectometry improved analysis of the step waveform, Adv. in Mol. Relax. Processes, Vol. 7, pp. 45-59.

Grant, E., Buchanan, T., and Cook, T., 1957, Dielectric behavior of water at microwave frequencies, J. Chem. Phys., Vol. 26, pp. 156-161

Hager III, N.E., 1994, Broadband time-domain-reflectometry dielectric spectroscopy using variable-time-scale Sampling, Rev. Sci. Instrum., Vol. 65, pp. 887-891.

Hallikainen, M. T., Ulaby, F. T., Dobson, M. C., El-Rayes, M.A., and Wu, L-K., 1985, Microwave dielectric behavior of wet soil part I: empirical models and experimental observations, IEEE Trans. Geoscince and Remote sensing, Vol. GE-23, No.1, 25-34.

Hasted, J. B., 1973, *Aqueous Dielectrics*, Chapman and Hall, London

Heimovaara, T. J., 1992, Comments on "time domain reflectometry measurements of water content and electrical conductivity of layered soil columns", Soil Sci. Soc. Am. J., Vol. 56, pp. 1657-1658.

Heimovaara, T. J., 1993, Design of triple-wire time domain reflectometry probe in practice and

theory, Soil Sci. Soc. Am. J., Vol. 57, pp. 1410-1417.

Heimovaara, T. J., 1994, Frequency domain analysis of time domain reflectormetry waveforms: 1 measurement of the complex dielectric permittivity of soils, Water Resources Research, Vol. 30, No. 2, pp. 189-199.

Heimovaara, T. J., 2001, Frequency domain modeling of TDR waveforms in order to obtained frequency dependent dielectric properties of soil samples: a theoretical approach, 2nd International Symposium and Workshop on Time Domain Reflectometry for Innovative Geotechnical Applications, Evanston, Illinois, Sept. 5-7, 2001.

Heimovaara, T. J. and Bouten, W., 1990, A computer-controlled 36-channel time domain reflectometry system, Water Resources Research, Vol. 36, No. 10, pp. 2311-2316.

Heimovaara, T. J., Bouten, W., and Verstraten, J. M., 1994, Frequency domain analysis of time domain reflectormetry waveforms: 2. a four-component complex dielectric mixing model for soils, Water Resources Research, Vol. 30, No. 2, pp. 201-209.

Heimovaara, T. J., Focke, A. G., Bouten, W., and Verstraten, J. M., 1995, Assessing temporal variation in soil water composition with time domain reflectometry, Soil Sci. Soc. Am. J., Vol. 59, pp. 689-698.

Heimovaara, T. J., de Winter, E. J. G., van Loon, W. K. P., and Esveld, D. C., 1996, Frequency-dependent dielectric permittivity form 0 to 1 GHz: time domain reflectomrtry measurement compared with frequency domain network analyzer measurements, Water Resources Research, Vol. 32, No. 12, pp. 3603-3610.

Herkelrath, W. N., Hamburg, S. P., and Murphy, F., 1991, Automatic real-time monitoring of soil moisture in a remote field area with time-domain reflectometry, Water Resour. Res., Vol. 27, pp. 857-864.

Hillhorst, M. A., 1998, *Dielectric Characterization of Soil*, Ph.D. Thesis, Wageningen, Netherlands.

Hilhorst, M. A. and Dirkson, C., 1994, Dielectric water content sensors: time domain versus frequency domain, Symposium and Workshop on Time domain Reflectometry in Environmental, Infrastructure, and Mining Applications, Evanston, IL., Spec. Publ. SP 19-94, pp. 23-33.

Huisman, J. A., and Bouten, W., 1999, Comparison of calibration and direct measurement of cable and probe properties in time domain reflectometry, Soil Sci. Soc. Am. J., Vol. 63,

pp. 1615-1617.

Kamey, T., and Iawasaki, K., 1995, Evaluation of undrained shear strength of cohesive soils using a flat dilatometer, Soils and Foundations, Vol. 35, pp. 111-116.

Kirkby, D., 1996, Finding the characteristics of arbitrary transmission lines, Amateur Radio Journal QEX December, pp. 3-10.

Klein, L. A., and Swift, C. T., 1977, An improved model for the dielectric constant of sea water at microwave frequencies, IEEE Trans. Antennas Propag., Vol. 25, pp. 104-111.

Klemunes, J. A., Mathew, W. W., and Lopez, Jr, A., 1997, Analysis of methods used in time domain reflectometry response, Trans. Res. Rec., Vol. 1548, pp. 89–96.

Knight, J. H., 1992, Sensitivity of time domain reflrctometry measurements to lateral variations in soil water content, Water Resource Research, Vol. 28, pp. 2345-2352.

Knight, J. H., Ferre, P. A.., Rudolph, D. L., and Kachanoski, R. G., 1997, A numerical analysis of the effects of coatings and gaps upon relative dielectric permittivity measurement with time domain reflectimetry, Water Resource Research, Vol. 33, pp. 1455-1460.

Knowlton, R., Strong, W., Onsurez, J., and Rogoff, E., 1995, Advances in hydrologic measurement techniques – in situ and cone penetrometer applications, Environmental Monitoring and Hazardous Waste Site Characterization, Proceedings of SPIE, Vol. 2504, pp. 592-599.

Lewis, A. J., and Rasmussen, T. C., 1996, *A New, Passive Technique for the In Situ Measurement of Total Suspended Solids Concentrations in Surface Water*, Technical Completion Report for Project # 14-08-001-G-2013 (07), U.S. Department of the Interior, Geological Survey.

Li, X., Lei, T., Wang, W., Xu, Q., and Zhao, J., 2005, Capacitance sensors for measuring suspended sediment concentration, Catena, Vol. 60, pp. 227–237.

Lin, C. -P., 1999, *Time Domain Reflectometry for Soil Properties*, PhD, Thesis, Purdue University, U.S.

Lin, C. -P., Drnevich, V. P., Feng, W., and Deschamps, R. J., 2000, Time domain reflectometry for compaction quality control, Use of Geophysical Methods in Construction, Geotechnical Special Publication No. 108, ASCE, pp. 15-34.

Lin, C. –P., 2003a, Analysis of a non-uniform and dispersive TDR measurement system with application to dielectric spectroscopy of soils, Water Resources Research Vol. 39, 1012, doi:10.1029/2002WR001418.

Lin, C. –P., 2003b, Frequency domain versus travel time analyses of TDR waveforms for soil moisture measurement, Soil Sci. Soc. Am. J., pp.720-729.

Lin, C.-P., and Tang, S. -H., 2007, Comprehensive wave propagation model to improve TDR interpretations for geotechnical applications, Journal of Geotechnical and Geoenvironmental Engineering, Vol. 30, Paper ID GTJ 100012.

Logsdon, S. D., 2000, Effect of cable length on time domain reflectometry calibration for high surface area soils, Soil Sci. Soc. Am. J., Vol. 64, pp. 54-61.

Marchetti, S., 1980, In situ tests by flat dilatometer, Journal of Geotechnical Engineering Division, ASCE, Vol. 106(GT3), pp. 299-321.

Marchetti, S. and Crapps, D. K., 1981, *Flat Dilatometer Manual*, Internal Report of G.P.E. Inc.

Mattei, E., Di Matteo, A., De Santis, A., and Pettinelli, E., 2006, Role of dispersion effects in determining probe and electromagnetic parameters by time domain reflectometry, Water Resour. Res, Vol. 42, W08408.

Maxwell Garnett, J. C., 1904, Colours in metal glasses and metal films, Trans. of the Royal Society, (London), Vol. CCIII, pp. 385-420.

Mironov, V. L., Dobson, M. C., Kaupp, V. H., Komarov, S. A., and Kleshchenko, V. N., 2004, Generalized refractive mixing dielectric model for moist soils, IEEE, Trans. on Geoscience and Remote Sensing, Vol. 42, pp. 773-785.

Mitchell, J. K., 1992, *Fundamentals of Soil Behavior 2nd Edition*, John Wiley & Sons, Inc., US.

Morris, G. L., and Fan, F., 1998, *Reservoir Sedimentation Handbook*, McGraw-Hill, USA.

Mualem, Y., and Friedman, S. P., 1991, Theoretical prediction of electrical conductivity in saturated and unsaturated soil, Water Resources Research, Vol. 27, pp. 2771-2777.

Nadler, A., Dasberg, S., and Lapid, I., 1991, Time domain reflectometry measurements of water content and electrical conductivity of layered soil columns, Soil Sci. Soc. Am. J., Vol. 55, pp. 938-943.

Nadler, A., Green, S. R., Vogeler, I., and Clothier, B. E., 2002, Horizontal and vertical TDR measurements of soil water content and electrical conductivity, Soil Sci. Soc. Am. J., Vol. 66, pp. 735-743.

National Research Council, 2000, *Seeing into the Earth: Noninvasive Characterization of the Shallow Subsurface for Environmental and Engineering Application*, National Academy Press, Washington D. C., USA.

Nazarian, S. and Stoke II, K.H., 1986, In situ determination of elastic module of pavements systems by spectral analysis of surface waves method (theoretical aspects), Research Report Number 437-2. US Department of Transportation, Federal Highway Administration, pp. 2–6.

Nelder, J. A., and Mead, R., 1965, A simplex method for function minimization, Comput. J., Vol. 7, pp. 308-313.

Nicholson, A. M., and Ross, G. F., 1970, Measurement of the intrinsic properties of materials by time domain techniques, IEEE Trans. Instrum. Meas., Vol. IM-19, pp. 377-383.

Nissen, H. H., Moldrup, P., Olesen, T., and Jensen, O. K., 2001, Time domain reflectometry sensitivity to lateral variations in bulk soil electrical conductivity, Soil Sci. Soc. Am. J., Vol. 65, pp. 1351-1360.

Nozaki, R., and Bose, T. A., 1990, Broadband complex permittivity measurement by time-domain spectroscopy, IEEE Trans. Instrum. Meas., Vol. 39, No. 6, 945-951.

Oppenheim, A. V. and Schafer, R. W., 1999, *Discrete-time Signal Processing 2nd Edition*, Prentice-Hall, Inc.

Or, D., and Rasmussen, V. P., 1999, Effective frequency of TDR travel time-based measurement of soil bulk dielectric permittivity, Third Workshop on Electromagnetic Wave Interaction with Water and Moist Substances, Russell Agricultural Research Center, Athens, GA, 12-13 April, 1999, pp. 257–260.

Or, D., and Wraith, J. M., 1999, Temperature effects on soil bulk dielectric permittivity measured by time domain reflectometry: a physical model, Water Resour. Res, Vol. 35, pp. 371–383.

Pepin, S., Livingston, N. J., and Hook, W. R., 1995, Temperature-dependent measurement errors in time domain reflectometry determinations of soil water, Soil Sci. Soc. Am. J., Vol. 59, pp. 38-43.

Purvance, D.T., and Andricevic, R., 2000, On the electrical-hydraulic conductivity correlation in aquifers, Water Resources Research, Vol. 36, pp. 2905-2913.

Ramo, S., Whinnery, J. R., and Duzer, T. V., 1994, *Fields and Waves in Communication Electromagnetics, 3rd edition,* Jown Wiley & Sons.

Reece, C.F., 1998, Simple method for determining cable length resistance in time domain reflectometry systems, Soil Sci. Soc. Am. J., Vol. 62, pp. 314-317.

Rhoades, J. D., Manteghi, N. A., Shouse, P. J., and Alves, W. J., 1989, Soil electrical conductivity and soil salinity: new formulation and calibrations, Soil Sci. Soc. Am. J., Vol. 53. pp. 433-439.

Robinson, D. A., Jones, S. B., Wraith, J. M., Or, D., and Friedman, S. P., 2003, A review of advances in dielectric and electrical conductivity measurement in soils using TDR, Vadose Zone J., Vol. 2, pp. 444-475.

Robinson, D. A., Schaap, M., Jones, S. B., Friedman, S. P., and Gardner, C. M. K., 2003, Considerations for improving the accuracy of permittivity measurement using time domain reflectometry: air-water calibration, effects of cable length, Soil Sci. Soc. Am. J., Vol. 67, pp. 62–70.

Robinson, D. A., Schaap, M. G., Or, D., and Jones, S. B., 2005, On the effective measurement frequency of time domain reflectometry in dispersive and non-conductive dielectric materials, Water Resour. Res., Vol. 40, W02007, doi:10.1029/2004WR003816.

Santamarina, J. C., Klein, K. A., and Fam, M. A., 2001, *Soils and Waves: Particulate Materials Behavior, Characterization and Process Monitoring*, John Wiley, New York.

Schaap, M. G., Robinson, D. A., Friedman, S. P., and Lazar, A., 2003, Measurement and modeling of the TDR signal propagation through layered dielectric media, Soil Sci. Soc. Am. J., Vol. 67, pp. 1113-1121.

Siddiqui, S. I. and Drnevich, V. P., 1995, *Use of Time Domain Reflectometry for the Determination of Water Content and Density of Soil*, FHWA/IN/JHRP-95/9, Purdue university

Siddiqui, S. I., Drnevich, V. P., and Deschamps, R. J, 2000, Time domain reflectometry development for use in geotechnical engineering, Geotechnical Testing Journal, Vol. 23, pp. 9-20.

Sihvola, A., 1999, *Electromagnetic Mixing Formulas and Applications*, The Institute of Electrical Engineers, IEE.

Singh G., Das, B. M., and Chong, M. K., 1997, Measurement of moisture content with a penetrometer, Geotechnical Testing Journal, Vol.20, pp. 317-323.

Spaans E. J. A. and Baker, J. M., 1993, Simple baluns in parallel probes for time domain reflectometry, Soil Sci. Soc. Am. J., Vol. 57, pp. 668–673.

Starr, G. C., 2005, Basal sediment concentration measurement using a time domain reflectometry method, Transactions of the ASAE, Vol. 48, pp. 205-209.

Starr, J. L., and Paltineanu, I. C., 1998, Real-time soil water dynamics over large areas using multisensor capacitance probes and monitoring system, Soil and Tillage Research, Vol. 47, pp. 43-49.

Stogryn, A. 1971, Equations for calculating the dielectric constant of saline water, IEEE Trans. Microwave Theory Techn., Vol. 19, pp. 733-736.

Su, M. B., 1987, *Quantification of Cable Deformation with Time Domain Reflectometry*, Ph.D. Dissertation, Northwestern Univ., Evanston, IL.

Sutherland, T. F., Lane, P. M., Amos, C. L., and Downing, J., 2000, The calibration of optical backscatter sensors for suspended sediment of varying darkness levels, Marine Geology, Vol. 162, pp. 587-597.

Tang, S. -H., 2007, *Effect of Cable Resistance on TDR Measurements – Theoretical Modeling and Applications*, Ph.D. Thesis, National Chiao Tung University, Taiwan, R.O.C.

Timlin, D. J., and Pachepsky, Y. A., 1996, Comparison of three methods to obtain the apparent dielectric constant from time domain reflectometry wave traces, Soil Sci. Soc. Am. J., Vol. 60, pp. 970–977.

Thorne, P. D., and Hanes, D. M., 2002, A review of acoustic measurements of small-scale sediment processes, Continental Shelf Research, Vol. 22, pp. 1-30.

Topp, G. C., Davis, J. L., and Annan, A. P., 1980, Electromagnetic determination of soil water content and electrical conductivity measurement using time domain reflectometry, Water Resources Research, Vol. 16, pp. 574-582.

Topp, G. C., and Ferre, P. A., 2002, Water Content, in Methods of Soil Analysis, part 4, Physical Methods, SSSA Book Ser., vol. 5, edited by J. H. Dane and G. C. Topp,

pp.417-421, Soil Sci. Soc. of Am., Madison, Wis.

Topp, G. C., Yanuka, M., Zebchuk, W. D., and Zegelin, S., 1988, Determination of electrical conductivity using time domain reflectometry: soil and water experiments in coaxial lines, Water Resources Research, Vol. 24, pp. 945-952.

Topp, G.C., Yanuka, M., Zebchuk, W. D., and Zegelin, S., 1988, Determination of electrical conductivity using time domain reflectometry: soil and water experiments in coaxial lines, Water Resour. Res., Vol. 24, pp. 945-952.

Topp, G. C., Zegelin, S., and White, I., 2000,"Impacts of the real and imaginary components of relative permittivity of time domain reflectometry measurement in soils, Soil Sci. Soc. Am. J., Vol. 64, pp. 1244-1252.

Vanclooster, M., Mallants, D., Vanderborght, J., Diels, J., van Orshoven, J., and Feyen, J., 1995, Monitoring solute transport in a multi-layered sandy lysimeter using time domain reflectometry, Soil Sci. Soc. Am. J., Vol. 59, pp. 337–344.

Vaz, C. M. P., and Hopmans, J. W., 2001, Simultaneous measurement of soil penetration resistance and water content with a combined penetrometer–TDR moisture probe, Soil Sci. Soc. Am. J., Vol. 65, pp. 4–12.

Vaz, C. M. P., Bassoi, L. H., and Hopmans, J. W., 2004, Contribution of water content and bulk density to field soil penetration resistance as measured by a combined cone penetrometer–TDR probe, Soil and Tillage Research, Vol. 60, pp. 35-42.

Von Hippel, A. R., 1954, *Dielectrics and Waves*, John Wiley, Hoboken, N. J.

Ward, A. L., Kachanoski, R. G., and Elrick, D. E., 1994, Laboratory measurements of solute transport using time domain reflectometry, Soil Sci. Soc. Am. J., Vol. 58, pp. 1031–1039.

Weast, R. C., 1986, *CRC Handbook of Chemistry and Physics*, 67th ed., CRC Press, Boca Raton, Fla.

Weerts, A. H., Huisman, J. A., and Bouten, W., 2001, Information content of time domain reflectometry waveforms, Water Resour. Res., Vol. 37, pp. 1291-1299.

Wren, D.G., Barkdoll, B. D., Kuhnle, R. A., and Derrow, R. W., 2000, Field techniques for suspended-sediment measurement, J. Hydr. Engrg., ASCE, Vol. 126, pp. 97-104.

Yanuka, M., Topp, G. C., Zegelin, S., and Zebchuk, W. D., 1988, Multiple reflection and attenuation of time domain reflectometry pulses: theoretical consideration for application

to soil and water, Water Resour. Res., Vol. 24, pp. 939-944.

Young, G.D., Adams, B.A., and Topp, G.C., 1999, A portable data collection system for simultaneous cone penetrometer force and volumetric soil water content measurements, Canadian Journal of Soil Science, Vol. 80, pp. 23-31.

Yu, X. and Drnevich, V.P., 2004, Soil water content and dry density by time domain reflectometry, Journal of Geotechnical and Geoenvironmental Engineering, ASCE, Vol. 130, pp.922-934.

Zegelin, S., White, I., and Jenkins, D. R., 1989, Improved filed probes for soil water content and electrical conductivity measurement using time domain reflectometry, Water Resources Research, Vol. 25, pp. 2367-2376.

Appendix: Elementary Dyadic Analysis

Notation and definitions

The dyadic product, which combines two vectors without any operation in between. The simple vector pair **ab** is called a dyad, which is defined as:

$$
\begin{aligned}
ab &= \left(a_x u_x + a_y u_y + a_z u_z \right)\left(b_x u_x + b_y u_y + b_z u_z \right) \\
&= a_x b_x u_x u_x + a_x b_y u_x u_y + a_x b_z u_x u_z \\
&\quad a_y b_x u_y u_x + a_y b_y u_y u_y + a_y b_z u_y u_z \\
&\quad a_z b_x u_z u_x + a_z b_y u_z u_y + a_z b_z u_z u_z
\end{aligned}
\qquad \text{[A-1]}
$$

where u_i is unit vectors.   A general dyadic is a polynomial of dyads:

$$
\overline{\overline{A}} = \sum_{i=1}^{n} a_i b_i
\qquad \text{[A-2]}
$$

As defined in Eq. [A-2], the dyadic character of the quantity $\overline{\overline{A}}$ is emphasized by a double overbar.   A dyadic, like a matrix, can be interpreted as an operation on a vector, the result of which is another vector:

$$
d = \overline{\overline{A}} \cdot c = \left(\sum_{i=1} a_i b_i \right) \cdot c = \sum_{i=1} a_i \left(b_i \cdot c \right)
\qquad \text{[A-3]}
$$

From this it can be seen that the vectors c and d are not necessarily parallel.   Other operations are shown as:

$$\overline{\overline{A}}_1 \cdot \left(\overline{\overline{A}}_2 \cdot c \right) = \left(\overline{\overline{A}}_1 \cdot \overline{\overline{A}}_2 \right) \cdot c \qquad \text{[A-4]}$$

$$\overline{\overline{A}}_1 \cdot \left(\overline{\overline{A}}_2 \cdot \overline{\overline{C}} \right) = \left(\overline{\overline{A}}_1 \cdot \overline{\overline{A}}_2 \right) \cdot \overline{\overline{C}} \qquad \text{[A-5]}$$

$$\overline{\overline{A}} \cdot \left(\overline{\overline{B}} + \overline{\overline{C}} \right) = \overline{\overline{A}} \cdot \overline{\overline{B}} + \overline{\overline{A}} \cdot \overline{\overline{C}} \qquad \text{[A-6]}$$

however, it is not commutative: in general

$$\overline{\overline{A}} \cdot \overline{\overline{B}} \neq \overline{\overline{B}} \cdot \overline{\overline{A}} \qquad \text{[A-7]}$$

A useful dyadic is the unit dyadic with the property that it relates any vector with the same vector:
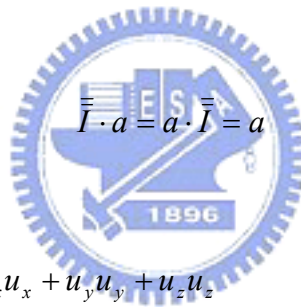
$$\overline{\overline{I}} \cdot a = a \cdot \overline{\overline{I}} = a \qquad \text{[A-8]}$$

In the Cartesian system, $\overline{\overline{I}} = u_x u_x + u_y u_y + u_z u_z$

Operations and invariants

1. <u>Transpose operation and symmetry</u>

The transport switches between the two vectors in dyads and is denoted by a superscript T:

$$\overline{\overline{A}}^T = \left(\sum_i a_i b_i \right)^T = \sum_i b_i a_i \qquad \text{[A-9]}$$

Every anti-symmetric dyadic can be represented in the form:

$$\overline{\overline{A}}_{as} = c \times \overline{\overline{I}} \qquad\qquad \text{[A-10]}$$

which is clear when one notes the anti-commutativity of the vector product:

$$\overline{\overline{A}}_{as} \cdot a = c \times a = -a \times c = -a \cdot \overline{\overline{A}}_{as} = -\overline{\overline{A}}_{as}^{\ T} \cdot a \qquad\qquad \text{[A-11]}$$

A projection of a vector on a plane can be performed by a two-dimensional unit dyadic:

$$\overline{\overline{I}}_t = \overline{\overline{I}} - uu \qquad\qquad \text{[A-12]}$$

where u is the unit vector perpendicular to the plane.

2.   Double-dot and double-cross products

The double-dot product $\overline{\overline{A}} : \overline{\overline{B}}$ between two dyadics can be written with the following rule:

$$(ab):(cd) = (a:c)(b:d) \qquad\qquad \text{[A-13]}$$

and the result is a scalar obeying the symmetry relations $\overline{\overline{A}} : \overline{\overline{B}} = \overline{\overline{B}} : \overline{\overline{A}} = \overline{\overline{A}}^T : \overline{\overline{B}}^T$. Correspondingly, the double-cross product $\overline{\overline{A}} \, {}^\times_\times \, \overline{\overline{B}}$ between two dyadics is defined with the rule for dyads:

$$(ab) {}^\times_\times (cd) = (a \times c)(b \times d) \qquad\qquad \text{[A-14]}$$

This product gives as its output another dyadic, and the double-cross is commutative.

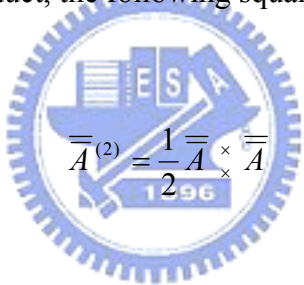As examples, the double-cross products between two unit dyadics obey:

$$\bar{\bar{I}} : \bar{\bar{I}} = 3 , \; \bar{\bar{I}} \; {\overset{\times}{\times}} \; \bar{\bar{I}} = 2\bar{\bar{I}} \qquad \text{[A-15]}$$

which are transparently satisfied; Furthermore:

$$\bar{\bar{I}}_t : \bar{\bar{I}}_t = 2 , \; \bar{\bar{I}}_t \; {\overset{\times}{\times}} \; \bar{\bar{I}}_t = 2uu \qquad \text{[A-16]}$$

where u is the unit vector normal to the plane of the transversal unit dyadic.

With the double-cross product, the following square of a dyadic can be defined:

$$\bar{\bar{A}}^{(2)} = \frac{1}{2} \bar{\bar{A}} \; {\overset{\times}{\times}} \; \bar{\bar{A}} \qquad \text{[A-17]}$$

which is a very important definition. This cross-product square must be distinguished form the ordinary second power of a dyadic, which is

$$\bar{\bar{A}}^2 = \bar{\bar{A}} \cdot \bar{\bar{A}} \qquad \text{[A-18]}$$

The rarer mixed double-product are sometimes useful. In obvious manner, we have

$$(ab) \; {\overset{\times}{\cdot}} \; (cd) = (a \times c)(b \cdot d) \qquad \text{[A-19]}$$

$$(ab) \; {\overset{\cdot}{\times}} \; (cd) = (a \cdot c)(b \times d) \qquad \text{[A-20]}$$

These operations can be used to extract the anti-symmetric part of a dyadic. The vector c corresponding to the anti-symmetric part of a dyadic $\overline{\overline{A}}$ is

$$c = \frac{1}{2}\overline{\overline{I}} \overset{\times}{\cdot} \overline{\overline{A}} = \frac{1}{2}\overline{\overline{A}} \overset{\cdot}{\times} \overline{\overline{I}} \tag{A-21}$$

because $\overline{\overline{S}} \overset{\cdot}{\times} \overline{\overline{I}} = 0$ for any symmetric dyadic $\overline{\overline{S}}$, and $\left(c \times \overline{\overline{I}}\right) \overset{\cdot}{\times} \overline{\overline{I}} = 2c$. This operation is also connected to the replacement of the dyadic products by cross products:

$$\left(\sum_i a_i b_i\right) \overset{\times}{\cdot} \overline{\overline{I}} = \sum_i a_i \times b_i \tag{[A-22]}$$

3. Trace and determinant

An important scalar function of a dyadic is its *trace* (tr). The trace can be calculated by taking the double-dot product with unit dyadic:

$$tr\overline{\overline{A}} = \overline{\overline{A}} : \overline{\overline{I}} \tag{[A-23]}$$

In practical dyadic work, the trace of a dyadic can be calculated easily by taking the sum of the scalar products of the vector pairs:

$$tr\overline{\overline{A}} = \left(\sum_i a_i b_i\right) : \overline{\overline{I}} = \sum_i a_i \cdot b_i \tag{[A-24]}$$

Another invariant is the sum of principle minors (spm),

$$spm\overline{\overline{A}} = \frac{1}{2}\overline{\overline{A}} \overset{\times}{\underset{\times}{}} \overline{\overline{A}} : \overline{\overline{I}} \qquad\qquad [\text{A-25}]$$

and it can be equal to the trace of the $\overline{\overline{A}}^{(2)}$

$$spm\overline{\overline{A}} = tr\overline{\overline{A}}^{(2)} \qquad\qquad [\text{A-26}]$$

The determinant (det) is a very important cubic function of a dyadic:

$$\det \overline{\overline{A}} = \frac{1}{6}\overline{\overline{A}} \overset{\times}{\underset{\times}{}} \overline{\overline{A}} : \overline{\overline{A}} \qquad\qquad [\text{A-27}]$$

Equipped with a definition for the determinant, the inverse of a dyadic can be written:

$$\overline{\overline{A}}^{-1} = \frac{\overline{\overline{A}}^{(2)T}}{\det \overline{\overline{A}}} = 3\frac{\left(\overline{\overline{A}} \overset{\times}{\underset{\times}{}} \overline{\overline{A}}\right)^{T}}{\overline{\overline{A}} \overset{\times}{\underset{\times}{}} \overline{\overline{A}} : \overline{\overline{A}}} \qquad\qquad [\text{A-28}]$$

Note that the inverse of a dyadic exists only for those dyadics that have a nonzero determinant. Such dyadics are called *complete* dyaidcs.

The inverse of a dot-product of dyadics can be calculated be inverting the order of inverses:

$$\left(\overline{\overline{A}} \cdot \overline{\overline{B}}\right)^{-1} = \overline{\overline{B}}^{-1} \cdot \overline{\overline{A}}^{-1} \qquad\qquad [\text{A-29}]$$

One often encounters the term the dyadic *adjoint* to a given dyadic, which simply is

$$adj\overline{\overline{A}} = \overline{\overline{A}}^{(2)T} = \frac{1}{2}\left(\overline{\overline{A}} \underset{\times}{\times} \overline{\overline{A}}\right)^{T} \qquad\qquad \text{[A-30]}$$

The adjoint of the unit dyadic is itself: $adj\overline{\overline{I}} = \overline{\overline{I}}$. The determinant of the unit dyadic is unity, and its sum of principle minor is three.